UNIVERSITY OF LIVERPOOL

Multifunctional Magnetic Nanoparticles for Biomedical Applications

Thesis submitted in accordance with the requirements of the University of Liverpool for the degree of

Doctor in Philosophy

by

Cristina I. Olariu

August 2012

Abstract

The objective of this thesis was to develop and prepare multifunctional magnetic nanoparticles with targeting and bimodal imaging capabilities for cancer diagnostic applications.

Superparamagnetic iron oxide nanoparticles (SPIONs) were the key component in the multifunctional nanoparticles prepared. In a first approach, alkoxysilane ligands were used to introduce functional groups such as amino, bromo, iodo, nitrile, and vinyl on the surface of SPIONs. Physicochemical analyses showed that each silane ligand formed a dense silane monolayer covalently attached to the nanoparticle surface. The amino-functionalised SPIONs were successfully modified yielding amino and carboxylic acid-bifunctionalised SPIONs using a succinylation reaction. This nanoparticle system showed no cytotoxicity during cell viability evaluations. Further conjugation with fluorescent dye and antibodies produced targeted bimodal optical/magnetic resonance imaging (MRI) agents, confirmed by good contrast enhancement capabilities. The conjugated antibody successfully enabled the targeted delivery of SPIONs to pancreatic cancer cells *in vitro*. The targeting efficiency and the nanoparticle cellular uptake were monitored using fluorescence and confocal microscopy.

In a second approach, hydrophobic and monodisperse SPIONs were coated with amphiphilic polyoxazoline to produce colloidally stable magneto-micelles. This magneto-micellar system showed high colloidal stability in water, phosphate buffered saline as well as at different pH values. Fluorescent dyes were successfully co-assembled into the magneto-micelles providing for the localisation of the nanoparticles in the cells by confocal microscopy. Antibodies conjugated to nontoxic magneto-micelles allowed for binding to specific receptors present on pancreatic cancer cells. The targeting efficiency and accumulation of the antibody labelled magneto-micelles into pancreatic cancer cells was evaluated using live cell confocal microscopy. Their performance as MRI contrast agents was evaluated using relaxivity measurements and it was shown that the clustering effect of the SPIONs within the core of the micelle is particularly favourable for enhancing the contrast on MRI images. Both approaches provided efficient routes of preparation of multifunctional platforms to achieve the desired targeting and bimodal imaging capabilities.

Table of contents

Abbreviations

Abs	Antibodies
APTES	3-aminopropyltriethoxy silane
ATRP	Atom transfer radical polymerisation
BPTMS	3-bromopropyltrimethoxy silane
BSA	Bovine serum albumin
BxPC-3	Cell line derived from human primary pancreatic adenocarcinoma
CD	Cluster of differentiation
CEA	Carcinoembryonic antigen
CLIO	Cross-linked iron oxide
CPTES	3-cyanopropyltriethoxy silane
CytC	Cytochrome C
DAPI	4',6-diamidino-2-phenylindole dilactate
DLS	Dynamic Light Scattering
DMEM	Dulbecco modified eagle medium
DMF	Dimethylformamide
DMSO	Dimethylsulfoxide
E-14	Embryonic stem cell line derived from mouse
EDC	Ethyl-3-dimethylaminopropyl carbodiimide
EGFR	Endothelial growth factor
EPCAM	Epithelial cell adhesion molecule
EPR	Enhanced permeability and retention
FDA	Food and drug administration
$Fe(acac)_3$	Iron acetylacetonate
$Fe(CO)_5$	Iron pentacarbonyl
$Fe(Cup)_3$	Iron cupferron

FITC	Fluorescein isothiocyanate
FTIR	Fourier transform infrared spectroscopy
HIV	Human immunodeficiency virus
IgG	Immunoglobulin G
IO	Iron oxide
IPTMS	3-iodopropyltrimethoxy silane
ISO	Isotype control antibody
MCL	Cationic liposomes
MMM	Multifunctional magneto-micelles
MPS	Mononuclear phagocytic system
MRI	Magnetic resonance imaging
MTS	3-(4,5-dimethylthiazol-2-yl)-5-(3-carboxymethoxyphenyl)-2-(4-sulfophenyl)-2H-tetrazolium
MTX	Methotrexate
MWCO	Molecular weight cut off
NBAMS	Nanoprobe-based affinity mass spectrometry
NHS	N-hydroxysuccinimide
NIR	Near infrared
NIRF	Near infrared fluorescence
NMR	Nuclear magnetic resonance
NPs	Nanoparticles
PAA	Polyacrylic acid
PAION	Poly(amino acid) coated iron oxide nanoparticles
Panc-1	Epithelial-like cell line derived from human pancreatic carcinoma
PBS	Phosphate buffered saline
PDEAEMA	Poly(2-(diethylamino)ethyl methacrylate)
PEG	Polyethylene glycol

PEtOX	Poly(2-ethyl-2-oxazoline)
PLGA	Poly-lactic-*co*-glycolic acid
Pluronic	Poly(ethylene glycol)-poly(propylene glycol)-poly(ethylene glycol)
PTA	Phosphotungstic acid
PVA	Polyvinyl alcohol
PXRD	Powder x-ray diffraction
RGD	Arginylglycylaspartic acid tripeptide
Rh	Octadecyl rhodamine B chloride
RITC	Rhodamine B isothiocyanate
rt	Room temperature
scFv	Single-chain variable fragment
sulfo-NHS	N-hydroxysulfosuccinimide
SPIONs	Superparamagnetic iron oxide nanoparticles
SQUID	Superconducting quantum interference device
SUIT-2	Cell line derived from metastatic human pancreatic carcinoma
T_2	Transverse relaxation time
TEM	Transmission electron microscopy
TGA	Thermogravimetric analysis
THF	Tetrahydrofuran
TRIZMA	Tris(hydroxymethyl) aminomethane
USPIO	Ultrasmall superparamagnetic iron oxide
VTMS	vinyltrimethoxysilane
WST-8	2-(2-methoxy-4-nitrophenyl)-3-(4-nitrophenyl)-5-(2,4-disulfophenyl)-2H-tetrazolium

Chapter 1

Introduction - Superparamagnetic iron oxide nanoparticles in biomedicine

1.1 Overview

Nanomaterials have significantly influenced modern science and have found their way into important applications such as information storage[1-3], catalysis,[4-5] sensing,[6-8] energy storage,[9-10] coatings,[11-12] food industry,[13] water purification[14] and biomedicine.[15-16] Biomedicine is a particularly promising direction for nanosciences as it can potentially transform the current therapeutic and diagnostic techniques.

Amongst all types of nanomaterials, superparamagnetic iron oxide nanoparticles (SPIONs) are perhaps the most studied type of nanoparticles for biomedicine. The high interest for using SPIONs for biomedical diagnosis and therapy is attributed to their superparamagnetic properties at room temperature (actuated by an external magnetic field but no magnetic remanence once the field has been removed), biocompatibility, and low cost. While the *in vivo* application of other types of nanoparticles is still impeded by concerns over their toxicity, SPIONs have received the approval of the Food and Drug Administration (FDA) for clinical use in humans, for example, as magnetic resonance imaging (MRI) signal enhancers and hyperthermia therapeutical agents.[17-18]

Three key biomedical areas of application of SPIONs, diagnosis, therapy and separations, are shown in **Figure 1.1**. Within these areas there are several specialised

domains such as cell isolation,[19-20] bio-sensing,[21-22] drug delivery,[23-26] hyperthermia [18,27] and MRI.[15,28-29]

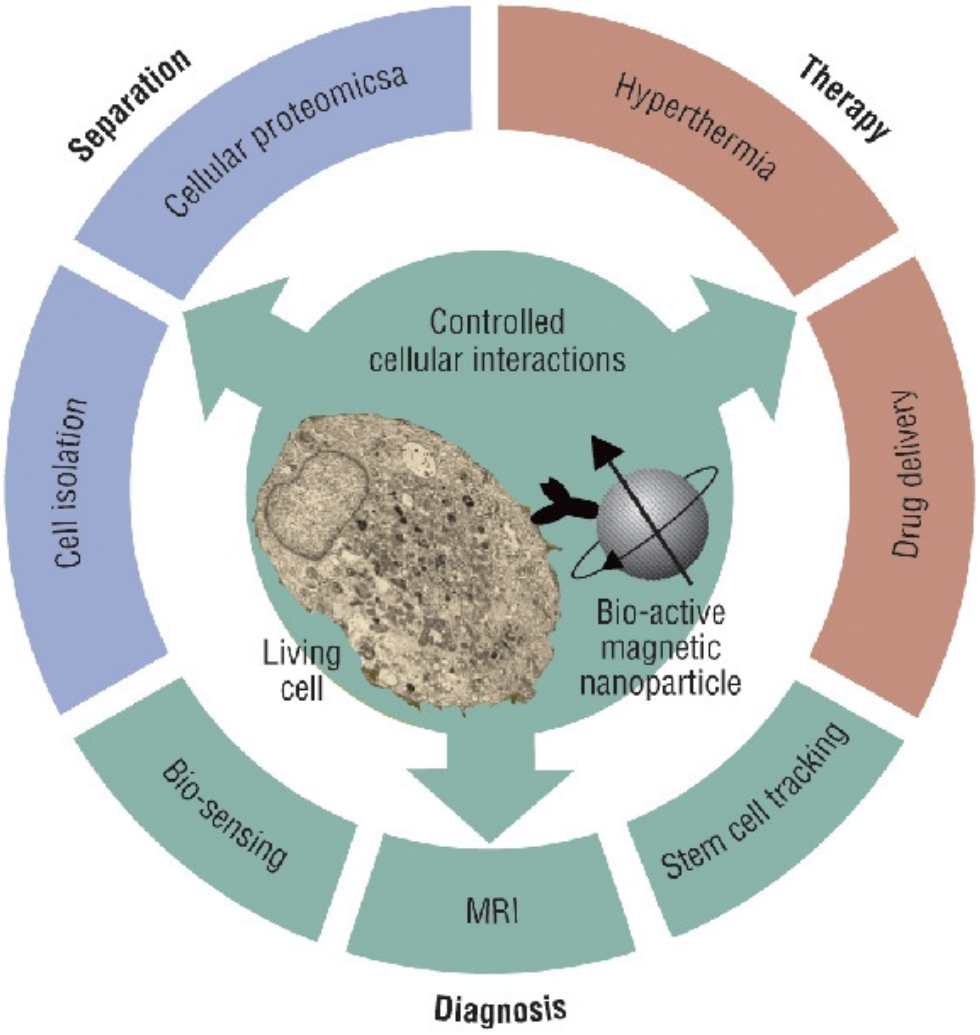

Figure 1.1 Possible areas of application for superparamagnetic iron oxide nanoparticles. The schematic is taken from ref. 30

This chapter will review some of the most recent work with respect to synthesis, surface modification and functionalisation of SPIONs. The recent advances of SPIONs application in MRI, hyperthermia, drug delivery and the current tendency of combining SPIONs with other functional components to form multifunctional nanocomposites will be reviewed as well in this chapter.

1.2 Synthesis of SPIONs

1.2.1 Background on magnetic properties

An unpaired electron which rotates around its own axis has a "spin". The spin induces a magnetic moment that means that the electron behaves as a small magnet. Therefore, the availability of unpaired electrons in a substance can lead to a variety of magnetic effects. Applying an external magnetic field to a material aligns the electrons within the field. In this case, the material is magnetised and responds with a force to the field. As a result the value of the magnetisation, M is proportional to the magnetic field, H and is defined as:

$$M = \chi H \tag{1.1}$$

The proportion constant χ is called susceptibility. The susceptibility can depend on the number of oriented electrons per mol (χ_{mol}), volume (χ_{vol}) or gram (χ_g) of the material. As both M and H can be measured with high precision, for example, by measurements in superconducting quantum interference device (SQUID), the magnetic properties of solid materials can be evaluated and divided depending on the value of χ.

$\chi < 0$ – *diamagnetic*

$\chi > 0$ – *paramagnetic*

$\chi >> 0$ – *ferro-* or *ferrimagnetic*

Substances, which have only paired electrons, are called *diamagnetics*. Quantum theory allows only two orientations of the electron spins with identical quantum number. Therefore, two paired electrons, which are characterised by magnetic spin number $m_s=S=+1/2$ (spin up) or $m_s=S=-1/2$ (spin down), would compensate each other. *Diamagnetics* show only weak magnetic response by being expelled from the applied magnetic field due to a weak electromagnetic field generated by rotating electrons. Diamagnetism is a property of every material due to eminent presence of paired electrons.

Paramagnetics are characterised by presence of unpaired electrons which are randomly oriented on different atoms within the material. If an external magnetic field is applied to this material the electron spins tend to align themselves in the field and the material is magnetised as shown in the **Figure 1.2a**. Switching the field off returns the material into its original state due to the thermal motion. Thermal motion randomises the orientation of the electrons and therefore, the higher the temperature the smaller is the magnetisation of the paramagnetic material in an applied field.

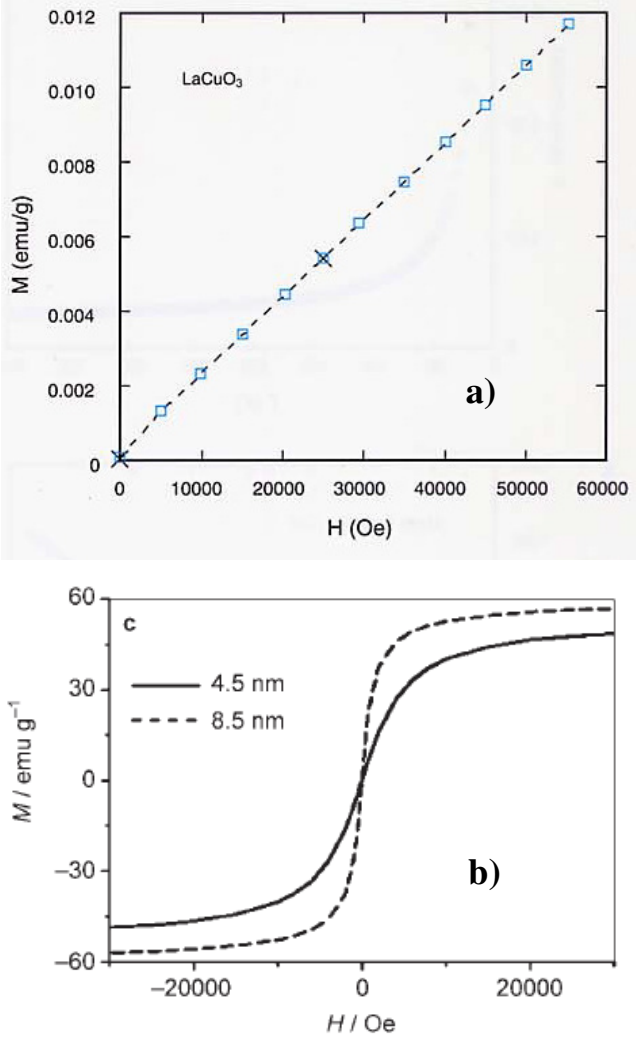

Figure 1.2 Dependence of magnetisation (M) from applied magnetic field (H) for (a) a paramagnetic compound, $LaCuO_3$ at T=100K and (b) superparamagnetic Fe_3O_4 nanoparticles at T=300K. Reproduced from ref. 31 and 32

In a *ferro-* and *ferrimagnetic* material the unpaired electrons are parallel to each other and act cooperatively. Due to magnetic domain formation, the magnetisation in such materials does not return to zero if the applied field is removed. Therefore, unlike *paramagnetics*, where thermal fluctuations negate alignment of the unpaired electrons, *ferro-* and *ferrimagnetics* show very strong magnetic properties. The cooperative action

of the unpaired electrons within adjusted domains prevents the misalignment which helps to retain the individual magnetic moments of the atoms lined up even in a zero field. *Ferro-* and *ferrimagnets* are important industrial materials and are used in electromagnets, generators, transformers and hard disks due to their magnetic properties. Magnetite, Fe_3O_4 is a particularly interesting example which is used in water decontamination, in catalysis or in magnetic storage.[33-34]

Bulk magnetite, Fe_3O_4 is *ferrimagnetic* and crystallizes in an inverse spinel structure type.[35] Within the structure there are two types of Fe cations – Fe^{2+} and Fe^{3+} which are coordinated tetrahedrally and octahedrally by oxygen atoms. Both Fe^{2+} and Fe^{3+} cations are in a high spin configuration that means they have four and five unpaired electrons respectively. However, in magnetite the unpaired electrons from Fe^{3+} cations compensate each other and the net magnetic moment originates only from the Fe^{2+} cations as shown in the **Figure 1.3**. In the bulk due to the presence of magnetic domains Fe_3O_4 shows very similar behaviour to a typical *ferromagnetic* material, for example, remanent magnetisation after the applied field is zero. However, if the magnetic domains in magnetite could be individually isolated, for example, in a form of magnetite (Fe_3O_4) nanoparticle, this can lead to an interesting property called *superparamagnetism*.

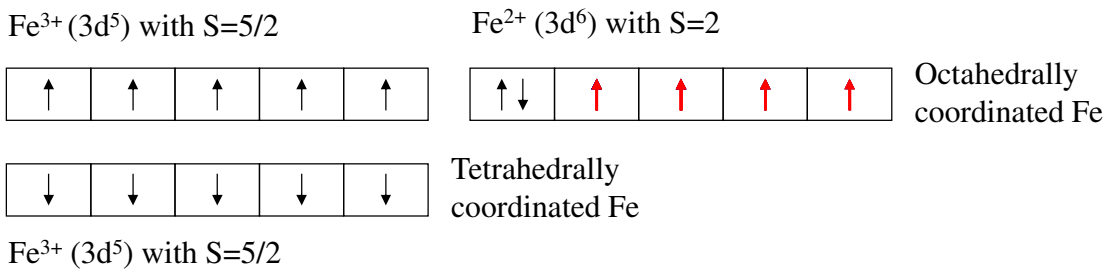

Figure 1.3 Spin arrangement in Fe_3O_4. The unpaired electrons from the Fe^{3+} cations are compensating each other and the net moment is from four unpaired electrons from the Fe^{2+} cation which are shown in red.

In a superparamagnetic state the material behaves paramagnetic while retaining the exceptionally strong magnetic properties of the corresponding bulk *ferro-* or *ferrimagnetic* material. For example, *superparamagnetics* show no remanent magnetic moment after applied field is switched to zero (**Figure 1.2b**). This effect makes superparamagnetic materials such as Fe_3O_4 nanoparticles especially appealing for biomedical applications as they can be manipulated by magnetic field without induced aggregation.

Superparamagnetism is observed in iron oxide nanoparticles with sizes between 2 and 30 nm.[29] Within the nanoparticle the unpaired electrons are aligned and as a result each nanoparticle possesses an individual magnetic moment. However, as the nanoparticles in a superparamagnetic material consist of a single magnetic domain the thermal energy is enough to induce random fluctuations of the magnetic moments. The fluctuation of the magnetic moment of each nanoparticle is then determined by equation 1.2:

$$\tau = \tau_0 \exp\left(\frac{KV}{k_B T}\right) \qquad (1.2),$$

where τ is the mean time between flips, τ_0 is the relaxation time at one orientation, K is the magnetic anisotropy constant of the nanoparticle, V is the particle volume, k_B is the Boltzmann constant and T is the temperature.

From this equation it is evident that the nanoparticle volume (V) plays an important role in determining the superparamagnetic character. As the size of a nanoparticle decreases to a level where KV (free-energy barriers) becomes comparable to k_BT (thermal energy), its magnetic moment starts to fluctuate from one orientation to another, leaving the overall magnetisation zero. Therefore, superparamagnetic nanoparticles exhibit a net magnetisation only when submitted to an external magnetic field and relax to the initial state once the field has been removed.

Magnetite (Fe_3O_4) and maghemite (γ-Fe_2O_3) are two forms of iron oxide nanoparticles which are commonly used for biomedical applications.[36-37] In the biomedical field the two forms are not distinguished and are generally called SPIONs. In bulk form iron oxides are strongly magnetic with saturation magnetisation values reaching 92 emu/g and 78 emu/g for magnetite and maghemite respectively. For the corresponding nanoparticle forms of iron oxides the saturation magnetisation is lower and is attributed to the size decrease and surface effects.[38-41]

1.2.2 Characterisation of nanoparticles

The characterisation of the physicochemical properties of nanoparticle is very important because these properties will determine their behaviour in the human body. This section provides a summary of the characterisation techniques that were used in this thesis

together with the advantages and disadvantages associated with the use of each technique.

Transmission electron microscopy (TEM), X-ray diffraction (XRD) and dynamic light scattering (DLS) are three common methods which are used for evaluation of the size of the nanoparticles. The TEM operates by recording the interaction between electron and the analysed material using a digital camera. Due to the short wavelength of the electrons of 0.1nm TEM is capable of resolving small details in a material down to atomic level.[42] Therefore, this technique can provide information about the size as well as the mono- or polydispersity of nanoparticles in the sample. Additionally it can give information about the morphology and aspect ratio of the nanoparticles. However, this technique requires sufficient electron densities in order to produce high quality TEM imaging because polymeric shells and organic ligands are poor scatters of the electron and appear transparent in an electron beam. Therefore, heavy-metal special staining or cryogenic methods are required for achieving enhanced contrast. Additionally an analysis by image treatment on a statistically significant number of particles is required in order to achieve a proper representation of the sample. Sample preparation can sometimes induce aggregation of the nanoparticles and as a result TEM measurements may be non-representative of the size and the distribution of the nanoparticles in a solution. Finally, the method is extremely time consuming, expensive to operate and subject to the operator abilities.

Powder X-ray diffraction (XRD) can be used to provide information about the size of the iron oxide cores. This is a bulk method that means it can give representative information for a whole sample. In addition to probing the size of nanoparticles it can be

used for assessment of phase composition and potential impurities. It is easy to perform and does not require sophisticated preparation of the probe. The size of the nanoparticles can be calculated using the Scherrer equation, where the nanoparticles diameter is inversely proportional to the crystalline peak width:

$$\tau = \frac{K\lambda}{\beta cos\theta} \quad (1.3),$$

Where τ- is the particles size, β- is the line broadening at half the maximum intensity (FWHM), k- the shape factor (k=0.9), λ- is the X-ray wavelength (Mo, λ = 0.7107 Å), θ- is the Bragg diffraction angle.

The major drawback of this method is that it can only be applied for crystalline materials and assumes a spherical shape of the nanoparticles. This method does not provide information about the morphology of the nanoparticles. However, it is an excellent complementary tool to TEM for confirmation the size of the nanoparticles, e.g. Fe_3O_4 cores.

DLS is a technique that can be used to determine the hydrodynamic size and the size distribution of nanoparticles in solution. During the DLS measurements, a laser beam passes through a sample (nanoparticle dispersion) and the light is scattered by the nanoparticles in solution. Small time-dependent fluctuations in the intensity of the scattered light are monitored using a photodetector. These fluctuations in the intensity are due to the nanoparticle Brownian diffusion and are dependent on the nanoparticle size. The Stokes-Einstein equation relates the diffusion coefficient (D) to the hydrodynamic diameter of the nanoparticles by taking into account the viscosity of the solution and the temperature during measurement: [43]

$$D = \frac{k_B T}{6\pi\eta R} \quad (1.4),$$

Where k_B is the Boltzmann constant, T is the temperature, η is the viscosity and R is the particle radius. The hydrodynamic diameter obtained from this technique corresponds to that of a rigid sphere (equivalent-sphere hydrodynamic diameter) that diffuses at the same rate as the measured nanoparticle. In a DLS measurement the equivalent-sphere hydrodynamic diameter is assumed and therefore no information can be provided about the shape of the particles. For a non-spherical particle the shape would be assumed as diameter of a sphere with a corresponding diffusion coefficient. As a result this technique is non-reliable for non-spherical shaped particles. Furthermore, the intensity of scattered light is proportional to the diameter of the nanoparticles to the power of 6th (from Rayleighs approximation) and therefore, larger nanoparticles scatter more the light comparing to smaller nanoparticles. The size dependence of the scattered intensity of light will skew the results towards the larger nanoparticles. The advantage of DLS is rapid measurement times, along with facile operation and suitability for qualitative monitoring of agglomeration.[44] Therefore, it is common to complement TEM and XRD with DLS measurements.

1.2.3 Synthetic methods

In general, it is desirable that the synthetic process of nanoparticles should be high-throughput with the ability to scale to industrial level, high reproducibility from batch to batch, inexpensive and capable of producing monodisperse nanoparticles. Several synthetic methods to produce SPIONs have been intensively investigated for more than 30 years including co-precipitation, hydrothermal synthesis, microemulsion and thermal

decomposition (thermolysis).[29] Two methods were chosen for this work: the co-precipitation and thermal decomposition as they can deliver high-scale synthesis and monodisperse nanoparticles respectively. Therefore, they will be discussed here in more details.

The most early and widely used synthetic method is based on the alkaline co-precipitation of iron salts in aqueous solution. Specifically, ferrous and ferric salts (Fe^{+2} and Fe^{+3}) are co-precipitated under aqueous conditions with a strong base (NH_4OH or NaOH) to yield either magnetite (Fe_3O_4) or maghemite (γ-Fe_2O_3) according to equations 1.5 and 1.6:

$$Fe^{2+} + 2Fe^{3+} + 8OH^- \rightarrow Fe_3O_4 + 4H_2O \quad (1.5)$$

$$Fe_3O_4 + 2H^+ \rightarrow \gamma\text{-}Fe_2O_3 + Fe^{2+} + H_2O \quad (1.6)$$

The co-precipitation method can produce SPIONs coated with surface stabilisers in a one-pot reaction either during or after the synthesis.[45-49] Various polymers, such as dextran, poly-vinyl alcohol (PVA) or poly-lactic-co-glycolic acid (PLGA) can be added during the synthesis in order to stabilise the nanoparticles from agglomeration.[50-52] The polymers are non-specifically interacting with the nanoparticle surface *via* hydrogen bonding. However, this type of interaction makes the polymer susceptible to detachment from the SPIONs surface leading to agglomeration of nanoparticles.[23,53]

The major advantages of the co-precipitation method are the operational simplicity and scaling-up possibilities up to kilogram levels. The disadvantages are poor shape control and broad size distributions of nanoparticles (**Figure 1.4**); in addition reduced nanoparticle crystallinity can be a significant problem when the synthesis is carried out at room temperature.[45,48,54]

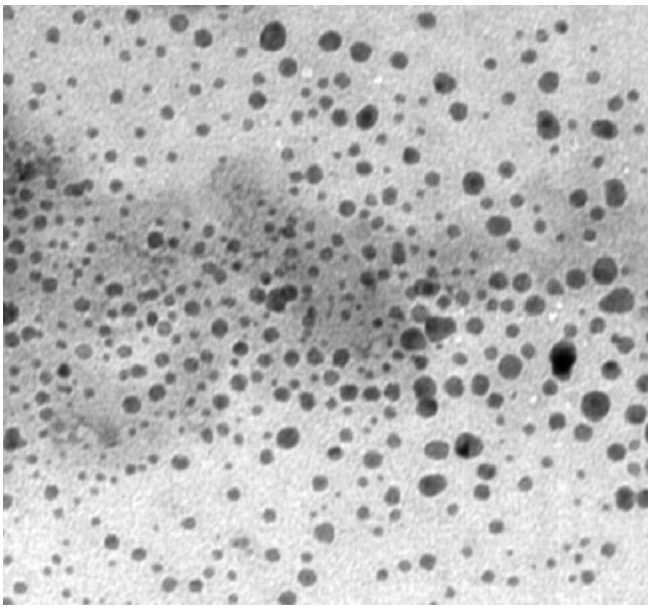

Figure 1.4 Representative TEM image of superparamagnetic iron oxide nanoparticles produced by co-precipitation method. The image is taken from ref. 45

Major improvements with respect to nanoparticle size control and magnetic properties were obtained with the movement from low-temperature co-precipitation methods towards thermolytic procedures. These methods rely on the high temperature pyrolysis of iron-organic ligands in the presence of capping agents such as oleic acid.[55-60] The types of iron-organic ligand precursors used in organic phase synthesis of SPIONs are iron cupferron $Fe(Cup)_3$, iron pentacarbonyl $Fe(CO)_5$, iron acetylacetonate $Fe(acac)_3$ and iron oleate, structures shown in **Figure 1.5**.

Alivisatos and co-workers used the injection of iron cupferron precursor into hot trioctylamine at 300 °C to produce single-crystal maghemite (γ-Fe_2O_3) nanoparticles of 10 nm with 10–15% size distribution.[55] Trioctylamine acts as coordinating ligand and as a high boiling point solvent.

a)

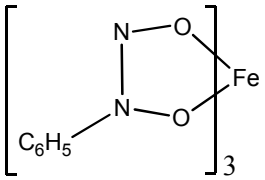

iron cupferron
tri-(N-nitrosophenylhydroxylamine)
iron(III)

b)

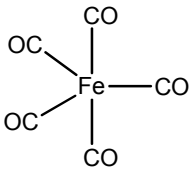

iron pentacarbonyl

c)

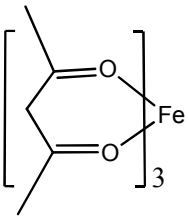

iron (III) acetylacetonate

d)

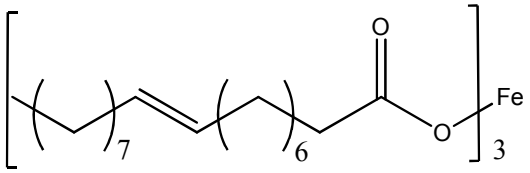

iron oleate

Figure 1.5 Structure of iron-organic ligand precursors used in the high temperature synthesis of iron oxide nanoparticles: a) iron cupferron, b) iron pentacarbonyl, c) iron acetylacetonate and d) iron oleate.

Significant improvement was achieved by Hyeon *et al.* who utilised iron pentacarbonyl precursors for the synthesis of monodisperse maghemite (γ-Fe_2O_3) nanoparticles.[56] The precursor was injected into a hot solution of oleic acid, oleylamine and 1,2-hexadecanediol in octyl ether. The initially formed Fe metal nanoparticles were subsequently oxidised to maghemite using trimethylamine oxide as a mild oxidant.

The same group demonstrated the synthesis of iron oxide nanoparticles with sizes ranging from 4 to 15 nm with one-nanometer defined control.[57] Monodisperse iron

nanoparticles with 4, 8 and 11 nm were obtained from thermal decomposition of iron pentacarbonyl precursor with oleic acid at 1:1, 1:2 and 1:3 molar ratios. Iron nanoparticles with particle sizes of 6, 7, 9, 10, 12, 13 and 15 nm were synthesised by a seed mediated growth process (**Figure 1.6**). The process involved using different ratios of the nanoparticles seeds and iron oleate, pre-prepared by heating appropriate amounts of iron pentacarbonyl and oleic acid in dioctyl ether.

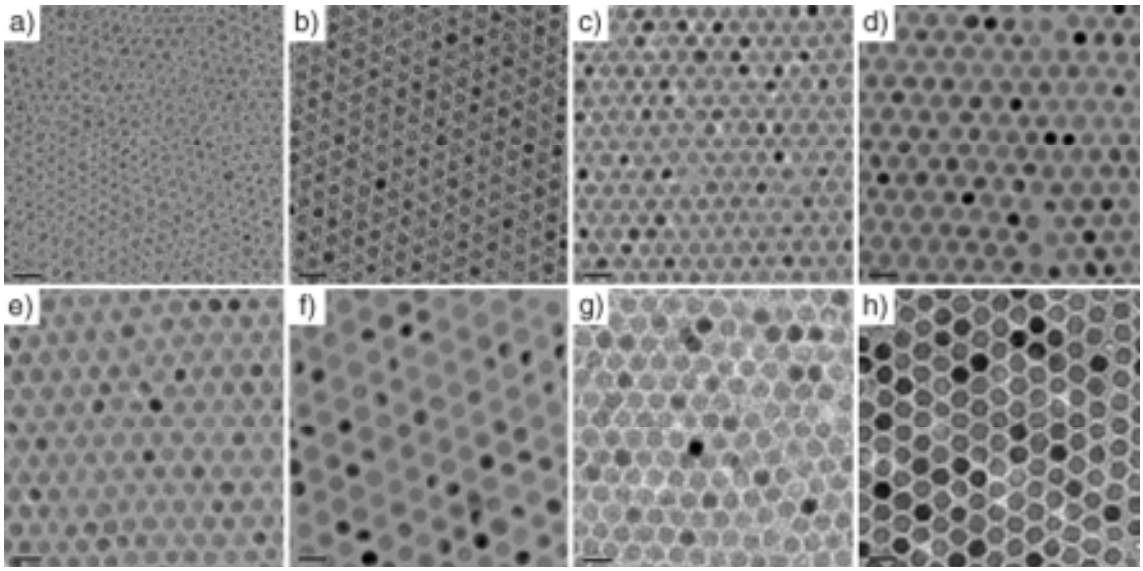

Figure 1.6 TEM images of monodisperse iron oxide nanoparticles of a) 6-, b) 7-, c) 8-, d) 9-, e) 10-, f) 11-, g) 12-, and h) 13-nm showing the one nanometer level increments in diameter. The images are taken from ref. 49

Similarly, synthesis of monodisperse magnetite (Fe_3O_4) nanoparticles was established for the first time by Sun *et al.*[58,60] The group used another type of iron-organic ligand precursor, namely iron acetylacetonate, which has evolved to be the most typical precursor for synthesis of metal oxide nanoparticles. In this synthetic procedure a mixture of iron acetylacetonate, 1,2-hexadecanediol, oleylamine and oleic acid in benzyl ether (high boiling solvent) are stepwise heated to reflux. 1,2-hexadecanediol is used as

reducing agent, while oleylamine and oleic acid are used as capping molecules which restrict the nanoparticles growth. This method was adopted for some of the work presented in this thesis and is further detailed in Chapter 5. Another advantage offered by this method is that the magnetic properties of nanoparticles can be tuned by changing the chemical composition of the initial precursor.[58,61] For instance, other types of metal oxide nanoparticles such as MFe_2O_4 (M = Mn, Co or Ni) were synthesised by mixing the corresponding $M(acac)_2$ (M = Mn, Co, or Ni) and $Fe(acac)_3$ in an 2:1 ratio and following the same synthetic procedure.

At the same time, stimulated by the idea that metal carboxylate salts are generated *in situ* during the thermolytic methods described previously, other groups have adopted iron-carboxylate salts (iron-oleate) as staring materials for the synthesis of iron oxide nanoparticles.[59,62-63] It is known that metal carboxylate complexes decompose at elevated temperatures and metal oxides are common decomposition products.[64-65] One notable procedure was reported by Park *et al*. who used iron chloride and sodium oleate first to form the iron oleate complex. In a second step, this complex was decomposed in 1-octadecene and yielded tens of grams of monodisperse iron oxide nanoparticles in a single pot reaction.[59]

The thermolytic methods are therefore generally more favoured due to the flexibility of the organic solvent for dissolving various precursors and surfactants that contribute to the control of nucleation and growth.[66] Large-scale synthesis of iron oxide nanoparticles using the thermolytic method is already achievable when the synthesis parameters such as precursors, surfactants, heating rate and boiling point (solvent choice) are carefully considered and controlled.

The thermolytic methods reviewed here produce hydrophobic SPIONs which are insoluble in water as their surface is capped by the surfactant molecule used during the synthesis. A direct application of such SPIONs in a living organism would cause an immediate threat to health, since they would produce the embolisation of blood vessels and obstruct the blood circulation. It is therefore necessary to exchange the hydrophobic protection shell with hydrophilic coatings which are compatible with the physiological environment.

1.3 Surface coating and functionalisation

Coating of the SPION surface is important because it determines the fate of the nanoparticle in the physiological environment. Ideally the coating material should have high affinity for the SPION surface, be able to provide organic functional groups for conjugation of biomolecules as well as be nonimmunogenic and minimise the interaction with plasma proteins. Finally, it should provide colloidal stability so the nanoparticles would be able to resist agglomeration and precipitation. Colloidal stability can be achieved either by electrostatic or by steric repulsion as exemplified in **Figure 1.7**.

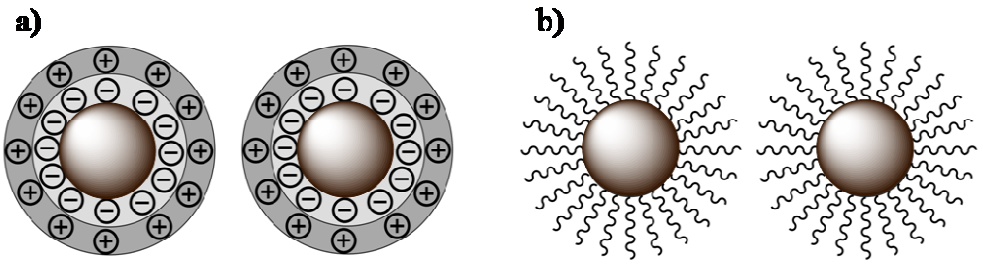

Figure 1.7 Types of colloidal stabilisation: a) electrostatic repulsion and b) steric repulsion. The figure is adapted from ref. 67

Electrostatic stabilisation can be achieved by producing an electrical double layer around the nanoparticles which enhances the repulsion between charged nanoparticles. Steric stabilisation can be achieved by grafting polymers to the surface of nanoparticles.

Typically there are two general strategies utilised to coat and functionalise the surface of SPIONs. First approach uses small molecules while the second approach uses polymers.

1.3.1 Surface coating using small molecules

Small organic molecules containing carboxylic acids, catechol, phosphonic acid and silane functional groups are typically used to coat the surface of SPIONs. These molecules can bind to the surface of SPIONs *via* coordination and covalent interactions as schematically summarized in **Figure 1.8**.[68]

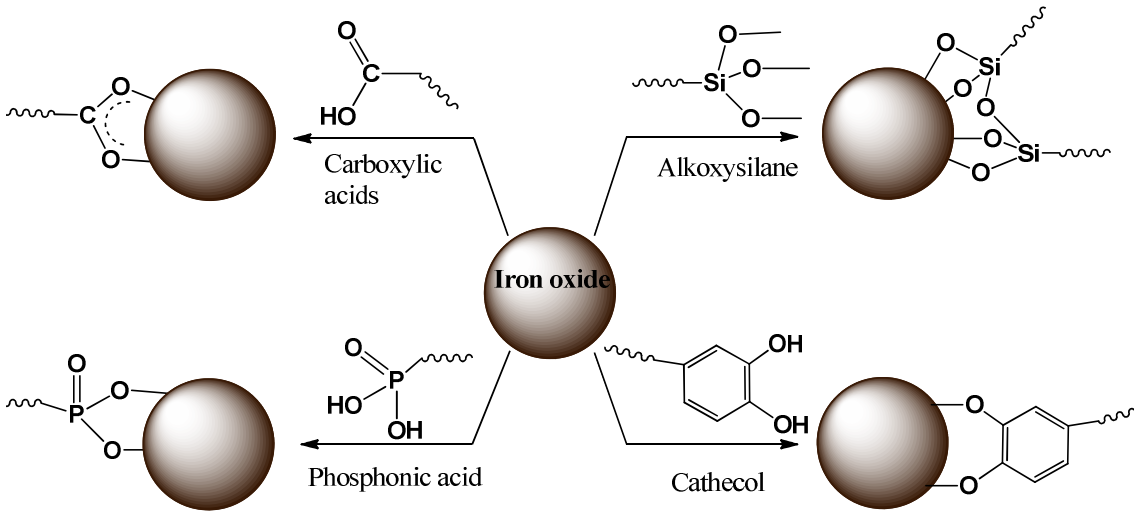

Figure 1.8 Small molecules containing carboxylic acid, catechol, silane, and phosphonic acid functionalities used for surface coating of SPIONs. Figure is adapted from ref. 68

Each type of anchoring functionality has advantages and disadvantages as can be illustrated by the following examples.

Organic ligands containing carboxylic acid functionality, such as citric or oleic acid, bind with the surface of iron oxide nanoparticle by coordination interactions.[69-70] The carboxylic groups bind to the iron ions in a bidentate coordination configuration.[71] However, the coordination bond can become unstable under certain conditions including temperature increase or acidic environment and therefore, induce detachment of the coating and precipitation of the nanoparticles.[68]

Small organic ligands containing catechol groups, such as dopamine, have been reported to have strong affinity for the surface of SPIONs.[72-73] The catechol functional groups bind to the surface of iron oxide nanoparticles also *via* coordination interactions. However, it has been reported that catechol groups of dopamine are displaced from the

nanoparticle surface and undergo redox transformations (**Figure 1.9**).[74] These processes promote the loss of colloidal stability leading to the precipitation of nanoparticles. The main advantage of using such ligands is associated with the rich chemistry they provide for post-functionalisation and bioconjugation reactions.

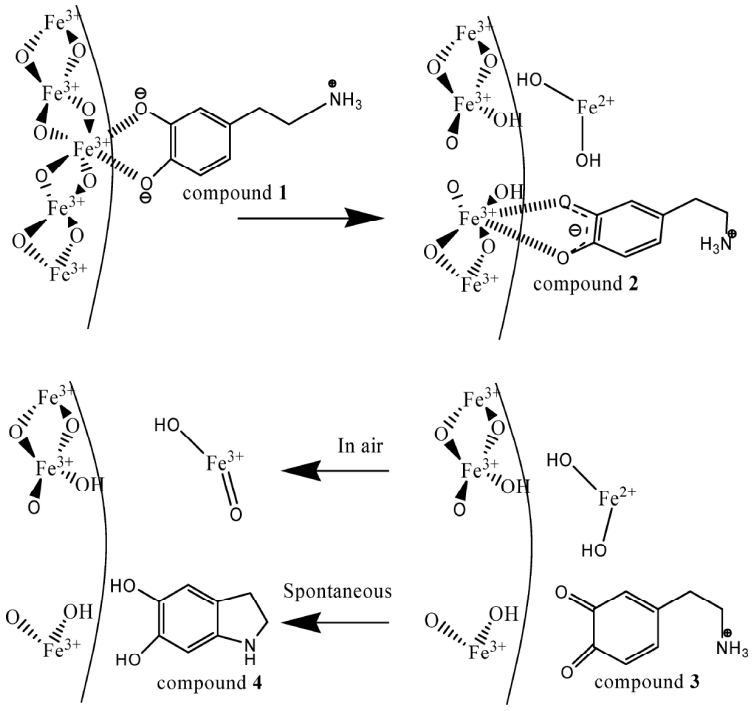

Figure 1.9 Schematic representation of the proposed mechanism for the decomposition of iron oxide nanoparticles by dopamine in an aqueous solution. The figure is taken from ref. 74

Small ligands containing phosphonic acid functional groups, for example dodecylphosphonic acid or hexadecylphosphonic acid, were also employed for coating the surface of SPIONs.[75-76] The phosphonic acid functionality interacts with the surface metal ions also *via* coordination bonds.[77] In a comparison study, which looked at oleic acid and dodecylphosphonic acid coated SPIONs, it was shown that both types of

ligands generate SPIONs dispersible in organic solvent but the phosphonic acid coated nanoparticle are less colloidally stable than their oleic acid counterparts.[75]

The small ligands presented up to now rely on the coordinative attachment of their organic functional groups to the metal ions of the SPIONs surface. As alternatives, alkoxysilanes are frequently utilised to coat the surface of SPIONs due to their ability to form stable covalent bonds with metal oxide surfaces.[78-82] The process is usually termed as silanisation and offers a viable approach for surface functionalisation of SPIONs due to the high stability of the bond between the ligand and the nanoparticle. As there are many commercially available functional silane ligands the process can supply a range of organic functionalities at the periphery of SPIONs which can be used for subsequent bioconjugations. In addition, the alkoxysilanes generate a biocompatible and thin silica monolayer on the surface of nanoparticles which provides protection for the nanoparticle core against the electrolytes present in the physiological fluids.[83] The potential drawback of the silanisation process is the chance of inducing particle agglomeration during the reaction. However, the agglomeration can be overcome by using dilute nanoparticles dispersions, controlled silane concentrations and catalysts to promote the condensation reaction predominantly on the nanoparticle surface.[79]

1.3.2 Surface coating using polymers

Hydrophilic polymers, particularly dextran,[84-86] polyethylene glycol (PEG)[87-90] and polyacrylic acid (PAA) [91-94] are very common coatings for SPIONs. The structures of these polymers are shown in **Figure 1.10**.

Dextran was the first generation of material used for coating SPIONs (**Figure 1.8a**). It contains multiple hydroxyl groups which provide fairly stable hydrogen bonding interaction between the SPIONs and the polymer.

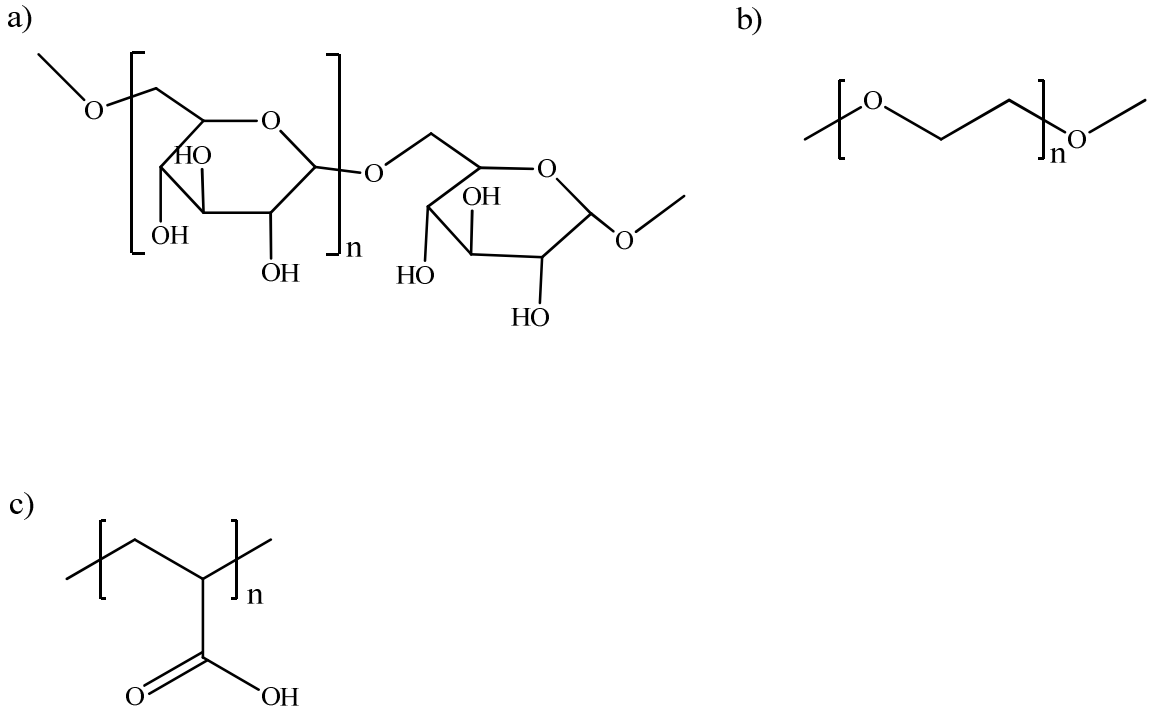

Figure 1.10 Examples of hydrophilic polymers employed for SPIONs surface coating, a) dextran, b) polyethylene glycol (PEG) and c) polyacrylic acid (PAA).

All clinically approved SPIONs for use in MRI are almost exclusively coated with dextran and its derivates due to biocompatibility (dextran is clinically approved by FDA as an anticoagulant), affinity to the SPIONs surface and simplicity of coating procedures which can be achieved during the synthesis of SPIONs *via* the co-precipitation method.[53,95] However, the dextran coating can detach from the SPIONs surface, especially, when post-modification reactions for conjugation of biomolecules are desired.[23] One way to address the stability issues has involved cross-linking of the

dextran shell with epichlorohydrin to form cross-linked iron-oxide (CLIO) nanoparticles.[96] Although this platform has shown promising results due to non-biodegradability it has not been tested in clinical applications.

Polyethylene glycol (PEG) is the most widely used synthetic polymer for coating the surface of SPIONs owing to its hydrophilicity and protein resistant properties, *i.e* stealth properties[97] (**Figure 1.10b**). For example, carboxylic acid-terminated PEG coated SPIONs have been synthesised using thermal decomposition of iron acetylacetonate in 2-pyrrolidone and α,ω-dicarboxylterminated PEG.[88] Investigators demonstrated that these SPIONs have good colloidal stability and free carboxylic groups accessible for further functionalisations. A more sophisticated design was implemented by Kohler *et al*.[82] who have used a tailored bifunctional PEG containing a silane at one terminus and an amino functional group at the other. The silane terminus was covalently attached to the nanoparticle surface while the amino groups were conjugated with folic acid which acted as a targeting ligand for tumour cells.

Polyacrylic acid (PAA) is a synthetic anionic polymer which is hydrophilic and capable to coordinate with the SPIONs surface (**Figure 1.10c**). PAA coated SPIONs show good aqueous dispersibility due to both electrostatic and steric repulsion induced through the coating. Zhang *et al*.[93] transferred the hydrophobic SPIONs into water by using a ligand exchange procedure in which hydrophilic PAA chains replaced the original oleic acid ligands. PAA binds to the nanoparticle surface through multiple carboxylic acid groups, providing more robust surface adhesion than the original oleic acid.

This ligand exchange route can be generally applied to other types of hydrophobic metal oxide nanoparticles for transfer into aqueous solutions.

Amphiphilic polymers, consisting of a hydrophobic and a hydrophilic segment, represent an important category of materials which have been used for coating of SPIONs. These polymers at the right hydrophilic-hydrophobic ratio can self-assemble in aqueous solution into micellar structures. Such micelles have a well-defined core–shell structure with a core consisting of the hydrophobic segments and a shell or corona of the hydrophilic chains exposed to the aqueous environment (**Figure 1.11**).[98]

Figure 1.11 Schematic representation of an amphiphilic polymer (brown-hydrophobic segment, green-hydrophilic segment) and its self-assembly into polymeric micelle. The figure is adapted from ref. 98

Typically, the hydrophobic-hydrophobic interactions between the hydrophobic segment of the polymer and the oleic acid coated-SPIONs yields a core-shell structure with particles in core; while the hydrophilic segment is exposed into aqueous solution, offering the nanoparticles hydrophilicity and stability. Therefore, polymeric micelles can act as ideal carriers of nanoparticle imaging agents in physiological environment.

In general, PEG-phospholipids are the most widely used amphiphilic polymers for coating of hydrophobic SPIONs due to the protein resistant properties offered by the PEG segment which enhance the nanoparticle 'stealth' behaviour in the biological environment.[97,99-102] Additionally this amphiphilic polymer is commercially available with a variety of chain-end functional groups such as amino, carboxylic acid or thiol which allow for bioconjugation reactions (**Figure 1.12**).

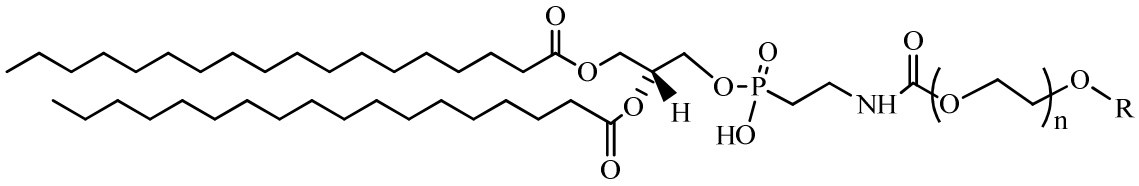

Where R, - NH_2

- COOH

- SH

- Biotin

Figure 1.12 Amphiphilic PEG-phospholipids with different terminal functional groups such as amino, carboxylic acid, thiol or biotin.

Park *et al.*[100] synthesised SPIONs coated with PEG-phospholipids using a one-step nanoemulsion method (**Figure 1.13**). The authors showed that the amphiphilic polymer-coated SPIONs were less than 30 nm in diameter and have high dispersibility and stability under physiological conditions for weeks without aggregation.

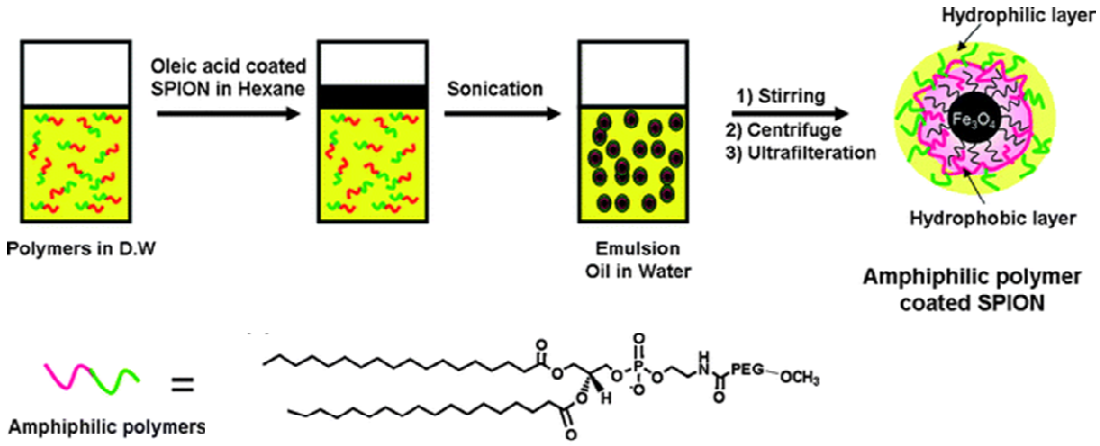

Figure 1.13 Schematic representation of the nanoemulsion procedure used for coating hydrophobic SPIONs with amphiphilic polymers. The figure is taken from ref. 100

Although PEG based polymers are considered as the "gold standard" for "stealth" polymeric coatings, recent clinical experiments found that they not only bring benefits but also some side effects and complications. The side effects are linked to hypersensitivity, non-biodegradability, toxic side products and a tendency to auto-oxidation, which promotes loss of its protein resistant ability over time.[103-104]

As alternative to PEG, polyoxazolines are documented for their capability of resisting opsonisation, hence increasing the SPIONs blood circulation time.[105-106] Polyoxazolines have a biomimetic structure meaning they are regarded as analogues of polypeptides due to the amide bonds present in their structure (**Figure 1.14**).

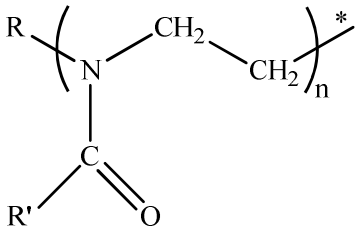

Figure 1.14 General structure of polyoxazoline polymer

Polyoxazolines offer more versatile structures because of the greater variety of initiators, monomers and chain-end functionalities which can be used during their synthesis. Additionally polyoxazolines bearing short alkyl substituent are water-soluble, biocompatible and have been approved by the FDA as a food additive.[107]

Therefore, in this thesis, amphiphilic polyoxazoline containing a C_{16} alkyl chain at one terminus and a carboxylic acid group at the other end was investigated as a coating material for hydrophobic SPIONs. The carboxylic acid groups present at the periphery of the micelle corona have been used for functionalisation with antibody molecules.

1.3.3 Biocompatibility and biodistribution of SPIONs

One of the key advantages for using SPIONs in biomedical applications is their biocompatibility. Although different SPIONs have different fates in the human body depending on composition of the coating and the iron oxide core, standard toxicological tests have shown that iron oxides are safe to be used in the human body.[108-110]

In most cases, such as MRI, drug delivery or hyperthermia, SPIONs are subject to intravenous administration, and reach the targeted tissues through blood circulation. The biodistribution and elimination of the nanoparticles depend on their hydrodynamic size and the nature of the surface coating.

A maximum size requirement is given by the spleen filaments which are spaced at roughly 200 nm.[111] Similarly, to traverse the liver, nanoparticles must be small enough to pass through the liver 150-200 nm sized fenestrated capillaries and avoid the Kupffer phagocytic cells.[112] However, nanoparticles smaller than 10 nm are easily subjected to renal clearance and can be rapidly removed from the circulation.[113] Hence, nanoparticles

with diameters between 10 and 200 nm are considered to be optimal for intravenous administration.

The SPIONs biodistribution can also depend on the nature of the surface coating. Once injected intravenously, the SPIONs are exposed to the plasma proteins including opsonins which can adsorb onto the nanoparticle surface, a process called opsonisation. The adsorbed opsonins will enhance the elimination of the SPIONs from circulation through the macrophages belonging to the mononuclear phagocytic system (MPS). In this context some coating materials, like PEG and more recently polyoxazolines, are recognised for their capability of resisting opsonisation, hence increasing the SPIONs blood circulation time.[114-115]

The SPIONs which are taken up by the cells, either by the phagocytic cells or the targeted cells, will be eventually degraded by intracellular digestive enzymes. The dextran coating was reported to be eliminated in the urine after degradation,[116] while iron from the cores is metabolised in the liver and subsequently used in the formation of red blood cells or excreted *via* kidneys.[17] Although iron is an essential nutrient, it can be toxic when very large amounts are ingested. In MRI diagnostics the recommended dose for humans is 0.56 mg iron/kg body weight in case of Feridex I.V. which is much lower than the human total iron stores of 3500 mg.[113] Therefore if SPIONs are administered within the safe limits, the body has the ability to metabolise and finally eliminate them. However for each type of new SPION the safe limits have to be determined *via* toxicological safety studies.

1.3.4 Bioconjugations

Coating the surface of SPIONs with a protective shell is important for colloidal stability and biocompatibility. However, the shell should additionally provide functional groups for the bioconjugation of active targeting ligands. Such nanoparticles are able to reach the tumour sites *via* a mechanism called active tumour targeting and significant amount of research has been put into achieving this goal.[23]

To achieve the active targeting requirement, the coating material should have chemically active functional groups, such as amines, carboxylic acids or thiols. The functional groups can react with the active groups on the biomolecules directly or *via* an intermediate activation step (**Table 1.1 and 1.2**).[23] For example, SPIONs with PEG-silane coatings containing multiple amino groups cannot be directly conjugated with thiol-containing targeting peptides. The amino groups have to be converted to an iodoacetyl functionality which is reactive towards the thiol-containing peptides, for example chlorotoxin. Such nanoparticle bioconjugates were shown to be able to target brain cancer cells *in vitro* and to be detectable by MRI analysis.[117]

Carbodiimide coupling chemistry is another frequently employed strategy for chemical conjugation of bioactive molecules. For example, the carboxylic acid groups present on the surface PEG-coated SPIONs formed a covalent amide bond with single chain Fv antibody fragments (scFv) after activation with EDC/NHS as catalyst.[118] The scFv-SPION conjugates were able to specifically bind to the Carcinoembrionyc antigen-expressing cancers cells *in vitro.* Therefore surface functional groups play an important role at the last chemical design stage, when the conjugation of biomolecules is required for achieving tumour active targeting.

Table 1.1 Examples of direct bioconjugation chemistry on SPIONs surface.

Nanoparticle	*Reactive ligand*	*Conjugate*	*Notes*
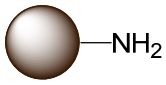	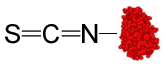	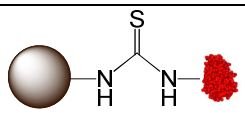	
	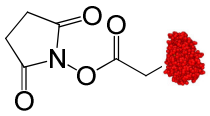	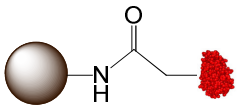	Stable link
	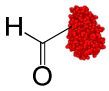	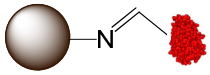	Cleaved under acid conditions
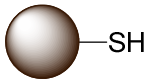	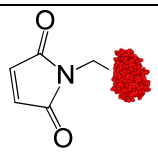	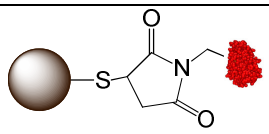	Interparticle disulfide linkage may form
	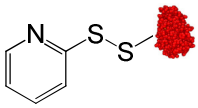	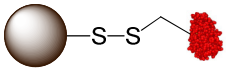	

Table 1.2 Examples of bioconjugation chemistry using intermediate activation.

Nanoparticle	*Intermediate activation*	*Reactive ligand*	*Conjugate*	*Notes*
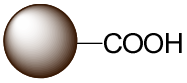	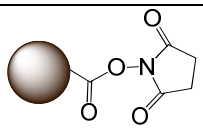 EDC/NHS	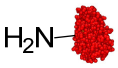	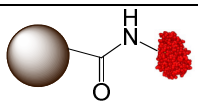	Stable link
	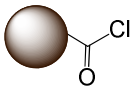 Thionyl chloride	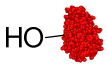	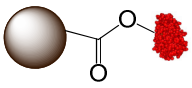	Cleaved in alkaline condition
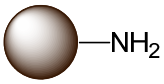	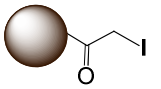 Iodoacetyl	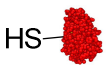	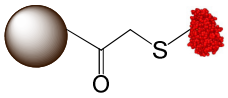	Stable link
	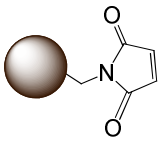 Maleimide	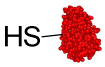	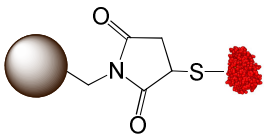	Sulfhydryl selective
	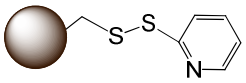 Pyridyl Disulfide	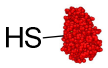	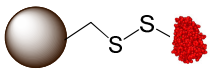	Sulfhydryl selective

1.4 Applications of SPIONs in biomedicine

1.4.1 Magnetic resonance imaging (MRI)

MRI is a non invasive imaging technique for visualisation of the structure and function of soft tissues in the body. It relies on the property of the hydrogen protons to align and precess in the presence of an applied magnetic field (B_0) generated by the MRI scanner. Upon application of a transverse radiofrequency pulse, these protons are perturbed from their initial alignment in the direction of B_0. When the magnetic field is turned off, a relaxation phenomenon takes place and these protons return to their original state from the excited state. Two independent processes, called longitudinal relaxation (T_1) and transverse relaxation (T_2), can be monitored to generate an MRI image. The image contrast is based upon the local variation in relaxation which arises from proton density as well as the chemical and physical nature of the tissue under investigation.[119] To obtain more well-defined structural images, contrast agents can be utilised during the imaging recording procedure. The role of the constrast agent is to decrease relaxation times of the tissues, either T_1 or T_2, depending on the nature of the contrast agent.[120]

Typically, gadolinium based agents are clinically used to modify T_1 relaxation,[121] producing brighter images (hyperintensity), while SPIONs are used as T_2 contrast agent, producing a darker contrast (hypointensity) on the MR image, corresponding to the tissue area where they are accumulated (**Figure 1.15**).[120] Clinically approved SPIONs for MRI contrast enhancement are summarised in **Table 1.3**.

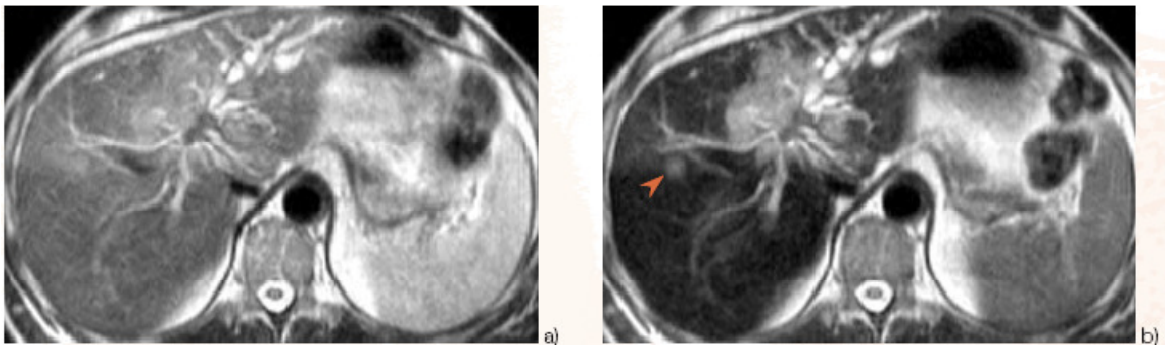

Figure 1.15 (a) Non-contrasted T_2-weighted MR image in which the liver tumour is not visible. (b) Demarcation of liver tumour after Resovist intravenous injection. The Resovist-enhanced MR image depicts a satellite tumour nodule (arrow). Images taken from ref. 122

Table 1.3 Examples of clinically approved SPIONs.

Name	*Application*	*Administration*	*Relaxivity mmol×s^{-1} at 1.5 T*	*Coating*	*Hydrodynamic diameter (nm)*
Ferumoxides AMI-25 (Feridex I.V./ Endorem)*	Liver and spleen imaging	I.V.	r_2=120 r_1=10.1	Dextran T10	120-180
Ferumoxtran-10 AMI-227 (Sinerem/ Combidex)	Lymph node imaging	I.V.	r_2=65 r_1=9.9	Dextran T10, T1	15-30
Ferucarbotran SHU-555A (Resovist)	Liver imaging	I.V.	r_2=189 r_1=9.7	Carboxy-dextran	60
Ferumoxsil AMI-121 (Lumirem/ Gastromark)	GI imaging	Oral	n.a.	Silica	300
Ferumoxytol AMI-228 (Feraheme)	Iron replacement therapy	I.V.	r_2=89 r_1=15	Carboxy methyl-dextran	30

*No longer commercialised

The clinically approved MRI constrast agents based on SPIONs mainly consist of iron oxide nanoparticle cores of 5 to 10 nm size and a dextran stabilisation coating. The major drawbacks associated with currently available MRI agents are:

(1) broad size distributions of iron oxide cores,

(2) lack of strong covalent attachment of the coating material to the iron oxide nanoparticles cores as conventional dextran coatings are attached to the core *via* hydrogen bonding making them susceptible to detachment,

(3) lack of surface functional groups which limits bioconjugation ability and results in a lack of selective binding to targeted cancer cells,

(4) applicability only to hepatic, gastrointestinal or lymph nodes imaging.

These limitations motivated the search for improved syntheses of high quality monodisperse and crystalline iron oxide nanoparticles with enhanced magnetic properties. At the same time it stimulated the research for alternative surface modification methods and novel coating materials capable of promoting defined and controllable interactions between SPIONs and living cells.

For example, polyvinylpyrrolidone-coated SPIONs with 40-50 nm particle size distribution were shown to have higher macrophage uptake *in vitro* and *in vivo* than Feridex I.V. (**Figure 1.16**).[123] As polyvinylpyrrolidone is a water-soluble, non-charged and non-toxic polymer such SPIONs can potentially be better contrast agents, for example, for inflammation detection.

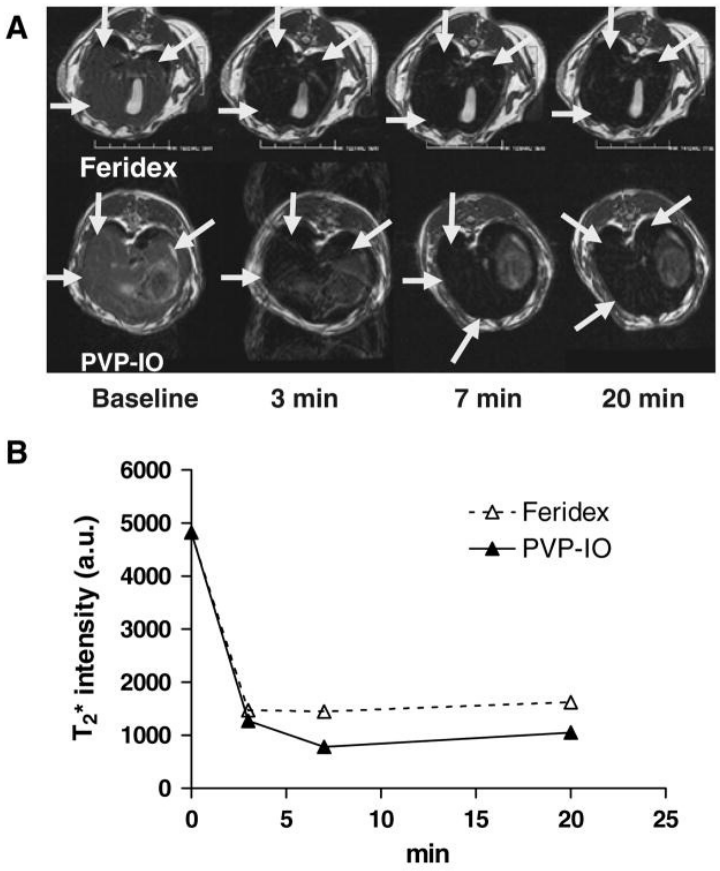

Figure 1.16 (a) T_2-weighted MR images of rabbit liver after intravenous injection of Feridex I.V. (top row) and polyvinylpyrrolidone-coated SPIONs (bottom row). (b) T_2 signal intensity for Feridex I.V. and polyvinylpyrrolidone-coated SPIONs. Image is taken from ref. 123

Park *et al.*[100] synthesised a series of amphiphilic polymer coated SPIONs with an average size of 30 nm. The authors tested each type of these non-toxic and stable SPIONs as an MRI contrast agent for *in vivo* cancer detection. The MRI studies with lung tumour-bearing mice resulted in a T_2 signal drop in the tumour tissues, indicating that the SPIONs reached the tumour tissues (**Figure 1.17**).

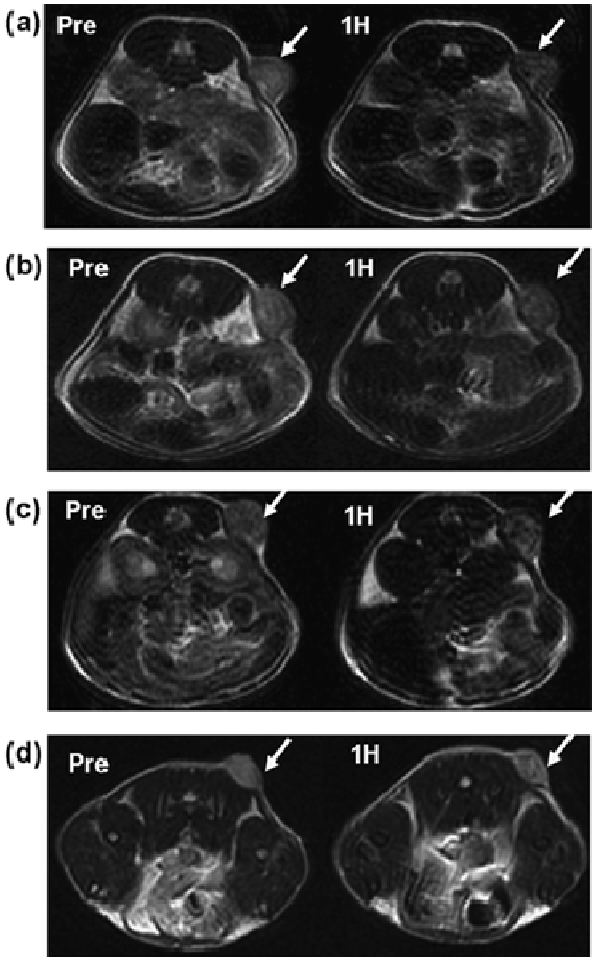

Figure 1.17 T_2-weighted MRI images taken before and after injection of 15 mg Fe/kg of (a) poly(dodecyl methacrylate-*b*-ethylene glycol methyl ether methacrylate-*b*-methacrylic acid)-coated SPIONs, (b) Pluronic-coated SPIONs, (c) PEG phospholipid-coated SPIONs and (d) Feridex I.V. The arrows denote the tumour region. The images are taken from ref. 100

Active targeted SPIONs were investigated for MRI imaging and a notable study was carried out by Zhang *et al.*[124] In this study, SPIONs were coated with 3-aminopropyltrimethoxysilane and conjugated with arginine-glycine-aspartic acid (RGD) peptides. These peptides bind to the $\alpha_v\beta_3$ integrin which is a specific marker of angiogenesis and tumour growth. After RGD-SPIONs injection in mice bearing brain

tumours the targeted nanoparticles accumulated in the tumour regions as shown in **Figure 1.18,** while the non-targeted nanoparticles did not.

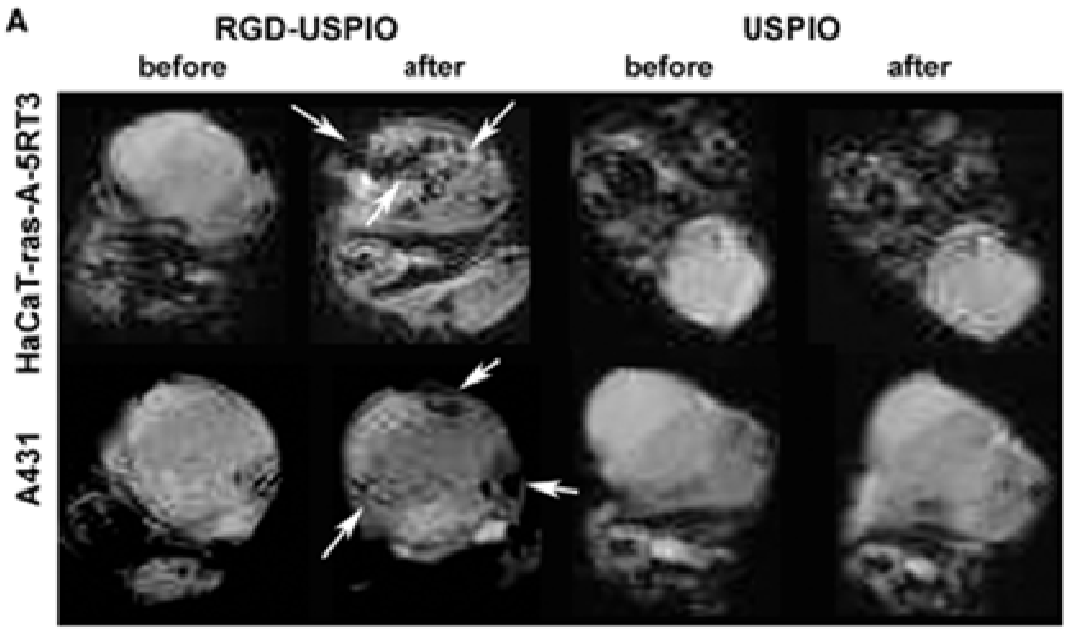

Figure 1.18 T_2-weighted MR images of nude mice bearing HaCaT-ras-A-5RT3 (top row) and A431 tumors (bottom row) before and 6 hours after I.V. injection of RGD- USPIO and USPIO. The images are taken from ref. 124

1.4.2 Magnetic separations

The use of SPIONs is not limited to MRI contrast agents, their superparamagnetic properties allow them to be efficiently used in magnetic separations.[125-126] Magnetic separation techniques have several advantages in comparison to traditional separation procedures. The process is simple as the separation is assisted by an external magnetic field and all purification steps take place in one test tube.[127] Typically the procedure involves the capture and separation of the biomolecule of interest using ligand functionalised SPIONs. For example, SPIONs have been widely used for affinity isolation of peptides,[72] for detection and isolation of bacteria[128] and for separation of proteins from biological samples.[129]

Lin *et al.*[130] developed a technique known as nanoprobe-based affinity mass spectrometry, NBAMS (**Figure 1.19**). In this technique, antibody-conjugated SPIONs were used for separation and detection of protein biomarkers in human serum. This technique was efficiently used to detect C-reactive protein, serum amyloid A and it involved three simple steps: (a) incubation of antibody-conjugated SPIONs with serum containing the targeted biomarker, (b) magnetic isolation of the SPIONs-biomarker conjugates and (c) direct mass spectrometry analysis of the biomarker captured on SPIONs.

In another study, SPIONs were used to separate biological samples in a microfluidic device. Chen *et al.*[131] produced a magnetic microfluidic device for separation of human immunodeficiency virus (HIV) from plasma. Anti-CD44 antibody conjugated SPIONs were used to capture the virus. Then the HIV-SPIONs conjugates were passed through a

packed bed of iron oxide particles. An external magnet was applied to magnetise the packed bed, which caused the HIV-SPIONs conjugates to be trapped, thus separating and concentrating the virus from the plasma.

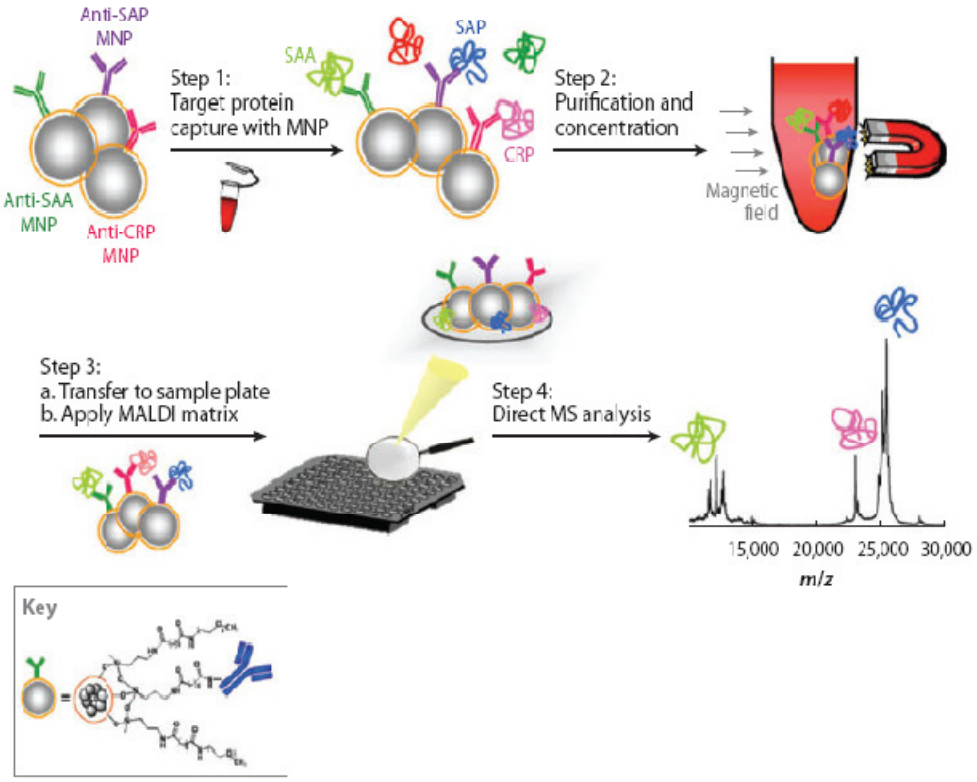

Figure 1.19 Role of the SPIONs in separations and immunoassays. The antibody-conjugated SPIONs capture, separate, purify, concentrate the target biomarker and act as a platform for the mass spectrometry analysis. Figure is taken from ref. 130

1.4.3 Hyperthermia

SPIONs can be used as therapeutic agents by taking advantage of their hyperthermic ability. Hyperthermia can be induced by magnetic nanoparticles when an external alternating magnetic field forces oscillation of the magnetic moments of each

nanoparticle resulting in electromagnetic energy being converted into heat.[18,81] It is possible to deliver SPIONs specifically to the tumour cells and generate heat locally with magnetic fields and as tumour cells are more susceptible to high temperatures (*i.e.* 42-45 °C) than normal cells, they can be destroyed with minimal damage to normal cells.[18] SPIONs have been intensively studied as hyperthermic agents due to their biocompatibility, surface functionalisation capabilities and adequate heat evolution rate.

Most magnetic hyperthermia studies used SPIONs coated with either cationic liposomes or with aminosilane.[18,132-133] For *in vitro* and *in vivo* studies that used SPIONs coated with cationic liposomes (MCL), their efficiency in hyperthermia induced tumour regression was attributed to their affinity towards the tumour cells which was enhanced by the electrostatic interaction between positively charged MCL and negatively charged cell membranes.[132] Le *et al.*[134] have demonstrated that the MCL, not only could be used for tumour hyperthermia but also could be linked to a specific antibody fragment, which increased their specificity for tumour cells.

Human clinical studies of magnetic hyperthermia began in 2001 with Jordan *et al.*[135] who produced and presented a new system of magnetic field to generate hyperthermia for applications in the treatment of glioblastomas and prostate carcinoma. These studies used SPION coated with aminosilane and showed that this therapeutic technique is well tolerated by patients without side effects. In 2010 Maier-Hauff *et al.*[136] published the results of a clinical study on 69 patients with recurrent glioblastoma who underwent radiotherapy in combination with hyperthermia induced by SPIONs. The results of this study showed an increase in patient survival when compared with conventional therapies. From the first clinical trials, magnetic hyperthermia has been seen as a

promising complementary therapy when combined with other conventional therapies such as radiotherapy or chemotherapy.

1.4.4 Multifunctional nanocomposites

In recent years SPIONs have been combined with other types of species such as fluorescent, drug or targeting molecules in order to expand their capabilities and to produce multifunctional nanocomposites.[92,137-138]

The combination of SPIONs with fluorescent molecules holds great promise in enabling preoperative MRI localisation of the tumour and intraoperative tumour delineation *via* optical imaging. These nanocomposites will have dual imaging capabilities. One typical approach to add another function to SPIONs is by taking advantage of the organic chemical groups on their surface for conjugation with a molecule of interest. Another approach is to use hydrophobic interactions for combining different functionalities in the same nanoparticle platform. Santra *et al*.[92] prepared PAA-coated SPIONs using a step-wise synthetic procedure which involved co-precipitation of nanoparticles, surface stabilisation with PAA and chemical modification of the remaining carboxylic acid groups. The resulting PAA-coated SPIONs were functionalised with alkyne groups in order to attach an azide containing folate *via* click chemistry. In addition, hydrophobic fluorescent dyes and drug molecules were encapsulated within the hydrophobic pockets of the nanoparticles coating to yield multifunctional theranostic nanoparticles (**Figure 1.20**).

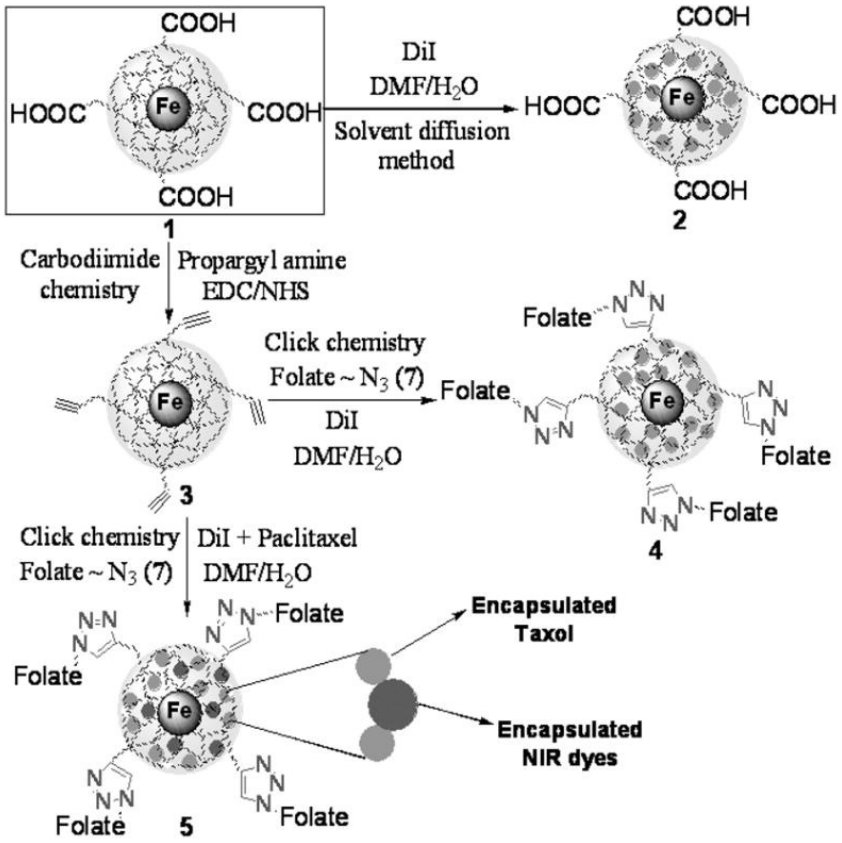

Figure 1.20 Schematic representation of the synthesis of theranostics and multimodal SPIONs. The image is taken from ref. 92

As previously mentioned, alkoxysilanes have also been commonly chosen as SPIONs coating material and as building platforms for multifunctional nanocomposites. For example, Kohler *et al.*[137] have synthesised aminosilane coated SPIONs and subsequently conjugated them with an anti-cancer drug Methotrexate (MTX) *via* amidation between the carboxylic acid end groups on MTX and the amine groups on the SPIONs surface (**Figure 1.21**). Methotrexate is an analogue of folic acid which exhibits not only a targeting role as folic acid but also a therapeutic effect to many types of cancer cells that overexpress the folate receptor on their surface.

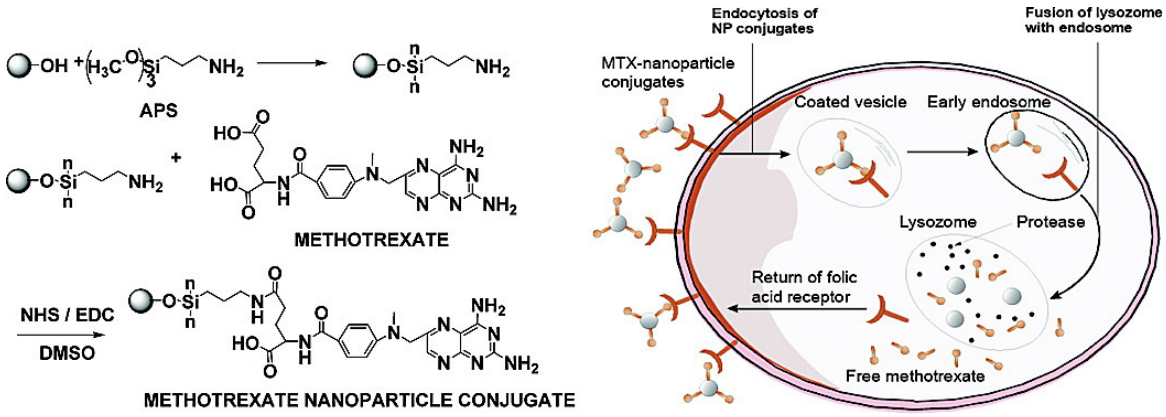

Figure 1.21 Surface conjugation of SPIONs with MTX, intracellular uptake of SPIONs-MTX conjugate and the following drug release. The figure is taken from ref. 137

The SPIONs-MTX conjugates were shown to have improved cellular uptake in glioma cancer cells. Following cellular uptake, the MTX was cleaved from the SPIONs surface in the lysosomes due to the low pH and presence of proteases. This method could potentially be extended to conjugate other drugs bearing chemically active groups for coupling.

A recent report by Sun *et al.*[138] showed a multifunctional PEG silane-coated SPION system which incorporated a near-infrared fluorescent (NIRF) dye (Cy5.5) and a targeting peptide (chlorotoxin). Using both MRI and optical imaging, the authors evaluated the nanoparticles capability to accumulate specifically in a brain tumour model after conjugation with the targeting peptide (**Figure 1.22**). The studies were performed both *in vitro* and *in vivo* in mice bearing brain tumour. The authors have also carried out preliminary biodistribution and toxicity assessment of the nanoparticles in mice using histological analysis of clearance organs and hematologic assays. The results

showed that the nanoparticles did not induce detectable cytotoxic effects on the liver and that the nanoparticles were well-tolerated at the doses evaluated in the study.

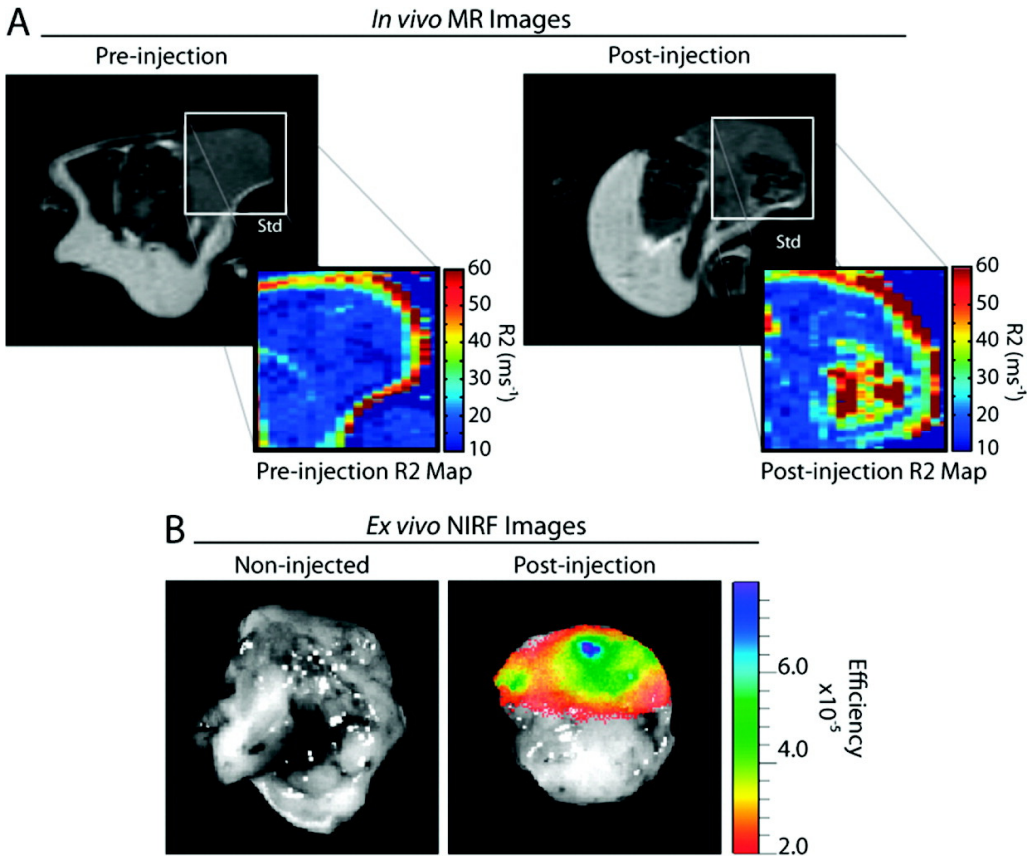

Figure 1.22 a) Representative MRI of the mouse bearing a brain tumour before and after injection of SPION/PEG-chlorotoxin-Cy5.5 (10 mg Fe/kg). Accumulation of the SPIONs was observed by negative contrast enhancement. b) Ex-vivo NIRF images of brain tumour acquired from a non-injected mouse (left) and the mouse receiving SPION/PEG-chlorotoxin-Cy5.5 (right). The image is taken from ref. 138

The introduction of suitable coatings with functional groups can allow the preparation of a nanoparticle platform capable of achieving different tasks simultaneously, with the final goal of improving diagnostics and therapeutic capabilities.

1.5 Thesis aims

Superparamagnetic iron oxide nanoparticles possess a highly desirable combination of properties including superparamagnetism, biocompatibility, stability, imaging capabilities and flexibility for surface functionalisations which make them attractive for a variety of biomedical applications.

The overall goal of this work was to synthesise multifunctional magnetic nanoparticles with several integrated properties that can be applied for early stage diagnosis of cancer using biomedical imaging. The multifunctionality refers to the combination of SPIONs with fluorescent molecules and antibodies to create a nanoparticle system capable of active targeting, optical and MR imaging of cancer cells overexpressing a specific marker.

The specific aims of this PhD thesis were as follows:

1. Synthesis of superparamagnetic iron oxide nanoparticles using high temperature decomposition of iron-organic ligands in the presence of capping agents
2. Developing surface modification chemistries for superparamagnetic iron oxide nanoparticles using as safe and biocompatible materials as possible.
3. Surface coating and functionalisation of the iron oxide nanoparticles using covalent interactions. Use of alkoxysilanes to introduce chemically reactive groups such as amino, bromo, iodo, nitrile and vinyl on the surface of iron oxide nanoparticles.

4. Surface coating and modification of hydrophobic iron oxide nanoparticles using bioinspired amphiphilic polyoxazoline polymers to form multifunctional magneto-micelles.
5. Chemical bioconjugation of fluorescent dyes and biomolecules such as antibodies to the surface of functionalised nanoparticles and their use as a platform for targeting and biomedical imaging of cancer cells, in particular pancreatic cancer cells.
6. Characterise all the materials used for this thesis to understand their physicochemical properties.

Although the principal aim of the work was to develop multifunctional magnetic nanoparticles for biomedical imaging and diagnosis, the developed nanoparticles could also be employed for other biological applications such as bioseparations or magnetic hyperthermia.

The report of this PhD work includes in chapter 1, a review of the most recent work with respect to synthesis, surface coating and functionalisation of superparamagnetic iron oxide nanoparticles. Chapter 1 also reviews the advances of SPION applications in MRI, hyperthermia, bioseparations and multifunctional applications.

Chapter 2 describes the chemical modification of iron oxide nanoparticles using silanisation as an effective method for introducing functional groups such as amino, bromo, vinyl onto the nanoparticle surface followed in some cases with post-modification reactions to further increase the potential for particle bioconjugations.

One application of amino/carboxylic acid bifunctional nanoparticles is described in chapter 3, where the nanoparticles bioconjugated with fluorescent molecules and antibodies are used for *in vitro* targeting and dual imaging of pancreatic cancer cells.

Chapter 4 describes a novel surface modification chemistry of monodisperse iron oxide nanoparticles using amphiphilic polyoxazolines. A multifunctional magneto-micellar (MMM) platform was developed with high colloidal stability, targeting and dual fluorescent/MRI imaging capability for pancreatic cancer cells.

Chapter 5 summarises the final conclusions and outcomes of this work, followed by acknowledgements to all the people that helped make this work possible.

1.6 References

1. D. J. Sellmyer, R. Skomski. *Advanced magnetic nanostructures*, **2006**, Springer, New York.

2. M. Affronte, Molecular nanomagnets for information technologies, *J Mater Chem*, **2009**, 19, 1731-1737.

3. R. J. Tseng, C. L. Tsai, L. P. Ma, J. Y. Ouyang, Digital memory device based on tobacco mosaic virus conjugated with nanoparticles, *Nat Nanotechnol*, **2006**, 1, 72-77.

4. J. A. Enterkin, K. R. Poeppelmeier, L. D. Marks, Oriented Catalytic Platinum Nanoparticles on High Surface Area Strontium Titanate Nanocuboids, *Nano Lett*, **2011**, 11, 993-997.

5. H. M. T. Galvis, J. H. Bitter, C. B. Khare, M. Ruitenbeek, A. I. Dugulan, K. P. de Jong, Supported Iron Nanoparticles as Catalysts for Sustainable Production of Lower Olefins, *Science*, **2012**, 335, 835-838.

6. J. Kong, N. R. Franklin, C. W. Zhou, M. G. Chapline, S. Peng, K. J. Cho, H. J. Dai, Nanotube molecular wires as chemical sensors, *Science*, **2000**, 287, 622-625.

7. P. G. Collins, K. Bradley, M. Ishigami, A. Zettl, Extreme oxygen sensitivity of electronic properties of carbon nanotubes, *Science*, **2000**, 287, 1801-1804.

8. A. A. Ansari, M. Alhoshan, M. S. Alsalhi, A. S. Aldwayyan, Prospects of nanotechnology in clinical immunodiagnostics, *Sensors (Basel)*, **2010**, 10, 6535-6581.

9. M. S. Dresselhaus, I. L. Thomas, Alternative energy technologies, *Nature*, **2001**, 414, 332-337.

10. A. M. Seayad, D. M. Antonelli, Recent advances in hydrogen storage in metal-containing inorganic nanostructures and related materials, *Adv Mater*, **2004**, 16, 765-777.

11. F. Feil, W. Furbeth, M. Schutze, Nanoparticle based inorganic coatings for corrosion protection of magnesium alloys, *Surf Eng*, **2008**, 24, 198-203.

12. D. Lee, M. F. Rubner, R. E. Cohen, All-nanoparticle thin-film coatings, *Nano Lett*, **2006**, 6, 2305-2312.

13. J. Dingman, Nanotechnology: its impact on food safety, *J Environ Health*, **2008**, 70, 47-50.

14. T. Hillie, M. Hlophe, Nanotechnology and the challenge of clean water, *Nat Nanotechnol*, **2007**, 2, 663-664.

15. P. F. Hahn, D. D. Stark, R. Weissleder, G. Elizondo, S. Saini, J. T. Ferrucci, Clinical-Application of Superparamagnetic Iron-Oxide to MR Imaging of Tissue Perfusion in Vascular Liver-Tumors, *Radiology*, **1990**, 174, 361-366.

16. O. C. Farokhzad, R. Langer, Impact of Nanotechnology on Drug Delivery, *Acs Nano*, **2009**, 3, 16-20.

17. D. L. Thorek, A. K. Chen, J. Czupryna, A. Tsourkas, Superparamagnetic iron oxide nanoparticle probes for molecular imaging, *Ann Biomed Eng*, **2006**, 34, 23-38.

18. B. Thiesen, A. Jordan, Clinical applications of magnetic nanoparticles for hyperthermia, *Int J Hyperther*, **2008**, 24, 467-474.

19. V. M. Martin, C. Siewert, A. Scharl, T. Harms, R. Heinze, S. Ohl, A. Radbruch, S. Miltenyi, J. Schmitz, Immunomagnetic enrichment of disseminated epithelial tumor cells from peripheral blood by MACS, *Exp Hematol*, **1998**, 26, 252-264.

20. A. G. Tibbe, B. G. de Grooth, J. Greve, G. J. Dolan, C. Rao, L. W. Terstappen, Magnetic field design for selecting and aligning immunomagnetic labeled cells, *Cytometry*, **2002**, 47, 163-172.

21. J. B. Haun, T. J. Yoon, H. Lee, R. Weissleder, Magnetic nanoparticle biosensors, *Wires Nanomed Nanobi*, **2010**, 2, 291-304.

22. Y. R. Chemla, H. L. Crossman, Y. Poon, R. McDermott, R. Stevens, M. D. Alper, J. Clarke, Ultrasensitive magnetic biosensor for homogeneous immunoassay, *P Natl Acad Sci USA*, **2000**, 97, 14268-14272.

23. O. Veiseh, J. W. Gunn, M. Q. Zhang, Design and fabrication of magnetic nanoparticles for targeted drug delivery and imaging, *Adv Drug Deliver Rev*, **2010**, 62, 284-304.

24. M. Arruebo, R. Fernandez-Pacheco, M. R. Ibarra, J. Santamaria, Magnetic nanoparticles for drug delivery, *Nano Today*, **2007**, 2, 22-32.

25. S. C. McBain, H. H. P. Yiu, J. Dobson, Magnetic nanoparticles for gene and drug delivery, *Int J Nanomed*, **2008**, 3, 169-180.

26. N. S. Barakat, Magnetically modulated nanosystems: a unique drug-delivery platform, *Nanomedicine-Uk*, **2009**, 4, 799-812.

27. M. Johannsen, B. Thiesen, P. Wust, A. Jordan, Magnetic nanoparticle hyperthermia for prostate cancer, *Int J Hyperther*, **2010**, 26, 790-795.

28. Y. X. Wang, S. M. Hussain, G. P. Krestin, Superparamagnetic iron oxide contrast agents: physicochemical characteristics and applications in MR imaging, *Eur Radiol*, **2001**, 11, 2319-2331.

29. R. R. Qiao, C. H. Yang, M. Y. Gao, Superparamagnetic iron oxide nanoparticles: from preparations to in vivo MRI applications, *J Mater Chem*, **2009**, 19, 6274-6293.

30. E. Parton, Biomedical applications using magnetic nanoparticles, **2008**, from http://www.electroiq.com/articles/stm/2008/02/bbiomedical-applications-using-magnetic-nanoparticles-b.html

31. M. McElfresh, Fundamentals of Magnetism and Magnetic Measurements Featuring Quantum Design's Magnetic Property measurement system, *Quantum Design*, **1994**, 1-41.

32. Z. Li, B. Tan, M. Allix, A. I. Cooper, M. J. Rosseinsky, Direct coprecipitation route to monodisperse dual-functionalized magnetic iron oxide nanocrystals without size selection, *Small*, **2008**, 4, 231-239.

33. J. T. Mayo, C. Yavuz, S. Yean, L. Cong, H. Shipley, W. Yu, J. Falkner, A. Kan, M. Tomson, V. L. Colvin, The effect of nanocrystalline magnetite size on arsenic removal, *Sci Technol Adv Mat*, **2007**, 8, 71-75.

34. R. M. Cornell, U. Schwertmann. *The iron oxides : structure, properties, reactions, occurrence, and uses*, **1996**, VCH, Weinheim ; New York.

35. W. H. Bragg, The structure of magnetite and the spinels., *Nature*, **1915**, 95, 561-561.

36. R. M. Cornell, U. Schwertmann. *Crystal Structure*. The Iron Oxides, **2004**, Wiley-VCH Verlag GmbH & Co. KGaA, pp. 9-38.

37. T. Shen, R. Weissleder, M. Papisov, A. Bogdanov, T. J. Brady, Monocrystalline Iron-Oxide Nanocompounds (Mion) - Physicochemical Properties, *Magnet Reson Med*, **1993**, 29, 599-604.

38. M. P. Morales, S. Veintemillas-Verdaguer, M. I. Montero, C. J. Serna, A. Roig, L. Casas, B. Martinez, F. Sandiumenge, Surface and internal spin canting in gamma-Fe_2O_3 nanoparticles, *Chem Mater*, **1999**, 11, 3058-3064.

39. S. Verma, D. Pravarthana, One-Pot Synthesis of Highly Monodispersed Ferrite Nanocrystals: Surface Characterization and Magnetic Properties, *Langmuir*, **2011**, 27, 13189-13197.

40. C. E. Sjogren, C. Johansson, A. Naevestad, P. C. Sontum, K. BrileySaebo, A. K. Fahlvik, Crystal size and properties of superparamagnetic iron oxide (SPIO) particles, *Magn Reson Imaging*, **1997**, 15, 55-67.

41. M. P. Morales, O. Bomati-Miguel, R. P. de Alejo, J. Ruiz-Cabello, S. Veintemillas-Verdaguer, K. O'Grady, Contrast agents for MRI based on iron oxide nanoparticles prepared by laser pyrolysis, *J Magn Magn Mater*, **2003**, 266, 102-109.

42. R. F. Egerton. *Physical principles of electron microscopy : an introduction to TEM, SEM, and AEM*, **2005**, Springer, New York, NY.

43. B. Berne, R. Pecora. *Dynamic light scattering with applications to chemistry, biology and physics*, **2000**, Dover Publications NY.

44. M. Filella, J. Zhang, M. E. Newman, J. Buffle, Analytical applications of photon correlation spectroscopy for size distribution measurements of natural colloidal suspensions: capabilities and limitations, *Colloids and Surfaces A: Physicochemical and Engineering Aspects*, **1997**, 120, 27-46.

45. L. Babes, B. Denizot, G. Tanguy, J. J. Le Jeune, P. Jallet, Synthesis of iron oxide nanoparticles used as MRI contrast agents: A parametric study, *J Colloid Interf Sci*, **1999**, 212, 474-482.

46. Y. S. Kang, S. Risbud, J. F. Rabolt, P. Stroeve, Synthesis and characterization of nanometer-size Fe3O4 and gamma-Fe2O3 particles, *Chem Mater*, **1996**, 8, 2209-2211.

47. C. Pereira, A. M. Pereira, C. Fernandes, M. Rocha, R. Mendes, M. P. Fernandez-Garcia, A. Guedes, P. B. Tavares, J. M. Greneche, J. P. Araujo, C. Freire,

Superparamagnetic MFe_2O_4 (M = Fe, Co, Mn) Nanoparticles: Tuning the Particle Size and Magnetic Properties through a Novel One-Step Coprecipitation Route, *Chem Mater*, **2012**, 24, 1496-1504.

48. T. Fried, G. Shemer, G. Markovich, Ordered two-dimensional arrays of ferrite nanoparticles, *Adv Mater*, **2001**, 13, 1158-1161.

49. B. L. Cushing, V. L. Kolesnichenko, C. J. O'Connor, Recent advances in the liquid-phase syntheses of inorganic nanoparticles, *Chem Rev*, **2004**, 104, 3893-3946.

50. S. J. Lee, J. R. Jeong, S. C. Shin, J. C. Kim, Y. H. Chang, Y. M. Chang, J. D. Kim, Nanoparticles of magnetic ferric oxides encapsulated with poly(D,L latide-co-glycolide) and their applications to magnetic resonance imaging contrast agent, *J Magn Magn Mater*, **2004**, 272, 2432-2433.

51. R. Weissleder, G. Elizondo, J. Wittenberg, C. A. Rabito, H. H. Bengele, L. Josephson, Ultrasmall Superparamagnetic Iron-Oxide - Characterization of a New Class of Contrast Agents for Mr Imaging, *Radiology*, **1990**, 175, 489-493.

52. A. Petri-Fink, M. Chastellain, L. Juillerat-Jeanneret, A. Ferrari, H. Hofmann, Development of functionalized superparamagnetic iron oxide nanoparticles for interaction with human cancer cells, *Biomaterials*, **2005**, 26, 2685-2694.

53. C. W. Jung, Surface-Properties of Superparamagnetic Iron-Oxide Mr Contrast Agents - Ferumoxides, Ferumoxtran, Ferumoxsil, *Magn Reson Imaging*, **1995**, 13, 675-691.

54. Z. J. Zhang, Z. L. Wang, B. C. Chakoumakos, J. S. Yin, Temperature dependence of cation distribution and oxidation state in magnetic Mn-Fe ferrite nanocrystals, *J Am Chem Soc*, **1998**, 120, 1800-1804.

55. J. Rockenberger, E. C. Scher, A. P. Alivisatos, A new nonhydrolytic single-precursor approach to surfactant-capped nanocrystals of transition metal oxides, *J Am Chem Soc*, **1999**, 121, 11595-11596.

56. T. Hyeon, S. S. Lee, J. Park, Y. Chung, H. Bin Na, Synthesis of highly crystalline and monodisperse maghemite nanocrystallites without a size-selection process, *J Am Chem Soc*, **2001**, 123, 12798-12801.

57. J. Park, E. Lee, N. M. Hwang, M. S. Kang, S. C. Kim, Y. Hwang, J. G. Park, H. J. Noh, J. Y. Kini, J. H. Park, T. Hyeon, One-nanometer-scale size-controlled synthesis of monodisperse magnetic iron oxide nanoparticles, *Angew Chem Int Edit*, **2005**, 44, 2872-2877.

58. S. H. Sun, H. Zeng, D. B. Robinson, S. Raoux, P. M. Rice, S. X. Wang, G. X. Li, Monodisperse MFe_2O_4 (M = Fe, Co, Mn) nanoparticles, *J Am Chem Soc*, **2004**, 126, 273-279.

59. J. Park, K. J. An, Y. S. Hwang, J. G. Park, H. J. Noh, J. Y. Kim, J. H. Park, N. M. Hwang, T. Hyeon, Ultra-large-scale syntheses of monodisperse nanocrystals, *Nat Mater*, **2004**, 3, 891-895.

60. S. H. Sun, H. Zeng, Size-controlled synthesis of magnetite nanoparticles, *J Am Chem Soc*, **2002**, 124, 8204-8205.

61. J. Xie, S. Peng, N. Brower, N. Pourmand, S. X. Wang, S. H. Sun, One-pot synthesis of monodisperse iron oxide nanoparticles for potential biomedical applications, *Pure Appl Chem*, **2006**, 78, 1003-1014.

62. W. W. Yu, J. C. Falkner, C. T. Yavuz, V. L. Colvin, Synthesis of monodisperse iron oxide nanocrystals by thermal decomposition of iron carboxylate salts, *Chem Commun*, **2004**, 2306-2307.

63. N. R. Jana, Y. F. Chen, X. G. Peng, Size- and shape-controlled magnetic (Cr, Mn, Fe, Co, Ni) oxide nanocrystals via a simple and general approach, *Chem Mater*, **2004**, 16, 3931-3935.

64. G. R. Paz-Pujalt, W. Nieand, C. Lurin, Comparative Study of the Sol-Gel and Metallo-Organic Decomposition (MOD) Processes for the Preparation of Inorganic Materials, *Mat Res Soc Symp Proc*, **1992**, 271, 193-197.

65. Q. Song, Y. Ding, Z. L. Wang, Z. J. Zhang, Tuning the thermal stability of molecular precursors for the nonhydrolytic synthesis of magnetic $MnFe_2O_4$ spinel nanocrystals, *Chem Mater*, **2007**, 19, 4633-4638.

66. U. Jeong, X. W. Teng, Y. Wang, H. Yang, Y. N. Xia, Superparamagnetic colloids: Controlled synthesis and niche applications, *Adv Mater*, **2007**, 19, 33-60.

67. S. Laurent, D. Forge, M. Port, A. Roch, C. Robic, L. V. Elst, R. N. Muller, Magnetic iron oxide nanoparticles: Synthesis, stabilization, vectorization, physicochemical characterizations, and biological applications, *Chem Rev*, **2008**, 108, 2064-2110.

68. C. Boyer, M. R. Whittaker, V. Bulmus, J. Q. Liu, T. P. Davis, The design and utility of polymer-stabilized iron-oxide nanoparticles for nanomedicine applications, *NPG Asia Mater*, **2010**, 2, 23-30.

69. N. Fauconnier, A. Bee, J. Roger, J. N. Pons, Adsorption of gluconic and citric acids on maghemite particles in aqueous medium, *Trends in Colloid and Interface Science X*, **1996**, 100, 212-216.

70. L. M. Bronstein, X. L. Huang, J. Retrum, A. Schmucker, M. Pink, B. D. Stein, B. Dragnea, Influence of iron oleate complex structure on iron oxide nanoparticle formation, *Chem Mater*, **2007**, 19, 3624-3632.

71. C. Rocchicciolideltcheff, R. Franck, V. Cabuil, R. Massart, Surfacted Ferrofluids - Interactions at the Surfactant-Magnetic Iron-Oxide Interface, *J Chem Res-S*, **1987**, 126-126.

72. C. J. Xu, K. M. Xu, H. W. Gu, R. K. Zheng, H. Liu, X. X. Zhang, Z. H. Guo, B. Xu, Dopamine as a robust anchor to immobilize functional molecules on the iron oxide shell of magnetic nanoparticles, *J Am Chem Soc*, **2004**, 126, 9938-9939.

73. E. Amstad, T. Gillich, I. Bilecka, M. Textor, E. Reimhult, Ultrastable Iron Oxide Nanoparticle Colloidal Suspensions Using Dispersants with Catechol-Derived Anchor Groups, *Nano Lett*, **2009**, 9, 4042-4048.

74. M. D. Shultz, J. U. Reveles, S. N. Khanna, E. E. Carpenter, Reactive nature of dopamine as a surface functionalization agent in iron oxide nanoparticles, *J Am Chem Soc*, **2007**, 129, 2482-2487.

75. Y. Sahoo, H. Pizem, T. Fried, D. Golodnitsky, L. Burstein, C. N. Sukenik, G. Markovich, Alkyl phosphonate/phosphate coating on magnetite nanoparticles: A comparison with fatty acids, *Langmuir*, **2001**, 17, 7907-7911.

76. J. D. Goff, P. P. Huffstetler, W. C. Miles, N. Pothayee, C. M. Reinholz, S. Ball, R. M. Davis, J. S. Riffle, Novel Phosphonate-Functional Poly(ethylene oxide)-Magnetite Nanoparticles Form Stable Colloidal Dispersions in Phosphate-Buffered Saline, *Chem Mater*, **2009**, 21, 4784-4795.

77. C. Yee, G. Kataby, A. Ulman, T. Prozorov, H. White, A. King, M. Rafailovich, J. Sokolov, A. Gedanken, Self-assembled monolayers of alkanesulfonic and -phosphonic acids on amorphous iron oxide nanoparticles, *Langmuir*, **1999**, 15, 7111-7115.

78. M. Rahimi, M. Yousef, Y. H. Cheng, E. I. Meletis, R. C. Eberhart, K. Nguyen, Formulation and Characterization of a Covalently Coated Magnetic Nanogel, *J Nanosci Nanotechno*, **2009**, 9, 4128-4134.

79. N. Frickel, R. Messing, T. Gelbrich, A. M. Schmidt, Functional Silanes as Surface Modifying Primers for the Preparation of Highly Stable and Well-Defined Magnetic Polymer Hybrids, *Langmuir*, **2010**, 26, 2839-2846.

80. R. De Palma, S. Peeters, M. J. Van Bael, H. Van den Rul, K. Bonroy, W. Laureyn, J. Mullens, G. Borghs, G. Maes, Silane ligand exchange to make hydrophobic superparamagnetic nanoparticles water-dispersible, *Chem Mater*, **2007**, 19, 1821-1831.

81. A. Jordan, R. Scholz, P. Wust, H. Schirra, T. Schiestel, H. Schmidt, R. Felix, Endocytosis of dextran and silan-coated magnetite nanoparticles and the effect of intracellular hyperthermia on human mammary carcinoma cells in vitro, *J Magn Magn Mater*, **1999**, 194, 185-196.

82. N. Kohler, G. E. Fryxell, M. Q. Zhang, A bifunctional poly(ethylene glycol) silane immobilized on metallic oxide-based nanoparticles for conjugation with cell targeting agents, *J Am Chem Soc*, **2004**, 126, 7206-7211.

83. A. Guerrero-Martinez, J. Perez-Juste, L. M. Liz-Marzan, Recent Progress on Silica Coating of Nanoparticles and Related Nanomaterials, *Adv Mater*, **2010**, 22, 1182-1195.

84. R. S. Molday, D. Mackenzie, Immunospecific Ferromagnetic Iron-Dextran Reagents for the Labeling and Magnetic Separation of Cells, *J Immunol Methods*, **1982**, 52, 353-367.

85. C. C. Berry, S. Wells, S. Charles, A. S. G. Curtis, Dextran and albumin derivatised iron oxide nanoparticles: influence on fibroblasts in vitro, *Biomaterials*, **2003**, 24, 4551-4557.

86. H. Pardoe, W. Chua-anusorn, T. G. St Pierre, J. Dobson, Structural and magnetic properties of nanoscale iron oxide particles synthesized in the presence of dextran or polyvinyl alcohol, *J Magn Magn Mater*, **2001**, 225, 41-46.

87. S. R. Wan, J. S. Huang, M. Guo, H. K. Zhang, Y. J. Cao, H. S. Yan, K. L. Liu, Biocompatible superparamagnetic iron oxide nanoparticle dispersions stabilized with poly(ethylene glycol)oligo(aspartic acid) hybrids, *J Biomed Mater Res A*, **2007**, 80A, 946-954.

88. F. Q. Hu, Z. Li, C. F. Tu, M. Y. Gao, Preparation of magnetite nanocrystals with surface reactive moieties by one-pot reaction, *J Colloid Interf Sci*, **2007**, 311, 469-474.

89. E. Occhipinti, P. Verderio, A. Natalello, E. Galbiati, M. Colombo, S. Mazzucchelli, A. Salvade, P. Tortora, S. M. Doglia, D. Prosperi, Investigating the structural biofunctionality of antibodies conjugated to magnetic nanoparticles, *Nanoscale*, **2011**, 3, 387-390.

90. G. Huang, C. F. Zhang, S. Z. Li, C. Khemtong, S. G. Yang, R. H. Tian, J. D. Minna, K. C. Brown, J. M. Gao, A novel strategy for surface modification of superparamagnetic iron oxide nanoparticles for lung cancer imaging, *J Mater Chem*, **2009**, 19, 6367-6372.

91. M. Lattuada, T. A. Hatton, Functionalization of monodisperse magnetic nanoparticles, *Langmuir*, **2007**, 23, 2158-2168.

92. S. Santra, C. Kaittanis, J. Grimm, J. M. Perez, Drug/Dye-Loaded, Multifunctional Iron Oxide Nanoparticles for Combined Targeted Cancer Therapy and Dual Optical/Magnetic Resonance Imaging, *Small*, **2009**, 5, 1862-1868.

93. T. R. Zhang, J. P. Ge, Y. P. Hu, Y. D. Yin, A general approach for transferring hydrophobic nanocrystals into water, *Nano Lett*, **2007**, 7, 3203-3207.

94. Y. H. Ma, S. Y. Wu, T. Wu, Y. J. Chang, M. Y. Hua, J. P. Chen, Magnetically targeted thrombolysis with recombinant tissue plasminogen activator bound to polyacrylic acid-coated nanoparticles, *Biomaterials*, **2009**, 30, 3343-3351.

95. A. M. G. C. Dias, A. Hussain, A. S. Marcos, A. C. A. Roque, A biotechnological perspective on the application of iron oxide magnetic colloids modified with polysaccharides, *Biotechnol Adv*, **2011**, 29, 142-155.

96. S. Palmacci, L. Josephson. Synthesis of polysaccharide covered superparamagnetic oxide colloids, Vol. U.S. Patent 5,262,176, 1993.

97. D. Leckband, S. Sheth, A. Halperin, Grafted poly(ethylene oxide) brushes as nonfouling surface coatings, *J Biomat Sci-Polym E*, **1999**, 10, 1125-1147.

98. A. M. Nystrom, K. L. Wooley, The importance of Chemistry in Creating Well-Defined Nanoscopic Embedded Therapeutics: Devices Capable of the Dual Functions of Imaging and Therapy, *Accounts Chem Res*, **2011**, 44, 969-978.

99. J. H. Gao, K. Chen, Z. Miao, G. Ren, X. Y. Chen, S. S. Gambhir, Z. Cheng, Affibody-based nanoprobes for HER2-expressing cell and tumor imaging, *Biomaterials*, **2011**, 32, 2141-2148.

100. J. Park, M. K. Yu, Y. Y. Jeong, J. W. Kim, K. Lee, V. N. Phan, S. Jon, Antibiofouling amphiphilic polymer-coated superparamagnetic iron oxide nanoparticles: synthesis, characterization, and use in cancer imaging in vivo, *J Mater Chem*, **2009**, 19, 6412-6417.

101. J. H. Park, G. von Maltzahn, E. Ruoslahti, S. N. Bhatia, M. J. Sailor, Micellar hybrid nanoparticles for simultaneous magnetofluorescent imaging and drug delivery, *Angew Chem Int Ed Engl*, **2008**, 47, 7284-7288.

102. L. Gu, R. H. Fang, M. J. Sailor, J.-H. Park, In Vivo Clearance and Toxicity of Monodisperse Iron Oxide Nanocrystals, *Acs Nano*, **2012**, 6, 4947-4954.

103. A. Hucknall, S. Rangarajan, A. Chilkoti, In Pursuit of Zero: Polymer Brushes that Resist the Adsorption of Proteins, *Adv Mater*, **2009**, 21, 2441-2446.

104. K. Knop, R. Hoogenboom, D. Fischer, U. S. Schubert, Poly(ethylene glycol) in Drug Delivery: Pros and Cons as Well as Potential Alternatives, *Angew Chem Int Edit*, **2010**, 49, 6288-6308.

105. R. Hoogenboom, Poly(2-oxazoline)s: A Polymer Class with Numerous Potential Applications, *Angew Chem Int Edit*, **2009**, 48, 7978-7994.

106. R. Hoogenboom, H. Schlaad, Bioinspired Poly(2-oxazoline)s, *Polymers*, **2011**, 3, 467-488.

107. T. X. Viegas, M. D. Bentley, J. M. Harris, Z. F. Fang, K. Yoon, B. Dizman, R. Weimer, A. Mero, G. Pasut, F. M. Veronese, Polyoxazoline: Chemistry, Properties, and Applications in Drug Delivery, *Bioconjugate Chem*, **2011**, 22, 976-986.

108. R. Weissleder, D. D. Stark, B. L. Engelstad, B. R. Bacon, C. C. Compton, D. L. White, P. Jacobs, J. Lewis, Superparamagnetic Iron-Oxide - Pharmacokinetics and Toxicity, *Am J Roentgenol*, **1989**, 152, 167-173.

109. S. Majumdar, S. S. Zoghbi, J. C. Gore, Pharmacokinetics of Superparamagnetic Iron-Oxide Mr Contrast Agents in the Rat, *Invest Radiol*, **1990**, 25, 771-777.

110. P. Bourrinet, H. H. Bengele, B. Bonnemain, A. Dencausse, J. M. Idee, P. M. Jacobs, J. M. Lewis, Preclinical safety and pharmacokinetic profile of ferumoxtran-10, an ultrasmall superparamagnetic iron oxide magnetic resonance contrast agent, *Invest Radiol*, **2006**, 41, 313-324.

111. L. T. Chen, L. Weiss, The role of the sinus wall in the passage of erythrocytes through the spleen, *Blood*, **1973**, 41, 529-537.

112. F. Braet, R. De Zanger, M. Baekeland, E. Crabbe, P. Van Der Smissen, E. Wisse, Structure and dynamics of the fenestrae-associated cytoskeleton of rat liver sinusoidal endothelial cells, *Hepatology*, **1995**, 21, 180-189.

113. A. Elias, A. Tsourkas, Imaging circulating cells and lymphoid tissues with iron oxide nanoparticles, *Hematology Am Soc Hematol Educ Program*, **2009**, 720-726.

114. S. Zalipsky, C. B. Hansen, J. M. Oaks, T. M. Allen, Evaluation of blood clearance rates and biodistribution of poly(2-oxazoline)-grafted liposomes, *J Pharm Sci-Us*, **1996**, 85, 133-137.

115. R. Konradi, B. Pidhatika, A. Muhlebach, M. Textor, Poly-2-methyl-2-oxazoline: A peptide-like polymer for protein-repellent surfaces, *Langmuir*, **2008**, 24, 613-616.

116. E. Schulze, J. T. Ferrucci, Jr., K. Poss, L. Lapointe, A. Bogdanova, R. Weissleder, Cellular uptake and trafficking of a prototypical magnetic iron oxide label in vitro, *Invest Radiol*, **1995**, 30, 604-610.

117. O. Veiseh, C. Sun, J. Gunn, N. Kohler, P. Gabikian, D. Lee, N. Bhattarai, R. Ellenbogen, R. Sze, A. Hallahan, J. Olson, M. Q. Zhang, Optical and MRI multifunctional nanoprobe for targeting gliomas, *Nano Lett*, **2005**, 5, 1003-1008.

118. K. L. Vigor, P. G. Kyrtatos, S. Minogue, K. T. Al-Jamal, H. Kogelberg, B. Tolner, K. Kostarelos, R. H. Begent, Q. A. Pankhurst, M. F. Lythgoe, K. A. Chester, Nanoparticles functionalised with recombinant single chain Fv antibody fragments (scFv) for the magnetic resonance imaging of cancer cells, *Biomaterials*, **2010**, 31, 1307-1315.

119. C. Sun, J. S. H. Lee, M. Q. Zhang, Magnetic nanoparticles in MR imaging and drug delivery, *Adv Drug Deliver Rev*, **2008**, 60, 1252-1265.

120. Y. W. Jun, J. H. Lee, J. Cheon, Chemical design of nanoparticle probes for high-performance magnetic resonance imaging, *Angew Chem Int Edit*, **2008**, 47, 5122-5135.

121. Z. P. Xu, N. D. Kurniawan, P. F. Bartlett, G. Q. Lu, Enhancement of relaxivity rates of Gd-DTPA complexes by intercalation into layered double hydroxide nanoparticles, *Chem-Eur J*, **2007**, 13, 2824-2830.

122. A. Blakeborough, J. Ward, D. Wilson, M. Griffiths, Y. Kajiya, J. A. Guthrie, P. J. A. Robinson, Hepatic lesion detection at MR imaging: A comparative study with four sequences, *Radiology*, **1997**, 203, 759-765.

123. H. Y. Lee, S. H. Lee, C. J. Xu, J. Xie, J. H. Lee, B. Wu, A. L. Koh, X. Y. Wang, R. Sinclair, S. Xwang, D. G. Nishimura, S. Biswal, S. H. Sun, S. H. Cho, X. Y. Chen, Synthesis and characterization of PVP-coated large core iron oxide nanoparticles as an MRI contrast agent, *Nanotechnology*, **2008**, 19.

124. C. Zhang, M. Jugold, E. C. Woenne, T. Lammers, B. Morgenstern, M. M. Mueller, H. Zentgraf, M. Bock, M. Eisenhut, W. Semmler, F. Kiessling, Specific targeting of tumor angiogenesis by RGD-conjugated ultrasmall superparamagnetic iron oxide particles using a clinical 1.5-T magnetic resonance scanner, *Cancer Res*, **2007**, 67, 1555-1562.

125. J. T. Kemshead, J. Ugelstad, Magnetic Separation Techniques - Their Application to Medicine, *Mol Cell Biochem*, **1985**, 67, 11-18.

126. J. M. Perez, L. Josephson, T. O'Loughlin, D. Hogemann, R. Weissleder, Magnetic relaxation switches capable of sensing molecular interactions, *Nat Biotechnol*, **2002**, 20, 816-820.

127. I. Safarik, M. Safarikova, Magnetic techniques for the isolation and purification of proteins and peptides, *Biomagn Res Technol*, **2004**, 2, 7.

128. H. W. Gu, P. L. Ho, K. W. T. Tsang, L. Wang, B. Xu, Using biofunctional magnetic nanoparticles to capture vancomycin-resistant enterococci and other gram-positive bacteria at ultralow concentration, *J Am Chem Soc*, **2003**, 125, 15702-15703.

129. S. Bucak, D. A. Jones, P. E. Laibinis, T. A. Hatton, Protein separations using colloidal magnetic nanoparticles, *Biotechnol Progr*, **2003**, 19, 477-484.

130. P. C. Lin, M. C. Tseng, A. K. Su, Y. J. Chen, C. C. Lin, Functionalized magnetic nanoparticles for small-molecule isolation, identification, and quantification, *Anal Chem*, **2007**, 79, 3401-3408.

131. G. D. Chen, C. J. Alberts, W. Rodriguez, M. Toner, Concentration and Purification of Human Immunodeficiency Virus Type 1 Virions by Microfluidic Separation of Superparamagnetic Nanoparticles, *Anal Chem*, **2010**, 82, 723-728.

132. M. Shinkai, M. Yanase, M. Suzuki, H. Honda, T. Wakabayashi, J. Yoshida, T. Kobayashi, Intracellular hyperthermia for cancer using magnetite cationic liposomes, *J Magn Magn Mater*, **1999**, 194, 176-184.

133. A. Ito, M. Shinkai, H. Honda, T. Kobayashi, Heat-inducible TNF-alpha gene therapy combined with hyperthermia using magnetic nanoparticles as a novel tumor-targeted therapy, *Cancer Gene Ther*, **2001**, 8, 649-654.

134. B. Le, M. Shinkai, T. Kitade, H. Honda, J. Yoshida, T. Wakabayashi, T. Kobayashi, Preparation of tumor-specific magnetoliposomes and their application for hyperthermia, *J Chem Eng Jpn*, **2001**, 34, 66-72.

135. A. Jordan, R. Scholz, K. Maier-Hauff, M. Johannsen, P. Wust, J. Nadobny, H. Schirra, H. Schmidt, S. Deger, S. Loening, W. Lanksch, R. Felix, Presentation of a new magnetic field therapy system for the treatment of human solid tumors with magnetic fluid hyperthermia, *J Magn Magn Mater*, **2001**, 225, 118-126.

136. K. Maier-Hauff, F. Ulrich, D. Nestler, H. Niehoff, P. Wust, B. Thiesen, H. Orawa, V. Budach, A. Jordan, Efficacy and safety of intratumoral thermotherapy using magnetic iron-oxide nanoparticles combined with external beam radiotherapy on patients with recurrent glioblastoma multiforme, *J Neuro-Oncol*, **2011**, 103, 317-324.

137. N. Kohler, C. Sun, J. Wang, M. Q. Zhang, Methotrexate-modified superparamagnetic nanoparticles and their intracellular uptake into human cancer cells, *Langmuir*, **2005**, 21, 8858-8864.

138. C. R. Sun, K. Du, C. Fang, N. Bhattarai, O. Veiseh, F. Kievit, Z. Stephen, D. H. Lee, R. G. Ellenbogen, B. Ratner, M. Q. Zhang, PEG-Mediated Synthesis of Highly Dispersive Multifunctional Superparamagnetic Nanoparticles: Their Physicochemical Properties and Function In Vivo, *Acs Nano*, **2010**, 4, 2402-2410.

Chapter 2

Surface modification of iron oxide nanoparticles using functional silane ligands

2.1 Introduction

The low toxicity profile and the magnetic properties of superparamagnetic iron oxide nanoparticles (SPIONs) have made them promising platforms for a wide range of biological applications such as magnetic resonance imaging (MRI), drug delivery, magnetic hyperthermia and magnetic separations of biomolecules.[1-9] In this context, surface coating and functionalisation of SPIONs is important as it can afford solubility and dispersibility in different environments as well as protection of the magnetic core from the biological medium. At the same time, the functionalisation should provide an opportunity for further chemical development such as conjugation of active biomolecules and complementary imaging labels such as fluorescent tags. Various strategies have been explored for introducing functional coatings on SPIONs. The use of coordinative, electrostatic, hydrophobic and covalent interactions has been demonstrated for SPION coating and functionalisation.[6,10] The detachment of weakly physisorbed coatings from SPIONs in commercially available MRI agents has already highlighted the importance of the nature of the interaction.[8,11] Covalently attached coatings can provide a robust bond with the surface of the nanoparticle while offering a great variety of surface functionalities and therefore can provide an excellent platform for use of SPIONs in the biomedical applications.

Organosilane ligands, in particular alkoxysilanes, can form stable covalent bonds with the metal oxide surfaces and thus offer a viable approach for surface modification of SPIONs.[3,7,12-17] The reaction of alkoxysilanes with the surface of SPIONs involves several steps as summarized in **Scheme 2.1**. Initilally, hydrolysis of the alkoxy groups of the silane to reactive silanol groups, condensation of the silanol groups, adsorption of silanols on the nanoparticle surface and covalent bond formation with the surface during the final dehydration reaction.[16,18] In addition to strong covalent bonding the silanes can be employed to introduce a variety of organic functionalities on the surface of SPIONs, which are useful for further biofunctionalisation.

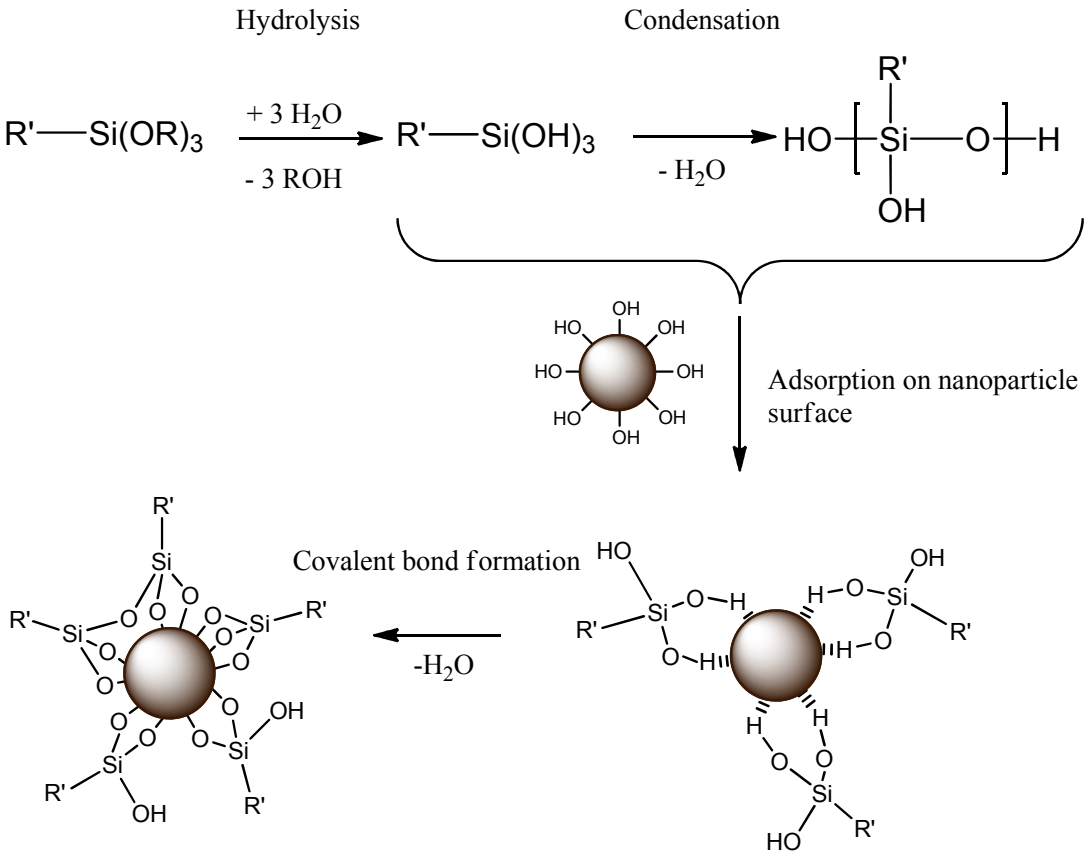

Scheme 2.1 Generalised mechanism for the hydrolytic silanisation of the metal oxide nanoparticle surface. Figure adapted from ref. 18

Amino functional groups (***-NH₂***) have been grafted on the surface of SPIONs using 3-aminopropyltriethoxy silane (APTES) which is one of the most used silane ligands for biological applications. The amine groups can facilitate conjugation of both biomolecules (proteins, folic acid) or fluorescent tags making APTES functionalised SPIONs promising platforms for application in biological systems.[16,19-22] Mikhaylova *et al*. used the silanisation of iron oxide nanoparticles (NPs) with APTES to prove that introduction of amino groups to the particle surface can promote the conjugation of bovine serum albumin (BSA) as shown in **Figure 2.1**.[19]

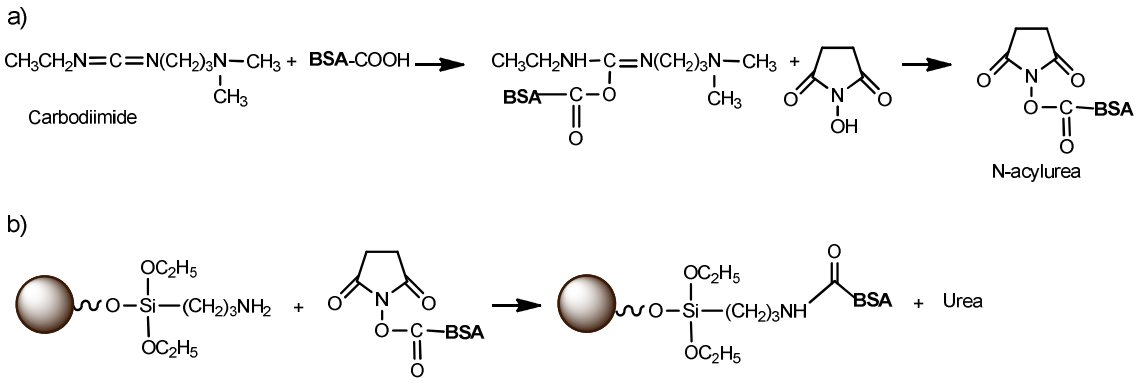

Figure 2.1 Schematic representation of a) carbodiimide and hydroxysuccinimide activation of carboxylic groups of BSA and b) coupling of activated BSA onto aminosilane-functionalised NPs. Figure adapted from ref. 19

Importantly, the authors showed that the NPs retain their superparamagnetic properties after the surface functionalisation with the silane and the BSA. *In vitro* cell studies using the BSA coated SPIONs demonstrated that the surface functionalisation has no effect on cell viability. Zhang *et al*.[20] adopted silane modifications of the SPIONs to introduce target-recognising molecules such as folic acid on the surface of the nanoparticles. In order to conjugate with the folic acid, APTES was modified with a polyethylene glycol (PEG) spacer and a terminal amino group. Using this tailored PEG silane, the ligand

successfully modified the surface of the SPIONs and functionalisation was confirmed using FTIR, UV/VIS and TEM.[20] In a follow-up paper, Zhang *et al.* used the tailored PEG silane with the terminal amino groups to conjugate a drug methotrexate (MTX) to the surface of the SPIONs.[21] MTX conjugated SPIONs were tested *in vitro* as a drug carrier system using brain cancer cells.

Polymerisable functional groups like methacrylates were introduced on the surface of SPIONs using organosilane ligands.[15,17] Flesh *et al*. copolymerised methacrylate-functionalised poly(ethyleneglycol) macromonomer from the surface of methacrylate-functionalised SPIONs.[15] Using direct copolymerisation and inverse emulsion polymerisation, the authors showed that only inverse emulsion produced high grafting densities of the polymer on SPIONs surface. Frickel *et al.* have used methacrylic and chlorobenzyl functional silanes to modify the surface of SPIONs and demonstrate the irreversible attachment of the silane monolayers.[17] These two functionalities were used to prepare magnetic core/polymeric brush hybrid particles.

The work in this chapter describes the surface modification chemistry of commercially available SPIONs (25 nm, Fe_3O_4) by a series of organosilane ligands. It was shown that a number of follow-up modification reactions become accessible leading to multifunctional organic-inorganic hybrids.

APTES was used to graft cationic amine groups (***–NH₂*** groups) on surface of the Fe_3O_4 NPs. Part of the amine groups were then converted to carboxylic acid groups using a reaction with succinic anhydride. As a result, robust silane linkages were introduced to the surface of NPs along with bifunctionality originating from amine and carboxylic acid groups. A full set of physico-chemical characterisations was undertaken to analyse

the bifunctionalised nanoparticles such as surface coverage by organic ligands, size of the NPs and their magnetic properties. Organic functional groups such as amines and carboxyls are of interest for biological applications because they allow coupling of biomolecules under mild conditions, such as reactions at ambient temperature and in physiological buffers. Furthermore chemical multifunctionality is important especially for use of independent conjugation chemistries to attach bioactive molecules. In addition to APTES functionalisation, Fe_3O_4 NPs were modified using other functional silanes to evaluate the formation of the silane layer and compare the level of surface coverage derived from the reaction with each silane reagent. These silane ligands were deliberately selected due to their structural similarity with APTES. This approach allowed introducing a range of functional groups, such as ***–Br***, ***–I***, ***–C≡N*** or vinyl (***–CH=CH₂***) on the surface of the nanoparticles. In a "grafting from" polymerisation reaction, the ***–Br*** functionalities were used as initiating groups for coating the nanoparticles with a pH sensitive polymer poly(2-(diethylamino)ethyl methacrylate), PDEAEMA. In another example, the vinyl silane functionalised nanoparticles were used in a *thiol-ene click* model reaction with mercaptopropionic acid to prepare a fully carboxylated surface. Full characterisation of the synthesised nanoparticles was undertaken to provide confirmation of the surface functionality. The coverage with different organic functionalities at each chemical modification step was detailed and additional evidence of chemical conjugation with fluorescent tags was provided by means of fluorescence microscopy.

2.2 Experimental section

2.2.1 Materials

Iron (II, III) oxide (Fe_3O_4, magnetite) nanoparticles were used as purchased from the commercial source Alfa Aesar (Nanopowder, 98% metal basis, 20-30 nm core size measured using TEM). 3-Aminopropyltriethoxysilane (APTES, 99%), 3-bromopropyltrimethoxysilane (BPTMS, ≥98.0%), 3-iodopropyltrimethoxysilane (IPTMS, ≥99.0%), vinyltrimethoxysilane (VTMS, 98%) and 3-cyanopropyltriethoxysilane (CPTES, 98%) were purchased from Fluorochem. Succinic anhydride (≥ 99%), 3-mercaptopropionic acid (≥ 99%), 2,2′-azobis(2-methylpropionitrile) (AIBN, 98%), Fluorescein-5-thiosemicarbazide, *N,N*-dimethylformamide anhydrous (DMF, 99.8%), 2- (diethylamino)ethyl methacrylate (DEAEMA, 99%), 2-propanol anhydrous (IPA, 99.5%), copper (I) bromide (99.99% trace metals basis), toluene (≥ 99.5%) and 2,2′-bipyridyl (≥ 99%) were purchased from Sigma Aldrich. All chemicals were used as received without any further purification except the DEAEMA monomer which was passed through an alumina column prior to use. Toluene was dried using 4Å molecular sieves (Sigma-Aldrich) activated at 300°C for 3 hours. All aqueous solutions were prepared using ultrapure water Milli-Q (Millipore, resistivity 18.2 MΩ.cm at 25°C). The magnet used was a rare earth NdFeB magnet (MagnetSales) with 10 mm diameter, 5 mm thickness and 1.18 T strength.

2.2.2 Synthetic methods

2.2.2.1 SPION Fe_3O_4 nanoparticles

Superparamagnetic iron (II, III) oxide (Fe_3O_4, magnetite) nanoparticles were purchased and used as received from Alfa Aesar (Nanopowder, 98% metal basis, core size 20-30 nm measured using TEM).

2.2.2.2 Surface functionalisation of Fe_3O_4 nanoparticles with $-NH_2$ groups using 3-aminopropyltriethoxysilane (APTES)

Fe_3O_4 nanoparticles (500 mg) were dispersed in anhydrous toluene (50 mL) using an ultrasonic bath for 10 minutes under ambient conditions. Subsequently to this suspension, APTES (0.5 mL) was added dropwise and the reaction mixture was heated to reflux using vigorous mechanical stirring. After 16 hours, the nanoparticles were retrieved using a permanent magnet and washed five times with excess acetone to remove all traces of unreacted silanes and toluene. The amino-functional nanoparticles (denoted as **Fe_3O_4–NH_2**) were dried overnight under vacuum at room temperature. This route is adapted from Xu *et al.*[7]

2.2.2.3 Surface functionalisation of Fe_3O_4 nanoparticles with $-Br$ groups using 3-bromopropyltrimethoxysilane (BPTMS)

Fe_3O_4 nanoparticles (500 mg) were dispersed in anhydrous toluene (50 mL) using an ultrasonic bath for 10 minutes under ambient conditions. To this, BPTMS (0.5 mL) was added dropwise and the reaction mixture was heated to reflux using mechanical stirring. After 16 hours, the nanoparticles were retrieved using a permanent magnet and washed five times with excess acetone to remove all traces of unreacted silane and toluene. The

bromo-functional nanoparticles (denoted as **Fe_3O_4–Br**) were dried overnight under vacuum at room temperature.

2.2.2.4 Surface functionalisation of Fe_3O_4 nanoparticles with *–I* groups using 3-iodopropyltrimethoxysilane (IPTMS)

Fe_3O_4 nanoparticles (500 mg) were dispersed in anhydrous toluene (50 mL) using an ultrasonic bath for 10 minutes under ambient conditions. Subsequently IPTMS (0.5 mL) was added dropwise to this suspension while sonicating, followed by refluxing the reaction mixture for 16 hours using mechanical stirring. The nanoparticles were then retrieved using a permanent magnet and washed five times with excess acetone to remove all traces of unreacted silane and toluene. The iodo-functional nanoparticles (denoted as **Fe_3O_4–I)** were dried overnight under vacuum at room temperature.

2.2.2.5 Surface functionalisation of Fe_3O_4 nanoparticles with *–CH=CH₂* groups using vinyltrimethoxysilane (VTMS)

Fe_3O_4 nanoparticles (500 mg) were dispersed in dry toluene (50 mL) using an ultrasonic bath for 10 minutes under ambient conditions. Subsequently to this suspension VTMS (0.5 mL) was added dropwise and the reaction mixture was heated to reflux using mechanical stirring. After 16 hours, the nanoparticles were retrieved using a permanent magnet and washed five times with excess acetone to remove all traces of unreacted silane and toluene. The vinyl-functional nanoparticles (denoted as **Fe_3O_4–$CH=CH_2$**) were dried overnight under vacuum at room temperature.

2.2.2.6 Surface functionalisation of the Fe_3O_4 nanoparticles with $-C\equiv N$ groups using 3-cyanopropyltriethoxysilane (CPTES)

Fe_3O_4 nanoparticles (500 mg) were dispersed in dry toluene (50 mL) using an ultrasonic bath for 10 minutes under ambient conditions. Subsequently to this suspension, CPTES (0.5 mL) was added dropwise and the reaction mixture was heated to reflux using mechanical stirring. After 16 hours, the nanoparticles were retrieved using a permanent magnet and washed five times with excess acetone to remove all traces of unreacted silane and toluene. The cyano-functional nanoparticles (denoted as **Fe_3O_4–C≡N**) were dried overnight under vacuum at room temperature.

2.2.2.7 Post-modification reaction of Fe_3O_4–NH_2 nanoparticles with succinic anhydride

Fe_3O_4–NH_2 nanoparticles (100 mg, 0.03 mmol ***–NH_2*** groups calculated as described in section 2.2.3.9) were suspended in anhydrous DMF (45 mL) under nitrogen atmosphere. Succinic anhydride (30 mg, 0.3 mmol) was then dissolved in anhydrous DMF (5 mL) and was added slowly to the nanoparticles suspension under nitrogen. The resulting mixture was stirred for 24 hours at room temperature under nitrogen. The resulting nanoparticles (denoted as **Fe_3O_4-NH_2/COOH**) were collected using a magnet and then washed five times with acetone before being dried overnight under vacuum at room temperature.

2.2.2.8 *Thiol-ene click* reaction of Fe_3O_4–CH=CH_2 nanoparticles with 3-mercaptopropionic acid

Fe_3O_4–CH=CH_2 nanoparticles (100 mg, 0.05 mmol ***–CH=CH_2*** groups) were suspended in anhydrous toluene (45 mL) under nitrogen atmosphere. 3-

mercaptopropionic acid (50 µL, 0.5 mmol) and AIBN (20 mg) pre-dissolved in toluene (5 mL) were then slowly added to the nanoparticle dispersion. The reaction mixture was stirred overnight at 85 °C under nitrogen. The resulting nanoparticles (denoted as **Fe_3O_4–S–COOH**) were collected using magnetic decantation and then washed five times with acetone before being dried under vacuum at room temperature.

2.2.2.9 Polymerisation of Fe_3O_4–Br nanoparticles using atom transfer radical polymerisation (ATRP): a grafting from approach

ATRP was used to graft 2-(diethylamino)ethyl methacrylate (DEAEMA) residues from the surface of **Fe_3O_4–Br** thus rendering the nanoparticles soluble in different solvents. Briefly, **Fe_3O_4–Br** nanoparticles (50 mg, 0.013 mmol **–Br** groups) were dispersed in anhydrous isopropanol (10 mL) using ultrasonic agitation. DEAEMA monomer (5 g, 27 mmol) was then added slowly to the magnetic suspension and the mixture was degassed using nitrogen bubbling. Copper (I) bromide (0.1 g, 0.7 mmol) and 2, 2'-bipyridine (0.33 g, 2 mmol) were added to the degassed mixture. The sealed reaction system was then agitated by rolling for 24 hours at room temperature. The resulting polymer-grafted nanoparticles (denoted as **Fe_3O_4–PDEAEMA**) were collected using magnetic decantation followed by repeated washes with water, ethanol and hexane. Particles were then dried under vacuum at room temperature.

This experiment was performed by Dr. Erol Hasan at the University of Liverpool, Centre for Materials Discovery.

2.2.3 Characterisation methods

2.2.3.1 Elemental analysis

Elemental analysis (C-H-N) was performed on a Thermo Flash EA1112 Series CHNS-O analyser and was used to analyse the organic content of the functionalised nanoparticle samples. The C-H-N content (C %, H %, N %) cited was an average of three measurements.

2.2.3.2 Thermogravimetric Analysis (TGA)

TGA was carried out using a TA instrument Q600 thermal balance. Typically 5-10 mg of nanoparticles were heated to 600 °C at 10 °C/min in air and kept at 600 °C for 30 min to determine the amount of organic content on the nanoparticle surface. The weight loss of non-coated nanoparticles was compared to the weight loss of coated nanoparticles. By subtracting the two, the difference was attributed to the extent of surface coverage. For a full description of this technique, see ref. 23.

2.2.3.3 Fourier Transform Infrared spectroscopy (FTIR)

FTIR spectra were recorded on powder samples using a Bruker Tensor 27 Spectrometer. Iron oxide nanoparticles functionalised with different organic ligands were analysed as powders. For each sample, 100 scans in the region from 400 to 4000 cm^{-1} with a resolution of 4 cm^{-1} were accumulated. Spectra were recorded and evaluated with OPUS/MAP version 4.0 software. FTIR were used to qualitatively identify each type of organic coating on the surface of functionalised iron oxide nanoparticles or to assess the chemical modifications made to the coating materials.[24]

2.2.3.4 Powder X-ray diffraction (PXRD) - Scherrer equation for size distribution

Powder X-ray diffraction patterns of the commercial Fe_3O_4 NPs sealed in a 0.5 mm glass capillary were collected on a Bruker D8 diffractometer using Mo Kα radiation (λ = 0.7107 Å). The PXRD data was used to identify the iron oxide phase composition and to confirm the average size specified by the manufacturer using automatic software (X'Pert Highscore Plus version 2.0). A particle size of 24 ± 2 nm was calculated using the Scherrer equation:

$$\tau = \frac{K\lambda}{\beta \cos \theta}$$

Where τ- is the particles size, β- is the line broadening at half the maximum intensity (FWHM), k- the shape factor (k=0.9), λ- is the x-ray wavelength (Mo, λ = 0.7107 Å), ϑ- is the Bragg diffraction angle.

2.2.3.5 Transmission Electron Microscopy (TEM)

TEM images of functionalised Fe_3O_4 NPs were recorded using a FEI Tecnai G2 Spirit BioTWIN instrument with a W filament and a SIS Megaview III digital camera, operating at 100 kV. All TEM samples were prepared by brief sonication of Fe_3O_4 NPs in appropriate solvent (ethanol or H_2O) and 50 µL sample was then deposited onto a carbon coated 300 mesh copper grid. The grids were then allowed to dry in air prior to imaging. The size distribution of the nanoparticles was derived from TEM images using ImageJ software and 400 measurements.

2.2.3.6 Measurements of magnetic properties

Magnetic measurements were performed in a Quantum Design MPMS XL Superconducting Quantum Interference Device (SQUID) magnetometer using the

system DC measurement capabilities. Milligram quantities of the sample were placed in a standard gelatine capsule. Magnetisation measurements were made at room temperature (300 K) by varying fields over a +1T to -1T range. The SQUID magnetic measurements were performed by Dr. Pavel Borisov at the University of Liverpool, Department of Chemistry.

2.2.3.7 Fluorescence microscopy

Fluorescence microscopy was employed to qualitatively analyse the chemical reactivity of functional groups on nanoparticles surface. The images were acquired using a Leica DM2500 inverted microscope equipped with a Leica DFC350 FX camera. The nanoparticles functionalised with different organic groups were conjugated with fluorescent molecules (fluorescein isothiocyanate-FITC and rhodamine B isothiocyanate-RITC). Since iron oxide does not fluoresce, the fluorescence microscopy provides high sensitivity for detecting the attached fluorophores.[25]

2.2.3.8 Dynamic Light Scattering (DLS)

The hydrodynamic diameters of the functionalised nanoparticles were measured using a Malvern Zetasizer NanoZS equipped with a helium laser at a wavelength of 633 nm. A 1 mL aliquot of nanoparticle dispersion in deionised H_2O (pH 6.5) was used in the measurements. Scattered light was collected at a fixed angle of 173° and the measurements were performed at 25 °C. The intensity-average hydrodynamic diameters reported are obtained from at 3 measurements; for each measurement at least 20 repeat runs were used.

2.2.3.9 Particle coverage calculations

The quantitative information on the silane layer formation is based on the carbon content from elemental analysis and TGA after careful isolation of functional particles. It should be stated that the analysis by ^{29}Si NMR is impeded by the magnetic nature of the cores. The general set of formulae used for characterising the surface coverage is presented below.

Taking into account the average nanoparticle diameter d = 25 nm of a spherical individual nanoparticle obtained from TEM, the surface area and the volume, S_{NP} and V_{NP}, can be calculated as:

$$S_{NP} = 4\pi r^2 = 4\pi \times (12.5 \times 10^{-9})^2 = 19.63 \times 10^{-16}\ \text{m}^2 \quad (2.1)$$

$$V_{NP} = \frac{4}{3}\pi r^3 = \frac{4}{3}\pi \times (12.5 \times 10^{-9})^3 = 8.16 \times 10^{-24}\ \text{m}^3 \quad (2.2)$$

The mass of this nanoparticle is, $m_{1NP:}$

$m_{1NP} = \rho \times V_{NP} = 5.17 \times 10^6 \times 8.16 \times 10^{-24} = 42.18 \times 10^{-18}$ g, where ρ is the density of Fe_3O_4. (2.3)

The number of NPs per g material is:

$$N_{NP} = \frac{1}{m_{1NP}} = \frac{1}{42.18 \times 10^{-18}} = 2.37 \times 10^{16}\ \text{g}^{-1} \quad (2.4)$$

The specific surface area is:

$$S = \frac{S_{NP}}{m_{1NP}} = 46.52\ \text{m}^2 \times \text{g}^{-1} \quad (2.5)$$

2.3 Results and discussion

2.3.1 Formation of dual (*–NH₂* and *–COOH*) functional groups on the surface of Fe_3O_4 nanoparticles

Bifunctional Fe_3O_4 nanoparticles with both ***–NH₂*** and ***–COOH*** functionalities co-existing on the surface were synthesised using a simple direct-grafting method which consisted in an initial reaction with APTES and a follow-up reaction with succinic anhydride. The functionalisation procedure of Fe_3O_4 NPs with APTES involved the reaction between the hydroxyl groups which are present on the NPs surface and the ethoxy groups of the aminosilane, forming a covalent Fe-O-Si bond.[26] The grafting reaction consists of the hydrolysis of ethoxy groups of APTES and the condensation of the silanol groups with the surface hydroxyl groups. During the reaction ethanol is eliminated as a byproduct as illustrated in **Scheme 2.2**. By grafting APTES on the surface of the Fe_3O_4 NPs, amine-functionalised nanoparticles were prepared and the sample was denoted as **Fe_3O_4-NH_2**.

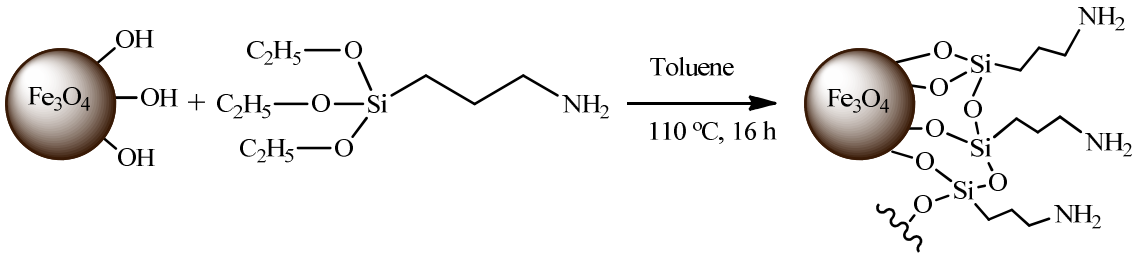

Scheme 2.2 Schematic representation of the grafting of an aminosilane molecule to the surface of a Fe_3O_4 nanoparticle.

Several techniques were used to characterise the functionalised nanoparticles after the washing and drying steps. Firstly, qualitative confirmation of the surface

functionalisation and presence of amino groups on the **Fe_3O_4-NH_2** was obtained from infrared spectroscopy and compared with the spectrum of unfunctionalised Fe_3O_4 nanoparticles (**Figure 2.2**). The successful grafting of silane molecules was confirmed in the FTIR spectrum of the **Fe_3O_4-NH_2** by the presence of the two broad bands at 3435 and 1600 cm^{-1} which were assigned to the N-H stretching vibration and N-H bending respectively. The bands observed at 2925 and 2850 cm^{-1} are due to the symmetric and the asymmetric CH_2 stretching modes respectively. The Fe-O-Si bonds are masked in the FTIR spectrum due to overlapping with the Fe-O vibrations of magnetite at 580 cm^{-1}.[27] On the other hand, the formation of the silane layer on the surface of nanoparticles was confirmed by the presence of the band at 1015 cm^{-1} corresponding to the Si-O-Si bond.[28]

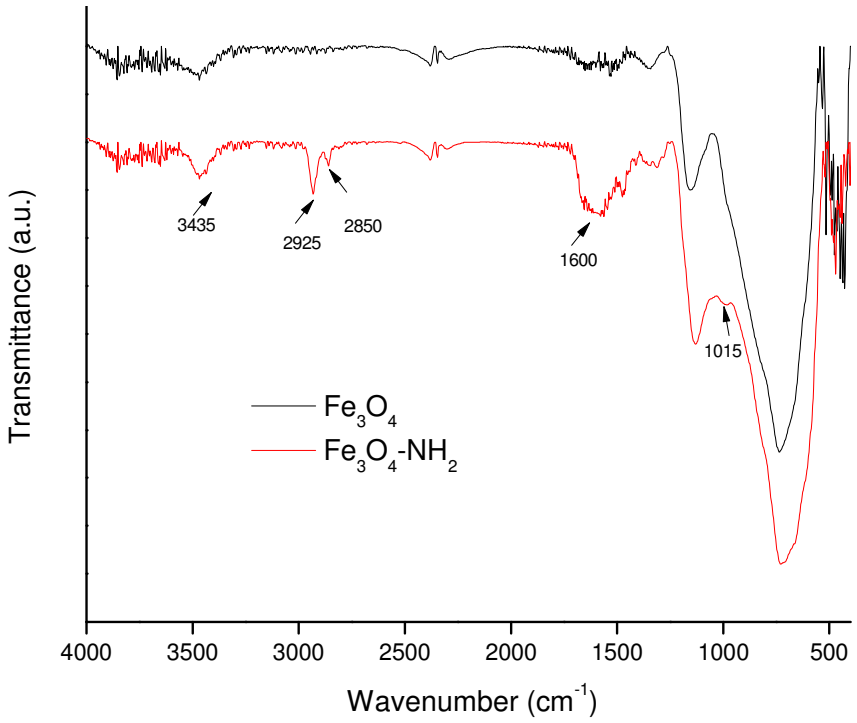

Figure 2.2 FTIR spectra of magnetic nanoparticles: **Fe_3O_4** (black line), **Fe_3O_4-NH_2** (red line) showing the presence of NH_2 groups.

In order to estimate the number of amino grafted groups on the surface quantitative analysis for the composition of the **Fe_3O_4-NH_2** was carried out using elemental analysis. Elemental analysis data showed the presence of nitrogen and an increase in the carbon content (C = 1.22%, H = 0.38%, N = 0.37%) compared with non-functionalised sample (C = 0.08%, H = 0.23%, N = 0%). From this data, the surface coverage of aminosilane ligands could be calculated as:

The mass of carbon in 1g of material: $1 \times \frac{1.22}{100} = 12.2 \text{ mg}$ (2.6)

Number of mols of carbon in 12.2 mg: $\frac{12.2}{12} = 1.02 \text{ mmol carbon}$ (2.7)

The degree of functionalisation per mass unit, $f = \frac{1.02}{3} = 0.34 \text{ mmol} \times \text{g}^{-1}$ (2.8)

(where 3 is the number of carbons in each APTES ligand).

From equations 2.5 (in section **2.2.3.9**) and 2.8 it is possible to calculate the surface coverage C:

$$C = \frac{f}{S} = 7.38 \text{ µmol} \times \text{m}^{-2}$$

The number of mols of ligands per nanoparticle is:

$$N_{mols} = \frac{f}{N_{NP}} = \frac{0.34 \times 10^{-3}}{2.37 \times 10^{16}} = 143 \times 10^{-22} \quad (2.9)$$

Therefore the number of aminosilane ligands per nanoparticle can be calculated as:

$$n_L = N_{mols} \times N_A = 143 \times 10^{-22} \times 6.022 \times 10^{23} = 8611$$

Where N_A is Avogadro's number. (2.10)

The results show good agreement with previously reported coverage values which were calculated based on space filling projections.[29] For an APTES monolayer formation, the surface functionalisation density varies between 2.8 µmol/m^2 and 12 µmol/m^2 depending on the nanoparticle size and the silane orientation with respect to the surface.[26,30-31] The

formation of the dense silane layer is an important feature if biological applications are in mind, as it would prevent possible degradation of the protective layer and leaching of iron into a biological environment. Another desired feature for the biomedical applications is multifunctionality which would allow the use of independent chemistries to attach biomolecules to the nanoparticle surface.

In order to introduce a second functionality on the surface and to test the reactivity of the amine groups on the **Fe_3O_4-NH_2** a reaction with succinic anhydride was carried out. This modification reaction was chosen because it is commonly used in biology to introduce terminal carboxylate functionalities from an existing amino group as illustrated in **Scheme 2.3**.[32] The sample derived from this reaction was denoted as **Fe_3O_4-NH_2/COOH.**

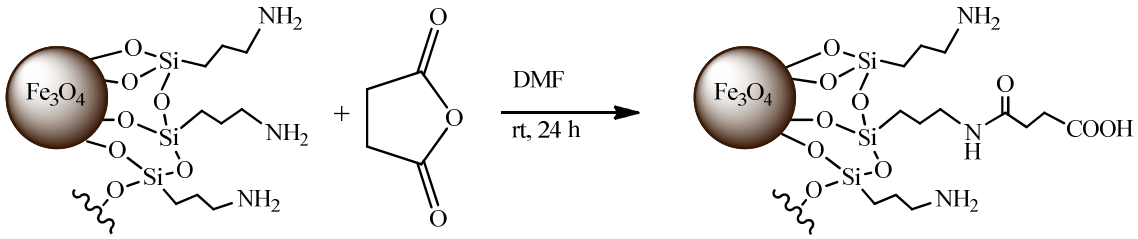

Scheme 2.3 Schematic representation of the reaction between succinic anhydride and the **Fe_3O_4-NH_2**.

The presence of the free carboxylic groups was assessed qualitatively using FTIR spectroscopy (**Figure 2.3**). The free carboxylic acid groups present were confirmed by the characteristic C=O stretching absorption at 1725 cm^{-1} in the spectrum of **Fe_3O_4-NH_2/COOH**. The frequencies in the region of 1640 cm^{-1} and 1560 cm^{-1} were assigned to the C=O stretching band and N-H bending band in the amide linkage respectively.

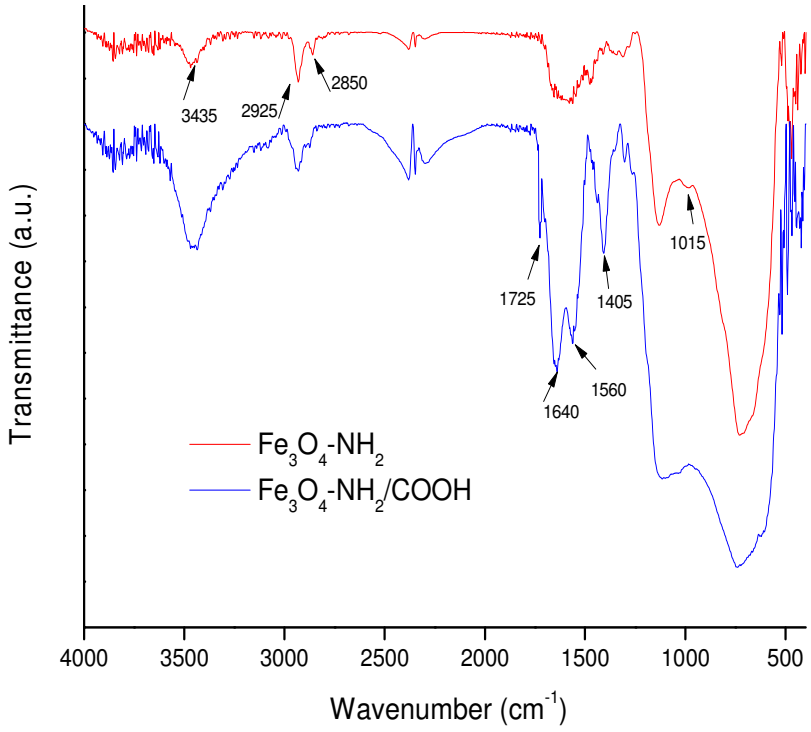

Figure 2.3 FTIR spectra of functionalised magnetic nanoparticles: **Fe_3O_4-NH_2** (red line) and **Fe_3O_4-NH_2/COOH** (blue line).

Elemental analysis of **Fe_3O_4-NH_2/COOH** nanoparticles showed an increase in carbon and hydrogen content (C = 1.62%, H = 0.41%, N = 0.38%) compared with **Fe_3O_4-NH_2**. Based on the elemental analysis values and applying the equations 2.6 to 2.8 the fraction of amine groups reacted with succinic anhydride can be estimated:

Mass of carbon in 1g of material = 16.2 mg (2.11)

Number of mols of carbon in 16.2 mg: $\frac{16.2}{12} = 1.35$ mmol carbon (2.12)

Assigning ‘x’ to be the amount of unreacted amine functional groups and ‘y’ to be the amount of reacted groups, and considering there are 3 carbon atoms in the unreacted amine functional group and 7 in the succinic anhydride-reacted functional group:

A: 3x + 7y = 1.35 mmol carbon, post succinic anhydride reaction

B: x + y = 0.34 as the total number of bound groups should be the same before and after the succinic anhydride reaction (from equation 2.8).

Solving simultaneous equations A and B, x and y were calculated as x= 0.25 mmol and y = 0.09 mmol, the number of un-reacted and reacted amine functional groups respectively. Thus the percentage of added ***–COOH*** groups is:

$$\frac{y}{x+y} = \frac{0.09}{0.34} \times 100 = 26.5\ \%$$

Following equations 2.9 and 2.10 the number of carboxylic groups per nanoparticle was determined to be 2300. The results showed that the amine groups were reactive towards succinic anhydride but the reaction did not go to completion. Such incomplete conversion was likely due to steric hindrance which prevented the reaction of succinic anhydride with all accessible amino groups. Performing the reaction at variable temperatures could provide additional control over the ratio of **–NH_2/–COOH** groups on the surface of the nanoparticles. At ambient temperature, the partial conversion of the amine groups to carboxylic acids offered a bifunctional surface with 75% amino and 25% of carboxylic acid groups.

TGA was additionally used to confirm the composition for the two sets of nanoparticles. The thermograms recorded for **Fe_3O_4-NH_2** and **Fe_3O_4-NH_2/COOH** nanoparticles presented in **Figure 2.4** show the weight losses associated with each sample.

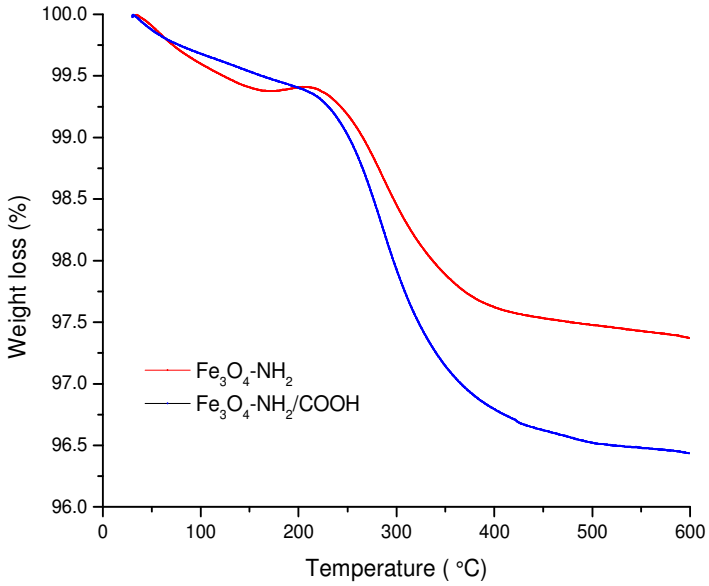

Figure 2.4 TGA thermograms of **Fe_3O_4-NH_2** (red line) and **Fe_3O_4-NH_2/COOH** (blue line) nanoparticles. The corresponding weight losses are 2.03% in **Fe_3O_4-NH_2** against 3.08% in **Fe_3O_4-NH_2/COOH**.

For **Fe_3O_4-NH_2**, two weight losses are evident: the first between 30 °C and 150 °C was due to the evaporation of physically absorbed moisture on the surface. The second weight loss (between 150 °C and 600 °C) corresponded to the decomposition of propylamine groups. Similar temperature decomposition profile was reported for aminosilane-coated cobalt ferrite nanoparticles.[26] TGA was also used to estimate the number of silane ligands anchored on the nanoparticles according to the following formula:

$$N = \frac{\omega N_A \varphi V}{MW} \qquad (2.13)$$

Where N is the number of ligands on one nanoparticle, ω is the mass loss in percent, N_A is Avogadro's number, ρ is the density of the nanoparticle, V is the volume of one nanoparticle core and MW is the molar weight of the ligands.

The weight loss of the **Fe_3O_4-NH_2** between 150 °C and 600 °C recorded by TGA was 2.03% (**Figure 2.4** red line) which led to approximately 8750 amine groups per nanoparticle. This value was in good agreement with the results obtained from the elemental analysis. The deconvolution of the TGA data (**Figure 2.4** blue line) for **Fe_3O_4-NH_2/COOH** (3.08% - 2.03% = 1.05% between 150 °C and 600 °C) allowed the estimation of the number of carboxylic acid groups as approximately 2300 per NP, which was also consistent with the result from the elemental analysis.

The size of the nanoparticles before and after surface modifications was examined using transmission electron microscopy (TEM). The nanoparticle images along with the histograms of the size distributions are presented in **Figure 2.5**.

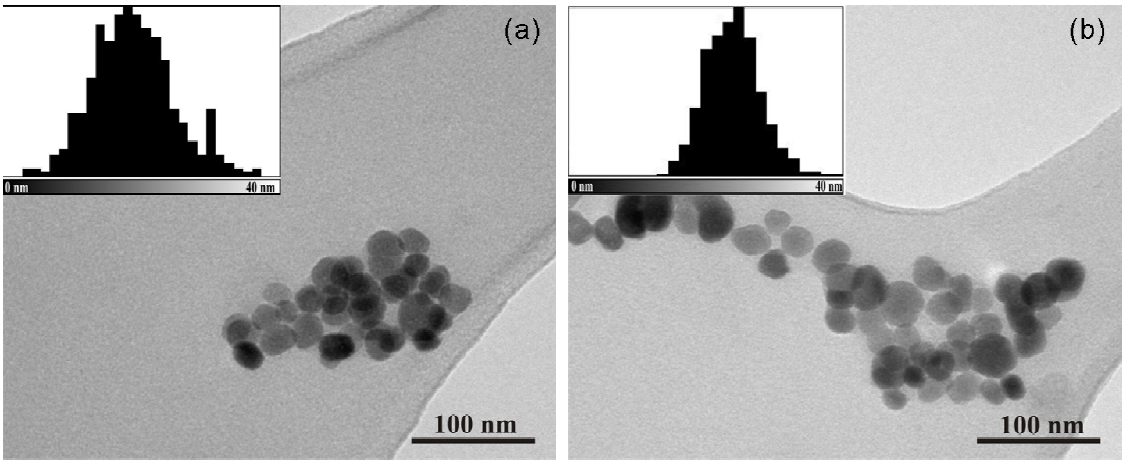

Figure 2.5 Transmission electron microscopy images of a) unfunctionalised **Fe_3O_4** and b) bifunctionalised **Fe_3O_4-NH_2/COOH** nanoparticles. The inset shows the histogram of the TEM particle size distribution.

The TEM images show that commercial Fe_3O_4 nanoparticles have monomodal distribution and their diameter is 25 ± 5 nm (**Figure 2.5a**). After chemical functionalisation with APTES and succinic anhydride, the morphology of the nanoparticles was not affected as shown in **Figure 2.5b**. The average particle size for **Fe_3O_4-NH_2/COOH** was 24 ± 4 nm.

In addition to the size measurement of the magnetic cores with TEM, the hydrodynamic diameter of the particles in aqueous solution was measured using DLS. The results showed that the average hydrodynamic size for the commercial unfunctionalised Fe_3O_4 nanoparticles was 164 ± 6 nm (**Figure 2.6**).

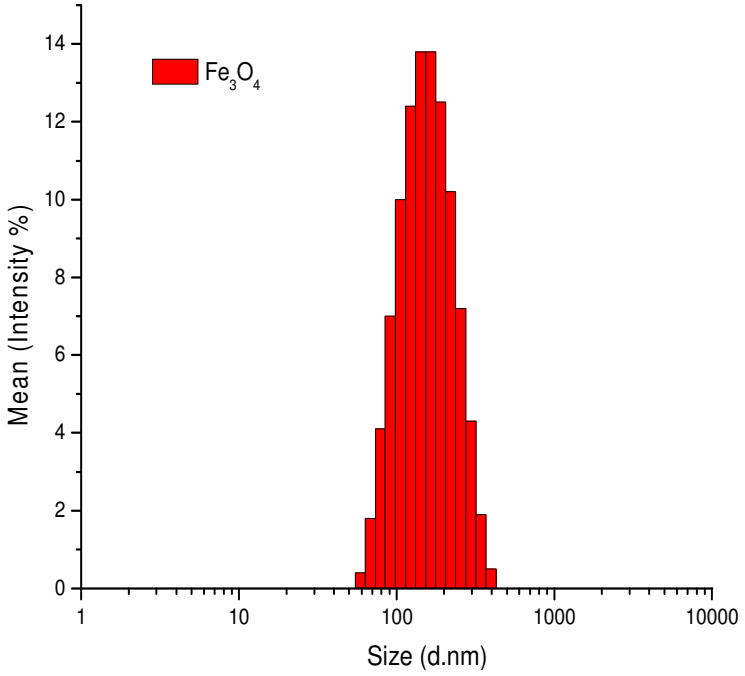

Figure 2.6 DLS histogram of unfunctionalised **Fe_3O_4** nanoparticles. The hydrodynamic particles size distribution for Fe_3O_4 nanoparticles is 164 ± 6 nm.

The difference between TEM and DLS results was attributed to the aggregation of the nanoparticles in solution. Due to the fact that larger nanoparticles or aggregates scatter

more the light compared with the smaller nanoparticles, the DLS results are skewed towards the larger nanoparticles. Compared with the unfunctionalised Fe_3O_4 nanoparticles, the hydrodynamic size for the **Fe_3O_4-NH_2/COOH** was 142 ± 8 nm as shown by the DLS distribution in **Figure 2.7**. It is important to notice that the chemical modifications on the surface did not introduce any major agglomeration between particles.

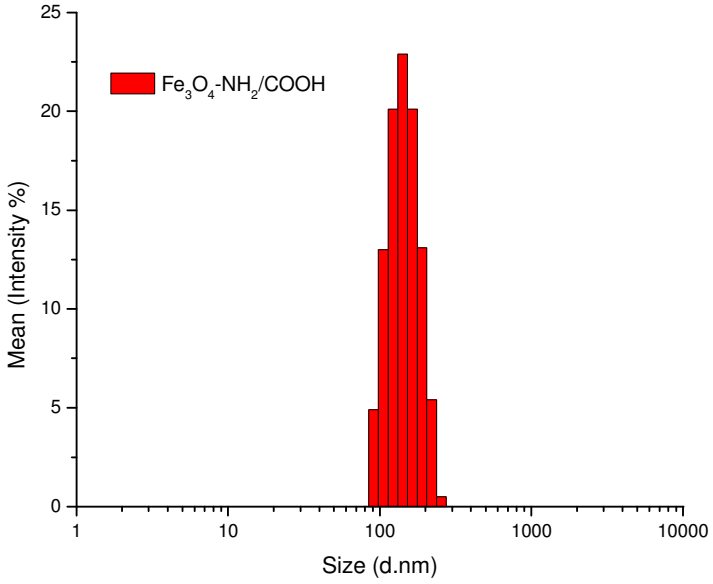

Figure 2.7 DLS histogram of bifunctionalised **Fe_3O_4-NH_2/COOH** nanoparticles. The hydrodynamic particles size distribution for **Fe_3O_4-NH_2/COOH** is 142 ± 8 nm.

Compared to the existing commercial MRI contrast agent Feridex I.V. (120-180 nm),[33] **Fe_3O_4-NH_2/COOH** exhibited a similar overall hydrodynamic diameter with a larger iron oxide core. This may prove advantageous for biological applications. At the same time, the **Fe_3O_4-NH_2/COOH** nanoparticles have a thinner organic shell compared with the Feridex I.V. agent (short silane ligand as opposed to high molecular weight dextran shell). In order to prove the effect of thinner shell on the magnetic properties of the

system and thus potentially greater MRI contrasting capability, the magnetic measurements were carried out on the **Fe_3O_4-NH_2/COOH**.

The magnetic properties of the bifunctional nanoparticles were compared with the starting material from a SQUID magnetometer data. **Figure 2.8** shows the field dependence of magnetisation measured at room temperature (300 K) from -1T to +1T. Both samples have a good magnetic response and exhibit the expected superparamagnetic behaviour as evident by no hysteresis at 300 K.

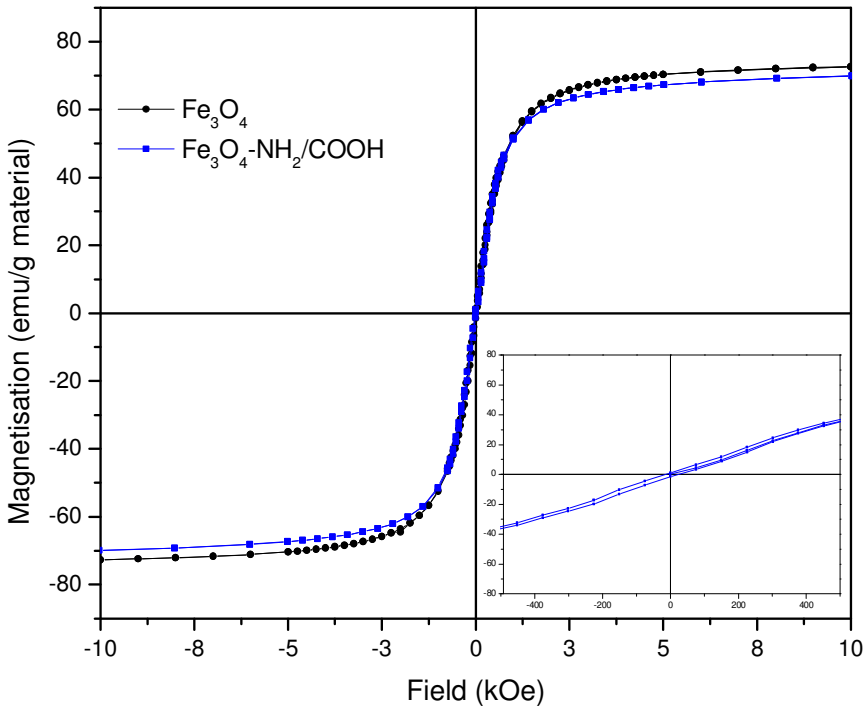

Figure 2.8 Magnetic field dependence of magnetisation at room temperature for unfunctionalised Fe_3O_4 (black) and **Fe_3O_4-NH_2-COOH** (blue) nanoparticles. Inset shows a zoom-in plot between -500 Oe and 500 Oe magnetic field.

The magnetisation values at saturation are 72.5 emu × g^{-1} and 69.3 emu × g^{-1} for unfunctionalised Fe_3O_4 and **Fe_3O_4-NH_2/COOH,** respectively. As expected, the value obtained for unfunctionalised Fe_3O_4 NPs is lower than that of bulk magnetite (92 emu ×

g^{-1}) which was attributed to particle size and to surface effects such the presence of a magnetically inactive layer.[34] The saturation magnetisation for the **Fe_3O_4-NH_2/COOH** is smaller than that of unfunctionalised Fe_3O_4 NPs by 5 % and is due to the non-magnetic shell around the nanoparticles. The results are in line with elemental analysis and TGA data. As anticipated, the saturation values for the **Fe_3O_4-NH_2/COOH** are significantly higher than that reported for the commercial formulation of iron oxide MRI agent Feridex I.V. (M_s= 9.5 emu × g^{-1}).[35] The higher magnetisation values can be attributed not only to the thinner organic coating on the surface of the NPs but also to the larger nanoparticle cores (25 nm compared with 5 nm). It is important to note that **Fe_3O_4-NH_2/COOH** nanoparticles maintained their superparamagnetic properties which are essential for the intended biological applications described in Chapter 3.

The dispersibility and stability of functionalised nanoparticles in water is dependent on the interaction between water and the functional groups present on their surface. The **Fe_3O_4-NH_2/COOH** dispersions resulted in almost transparent solutions indicative of the good interaction with water. On the other hand, for the unfunctionalised **Fe_3O_4** and **Fe_3O_4-NH_2** NPs opaque dispersions were obtained in which aggregation could be observed (**Figure 2.9**).

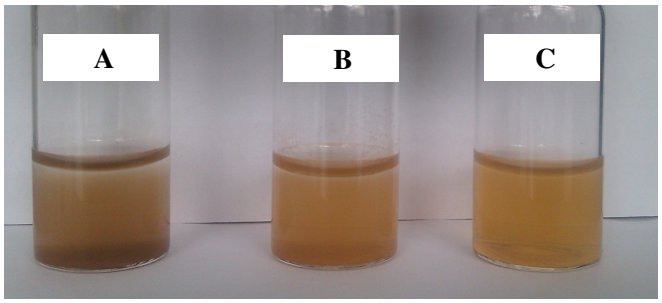

Figure 2.9 Images of 0.1 mg/mL nanoparticle dispersions of (A) **Fe_3O_4**, (B) **Fe_3O_4-NH_2** and (C) **Fe_3O_4-NH_2/COOH** in water.

The colloidal stability properties of **Fe_3O_4-NH_2/COOH** nanoparticles in comparison with the unfunctionalised Fe_3O_4 and **Fe_3O_4-NH_2** NPs were investigated using an absorbance method adapted from de Palma *et al.*[26] The absorbance of known nanoparticles concentrations in water was monitored at a fixed wavelength (850 nm) for five hours (**Figure 2.10**). A constant value of the absorbance as a function of time would indicate of a stable dispersion while a decrease in absorbance would indicate of sedimentation of the nanoparticles.

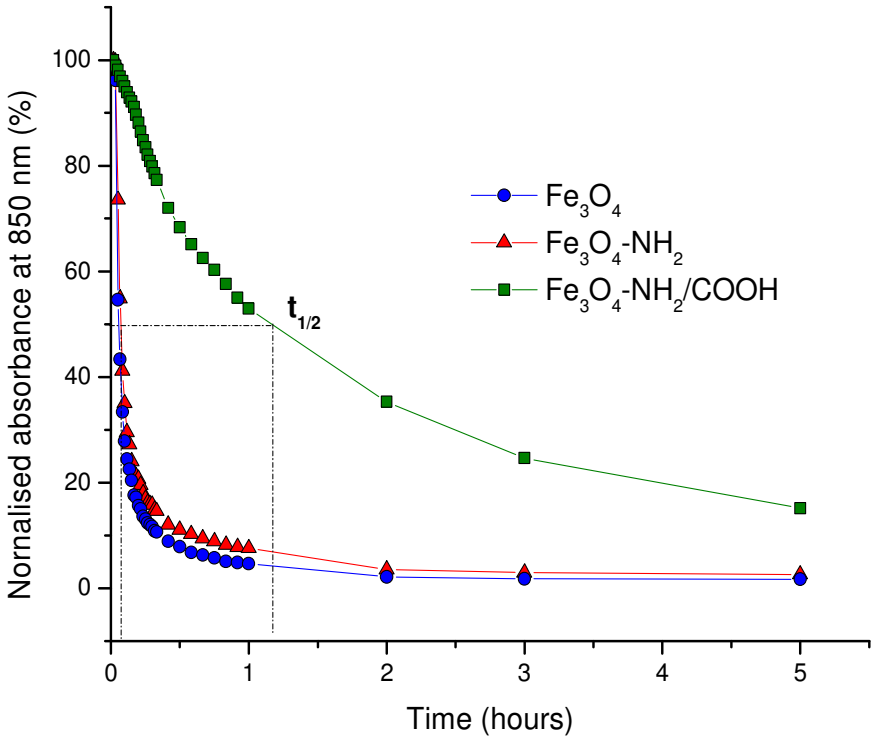

Figure 2.10 Colloidal stability of the **Fe_3O_4** (blue line), **Fe_3O_4−NH_2** (red line) and **Fe_3O_4-NH_2/COOH** (green line) NPs in water, at room temperature.

The results are concentration dependent but from the absorbance curves at the investigated concentration (0.1 mg/mL), it can be seen that the nanoparticles are settling with time. After a five hour period the absorbance of **Fe_3O_4** and **Fe_3O_4-NH_2** NPs

dispersions showed 100 % decrease. This is indicative of complete sedimentation of nanoparticles at the bottom of the vial. The **Fe_3O_4-NH_2/COOH** showed improved stability and hence slower sedimentation which can be attributed to the presence of the amino and carboxylic acid groups on the surface of the nanoparticles. Both functionalities act as a polyelectrolyte and help to stabilise the nanoparticles *via* electrostatic repulsion. The presence of the surface charge was confirmed using zeta potential measurements which showed that the **Fe_3O_4-NH_2/COOH** are negatively charged (-31.0 ±0.5 mV) when dispersed in water. As expected the surface charge influenced their colloidal stability.

Post-modification with succinic anhydride of the amino functionalised Fe_3O_4 nanoparticles is an efficient route for inducing bifunctional properties originating both from carboxylic acid and amine groups. The improved magnetic properties are making the bifunctionalised nanoparticles superior to the existing MRI contrast agent Feridex I.V. However, there is a room to improvement of the colloidal stability which could be possibly optimised by varying the size of the magnetic core and the ratio between carboxylic acid and amine groups present on their surface.

2.3.2 Surface modification Fe_3O_4 nanoparticles with other functional silane ligands

The commercial unfunctionalised Fe_3O_4 NPs were used in functionalisation experiments performed with ***–Br, –I, –CH=CH$_2$, –C≡N*** terminated silane ligands following the exact conditions developed for APTES functionalisation. The reactions with different terminated silane ligands were performed to obtain more information on the silane layer

formation (surface coverage) and to access iron oxide nanoparticles with various surface functionalities. The chemical structure of the silane molecules employed in this study for the functionalisation of iron oxide particles are shown in **Scheme 2.4**.

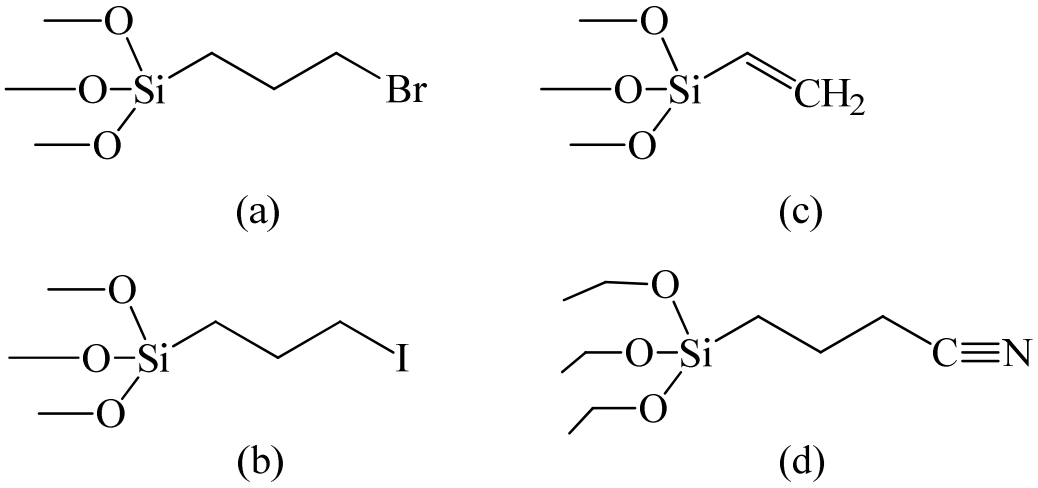

Scheme 2.4 Functional surface-modifying organosilanes employed for Fe_3O_4 nanoparticle functionalisation: (a) 3-bromopropyltrimethoxysilane (BPTMS), (b) 3-iodopropyltrimethoxysilane (IPTMS), (c) vinyltrimethoxysilane (VTMS), (d) 3-cyanopropyltriethoxysilane (CPTES).

The success of the surface modification with these organosilane molecules was qualitatively evaluated by FTIR spectroscopy and quantified by elemental analysis. In comparison with the unfunctionalised Fe_3O_4 nanoparticles, the infrared spectra (**Figure 2.11**) of the functionalised particles show the characteristic peaks of the respective modifying reagents. The formation of the silane layer was confirmed by the presence of the characteristic bands Si-O-Si in the fingerprint region between 1300 and 900 cm^{-1}.[28] These bands could be observed for all functionalised nanoparticles. The vibrational absorption of C-H, characteristic for all samples, is present in the fingerprint region between 2925 and 2850 cm^{-1}.

For **Fe_3O_4–Br** and **Fe_3O_4–I** nanoparticles the C-Br and C-I bands cannot be observed as they overlap with the footprint of Fe_3O_4. In case of **Fe_3O_4–CH=CH_2** nanoparticles, the spectrum shows two distinct signals: one at 3056 cm^{-1} and the other one at 1620 cm^{-1} indicative of the =C-H stretch in terminal vinyl and of the unsaturated hydrocarbon C=C stretch respectively. In case of **Fe_3O_4–C≡N** nanoparticles the typical stretching band for nitriles (–C≡N) which appears at 2252 cm^{-1} could be identified in the FTIR spectrum.

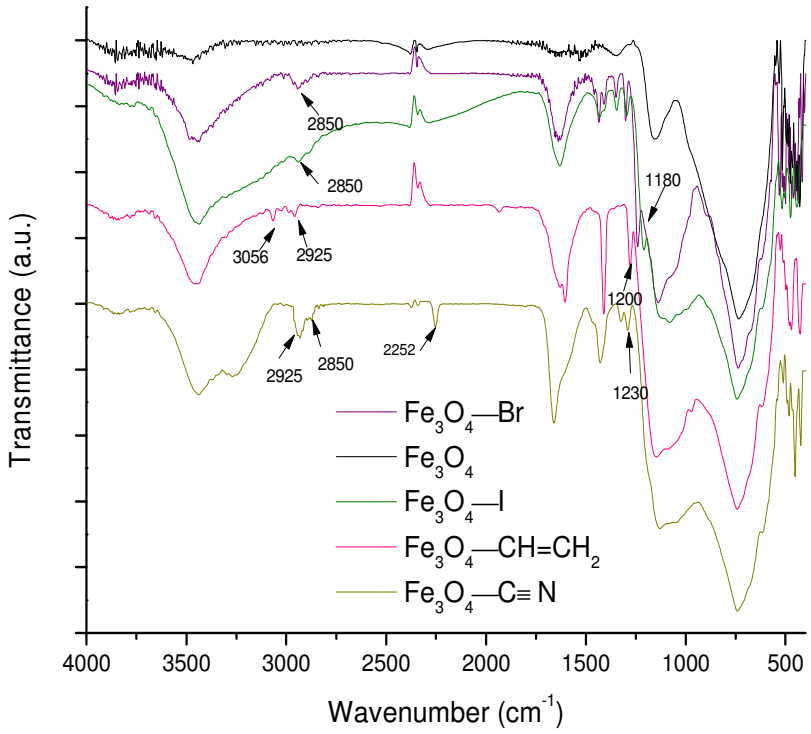

Figure 2.11 FTIR spectra of unfunctionalised Fe_3O_4 (black line), **Fe_3O_4−Br** (purple line), **Fe_3O_4−I** (green line), **Fe_3O_4−CH=CH_2** (pink line) and **Fe_3O_4−C≡N** (olive line).

Surface coverage was evaluated from the elemental analysis data for each type of functionalised-nanoparticle. The results (functionalisation degree per mass unit particles *f*, the surface coverage *C*, the number of ligands per nanoparticle n_L and the average number of ligands per surface area *A*) are summarised in **Table 2.1**. The surface

coverage calculations were carried out following the established line of equations from 2.1 to 2.10.

Table 2.1 Functionalisation degree *f* (from elemental analysis), calculated surface coverage *C*, number of ligands per nanoparticle n_L, average number of ligands per surface area *A* for Fe_3O_4 nanoparticles surface-modified with different silane molecules.

Functional silane	***f*** *(mmol × g^{-1})*	***C*** *(μmol × m^{-2})*	n_L *(×10^3 per particle)*	***A*** *(ligands/nm^2)*
APTES	0.34	7.30	8.61	4.38
BPTMS	0.26	5.58	6.62	3.37
IPTMS	0.27	5.80	6.86	3.5
VTMS	0.50	10.74	12.6	6.4
CPTES	0.26	5.58	6.62	3.37

It is important to note that the numbers presented are an estimation as to the extent of functionalisation because the reactivity of the silane ligands towards the surface depends on a number of factors including: silane binding mode to NPs surface, the nature of the terminal functional group, silane concentration, reaction temperature and nature of the anchoring group amongst other parameters.[14]

The calculated values of the surface coverage for all modified nanoparticles show the formation of a dense silane layer. Vinyl-modified nanoparticles show the highest surface coverage most probably because of the presence of a shorter aliphatic ethylene chain in the original silane ligand. In case of **Fe_3O_4–Br**, **Fe_3O_4–I** or **Fe_3O_4–C≡N** modified

nanoparticles the degree of functionalisation *f* is in the same range due to the structural similarity of the silane ligands. The results are comparable to other reported values for the monolayer formation of silanes on different surfaces.[26, 12]

Surface functionalisation could be achieved with all silane ligands. VTMS showed the highest coverage while all the other silanes had comparable coverage due to their similar structures.

The introduction of different chemical groups on surface of nanoparticles allowed the access to a number of post-modification reactions leading to multifunctional organic-inorganic hybrids. For example, the ***–Br*** functionalised nanoparticles were used to coat the nanoparticles with pH sensitive polymer chains like poly(diethyl 2-diethylamino) ethyl methacrylate (PDEAEMA); while the ***–CH=CH$_2$*** terminated nanoparticles were used in a *thiol-ene click* model reaction with mercaptopropionic acid.

2.3.3 pH-responsive PDEAEMA-functionalised Fe_3O_4 nanoparticles using the "*grafting from*" approach

The ***–Br*** groups on **Fe_3O_4–Br** particles were used as initiating groups to start polymerisation from the nanoparticle surface in a "*grafting from*" approach. Surface-initiated atom transfer radical polymerisation was used to graft (2-diethylamino) ethyl methacrylate (DEAEMA) chains on the surface thus enabling the synthesis of magnetic core-polymer brush like structures.[36-37] The resulting sample was denoted as **Fe_3O_4–PDEAEMA** (**Scheme 2.5**).

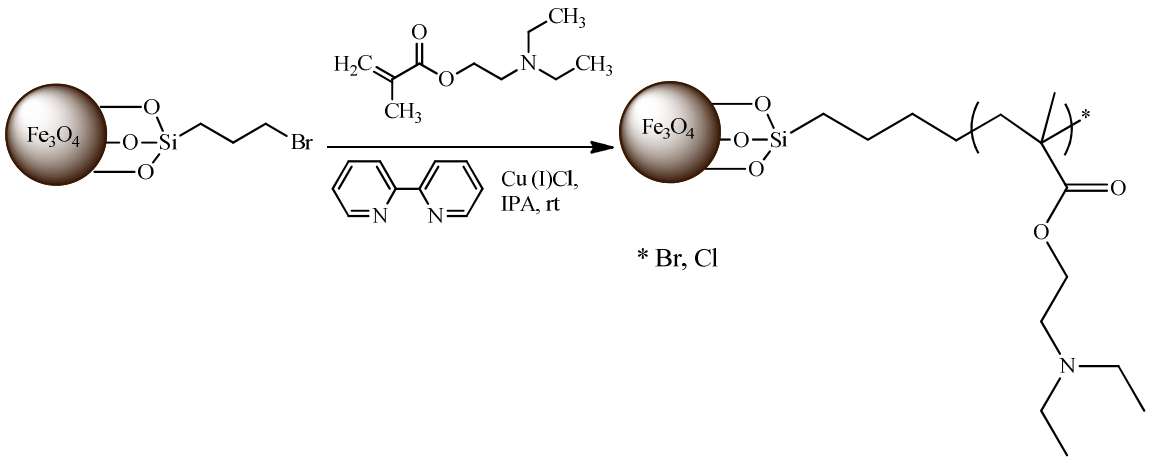

Scheme 2.5 Schematic illustration of PDEAEMA coating on the surface of Fe_3O_4 nanoparticles using a *grafting from* approach.

Successful grafting was confirmed by FTIR, elemental analysis and TGA. FTIR spectra of **Fe_3O_4-Br**, pure PDEAEMA polymer and **Fe_3O_4–PDEAEMA** nanoparticles are shown in **Figure 2.12**. The spectrum for **Fe_3O_4–PDEAEMA** showed the key bands origination from both nanoparticle and the polymer component. The characteristic bands for the C-H stretching vibrations of methylene and methyl are present in the region between 2980 and 2800 cm^{-1}. Additionally, the carbonyl peak at 1729 cm^{-1} together with the peaks at 1221 cm^{-1} (Si-O-Si bond) and at 580 cm^{-1} (Fe-O stretch) are evidence for the attached silane layer and grown PDEAEMA polymer chains.

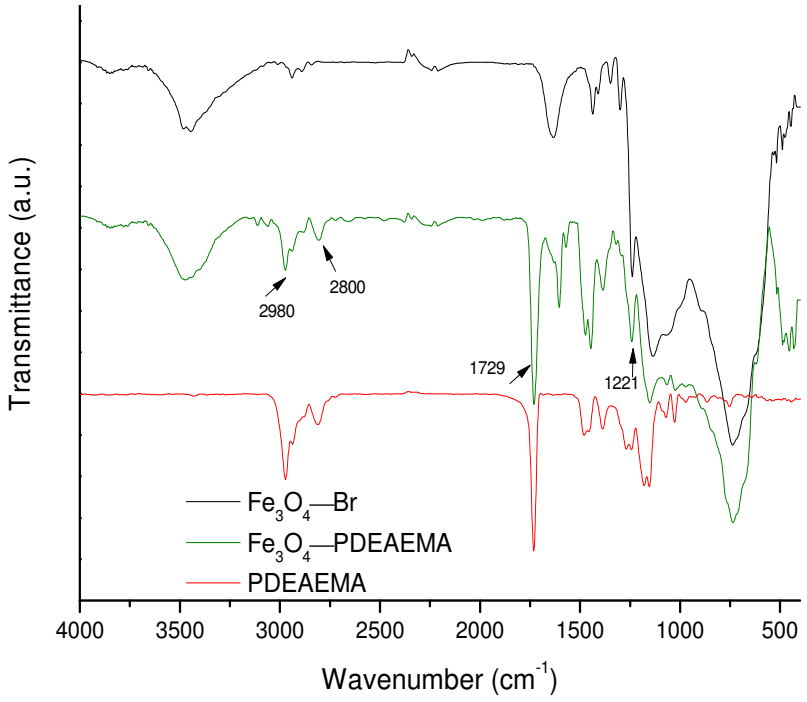

Figure 2.12 FTIR spectra of **Fe_3O_4–Br** (black line), **Fe_3O_4–PDEAEMA** (green line) hybrid nanoparticles and PDEAEMA pure polymer (red line).

The composition of the resulting **Fe_3O_4–PDEAEMA** nanoparticles was confirmed by thermogravimetric analysis. As expected, the polymer grafted nanoparticles showed a significant weight loss difference compared to the original **Fe_3O_4–Br** nanoparticles (**Figure 2.13**). The results show that the weight losses of **Fe_3O_4–Br** and **Fe_3O_4–PDEAEMA** are 4.1% and 15.5% respectively, when the samples are heated to 600 °C. In the case of the **Fe_3O_4–Br** nanoparticles, a large weight loss is observed in the region of 300-400 °C which can be attributed to the presence of heavy bromine atoms. This type of thermal decomposition profile was previously reported for other bromosilane functionalised nanoparticles.[38] Subsequently, the grafted polymer component was calculated by subtraction of the weight loss of **Fe_3O_4–Br** from the **Fe_3O_4–PDEAEMA**. The calculated polymer grafted fraction was 11.4% by weight

which shows that PDEAEMA chains are successfully grafted on the surface of the nanoparticles.

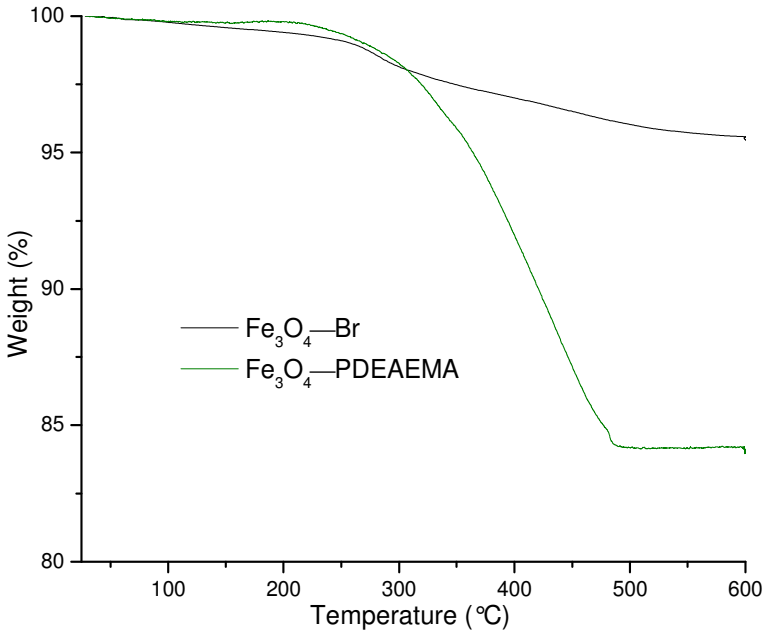

Figure 2.13 TGA curves of **Fe_3O_4−Br** (black line) and **Fe_3O_4−PDEAEMA** (green line).

Additionally the **Fe_3O_4−PDEAEMA** nanoparticles, after extensive purification performed to remove any potential free monomer or polymer, were water dispersible at low pH in contrast with the **Fe_3O_4−Br**. This is an indication of the change in the surface functionality of the nanoparticles and that the pH sensitivity properties of the polymer have been transferred to the particles. PDEAEMA above the pKa of 7.3 is neutral and not soluble in water.[39] In acidic environment below the pKa, the polymer becomes soluble as a weak cationic polyelectrolyte and the protonated chains have an extended conformation (**Scheme 2.6**).

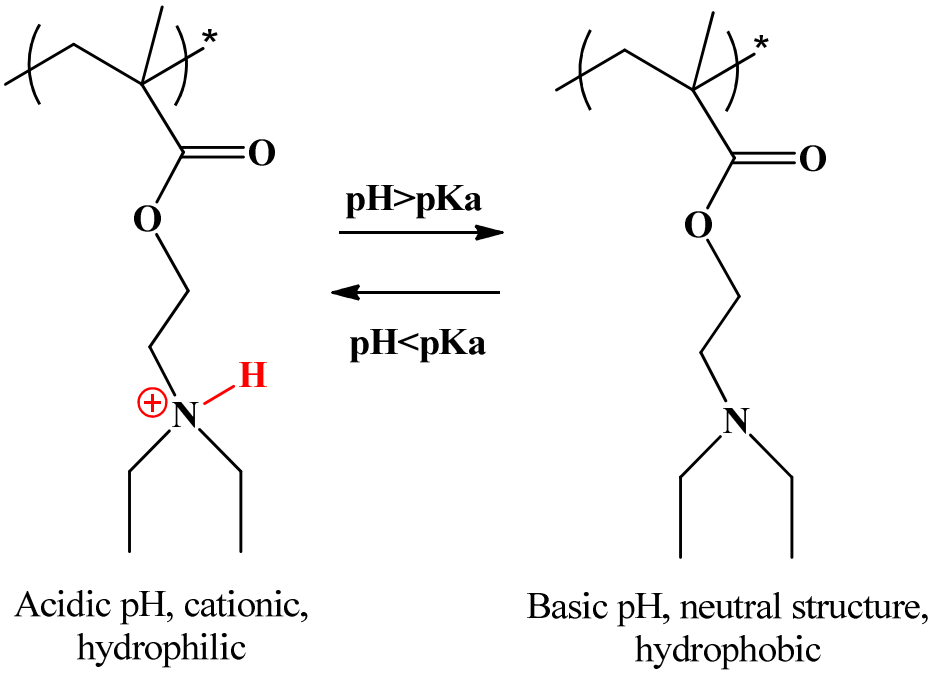

Scheme 2.6 Schematic representation of the structural changes of the PDEAEMA polymer chains in different pH environments.

After grafting the PDEAEMA chains on the surface of the nanoparticles, the pH-dependent dispersibility of 0.1 mg/mL of **Fe_3O_4–PDEAEMA** suspensions (pH 4 and pH 10) was optically monitored (**Figure 2.14**). In acidic environment (pH 4), the **Fe_3O_4–PDEAEMA** nanoparticles are stable in solution due to the polymer chains which become partly or entirely protonated. The electrostatic repulsions and strong steric effect of the extended chains help to stabilise the nanoparticles. However, in alkaline conditions, NPs flocculate and precipitate due to the collapse of the polymeric chains.

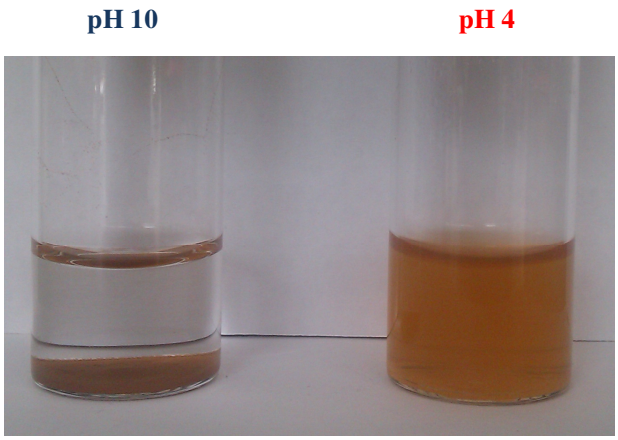

Figure 2.14 Images of **Fe_3O_4−PDEAEMA** nanoparticle dispersions at pH 10 and pH 4.

The **Fe_3O_4–PDEAEMA** nanoparticles could be used as pH-responsive materials, as solubility modifiers or in drug delivery systems where the pH control is required. In the drug delivery system, pH-responsive polymer chains on the nanoparticles would hold the drug molecules within the polymer shell during particle circulation. Whereas, upon exposure to a low pH environment, the polymer attached to the NPs would swell resulting in the release of the drug which would be beneficial in a case such as the treatment of tumours.[40-41]

2.3.4 *Thiol-ene click* reaction of Fe_3O_4–$CH=CH_2$ with 3-mercaptopropionic acid

Click reactions have created a great deal of attention for post-modification of materials due to their high efficiency, little or no side reactions, aqueous and low temperature competency, avoidance of protecting groups and broad applicability on different substrates.[42]

Among these reactions, *thiol-ene click* is a type of free-radical reaction that proceeds by a step-growth mechanism involving two main steps: a free-radical addition followed by a chain transfer reaction (**Scheme 2.7**).[43]

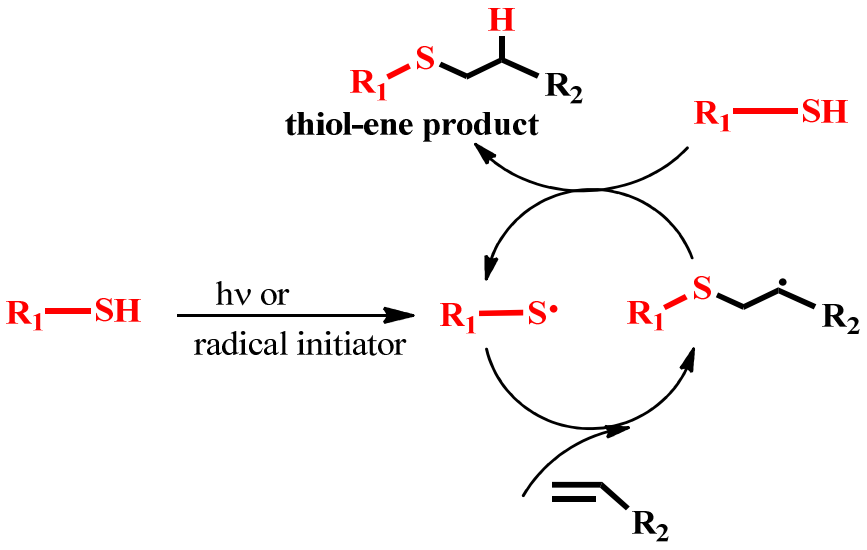

Scheme 2.7 Generalised *thiol-ene click* coupling mechanism.

The accessible double bonds on the surface of **Fe_3O_4–CH=CH_2** nanoparticles allow direct coupling with 3-mercaptopropionic acid. Using this approach, carboxylic acid functionalities were introduced on the surface of nanoparticles. The surface modified nanoparticles, denoted **Fe_3O_4–S–COOH**, were characterized by TGA, FTIR spectroscopy and fluorescence imaging. The chemical composition of the nanoparticles after the addition of 3-mercaptopropionic acid at the surface was investigated using TGA. **Figure 2.15** shows the TGA curves of **Fe_3O_4–CH=CH_2** and **Fe_3O_4–S–COOH** nanoparticles.

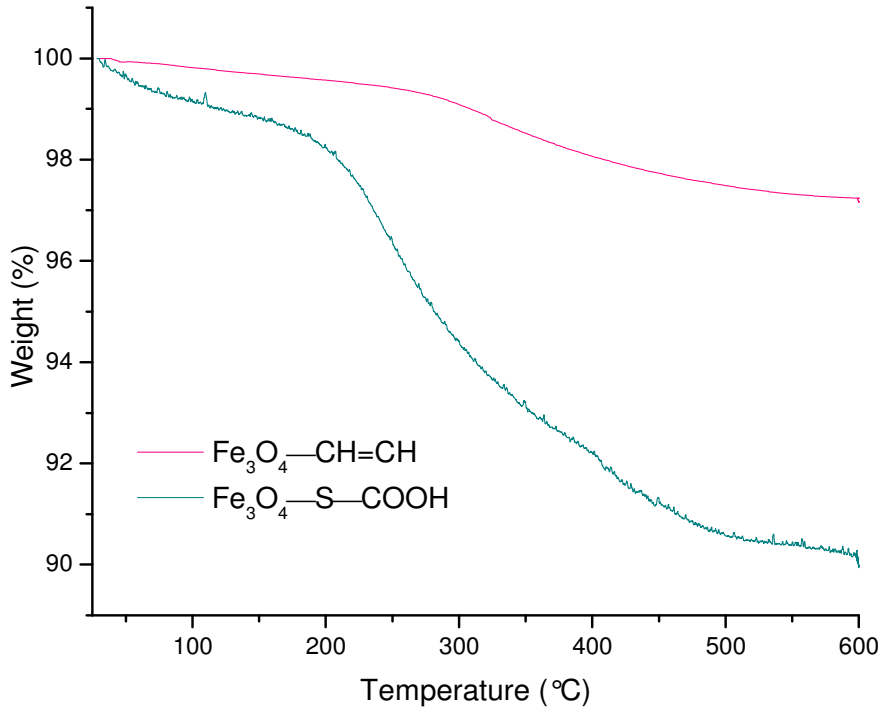

Figure **2.15** TGA curves of **Fe_3O_4−CH=CH_2** (pink line) and **Fe_3O_4−S−COOH** (cyan line) nanoparticles.

The TGA results show that the associated weight losses for **Fe_3O_4−CH=CH_2** and **Fe_3O_4−S−COOH** nanoparticles are 2.5% and 8.5% respectively when the nanoparticles are heated to 600 °C. From this data, the number of vinyl ligands which were modified during the *thiol-ene* reaction was calculated using the formula **2.13** presented in section **2.3.1** of this chapter. The deconvoluted weight loss is 6% wt which allowed estimation of the number of carboxylic acid as 11.4×10^3 groups per nanoparticle**.** When compared with the total number of ***−CH=CH_2*** calculated per nanoparticles (**Table 2.1**) it is clear that the reaction yield is very high (~ 90%). This is another demonstration of the efficiency of *thiol-ene click* chemistry.

Figure 2.16 shows the FTIR transmission spectra of the thiol-ene modified **Fe_3O_4–S–COOH** nanoparticles and the native **Fe_3O_4–CH=CH_2** nanoparticles for comparison. The characteristic band for C=O stretching vibration of the carboxylic acid groups at 1702 cm^{-1} are present in the spectrum of **Fe_3O_4–S–COOH**. Additionally, after the reaction with mercaptopropionic acid, the =C-H stretching band for the vinyl group in the region of 3056 cm^{-1} has disappeared indicating that all the vinyl groups have reacted during the thiol addition reaction.

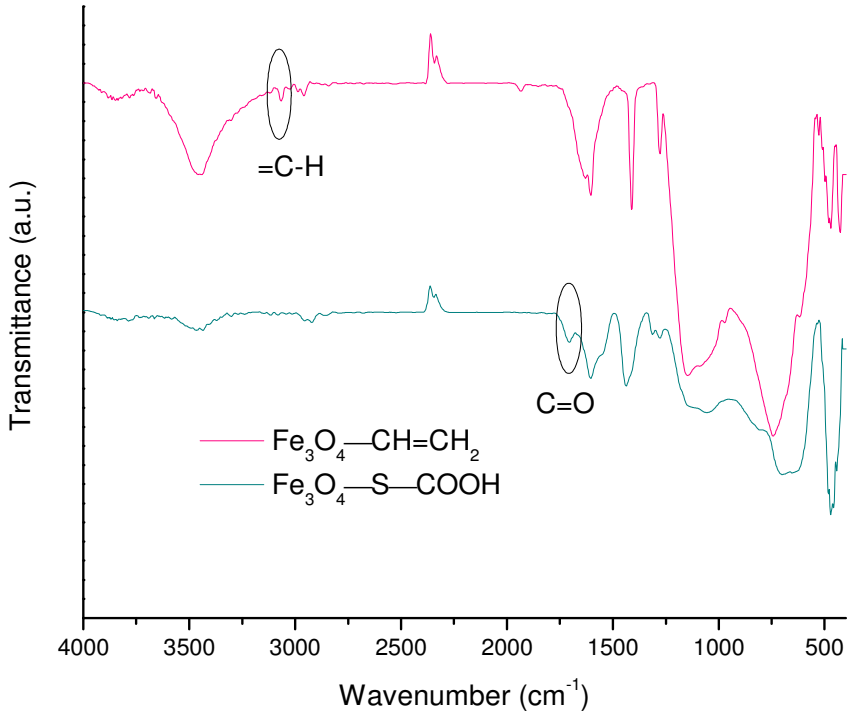

Figure 2.16 FTIR spectra of *thiol-ene* reaction with 3-mercaptopropionic acid. Spectra of **Fe_3O_4–S–COOH** (cyan) and **Fe_3O_4–CH=CH_2** (pink) nanoparticles**.**

To demonstrate the reactivity of the carboxylic acid groups on the outer layer of **Fe_3O_4–S–COOH,** fluorescein-5-thiosemicarbazide (FITC, λ_{ex} =492 nm, λ_{em} =517 nm) a

green fluorescent tag, was used to label and visualise the nanoparticles. The fluorescent tag was covalently conjugated to the carboxyl groups on **Fe_3O_4–S–COOH** nanoparticles *via* EDC/sulfo-NHS coupling as shown in **Scheme 2.8**.

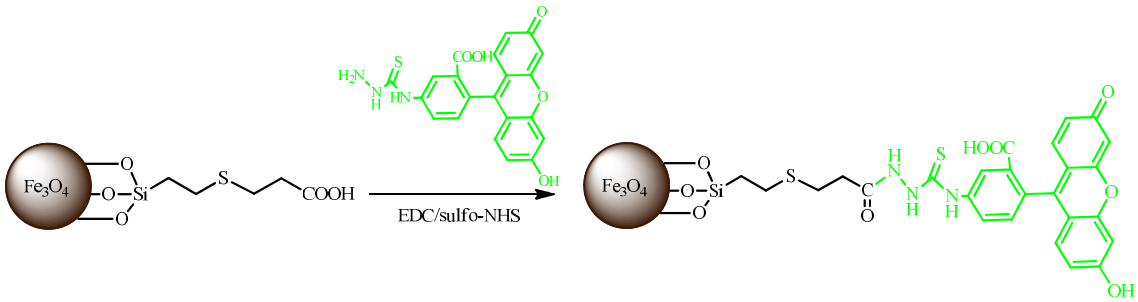

Scheme 2.8 Fluorescein-5-semithiocarbazide covalent conjugation to **Fe_3O_4–S–COOH** nanoparticles using EDC/sulfo-NHS coupling.

The excess of fluorescent dye was removed by washing the nanoparticles repeatedly with DMSO and water. The fluorescently labelled nanoparticles were evaluated using fluorescence microscopy. **Figure 2.17** shows a representative fluorescence micrograph of the fluorescein-labelled Fe_3O_4 nanoparticles.

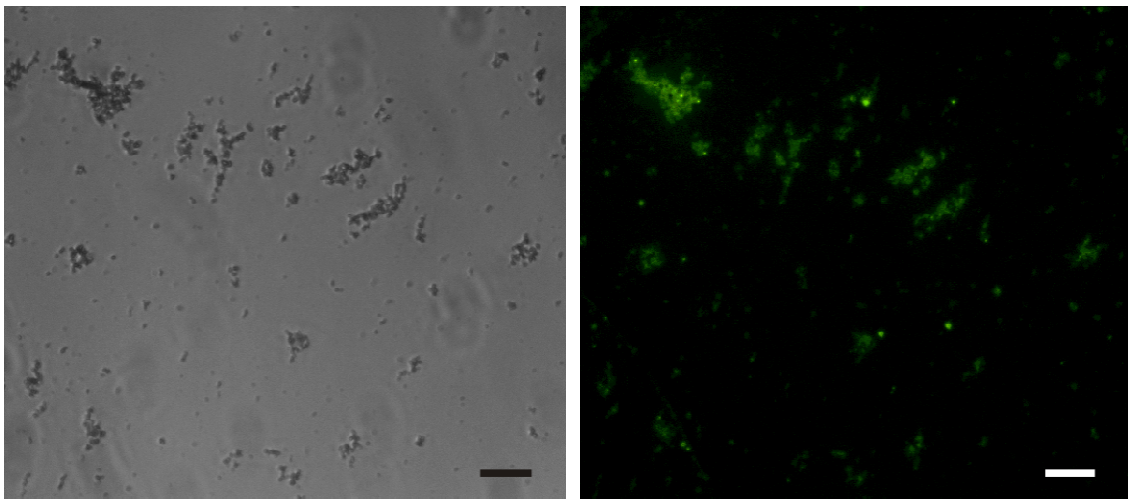

Figure 2.17 Bright field (left) and green fluorescent image (right) of fluorescein-labelled magnetic nanoparticles. Scale bar represents 10 μm.

The fluorescent emission in green clearly confirms the selective functionalisation with fluorescein of the carboxylic acid groups on the surface *via* EDC/sulfo-NHS coupling chemistry. A control experiment, which was carried out under identical conditions except for the addition of EDC and sulfo-NHS to the **Fe_3O_4–S–COOH** particles, did not yield fluorescent nanoparticles. This demonstrated that the fluorescently labelled nanoparticles were not the result of a physical mixture but actual chemical binding.

The vinyl terminated nanoparticles can provide a convenient platform for conjugation of any thiol containing proteins or peptides to the surface of the nanoparticles. For example, the *thiol-ene* click reaction proved to have a good yield when 3-mercaptopropionic acid was used as a model compound.

2.4 Conclusions

The versatile silanisation strategy presented in this chapter is an effective method for introducing various functional groups directly onto the surface of unfunctionalised Fe_3O_4 nanoparticles. The value of this approach is to demonstrate that not only amino and carboxylic groups (commonly employed in the literature) but also other functional group can be used to attach biomolecules or biocompatible coatings. Five different silane ligands were used to introduce functional groups such as ***–NH₂***, ***–Br***, ***–CH=CH₂***, ***–I*** and ***–C≡N*** on the surface of Fe_3O_4 with each silane ligand to be shown capable of forming a dense silane monolayer covalently attached to the surface of the nanoparticle. This simple one-step procedure could be employed to commercially available nanoparticles and should provide an affordable route with good reproducibility and scaling up opportunities.

The nanoparticles functionalised by amino groups were further modified by a partial conversion $-NH_2$ to $-COOH$ groups using a simple succinylation reaction. The presence of the amino and the carboxylic acid groups on the surface of the nanoparticles afforded a bifunctional surface. Such surfaces can offer an advantageous possibility for independent attachment of fluorescent tags and bioactive molecules through conjugation reactions. The development of the bioconjugation protocols, MRI imaging and targeting of specific receptors on cancer cells using bifunctionalised nanoparticles will be explored in Chapter 3.

The other functional groups such as $-Br$ and $-CH=CH_2$ could be successfully engaged in post-modification reactions to further increase the potential for particle functionalisation. The pH sensitive properties of PDEAEMA polymeric chains can be directly transferred to the nanoparticles pre-functionalised with the bromine groups while *thiol-ene click* is a convenient platform for introducing functionalities on the vinyl terminated nanoparticles.

2.5 References

1. M. Ferrari, Cancer nanotechnology: Opportunities and challenges, *Nat Rev Cancer*, **2005**, 5, 161-171.
2. Y. M. Huh, Y. W. Jun, H. T. Song, S. Kim, J. S. Choi, J. H. Lee, S. Yoon, K. S. Kim, J. S. Shin, J. S. Suh, J. Cheon, In vivo magnetic resonance detection of cancer by using multifunctional magnetic nanocrystals, *J Am Chem Soc*, **2005**, 127, 12387-12391.
3. A. Jordan, R. Scholz, P. Wust, H. Schirra, T. Schiestel, H. Schmidt, R. Felix, Endocytosis of dextran and silan-coated magnetite nanoparticles and the effect of intracellular hyperthermia on human mammary carcinoma cells in vitro, *J Magn Magn Mater*, **1999**, 194, 185-196.
4. E. Amstad, M. Textor, E. Reimhult, Stabilization and functionalization of iron oxide nanoparticles for biomedical applications, *Nanoscale*, **2011**, 3, 2819-2843.
5. J. M. Perez, F. J. Simeone, Y. Saeki, L. Josephson, R. Weissleder, Viral-induced self-assembly of magnetic nanoparticles allows the detection of viral particles in biological media, *J Am Chem Soc*, **2003**, 125, 10192-10193.
6. A. H. Latham, M. E. Williams, Controlling transport and chemical functionality of magnetic nanoparticles, *Accounts Chem Res*, **2008**, 41, 411-420.
7. Z. H. Xu, Q. X. Liu, J. A. Finch, Silanation and stability of 3-aminopropyl triethoxy silane on nanosized superparamagnetic particles: I. Direct silanation, *Appl Surf Sci*, **1997**, 120, 269-278.
8. P. Bourrinet, H. H. Bengele, B. Bonnemain, A. Dencausse, J. M. Idee, P. M. Jacobs, J. M. Lewis, Preclinical safety and pharmacokinetic profile of

ferumoxtran-10, an ultrasmall superparamagnetic iron oxide magnetic resonance contrast agent, *Invest Radiol*, **2006**, 41, 313-324.

9. T. K. Jain, M. K. Reddy, M. A. Morales, D. L. Leslie-Pelecky, V. Labhasetwar, Biodistribution, clearance, and biocompatibility of iron oxide magnetic nanoparticles in rats, *Mol Pharm*, **2008**, 5, 316-327.
10. C. Boyer, M. R. Whittaker, V. Bulmus, J. Q. Liu, T. P. Davis, The design and utility of polymer-stabilized iron-oxide nanoparticles for nanomedicine applications, *Npg Asia Mater*, **2010**, 2, 23-30.
11. J. R. McCarthy, R. Weissleder, Multifunctional magnetic nanoparticles for targeted imaging and therapy, *Adv Drug Deliver Rev*, **2008**, 60, 1241-1251.
12. L. Bouffier, H. H. P. Yiu, M. J. Rosseinsky, Chemical Grafting of a DNA Intercalator Probe onto Functional Iron Oxide Nanoparticles: A Physicochemical Study, *Langmuir*, **2011**, 27, 6185-6192.
13. W. Brullot, N. K. Reddy, J. Wouters, V. K. Valev, B. Goderis, J. Vermant, T. Verbiest, Versatile ferrofluids based on polyethylene glycol coated iron oxide nanoparticles, *J Magn Magn Mater*, **2012**, 324, 1919-1925.
14. S. Onclin, B. J. Ravoo, D. N. Reinhoudt, Engineering silicon oxide surfaces using self-assembled monolayers, *Angew Chem Int Edit*, **2005**, 44, 6282-6304.
15. N. Frickel, R. Messing, T. Gelbrich, A. M. Schmidt, Functional Silanes as Surface Modifying Primers for the Preparation of Highly Stable and Well-Defined Magnetic Polymer Hybrids, *Langmuir*, **2010**, 26, 2839-2846.

16. I. J. Bruce, T. Sen, Surface modification of magnetic nanoparticles with alkoxysilanes and their application in magnetic bioseparations, *Langmuir*, **2005**, 21, 7029-7035.

17. C. Flesch, Y. Unterfinger, E. Bourgeat-Lami, E. Duguet, C. Delaite, P. Dumas, Poly(ethylene glycol) surface coated magnetic particles, *Macromol Rapid Comm*, **2005**, 26, 1494-1498.

18. B. Arkles, Tailoring Surfaces with Silanes, *Chemtech*, **1977**, 7, 766-778.

19. M. Mikhaylova, D. K. Kim, C. C. Berry, A. Zagorodni, M. Toprak, A. S. G. Curtis, M. Muhammed, BSA immobilization on amine-functionalized superparamagnetic iron oxide nanoparticles, *Chem Mater*, **2004**, 16, 2344-2354.

20. N. Kohler, G. E. Fryxell, M. Q. Zhang, A bifunctional poly(ethylene glycol) silane immobilized on metallic oxide-based nanoparticles for conjugation with cell targeting agents, *J Am Chem Soc*, **2004**, 126, 7206-7211.

21. N. Kohler, C. Sun, A. Fichtenholtz, J. Gunn, C. Fang, M. Q. Zhang, Methotrexate-immobilized poly(ethylene glycol) magnetic nanoparticles for MR imaging and drug delivery, *Small*, **2006**, 2, 785-792.

22. H. Kobayashi, T. Matsunaga, Amino-Silane Modified Superparamagnetic Particles with Surface-Immobilized Enzyme, *J Colloid Interf Sci*, **1991**, 141, 505-511.

23. H. Günzler, A. Williams. *Handbook of analytical techniques*, **2001**, Wiley-VCH, Weinheim ; New York.

24. P. Larkin. *Infrared and raman spectroscopy : principles and spectral interpretation*, **2011**, Elsevier, Amsterdam ; London.

25. I. Koh, X. Wang, B. Varughese, L. Isaacs, S. H. Ehrman, D. S. English, Magnetic iron oxide nanoparticles for biorecognition: Evaluation of surface coverage and activity, *J Phys Chem B*, **2006**, 110, 1553-1558.

26. R. De Palma, S. Peeters, M. J. Van Bael, H. Van den Rul, K. Bonroy, W. Laureyn, J. Mullens, G. Borghs, G. Maes, Silane ligand exchange to make hydrophobic superparamagnetic nanoparticles water-dispersible, *Chem Mater*, **2007**, 19, 1821-1831.

27. S. Bruni, F. Cariati, M. Casu, A. Lai, A. Musinu, G. Piccaluga, S. Solinas, IR and NMR study of nanoparticle-support interactions in a Fe2O3-SiO2 nanocomposite prepared by a sol-gel method, *Nanostruct Mater*, **1999**, 11, 573-586.

28. S. R. Hall, S. A. Davis, S. Mann, Cocondensation of organosilica hybrid shells on nanoparticle templates: A direct synthetic route to functionalized core-shell colloids, *Langmuir*, **2000**, 16, 1454-1456.

29. J. D. Miller, H. Ishida (eds.). Quantitative Monomolecular Coverage of Inorganic Particulates by Methacryl-Functional Silanes, **1984**.

30. M. Ma, Y. Zhang, W. Yu, H. Y. Shen, H. Q. Zhang, N. Gu, Preparation and characterization of magnetite nanoparticles coated by amino silane, *Colloid Surface A*, **2003**, 212, 219-226.

31. E. K. U. Larsen, T. Nielsen, T. Wittenborn, H. Birkedal, T. Vorup-Jensen, M. H. Jakobsen, L. Ostergaard, M. R. Horsman, F. Besenbacher, K. A. Howard, J. Kjems, Size-Dependent Accumulation of PEGylated Silane-Coated Magnetic Iron Oxide Nanoparticles in Murine Tumors, *Acs Nano*, **2009**, 3, 1947-1951.

32. G. T. Hermanson. *Bioconjugate techniques*, **1996**, Academic Press, San Diego.

33. C. Corot, P. Robert, J. M. Idee, M. Port, Recent advances in iron oxide nanocrystal technology for medical imaging, *Adv Drug Deliver Rev*, **2006**, 58, 1471-1504.

34. S. Verma, D. Pravarthana, One-Pot Synthesis of Highly Monodispersed Ferrite Nanocrystals: Surface Characterization and Magnetic Properties, *Langmuir*, **2011**, 27, 13189-13197.

35. H. J. Chung, H. Lee, K. H. Bae, Y. Lee, J. Park, S. W. Cho, J. Y. Hwang, H. Park, R. Langer, D. Anderson, T. G. Park, Facile Synthetic Route for Surface-Functionalized Magnetic Nanoparticles: Cell Labeling and Magnetic Resonance Imaging Studies, *Acs Nano*, **2011**, 5, 4329-4336.

36. K. Matyjaszewski, J. H. Xia, Atom transfer radical polymerization, *Chem Rev*, **2001**, 101, 2921-2990.

37. M. Kamigaito, T. Ando, M. Sawamoto, Metal-catalyzed living radical polymerization, *Chem Rev*, **2001**, 101, 3689-3745.

38. E. M. Brozek, I. Zharov, Internal Functionalization and Surface Modification of Vinylsilsesquioxane Nanoparticles, *Chem Mater*, **2009**, 21, 1451-1456.

39. P. van de Wetering, N. J. Zuidam, M. J. van Steenbergen, O. A. G. J. van der Houwen, W. J. M. Underberg, W. E. Hennink, A mechanistic study of the hydrolytic stability of poly(2-(dimethylamino)ethyl methacrylate), *Macromolecules*, **1998**, 31, 8063-8068.

40. J. O. You, D. Almeda, G. J. Ye, D. T. Auguste, Bioresponsive matrices in drug delivery, *J Biol Eng*, **2010**, 4, 15.

41. J. T. Sun, C. Y. Hong, C. Y. Pan, Fabrication of PDEAEMA-Coated Mesoporous Silica Nanoparticles and pH-Responsive Controlled Release, *J Phys Chem C*, **2010**, 114, 12481-12486.

42. N. W. Li, W. H. Binder, Click-chemistry for nanoparticle-modification, *J Mater Chem*, **2011**, 21, 16717-16734.

43. C. E. Hoyle, C. N. Bowman, Thiol-Ene Click Chemistry, *Angew Chem Int Edit*, **2010**, 49, 1540-1573.

Chapter 3

Tumour targeting and imaging potential of bifunctionalised nanoparticles

3.1 Introduction

Active tumour targeting refers to selective accumulation and uptake of superparamagnetic iron oxide nanoparticles (SPIONs) in tumours and can be achieved by using tumour-selective ligands. Carefully selected ligands *(e.g.* antibodies, peptides, small molecules) that are peripherally attached to the SPIONs surface specifically bind receptors that are overexpressed on the tumour cells.[1-3] In particular, antibody targeting is regarded as a promising strategy to selectively direct the SPIONs to the tumour region and accomplish early tumour detection. Various therapeutic antibodies are available on the market and have shown promising results for treatment of breast cancer (Herceptin®), colorectal cancer (Erbitux®), as well as brain cancer, colon cancer and kidney cancer (Avastin®). In addition, Hodgkin lymphoma (Adcetris®), prostate cancer (ProstaScint®) and non-Hodgkin's lymphoma (Zevalin®) could be treated when antibodies were used in combination with chemotherapeutic drugs or with radioisotopes.[4] However up to date there are no examples of clinically approved formulations of antibodies conjugated to SPIONs or other nanoparticles. The conjugation of antibodies to SPIONs can offer versatility through integration of the nanoparticle magnetic properties with the antibody-antigen affinity and therefore specificity for detecting cancer as illustrated in **Figure 3.1**.[5] Although certain challenges

should be overcome before the launch of clinical applications there are some examples of antibody-conjugated SPIONs systems that have shown promising *in vitro* and *in vivo* results.[6-12]

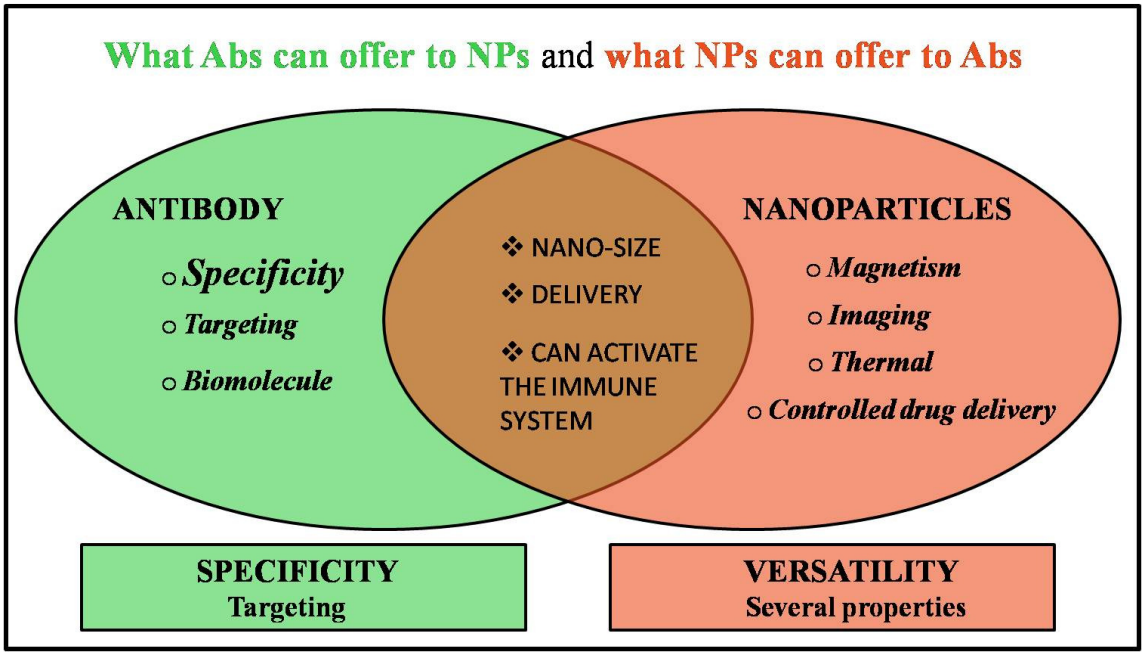

Figure 3.1 Advantages of antibody conjugation of to nanoparticles. The figure was adapted from ref. 5

In a notable study, Toma *et al*. evaluated binding ability of the monoclonal antibody A7 conjugated to SPIONs with human colonic carcinoma cells.[6] A larger amount of the specific A7-SPIONs was accumulated in the tumour cells when compared to a control experiment which involved SPIONs conjugated with a non-specific antibody. Furthermore, the specificity was demonstrated by the higher levels of A7-SPIONs detected in the tumour than in either blood or normal tissues. In MR imaging of nude mice bearing human colorectal carcinoma it was shown that in the tumour region the

intensity of transverse relaxation signal (T_2) was reduced due to the presence of the A7-SPIONs.

Antibody molecules such as Herceptin (commercial name Trastuzumab) have been explored in combination with SPIONs as targeting and biotherapeutic agents. Herceptin targets the Her2/neu receptor which is a growth factor and is essential for cell proliferation. The receptor is expressed on the surface of early stage breast cancer tumours and the interaction with Herceptin has been shown to lead to inactivation of the receptor and subsequent inhibition of cell proliferation.[7] As such, Yang *et al.* conjugated the Herceptin antibody to poly(amino acid)-coated iron oxide nanoparticles (PAION), which have abundant amine groups on their surface.[8] Bradford protein assay confirmed that there were about eight antibodies conjugated to the surface of each nanoparticle *via* amino groups. The authors showed that the T_2 relaxation is significantly different between the PAION-antibody-treated and untreated cells expressing the Her2 receptor. The results demonstrated that Herceptin antibody-conjugated PAION have specific targeting ability for Her2/neu receptors. Such Herceptin antibody-conjugated PAION with high sensitivity could potentially be used as an MRI contrast agent for the detection of Her2/neu positive breast cancer cells.

Recently, a number of studies have adopted the use of single chain antibodies (scFv) as tumour targeting ligands and their conjugation to SPIONs.[9-10] One important example of using SPIONs conjugated with sm3E, a high affinity scFv reactive to carcinoembryonic antigen (CEA) is the study of Vigor *et al.*[9] The group investigated the ability of sm3E, conjugated to three types of SPIONs, for selective targeting and imaging of CEA-expressing cells. It was shown that the specific targeting with sm3E/ nanoparticles

was achievable *in vitro* but improved MRI contrasting properties, colloidal stability and biocompatibility could be achieved only after further optimisation of the size and the coating of the nanoparticles. In their work Yang *et al.* have reported the use of a single-chain anti-EGFR (endothelial growth factor receptor) antibody (scFvEGFR) conjugated to amphiphilic polymer coated iron oxide nanoparticles (IO) for *in vivo* tumour imaging (**Figure 3.2**).[10]

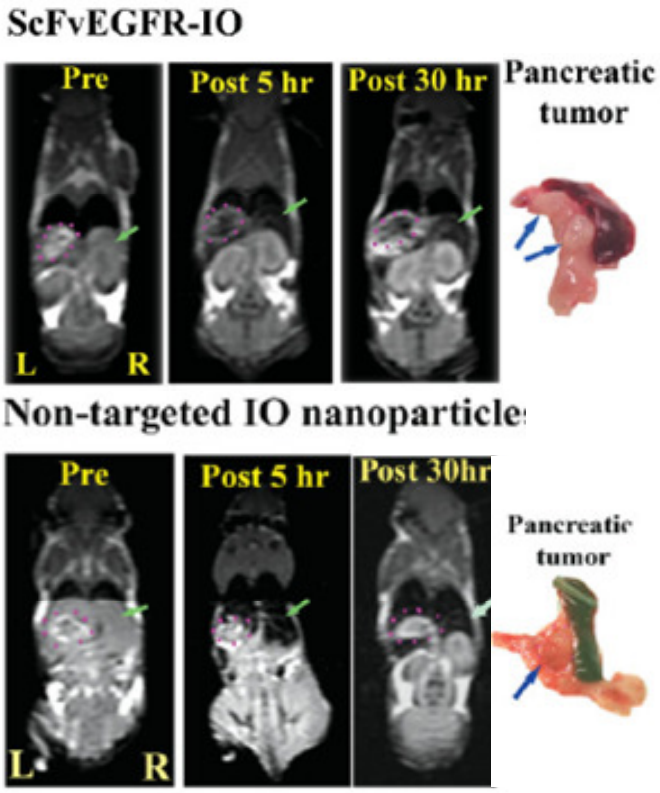

Figure 3.2 Examination of target specificity of ScFvEGFR-IO nanoparticles by MRI using a human pancreatic tumour model. The areas of the pancreatic tumour were marked as pink dash-lined circle. Right is the picture of tumour tissues, showing sizes and locations of two intra-pancreatic tumour lesions (arrows) that correspond with the tumour images of MRI. The figure was reproduced from ref. 10

ScFvEGFR was conjugated to IO nanoparticles using ethyl-3-dimethylaminopropyl carbodiimide (EDC) coupling. The *in vitro* results showed that the scFvEGFR-IO nanoparticles specifically bind to EGFR, as demonstrated by Prussian blue staining and MRI. For *in vivo* evaluation of targeting capabilities, EGFR-targeted or nontargeted IO nanoparticles were administrated *via* the tail vein to nude mice bearing orthotopical human pancreatic cancer xenograft. The results showed that the scFvEGFR-IO nanoparticles were selectively accumulated within the pancreatic tumours as evidenced by a decrease in MRI signal in the tumour region and further confirmed by histological examination.[10]

In this chapter, previously synthesised bifunctionalised **Fe_3O_4-NH_2/COOH** nanoparticles as described in Chapter 2 were evaluated for their targeting and imaging capabilities with epithelial pancreatic cancer cells overexpressing the epithelial cell adhesion molecule receptor (EPCAM). For achieving these objectives first the potential cytotoxicity of the **Fe_3O_4-NH_2/COOH** was investigated using different cells lines and three types of viability assays, *i.e.* MTS, WST-8 and live/dead assays. Then the **Fe_3O_4-NH_2/COOH** nanoparticles were conjugated with a fluorescent dye (**RITC**, Rhodamine B isothiocyante) and a monoclonal anti-EPCAM antibody. **RITC** was covalently conjugated to the nanoparticles using the available ***–NH_2*** groups, while EPCAM was conjugated with the ***–COOH*** groups *via* carbodiimide coupling chemistry. An essential requisite for successful conjugation of biomolecules was not to compromise their native conformation and binding profile. This can be a challenging task because for many biomolecules only limited chemical modifications can be tolerated in order not to lose their bioactivity.[13]

Quantification of the EPCAM antibodies conjugated to the surface of the functionalised nanoparticles was determined using an optimised protein Bradford assay. The MRI contrast capabilities of the bifunctionalised nanoparticles were evaluated by relaxation time measurements with specific focus on the T_2 relaxation time. The selectivity of the specific antibody-nanoparticle conjugates to the targeted cells *in vitro* was evaluated using fluorescence microscopy, while the internalisation of these was visualised *via* confocal microscopy.

3.2 Experimental Section

3.2.1 Materials

Sodium phosphate dibasic dihydrate ($Na_2HPO_4*2H_2O$, ≥ 99.5 %), potassium phosphate monobasic (KH_2PO_4, ≥99%), potassium phosphate dibasic (K_2HPO_4, ≥ 99%), sodium chloride (NaCl, ≥ 99.5%), potassium chloride (KCl, ≥ 99%), fluorescein isothiocyanate (FITC, 98%), rhodamine B isothiocyanate (RITC, BioReagent), albumin–fluorescein isothiocyanate conjugate (BSA-FITC, Bioreagent), tris(hydroxymethyl)aminomethane (TRIZMA base, ≥ 99.9 %), *N*-(3-dimethylaminopropyl)-*N′*-ethylcarbodiimide hydrochloride (EDC, ≥ 99.0 %), *N*-hydroxysulfosuccinimide sodium salt (sulfo-NHS, ≥ 98.5 %), Dulbecco's modified eagle's medium - high glucose (DMEM), fetal calf serum (FCS), L-glutamine solution, penicillin G sodium salt (BioReagent), streptomycin sulfate salt (BioReagent), trypsin-EDTA solution (0.5 g porcine trypsin and 0.2 g EDTA × 4Na per liter), Bradford assay, Vivaspin 500 centrifugal concentrators 30kDa, Nunc 2-wells chamber slide system, 2-(2-methoxy-4-nitrophenyl)-3-(4-nitrophenyl)-5-(2,4-disulfophenyl)-2H-tetrazolium monosodium salt (WST-8 assay), Live/Dead cell double staining kit, 4',6-diamidino-2-phenylindole dilactate (DAPI, ≥ 98%), 1,4-diazobicyclo-octane (DABCO), Mowiol 4-88 (MW 31000), glycerol (≥ 99%), dimethyl sulfoxide (DMSO, ≥ 99.9%) were purchased from Sigma-Aldrich, UK.

The 27 mm glass base IWAKI tissue culture dishes were purchased from Scientific Laboratory Supplies UK. 3-(4,5-dimethylthiazol-2-yl)-5-(3-carboxymethoxyphenyl)-2-(4-sulfophenyl)-2H-tetrazolium (MTS assay) was purchased from Biomedica, Vienna, Austria. The monoclonal anti-EPCAM antibody specific for human EPCAM antigen was purchased from Monosan, Cambridge, UK. The polyclonal antibody, an Isotype

control was obtained from Abcam, Cambridge, UK. A list of the buffer recipes prepared and used during bioconjugation reactions and cell work is detailed below.

Table 3.1 Solutions for RITC coupling to Fe_3O_4-NH_2/COOH nanoparticles

Buffers	Formula
500 mM Carbonate buffer	1.7 g Na_2CO_3, 2.8 g $NaHCO_3$ dissolved into 90 mL dH_2O. pH adjusted to 9.5 and volume topped-up to 100 mL.
PBS *[137 mM NaCl, 2.7 mM KCl,* *8 mM Na_2HPO_4, 1.46 mM KH_2PO_4]*	8 g NaCl, 0.2 g KCl, 1.424 g Na_2HPO_4*$2H_2O$, 0.2 g KH_2PO_4 dissolved into 900 mL dH_2O. pH adjusted to 7.4 and volume topped-up to 1 liter.
10 mM Tris buffer	0.142 g TRIZMA base, 0.87 g NaCl dissolved into 90 mL dH_2O. pH adjusted to 8.2 and volume topped-up to 100 mL.

Table 3.2 Solutions for BSA-FITC/ EPCAM coupling to Fe_3O_4-NH-RITC/COOH

Buffers	Formula
10 mM Phosphate buffer	0.14 g K_2HPO4, 1.24 g KH_2PO_4, 0.87 g NaCl dissolved in 90 mL dH_2O. pH adjusted to 5.5 and volume topped-up to 100 mL.
EDC/ sulfo-NHS activation solution	38.3 mg EDC and 10.8 mg sulfo-NHS dissolved in 1 mL potassium phosphate buffer.

Table 3.3 Solutions for cell culture

Buffers	Formula
Cell culture medium	10% Fetal calf serum, 2 mM L-glutamine, 2500 I.U./mL penicillin and 5 µg/mL streptomycin added to supplement DMEM cell culture medium
Freezing medium	90% Fetal calf serum, 10% DMSO

Table 3.4 Solutions for immunostaining of adherent cells

Buffers	Formula
4% PFA Fixating solution	4 g paraformaldehyde dispersed in 50 mL dH_2O heated to 60 °C. During heating 1 N NaOH was added drop by drop with stirring until the solution became clear. The solution was cooled down to room temperature and volume was adjusted with 40 mL dH_2O and 10 mL PBS. Finally the solution was filtered using a 0.2 µm syringe filter.
Blocking buffer	5% bovine serum albumin (BSA) in PBS.
DAPI solution	0.5 µg/mL in PBS. Stored in 1mL aliquots in the dark at -20 °C.
0.2 M Tris buffer pH 8.5	2.42 g TRIZMA base into 90 mL dH_2O. pH adjusted to 8.5 and volume topped-up to 100 mL.
Mowiol mounting solution	2.4 g of Mowiol 4-88 and 6 g of glycerol combined in 6 mL of dH_2O and mixed for 3 hours. 12 mL of 0.2 M Tris (pH 8.5)

	were added and the solution was incubated with mixing at 50°C for 10 min. To remove any insoluble material the solution was centrifuged at 5000g for 15 min. The anti-photobleaching agent DABCO was added to a final concentration of 2.5%. Finally the solution was stored in 500 μL aliquots at −20°C.

3.2.2 Bioconjugation methods

The bioconjugation methods for coupling of the fluorescent molecules and proteins with the bifunctionalised nanoparticles, **Fe_3O_4-NH_2/COOH**, were adapted from the Hermanson textbook.[14]

3.2.2.1 Fluorescent dye coupling to Fe_3O_4-NH_2/COOH nanoparticles

Fe_3O_4-NH_2/COOH nanoparticles (1 mg) were suspended by 2 minutes sonication in carbonate buffer (0.9 mL, pH=9.5, **Table 3.1**). Then **RITC** dissolved in DMSO (0.1 mL, 0.01% w/v) was added to the nanoparticle suspension. The reaction mixture was covered with aluminium foil to avoid any photobleaching and gently rotated overnight at room temperature. The fluorescently labelled nanoparticles were collected with a magnet and washed with Tris buffer (aliquots of 1 mL, pH=8.2, **Table 3.1**) until the solution ran clear. The resulting nanoparticles were re-dispersed in Tris buffer (1 mL) and stored at 4 °C fully covered with aluminium foil. The resulting nanoparticles labelled with fluorescent dye were denoted as **Fe_3O_4-NH-RITC/COOH**.

3.2.2.2 Bioconjugation of fluorescently labelled bovine serum albumin (BSA-FITC) with the Fe_3O_4-NH-RITC/COOH

The BSA protein labelled with a green fluorescent tag (**BSA-FITC**) was conjugated to the carboxylic acid groups of **Fe_3O_4-NH-RITC/COOH** *via* carbodiimide coupling chemistry using EDC and sulfo-NHS.

Fe_3O_4-NH-RITC/COOH nanoparticles (1 mg) were dispersed in potassium phosphate buffer (0.5 mL, pH=5.5, **Table 3.2**). To this dispersion, an aliquot of EDC/sulfo-NHS activation solution (0.5 mL, **Table 3.2)** was added and the mixture was gently rotated for 4 hours at room temperature. COOH activated nanoparticles were washed with PBS in order to remove residual EDC and sulfo-NHS. **BSA-FITC** was added to the nanoparticles (10 µg in 1 mL PBS) and the mixture was gently rotated overnight fully covered with aluminium foil. The resulting nanoparticles were collected with a magnet and repeatedly washed with PBS to remove any unbound **BSA-FITC**.

This bioconjugation protocol was also followed when coupling a specific antibody (EPCAM) or a non-specific isotype control antibody (ISO) to the **Fe_3O_4-NH-RITC/COOH** nanoparticles. Two different samples were prepared and denoted as **Fe_3O_4-NH-RITC/CO-EPCAM** and **Fe_3O_4-NH-RITC/CO-ISO** respectively.

3.2.3 Analysis of EPCAM conjugation to the Fe_3O_4-NH-RITC/COOH nanoparticles

The number of EPCAM antibody molecules conjugated to surface of the **Fe_3O_4-NH-RITC/COOH** nanoparticles was estimated using the Bradford assay. The EPCAM antibody was conjugated to the fluorescently labelled nanoparticles using the protocol

described in section **3.2.2.2**. The carboxylic acid groups of **Fe_3O_4-NH-RITC/COOH** nanoparticles (1 mg) were activated using EDC and sulfo-NHS for 4 hours. The activated nanoparticles were washed and then incubated overnight with the EPCAM antibody (23 µg in 1 mL PBS). After the conjugation, the nanoparticles were washed with PBS. The supernatants were collected, concentrated and mixed with Bradford reagent to give a blue coloured complex with a maximum absorbance at 595 nm. A calibration curve of known antibody concentrations was plotted and the unreacted EPCAM in the supernatants was determined. Finally the concentration of EPCAM bound to the nanoparticles was determined by difference from the initial concentration.

3.2.4 Magnetic Resonance Imaging (MRI) capability of bifunctionalised nanoparticles

To determine the MRI potential of the magnetic nanoparticles, serial dilutions of the unfunctionalised Fe_3O_4 and bifunctionalised **Fe_3O_4-NH_2/COOH** were prepared in 1% agarose solution at concentrations of 0.01, 0.05, 0.1 and 0.2 mM Fe. The samples were aliquoted in eppendorf tubes (300 µL) and placed in a polystyrene MRI holder. The samples were then scanned and images were acquired using a Bruker Avance III console and gradient system interfaced to a Magnex Scientific 7 T horizontal bore magnet at a ^1H resonant frequency of 300 MHz. T_2 relaxation time was calculated from a set of RARE[60] images acquired with TR=5000 ms and TE values of 11, 33, 55 and 77 ms.

The MRI measurements were carried out by Ms. Karen Davies at the Department of Imaging Science and Biomedical Engineering, University of Manchester.

3.2.5 Cell culture

Cell culture procedures were carried out inside a class II flowhood, following standard tissue culture techniques.[15] Culture medium (DMEM), PBS, trypsin/EDTA were pre-warmed to 37 °C in a water bath prior to use. Cells were incubated at 37 °C in a tissue culture incubator with humidified atmosphere of 5% CO_2.

3.2.5.1 Thawing frozen cells protocol

Cell lines purchased from American Type Culture Collection were stored in frozen aliquots upon arrival. To be able to use them in culture, the cell aliquots were thawed at 37 °C and resuspended by dropwise addition of pre-warmed culture medium (10 mL). The cells suspension was centrifuged at 1000 rpm to obtain a complete pellet. After centrifugation, the cells were gently resuspended in fresh culture medium (5 mL) and seeded into T25 culture flasks until confluent.

3.2.5.2 Passaging of adherent Panc-1 cells in culture

Once confluent, the cells were passaged regularly twice a week in a split ratio of 1:10. The spent culture medium was discarded and the cells were gently washed twice with PBS (10 mL). Extra care was taken in order to avoid disturbing the adherent cell layer. The PBS was discarded and the cells were detached from the flask (trypsinisation) by incubation with trypsin/EDTA (3 mL) for 4 min at 37 °C. For complete detachment of cells the flask was gently tapped twice and 7 mL of fresh culture medium was added to resuspend the cells. The cells were pelleted at 1000 rpm and resuspended in fresh culture medium (10 mL). At this stage the total number of cells was determined using a

hemocytometer. Two millilitres of resuspended cells were seeded into a T150 culture flask containing fresh culture medium (18 mL).

3.2.5.3 Counting cells using a hemocytometer

During the cells passaging procedure the total number of cells was determined using a hemocytometer. After trypsinisation and resuspension of the cells in fresh medium, an aliquot of the cells (10 μL) was added to a clean hemocytometer. Cells were counted in the four gridded squares of the hemocytometer (red areas in **Figure 3.3**). The averaged numbers from the four counts were multiplied by 10^4 to obtain the number of cells per mL. The counting procedure was repeated twice on two separate samples.

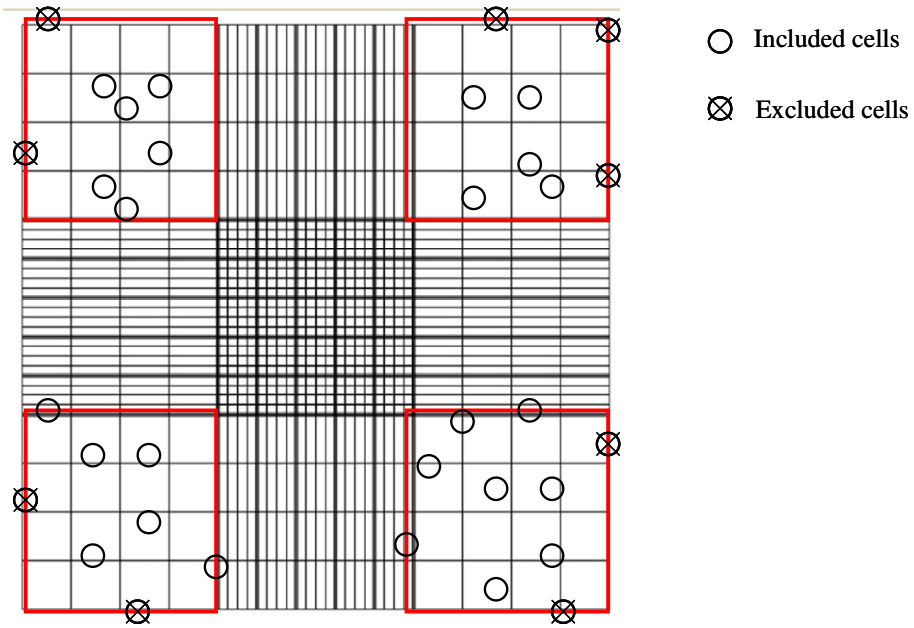

Figure 3.3 Graphic representation of a hemocytometer used for counting of the cells.

3.2.5.4 Cryogenic storage of cells

Once cells were confluent, culture medium was removed and cells washed with PBS (10 mL). The PBS wash was discarded and cells were detached from the flask by

trypsinisation (3 mL). Equal volume of fresh culture medium was added to resuspend the released cells. Cells were pelleted at 1000 rpm for 5 minutes. Media was removed and the cells were washed with PBS (10 mL) and the centrifuged for 5 minutes at 1000 rpm. The cells were resuspened in fresh medium (5 mL) and aliquoted into cryotubes (1 mL each). To each cryotube an aliquot of freezing medium (0.25 mL) was added (see **Table 3.3**). The cryotubes were placed on ice for 20 minutes before being stored at -80 ^{o}C.

3.2.6 Cytotoxicity of functionalised nanoparticles

3.2.6.1 Sterilisation of functionalised nanoparticles

Sterile magnetic nanoparticle dispersions were obtained by autoclaving the unfunctionalised Fe_3O_4 and **Fe_3O_4-NH_2/COOH** nanoparticles at 121 ^{o}C for 30 minutes. Once sterilised the nanoparticles were transferred into cell culture medium in the laminar flow hood before addition to the cells.

3.2.6.2 MTS cytotoxicity assay and pancreatic cancer cells

The effect of functionalised nanoparticles on pancreatic cancer cells (Panc-1) was assessed at 48 hours using the MTS assay according to the manufacturer's instructions. Panc-1 cells were seeded in 96-well plates (5000 cells/well) in medium (100 µL) and grown for 24 hours to allow cell adherence. The medium was then replaced with a fresh portion containing various concentrations of sterile Fe_3O_4 and **Fe_3O_4-NH_2/COOH** nanoparticles (10-500 µg/mL). Control wells containing cells with only fresh media were also included. Cells were incubated for a further period of 48 hours. Then, the MTS reagent (10 µL) was added to each well. Absorbance readings at 450 nm were

taken at 3 hours following incubation with the MTS reagent. Values were corrected for the medium-nanoparticles blank reading; medium-nanoparticles blanks comprised wells without cells. Experiments were performed in triplicate using eight wells for each treatment.

3.2.6.3 WST-8 cell proliferation assay and embryonic stem cells

Mouse embryonic stem cells (E14) were incubated in the presence of functionalised nanoparticles to examine if the nanoparticles influence the cell proliferation cycle. The cells were seeded in 96-well tissue culture plates (10000 cells/well) in medium (100 µL) and grown for 24 hours at 37 °C to allow cell adhesion. At 24 hours post-seeding, sterile Fe_3O_4 and **Fe_3O_4-NH_2/COOH** nanoparticles were diluted in fresh medium and added to the cells in the following concentrations: 10, 20, 50, 100 and 200 µg/mL. Control wells containing cells in medium were also included. After 72 hours, the reagent WST-8 (10 µL) was added in each well. Absorbance measurements were carried out at 450 nm following 4 hours of incubation with WST-8. Experiments were performed in triplicate using three wells for each treatment. Values were corrected for the medium-nanoparticles blank reading; medium-nanoparticles blanks comprised wells without cells. The cell viability was calculated against the control cells and presented in percentage.

These experiments were performed by Dr. Iryna Palona at the School of Biological Sciences, University of Liverpool.

3.2.6.4 Live/Dead cell assay

Live/Dead assay is a ready to use staining kit and was utilised to simultaneously visualise viable and dead pancreatic cancer cells in the presence of bifunctionalised

nanoparticles using fluorescence microscopy. Panc-1 cells were seeded into 35 mm dishes in medium (10000 cells/mL). After 24 hours, **Fe_3O_4-NH_2/COOH** nanoparticles were added to the cells in the following concentrations: 10, 25 and 50 µg/mL. Control dishes comprising of Panc-1 cells in fresh media were also included. Cells were incubated with nanoparticles for another 48 hours. The assay solution (100 µL) was added to each dish and the cells were incubated for 15 min at 37 °C. The cells fluorescence was detected using a fluorescence microscope with 490 nm excitation for simultaneous identification of viable (green) or dead cells (red). The cell viability was obtained from 5 different fields per sample and calculated by dividing the number of green by the total number of cells (green plus red cells).

3.2.7 Interaction of EPCAM labelled nanoparticles with Panc-1 cells

3.2.7.1 Evaluation of expression of EPCAM receptors on the cell surface

A Standard immunohystochemistry technique was used to evaluate the expression of the specific receptors EPCAM on the cells surface (**Figure 3.4).** Panc-1 cells (10000/well) were seeded in 2-well chamber slides in medium (2 mL) and grown for 24 hours to allow cell adhesion. Next the medium was discarded; the cells washed with PBS and fixed using paraformaldehyde (1 mL, 4%). The fixed cells were incubated with blocking solution (1 mL, **Table 3.4**) for 1 hour at room temperature. Cells were incubated overnight at 4 °C with EPCAM antibody **1** (1:50 in PBS). After washing three times with PBS, the cells were incubated with **2,** secondary antibody Cy3 labelled mouse anti-rabbit IgG (1:100 in PBS) for 1 hour at 4 °C. After washing three times with PBS, cells were stained with DAPI to visualise nuclei and then mounted with Mowiol solution. The

cells were imaged using fluorescence microscopy to show the localisation of the specific receptors for EPCAM antibody.

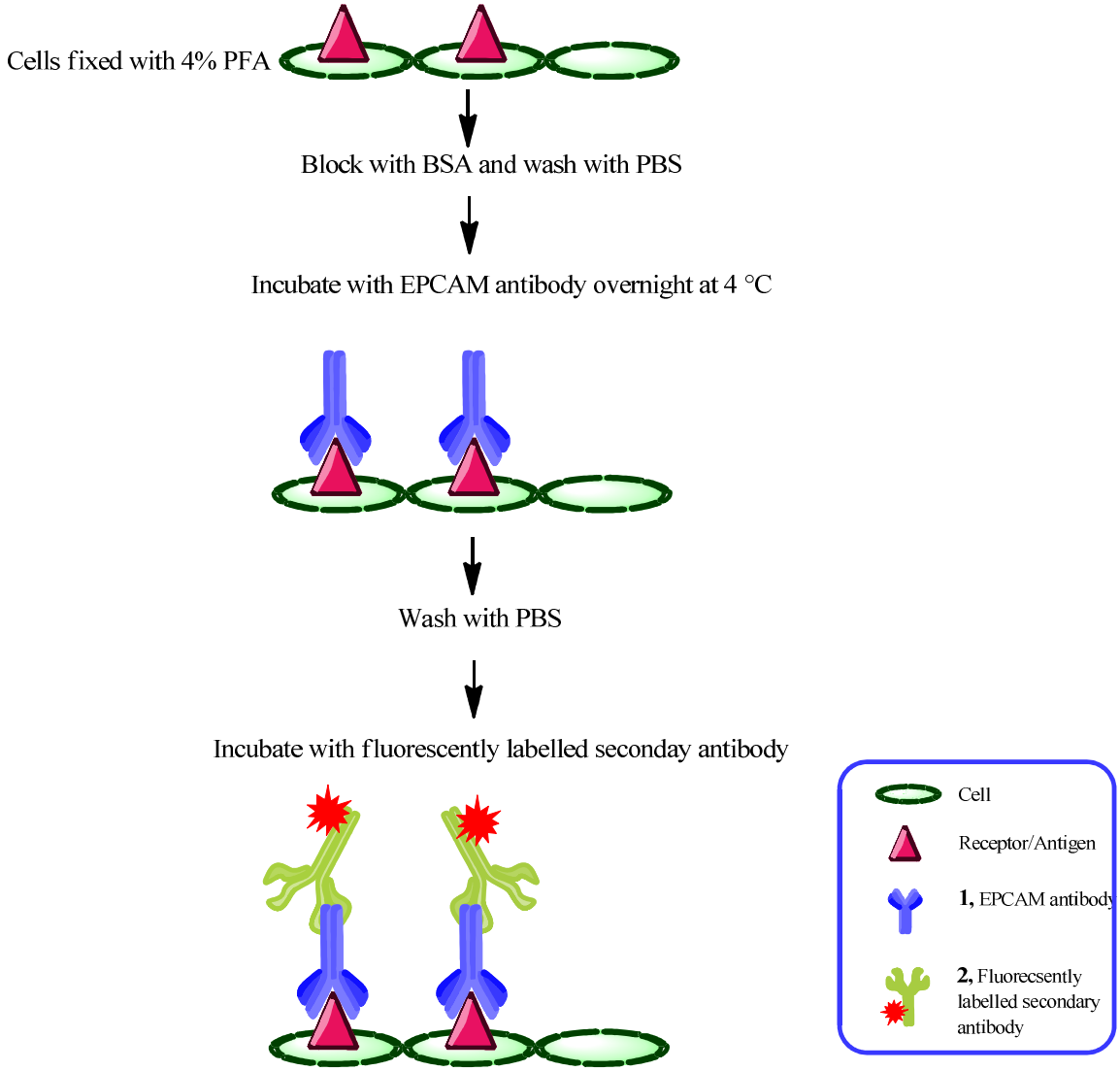

Figure 3.4 Immunostaining diagram for assessing the receptors expression on cancer cells.

3.2.7.2 Antibody targeting experiments

To determine the targeting abilities and the cellular uptake, Panc-1 cells (10000 cells/mL) were seeded in glassbase dishes 24 hours prior to the addition of 100 µg/mL nanoparticles (**Fe_3O_4-NH-RITC/CO-EPCAM**, **Fe_3O_4-NH-RITC/CO-ISO** and

Fe_3O_4-NH-RITC/COOH). The cells were incubated in the presence of the nanoparticles for 1, 6 and 24 hours. After the set time intervals, the cells were washed with PBS (2 mL, five times) and fixed with 4% paraformaldehyde solution for 20 minutes. Fixed cells were washed with PBS (2 mL, five times) and cellular nuclei were stained with DAPI solution (0.5 mL, **Table 3.4**).

Fluorescence microscopy and confocal laser scanning microscopy were used to investigate the targeting properties of each type of nanoparticle.

The confocal laser scanning microscopy imaging was performed by Dr. Alec Simpson at the Department of Cellular and Molecular Physiology, University of Liverpool.

3.2.8 Statistical analysis

Each cytotoxicity experiment was carried out in triplicate. Data are presented as means ± standard deviation. Differences between values of groups were tested for statistical significance using unpaired Student t-test. A *P* value of less than 0.05 was considered to indicate a significant difference. StatsDirect, version 2.7.2, statistical software was used for statistical analysis.

3.3 Results and discussion

3.3.1 Cytotoxicity of functionalised nanoparticles

3.3.1.1 *In vitro* cytotoxicity with pancreatic cancer cells

For functionalised nanoparticles to be suitable as diagnostic probes or therapeutic agents, they should show minimal toxicity to cells. *In vitro* toxicological studies and cell culture techniques were preferred due to their rapid, efficient and cost effective advantages.[16] Even though *in vitro* cytotoxicity experiments must be validated by *in vivo* assessments in order to be meaningful, simple *in vitro* toxicity assays provide a general sense on nanoparticles potential toxicity and risk assessment.

Cytotoxicity was evaluated using two different cell lines (Panc-1- pancreatic cancer cells and E-14 mouse embryonic stem cells) and at different concentrations in order to expand the outlook for potential signs of toxicity. As the designed nanoparticles are intended as targeting agents for pancreatic cancer, their toxicity was initially investigated with pancreatic tumour model cells (Panc-1) which were used in the targeting experiments. The degree of cell survival was evaluated by means of the standard MTS assay. The cells were incubated with unfunctionalised (Fe_3O_4) and bifunctionalised (**Fe_3O_4-NH_2/COOH**) nanoparticles for 48 hours and the cell viability measured after this period. The results from the MTS assay showed no evidence of toxicity for nanoparticle levels up to 100 µg/mL after 48 hours of treatment. At these levels the cell viability was above 92% compared to control cells (**Figure 3.5**).

For nanoparticle levels above 100 µg/mL the cell viability values were below 80% and there was a statistically significant difference compared to the controls. It has to be

mentioned that above 100 µg/mL the cells were overdosed intentionally to see where the maximum limit is. Therefore the decrease in viability was expected.

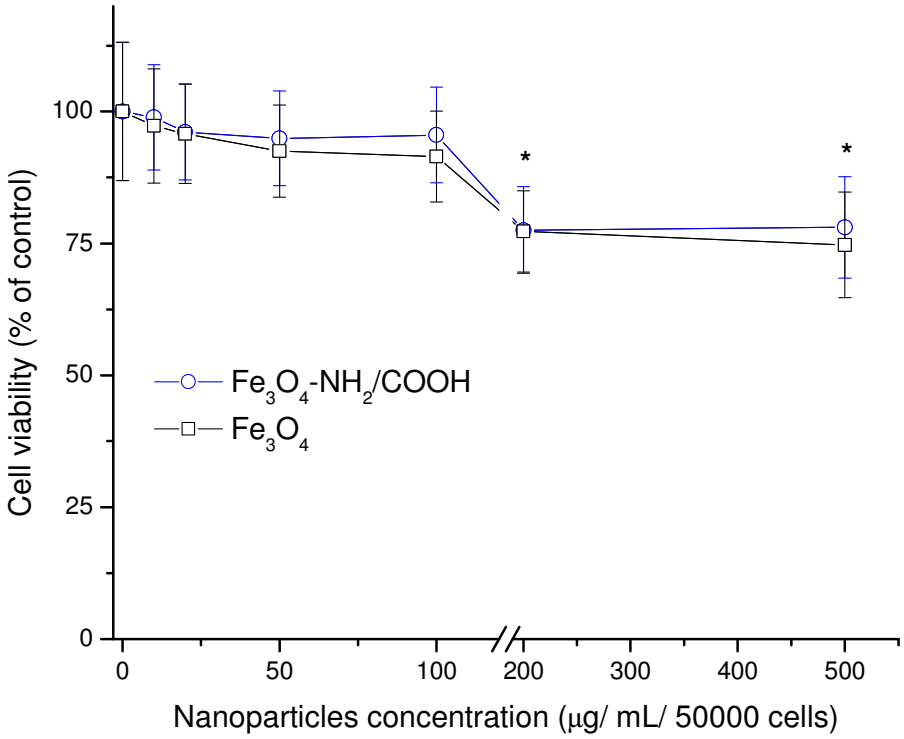

Figure 3.5 Cell viability of Panc-1 cells after 48 hours incubation with unfunctionalised (**Fe_3O_4**) and bifunctionalised (**Fe_3O_4-NH_2/COOH**) nanoparticles at different concentrations ranging from 10 to 500 µg/mL. The results are presented as average ± standard deviation. Significant difference in cell viability was observed at concentrations above 100 µg/mL (Students t test: *$p<0.05$).

It is important to notice that **Fe_3O_4-NH_2/COOH** nanoparticles did not cause any additional toxic effect over and above that of unfunctionalised Fe_3O_4. Other groups have also reported that coated iron oxide nanoparticles have good biocompatibility not only *in vitro* but also *in vivo* and that the cytotoxicity effect is dependent on dose, compositions, nanoparticle size and cell types.[17-21] In addition to these findings, this study showed that

the chemical modification of the nanoparticle surface does not induce toxicity. For the cell targeting experiments, concentrations of 100 µg/mL were used, and at this concentration, the results showed that the nanoparticles were not cytotoxic when compared with the controls.

3.3.1.2 *In vitro* cytotoxicity with embryonic stem cells

To establish if the functionalised nanoparticles can affect other types of cells, a second cell line was exposed to various concentrations of nanoparticles for a period of 72 hours. Embryonic stem cells (cell line E14) were chosen for this second evaluation because stem cells are known to be more sensitive to external factors like nanoparticles. The cell viability of embryonic stem cells was evaluated using the WST-8 assay which allows assessment of the cell viability after longer exposure times. The cell viability was calculated by comparing the absorption of nanoparticle-treated cells to that of control cells, which was defined as 100%. Nanoparticles were considered to have a toxic effect if the difference between cell growth of controls and cells exposed to nanoparticles was statistically significant at $p<0.05$, as determined by Student's t test. After 72 hours of incubation with nanoparticles concentrations up to 50 µg/mL there was no sign of toxicity. The viability values for both types of investigated nanoparticles, Fe_3O_4 and **Fe_3O_4-NH_2/COOH**, were above 95% compared to controls and there was no statistical difference between these groups (**Figure 3.6**). However at higher dose of nanoparticles, 100 and 200 µg/mL, the cell survival decreased below 70% and there was a statistically significant difference between these groups and the controls (*$p< 0.05$).

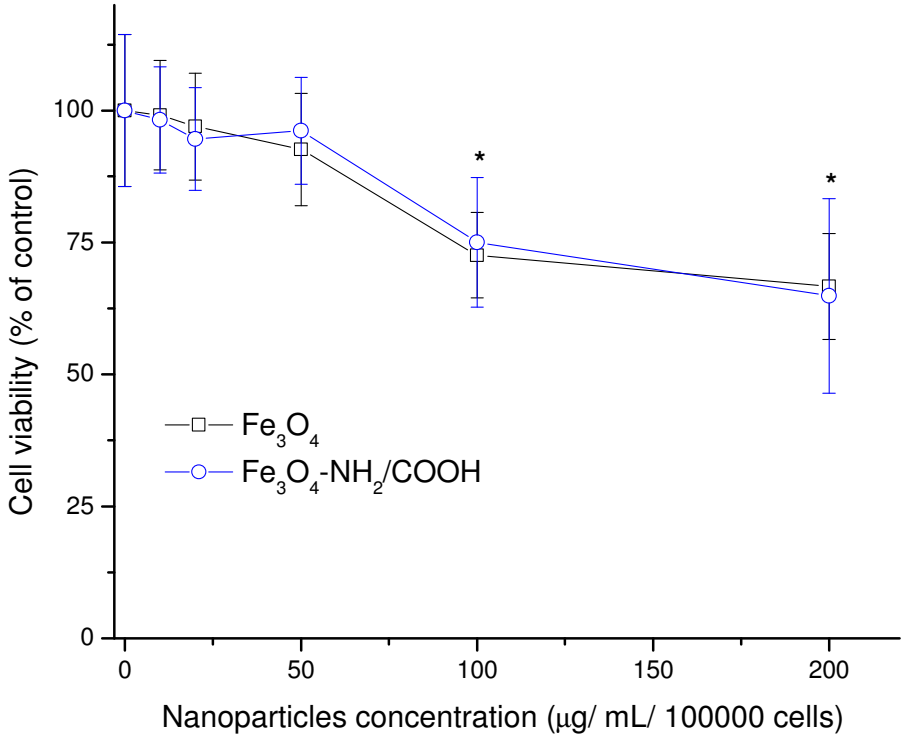

Figure 3.6 Cell viability of E-14 cells after 72 hours incubation with non-functionalised (**Fe_3O_4**) and bifunctionalised (**Fe_3O_4-NH_2/COOH**) nanoparticles at different concentrations ranging from 10 to 200 µg/mL. The results are presented as average ± standard deviation. Significant difference in cell viability was observed at concentrations above 50 µg/mL (Students t test: *$p<0.05$).

From the WST-8 results with embryonic stem cells it is evident that these cells appear to be more sensitive than Panc-1 cells. This was not entirely unexpected as these cells are reported to be more sensitive to nanoparticle exposure.[22-23] At the same time these results show that minimal concentrations of nanoparticles (10-50 µg/mL) do not cause toxic effects in these cells and are safe to be used for cell labeling and targeting experiments.

3.3.1.3 Live/Dead cell assay

Cell viability was also investigated using the live–dead assay (green–red) upon exposure to nanoparticles. Live–dead cell viability assay is a double colour fluorescence assay that is based on the simultaneous detection of the live and dead cells using one excitation wavelength at 490 nm. The live cells have intracellular enzymes (esterases) that convert the non-fluorescent cell-penetrating acetoxymethyl ester of calcein (calcein AM) to the intensely green fluorescent calcein (emission at 515 nm) which is retained within the cells. On the other hand, propidium iodide enters only through the damaged membranes of dead cells and upon binding with the nuclear DNA forms a bright red fluorescent complex (emission at 617 nm).

Pancreatic cancer cells, Panc-1, were grown in culture in the presence of different concentrations of bifunctionalised **Fe_3O_4-NH_2/COOH** nanoparticles. Representative fluorescence microscopy images of Panc-1 cells exposed to **Fe_3O_4-NH_2/COOH** nanoparticles are shown in **Figure 3.7**. The images showed that only the green fluorescence emission signal could be detected which implied that the cell viability was not affected after 48 hours of incubation with **Fe_3O_4-NH_2/COOH** nanoparticles. For all nanoparticle levels, five different fields per sample were analysed and the cell viability was estimated to be more than 98% under the tested conditions. The viability was determined by dividing the number of green cells by the total number of cells (green plus red cells).

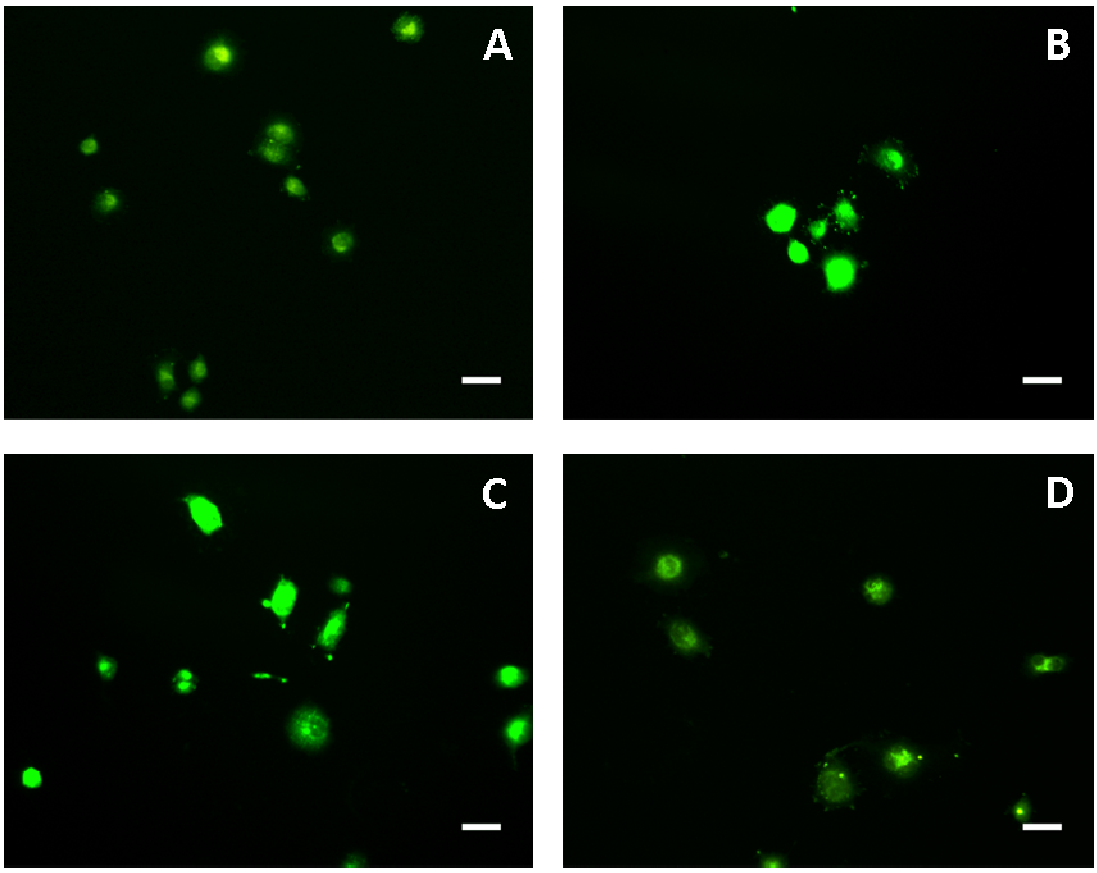

Figure 3.7 Representative fluorescence microscopy images demonstrating the viability of Panc-1 cells after 48 hours incubation with different concentrations of **Fe_3O_4-NH_2/COOH** nanoparticles (A) control cells (0 μg/mL), (B) 10 μg/mL, (C) 25 μg/mL and (D) 50 μg/mL. Scale bar represents 50 μm.

Overall the cytotoxicity tests showed that the **Fe_3O_4-NH_2/COOH** nanoparticles have minimal toxicity below 100 μg/mL and that the results are consistent with other literature reports.[16,21] Therefore bifunctionalised **Fe_3O_4-NH_2/COOH** nanoparticles can be safely used at levels below 100 μg/mL in combination with specific antibodies for targeting purposes.

3.3.2 Fluorescent dye and protein coupling to Fe_3O_4-NH_2/COOH nanoparticles

Rhodamine B isothiocyanate (**RITC**) is a frequently used fluorescent tag for labelling biomolecules which shows an orange-red emission wavelength (λ_{ex} = 543 nm, λ_{em} = 580 nm). Similar to other isothiocyanate modified fluorophores, **RITC** is reactive only towards the free amine groups (***–NH₂***) present in the lysine units of peptides and proteins. The free ***–NH₂*** groups on the **Fe_3O_4-NH_2/COOH** nanoparticles were labelled with the **RITC** fluorescent tag in order to localise and follow the nanoparticles using fluorescence microscopy during cell labelling experiments. The resulting nanoparticles were denoted as **Fe_3O_4-NH-RITC/COOH** and the reaction schematic is illustrated in **Scheme 3.1.**

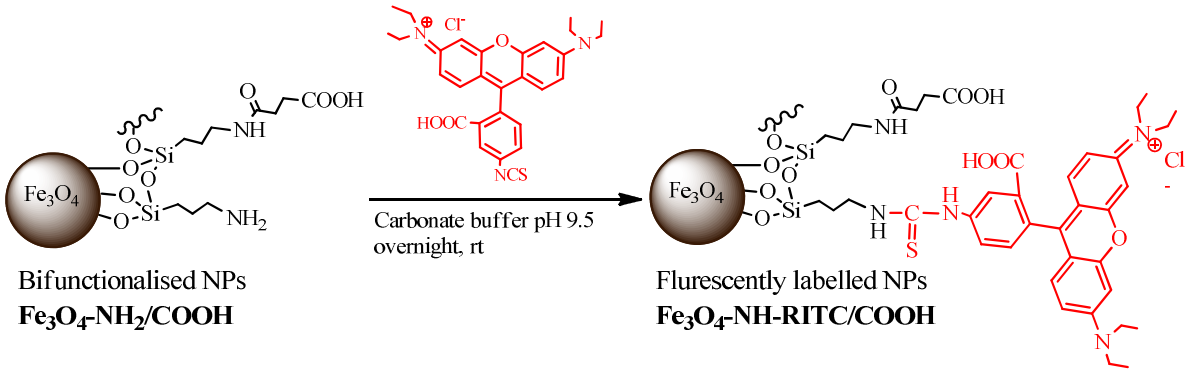

Scheme 3.1 Illustration of the chemical synthesis of red fluorescently labelled nanoparticles **Fe_3O_4-NH-RITC/COOH.**

The fluorescently labelled **Fe_3O_4-NH-RITC/COOH** nanoparticles were examined using fluorescence microscopy after washing the nanoparticles with Tris buffer (**Table 3.1**). **Figure 3.8** shows representative fluorescence microscopy images of the

Fe_3O_4-NH-RITC/COOH nanoparticles. The red fluorescence associated with the nanoparticles indicates that the **RITC** fluorescence dye molecules were successfully coupled to the amine groups of the nanoparticles. A control experiment, which was carried out under identical conditions with the exception of using unfunctionalised Fe_3O_4 nanoparticles instead of **Fe_3O_4-NH_2/COOH**, did not yield fluorescent nanoparticles. This demonstrated that the fluorescently labelled nanoparticles were not the result of a physical mixture but actual chemical binding.

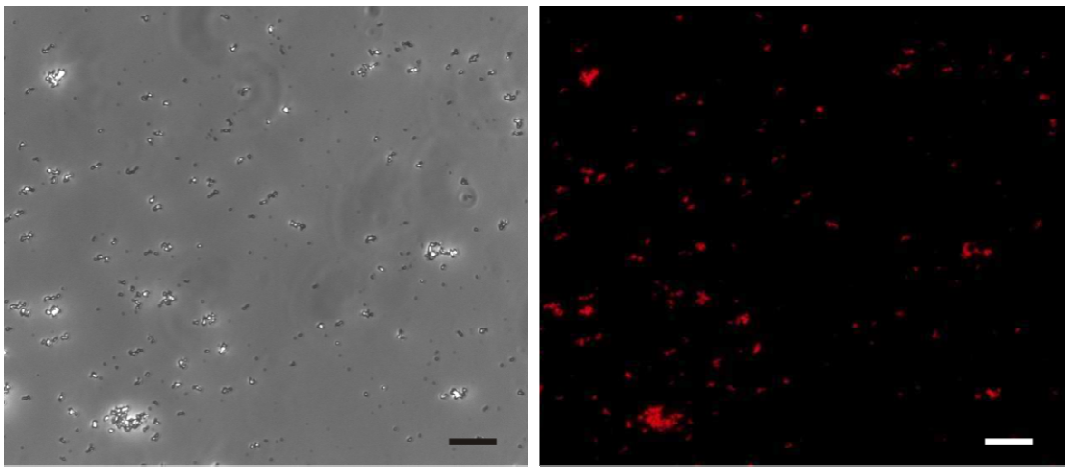

Figure 3.8 Bright field and fluorescence microscopy images of **Fe_3O_4-NH-RITC/COOH.** The red emission shows that the **RITC** fluorescent tag was coupled to the nanoparticles. Scale bar represents 10 μm.

The number of **RITC** molecules coupled to the nanoparticles was evaluated using elemental analysis. As expected, after the **RITC** binding the carbon content increased from 1.62% in **Fe_3O_4-NH_2/COOH** nanoparticles to 3.63% in **Fe_3O_4-NH-RITC/COOH** nanoparticles. Following the equations 2.1-2.10 presented in Chapter 2, a number of 2000 **RITC** molecules per nanoparticle could be calculated. This is equivalent to 30% coupling of the residual 75% free amine groups on the bifunctional **Fe_3O_4-NH_2/COOH**.

A 30% yield is reasonable considering that the ***–NH₂*** functional groups are rather close to each other (~0.3 nm between groups) while the width of a rigid **RITC** molecule is around 1.0 nm (measured with ChemBio3D Ultra 12.0 software). As shown in **Figure 3.9**, the two neighbouring ***–NH₂*** groups to the RITC are likely to be blocked for further reactions.

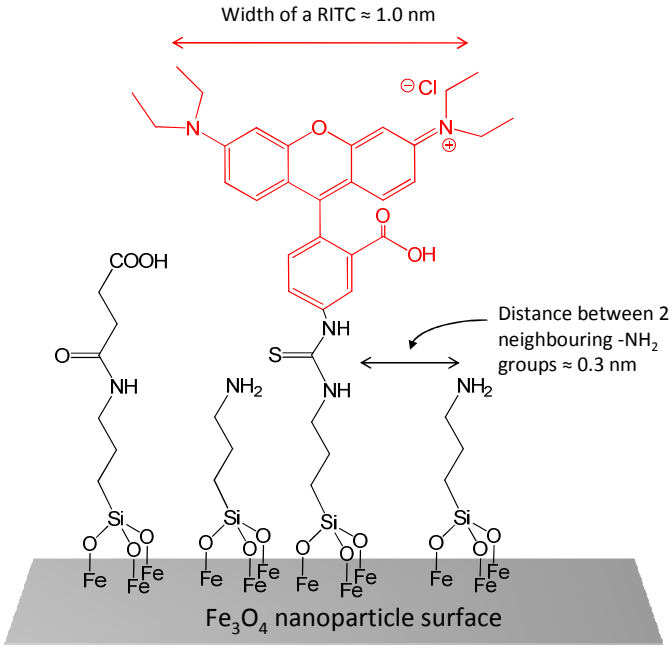

Figure 3.9 Schematic comparisons on the size of RITC molecules and the distance between amine groups on the surface of bifunctionalised **Fe_3O_4-NH_2/COOH** nanoparticles.

The conjugation of the **RITC** fluorescent dye to the amine groups required only mild reaction conditions (ambient temperature and a buffer solution with pH = 9.5) which implies that the ***–COOH*** functional groups are preserved and chemically reactive.

To investigate whether the carboxyl functional groups are still chemically reactive on the **Fe_3O_4-NH-RITC/COOH** nanoparticles, a fluorescent model protein, bovine serum

albumin labelled with fluorescein isothiocyante or **BSA-FITC** (**FITC,** λ_{ex} = 494 nm, λ_{em} = 520 nm), was used as a testing agent. The fluorescent protein was covalently attached by conjugating the carboxylic acid groups of **Fe_3O_4-NH-RITC/COOH** nanoparticles with the available amine groups (from the lysine residues) on the BSA using the carbodiimide coupling method. Since **BSA-FITC** shows green fluorescence, the nanoparticles conjugated with this fluorescent protein would show both red and green fluorescence. In **Figure 3.10** both the red and the green fluorescence emission was observed on the nanoparticles depicted in the bright field image. The presence of both fluorescent emissions indicated that the **BSA-FITC** had been successfully attached to the red-fluorescent **Fe_3O_4-NH-RITC/COOH** nanoparticles.

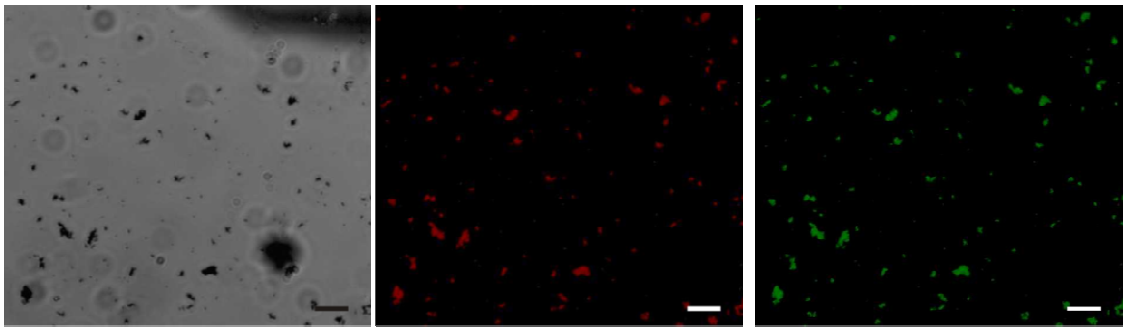

Figure 3.10 Bright field and fluorescence microscopy images of **Fe_3O_4-NH-RITC/COOH** coupled with **BSA-FITC**. The red and green emission confirms that the fluorescent protein was attached to the red labelled nanoparticles. Scale bar represents 10 μm.

A control experiment performed in the same condition except the addition of EDC/sulfo-NHS did not yield green fluorescence on the nanoparticles. Furthermore, the results demonstrated the accessibility of the carboxylic acid groups for other

bioconjugations. For this reason, the ***–COOH*** groups can be used to conjugate with any other targeting biomolecule containing amine groups (specific antibodies, peptides, proteins, growth factors). The combination between antibodies and nanoparticles would not only provide chemical versatility but also targeting specificity to the nanoparticle system.

3.3.3 Antibody coupling to Fe_3O_4-NH-RITC/COOH nanoparticles

The fluorescently labelled **Fe_3O_4-NH-RITC/COOH** nanoparticles were given tumour-targeting capabilities by decorating their surface with specific antibodies. The chosen antibody, EPCAM, is known to bind to specific proteins which are over-expressed on the surface of epithelial pancreatic cancer cells (Panc-1 cell line).[24-25] The EPCAM antibodies were conjugated with the available carboxylic acid groups of the **Fe_3O_4-NH-RITC/COOH** nanoparticles using the carbodiimide coupling chemistry (EDC/sulfo-NHS). These nanoparticles were denoted as **Fe_3O_4-NH-RITC/CO-EPCAM**, to illustrate that the EPCAM antibody is attached on the ***–COOH*** groups while the fluorescent tag **RITC** is bound to the ***–NH_2*** groups. After the bioconjugation of EPCAM, quantitative determination of the amount of unreacted antibody was used to calculate the number of antibodies bound to the ***–COOH*** functional groups. This approach was necessary to accurately determine the antibody binding since the absorption from the magnetic nanoparticles prevented the direct measurement of conjugation in the product. The amount of unreacted antibody was determined using absorbance measurements of the supernatant and washing solutions after bioconjugation. Bradford assay was employed to quantify the number of unreacted

antibodies. First a standard calibration curve was established using known concentrations of antibody (**Figure 3.11**).

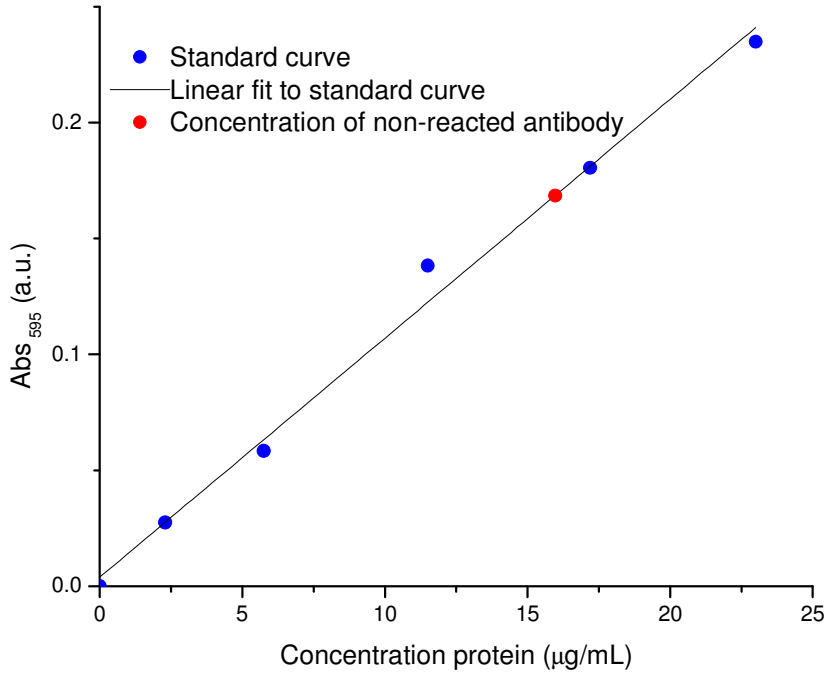

Figure 3.11 Antibody concentration measured by Bradford assay and matched to the calibration curve having the equation y= 0.0103x+0.0039, R=0.9924.

The amount of antibody bound to the nanoparticles was calculated using the equation:

$$Conjugated_{antibody} = Initial\ _{concentration} - Unreacted_{antibody}$$

Using the calibration curve, the unreacted antibody concentration in the supernatant and washing solutions was determined to be 15.97 µg/mL. This suggested that 7.03 µg/mL of EPCAM antibodies (equivalent to 32.07×10^{12} molecules) were bound onto the nanoparticles. Since there are 23.7×10^{12} nanoparticles in 1 mg material (Chapter 2, equations 2.1-2.4) the equivalent number of EPCAM molecules bound per nanoparticle was found to be 1.35. The approximate molecular dimensions for an Y shaped antibody

are 10 × 14 × 4.5 nm from published crystallographic data.[26] Based on these dimensions the calculated antibody footprint on the nanoparticles surface can vary from 63 to 140 nm^2 depending on binding orientation and assuming rectangular footprints. Therefore, the obtained results for conjugated antibodies on the nanoparticles surface reasonably fit with the available ***–COOH*** groups and a random orientation. In addition to the antibody surface conjugation, retention of its bioactivity is important for producing nanoparticles capable of targeting and bio-recognition. The bioactivity was evaluated during *in vitro* targeting experiments which are presented in section 3.3.5.

3.3.4 MRI capability of bifunctionalised nanoparticles

To evaluate the MRI potential of the bifunctionalised nanoparticles, their T_2 relaxation times was measured using a 7 T horizontal bore Magnex Scientific imaging system, operating at 300 MHz resonant frequency. Increasing concentrations of nanoparticles ranging from 0.01 to 0.2 mM Fe were prepared in 1% agarose gel and placed in a polystyrene holder for the measurements. Blanks consisting of 1% agarose gel were measured as a control. MRI analysis was performed at TR 5000 ms and multiple TE values of 11, 33, 55 and 77 ms for various concentrations of nanoparticles. These measurements were performed by Ms. Karen Davies at the Department of Imaging Science and Biomedical Engineering, University of Manchester.

Their efficiency as T_2 MRI enhancement agents was determined by calculation of the r_2 relaxivities as the slopes of the linear fit of the inverse relaxation times as a function of iron molar concentration (**Figure 3.12**). As expected, it was found that the inverse

relaxation times vary linearly with the iron concentration, according to the following equation (3.1):[27-28]

$$\frac{1}{T_2([Fe])} = r_2[Fe] + \frac{1}{T_2^0}, \quad (3.1)$$

r_2 is the transverse relaxivity, $1/T_2^0$ is the inverse relaxation time of the blank.

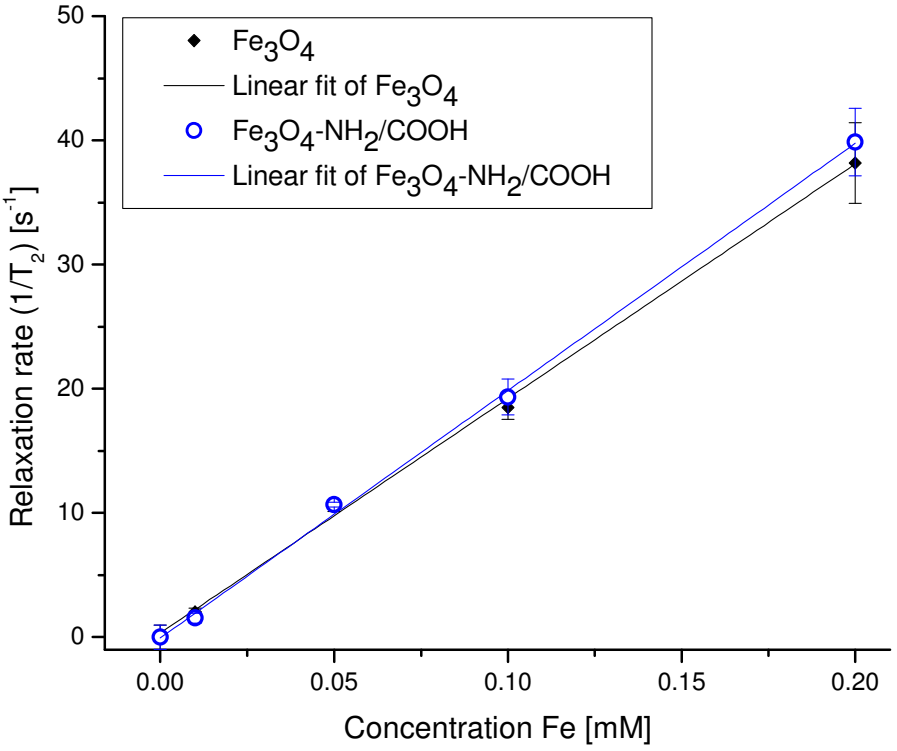

Figure 3.12 Inverse transverse relaxation times $1/T_2$ for unfunctionalised Fe_3O_4 and bifunctionalised **Fe_3O_4-NH_2/COOH** nanoparticles as a function of the iron molar concentration.

The r_2 relaxivity values were found to be 189 ± 5 $s^{-1}mM^{-1}$ and 199 ± 4 $s^{-1}mM^{-1}$ for Fe_3O_4 and **Fe_3O_4-NH_2/COOH** respectively. The bifunctionalised nanoparticles have similar r_2 relaxivity values as the starting material, Fe_3O_4 nanoparticles; therefore the surface chemical modifications did not diminish the MRI contrasting properties. The r_2

relaxivity value for bifunctionalised **Fe_3O_4-NH_2/COOH** nanoparticles is higher when compared with value of the clinical contrast agent Feridex I.V. (reported value of 148 ± 2, measured at 7 T).[29] As it was shown elsewhere, there are two major factors which can determine the enhancement of MRI signal: size of the nanoparticles and the coating thickness.[30] In this case the effective contrasting properties were attributed to the thin organic coating on the surface of the **Fe_3O_4-NH_2/COOH** nanoparticles and to the larger core size (25 nm compared with 5 nm). **Figure 3.13** shows T_2-weighted MRI images (TE/TR 11/5000 ms) of analysed nanoparticles at various concentrations in 1 % agarose gel.

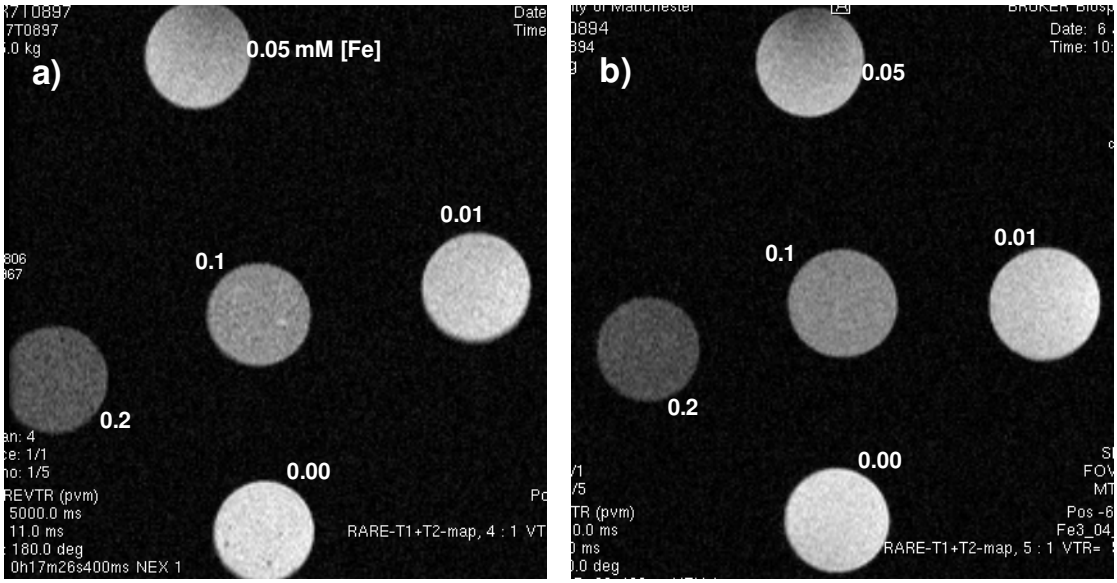

Figure 3.13 T_2 weighted magnetic resonance images of a) Fe_3O_4 and b)**Fe_3O_4-NH_2/COOH** nanoparticles in 1% agarose gel at various molar iron concentrations (0.01, 0.05, 0.1 and 0.2 mM) and at 25 °C, 7 T MRI, TR=5000 ms, TE=11 ms. Blanks consisting of 1% agarose gel were taken as a control.

Darkening of the grey discs in **Figure 3.13** corresponds to the improvement in MRI contrast capabilities due to the increased concentration of Fe_3O_4 and **Fe_3O_4-NH_2/COOH** nanoparticles.[31] When magnetic nanoparticles are present in the agarose gels, the large magnetic moment generated by these nanoparticles causes a local inhomogeneity in the magnetic field. This local inhomogeneity causes a shortening of the T_2 relaxation time of protons present in the agarose gels. Shortening of the T_2 relaxation time of the protons translates to a negative image contrast on the MRI images (darkening effect or hypointensity).

The **Fe_3O_4-NH_2/COOH** nanoparticles produce an observable change in image contrast at concentrations as low as 0.05 mM iron (corresponding to 4.1µg/mL), which is well within the safety range indicated by the cytotoxicity data (**Figure 3.5**). These results confirmed the effective MRI contrasting capabilities of the bifunctionalised magnetic nanoparticles. Therefore, the **Fe_3O_4-NH_2/COOH** nanoparticles potentially present suitable properties for usage as MRI contrasting agents.

3.3.5 Targeting capabilities of antibody labelled nanoparticles

3.3.5.1 Specificity of nanoparticles targeting

The EPCAM cell receptor, also known as cluster of differentiation 326 (CD 326), is a membrane glycoprotein with the molecular weight of 40 kDa.[32] It was reported to be ubiquitously overexpressed on the pancreatic cancer cells surface, making it an accessible target for binding and imaging.[25,33] The cellular expression of EPCAM receptor on the surface of Panc-1 cells was evaluated using immunofluorescence labelling and imaged using fluorescence microscopy (**Figure 3.14**).

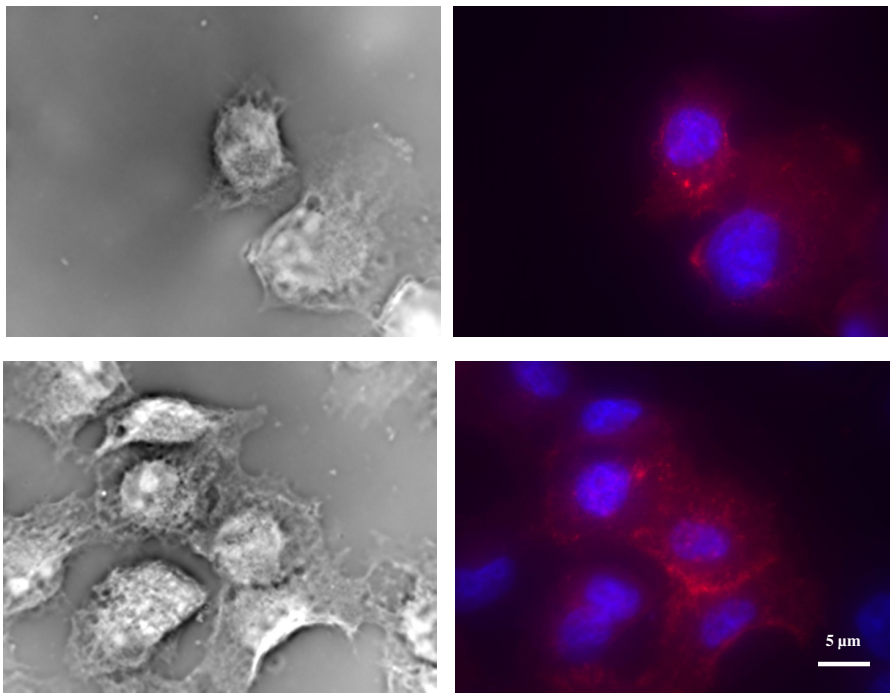

Figure 3.14 Phase contrast and fluorescent images showing the examination of EPCAM antigen expression on Panc-1 cells by immunofluorescence labelling. Cell nuclei stained with DAPI in blue. The EPCAM receptors visualised in red by labelling with IgG-Cy3 conjugates. Scale bar represents 5 µm.

The cell nuclei were stained with DAPI in blue and the expression of the EPCAM receptors was evidenced with rabbit anti-mouse IgG Cy3 conjugates (section **3.2.7.1**). The images show the Panc-1 cells are strongly positive with high levels of EPCAM expression as evidenced by the associated red fluorescence. Therefore, the EPCAM receptors could be also accessed using antibody-nanoparticles conjugates.

The nanoparticles used in the targeting experiments are summarised in **Table 3.5**.

Table 3.5 Summary of the nanoparticle samples employed in the cell targeting experiments.

Sample	***Properties***	***EPCAM receptor reactive***
Fe_3O_4-NH-RITC/CO-EPCAM	Targeting	YES
Fe_3O_4-NH-RITC/CO-ISO	Control 1	NO
Fe_3O_4-NH-RITC/COOH	Control 2	NO

All samples were applied at a concentration of 100 µg/mL. The red florescent tag (**RITC**) conjugated to the samples allowed the localisation of nanoparticles and their targeting abilities using fluorescence microscopy. The colocalisation of the cells was shown using the nuclear stain DAPI (blue).

Figure 3.15 shows the fluorescence images of Panc-1 cells incubated with the three types of samples for 1 hour. Fluorescence microscopy images in **Figure 3.15a** and **3.15b** show that the **Fe_3O_4-NH-RITC/CO-EPCAM** specifically target the Panc-1 cells. The targeting property was attributed to the surface-to-surface antibody-antigen interaction. This type of cell interaction has also been reported in case of dextran coated magnetic nanoparticle functionalised with monoclonal antibodies.[28,34]

In contrast, the control particles, **Fe_3O_4-NH-RITC/CO-ISO** or **Fe_3O_4-NH-RITC/COOH,** showed no binding to the cells in the first hour (**Figure 3.15c** and **3.15d**) and therefore the cells present no associated fluorescence signal. The addition of the non-specific isotype control antibody (ISO) did not enhance the targeting

properties of the nanoparticles due to the fact that this antibody does not present the same specific antigen binding region as the EPCAM antibody.

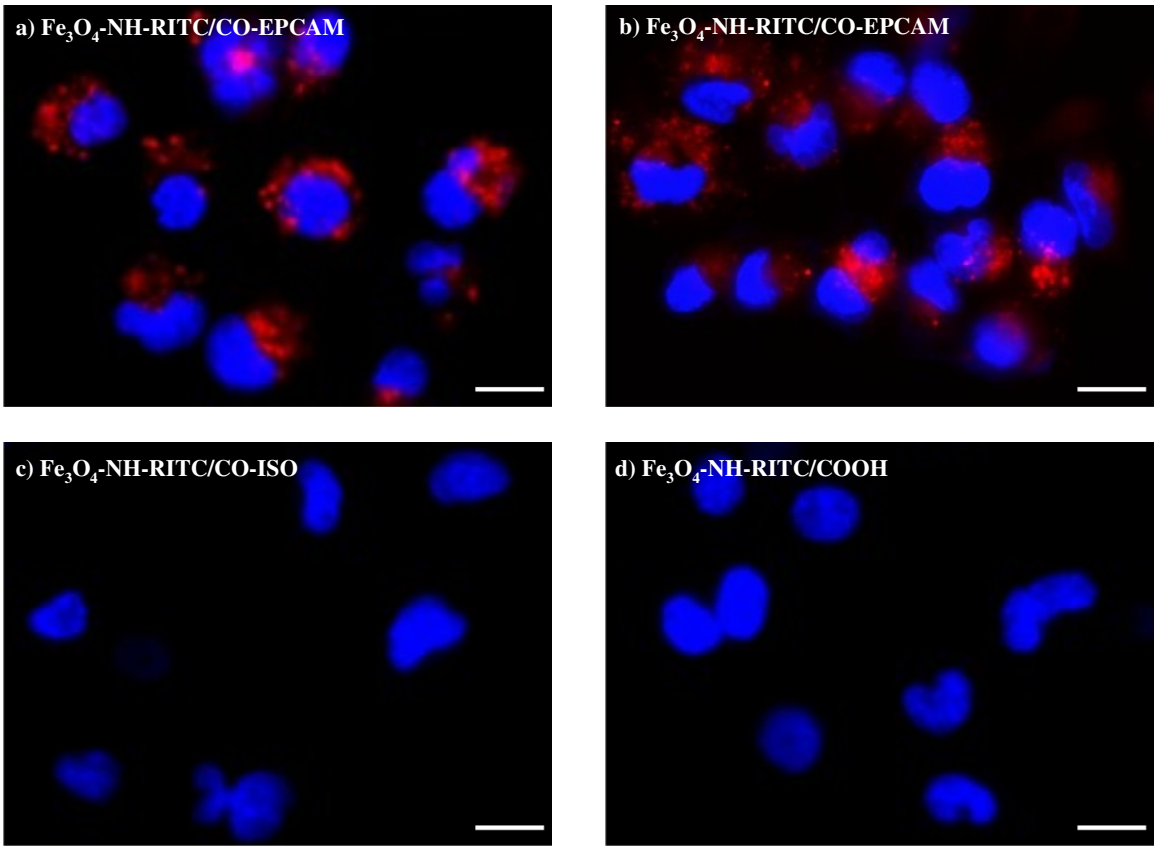

Figure 3.15 Fluorescence images of Panc-1 cells incubated for 1 hour with, a) and b) **Fe_3O_4-NH-RITC/CO-EPCAM**, c) **Fe_3O_4-NH-RITC/CO-ISO**, d) **Fe_3O_4-NH-RITC/COOH**. Detection of cell nuclei was performed by DAPI staining (blue). All nanoparticles were applied at 100 μg/mL. Scale bar represents 25 μm.

For cells incubated with **Fe_3O_4-NH-RITC/CO-EPCAM** nanoparticles, the red fluorescence signal was observed in the perinuclear region which is usually attributed to endosomal uptake as shown in **Figure 3.15a** and **3.15b**. This suggested that the internalisation of **Fe_3O_4-NH-RITC/CO-EPCAM** nanoparticles occurs within an hour.

The internalisation was further verified by examining sections of similarly treated Panc-1 cells by confocal laser scanning microscopy (**Figure 3.16a**). The zoom-in area in **Figure 3.16b** further confirmed that the nanoparticles accumulated in the cells. Therefore these nanoparticles were internalized *via* a receptor mediated endocytosis facilitated by the successful binding onto the EPCAM receptors on cell membranes.[34-35]

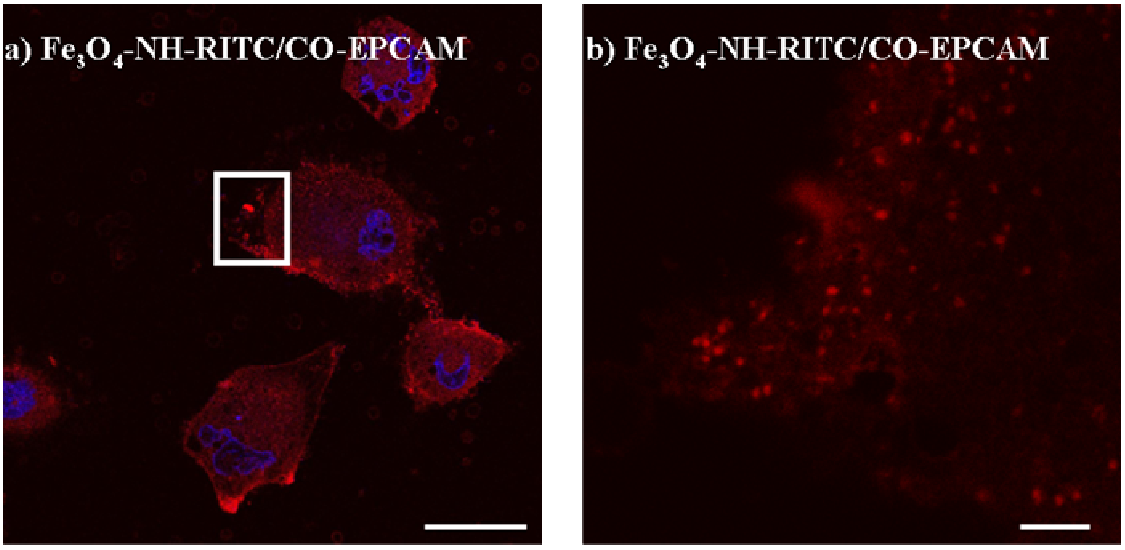

Figure 3.16 Confocal middle section images of Panc-1 cells incubated for 1 hour with, a) **Fe_3O_4-NH-RITC/CO-EPCAM** (scale bar represents 25 μm); b) Magnified images of the inset areas in (a), scale bar represents 5 μm. In blue the cell nuclei stained with DAPI and in red the nanoparticles tagged with RITC.

Most probably the nanoparticles would be localised in the endosomal vesicles but the exact colocalisation of nanoparticles was not further evaluated. The uptake mechanism could be investigated by using selective inhibition of the different paths of internalisation.[34] The nanoparticle colocalisation can be achieved by staining the different cell organelles and imaging with fluorescence microscopy.[9,35]

3.3.5.2. Effect of incubation period on cell uptake

The incubation period of nanoparticles with cells can affect their uptake into cells, in terms there is more probability for nanoparticle-cell interactions.

For comparison the targeting specificity and binding behaviour of the three types of nanoparticles was investigated for longer incubation times, 6 hours and 24 hours respectively. The experiments were carried out as in section **3.3.5.1** and fluorescence microscopy was used to visualise the targeting and binding behaviour of the nanoparticles. **Figure 3.17** shows the fluorescence images of Panc-1 cells after 6 hours of exposure to the three types of nanoparticles.

The images showed that **Fe_3O_4-NH-RITC/CO-EPCAM** nanoparticles have greater association with the cells and perinuclear localisation compared with the control nanoparticles (**Figure 3.17a** and **3.17b**). At the same time, both controls showed some association with Panc-1 cells although it must be mentioned that the levels were lower than the specifically labelled nanoparticles (**Figure 3.17c** and **3.17d**). Fluorescence images showed that the **Fe_3O_4-NH-RITC/CO-ISO** controls were mostly distributed on the cell membrane (**Figure 3.17c**), while a small amount of **Fe_3O_4-NH-RITC/COOH** nanoparticles (**Figure 3.17d**) were localised in the perinuclear region as the specifically labelled nanoparticles.

Prolongation of incubation time showed that non-specific interactions were encouraged, however the levels of control nanoparticles associated with the cells was lower when compared with **Fe_3O_4-NH-RITC/CO-EPCAM** nanoparticles (**Figure 3.17a** and **3.17b**). In case of **Fe_3O_4-NH-RITC/COOH**, a likely explanation for the observed behaviour could be the surface charge of the nanoparticles. Other research has suggested that

carboxylic groups on nanoparticles surfaces are involved in intracellular uptake.[36-37] Therefore according to the literature electrostatic attraction may have promoted the non-specific uptake by fluid phase endocytosis. Despite these observations, the **Fe_3O_4-NH-RITC/CO-EPCAM** nanoparticles showed clear advantage for cell localisation and enhanced internalisation compared with the controls, leading to earlier and increased levels of nanoparticle delivery to the Panc-1 cells.

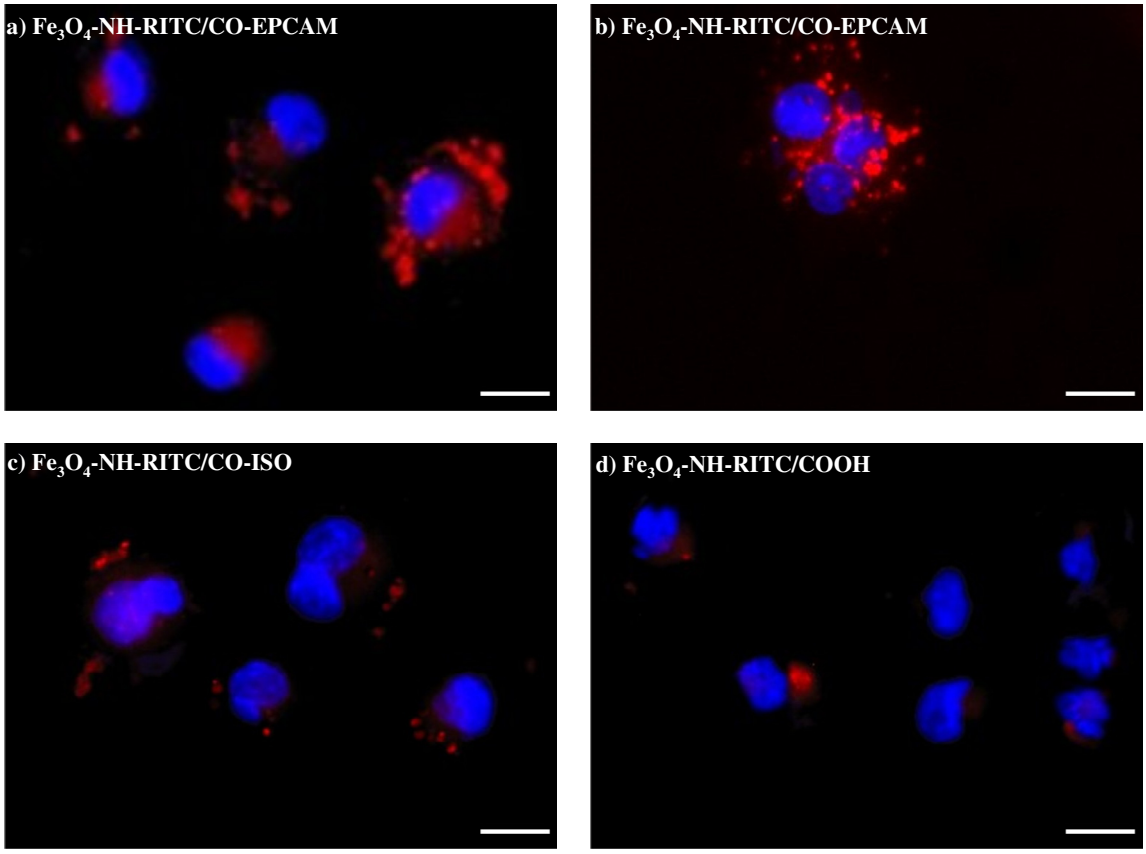

Figure 3.17 Fluorescence images of Panc-1 cells incubated for 6 hours with, a) and b) **Fe_3O_4-NH-RITC/CO-EPCAM**, c) **Fe_3O_4-NH-RITC/CO-ISO**, d) **Fe_3O_4-NH-RITC/COOH**. Detection of cell nuclei was performed by DAPI staining (blue). All nanoparticles were applied at 100 μg/mL. Scale bar represents 25 μm.

Similar results were obtained after 24 hours of incubation as evidenced in **Figure 3.18**.

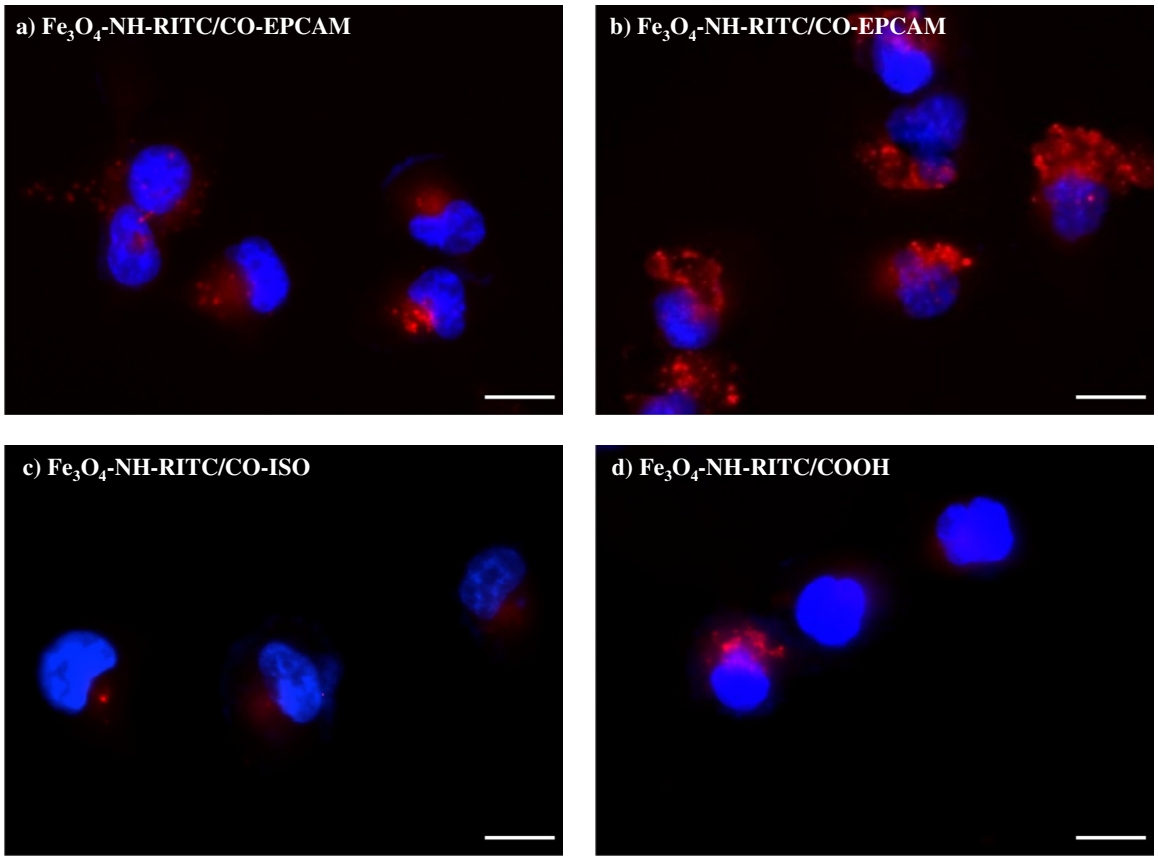

Figure 3.18 Fluorescence images of Panc-1 cells incubated for 24 hours with, a) and b) **Fe_3O_4-NH-RITC/CO-EPCAM**, c) **Fe_3O_4-NH-RITC/CO-ISO**, d) **Fe_3O_4-NH-RITC/COOH**. The cell nuclei were stained with DAPI in blue. All nanoparticles were applied at 0.1 mg/mL. Scale bar represents 25 μm.

At 24 hours the **Fe_3O_4-NH-RITC/CO-EPCAM** nanoparticles were internalised in the Panc-1 cells in greater levels (**Figure 3.18a** and **3.18b**). In comparison, the control nanoparticles are also associated with the cells (**Figure 3.18c** and **3.18d**) but the level of fluorescence associated with the cells is minimal compared with the **Fe_3O_4-NH-RITC/CO-EPCAM** nanoparticles. The control nanoparticles are thought to be internalised through non-specific endocytosis processes. Overall the cell targeting results indicate that the specific uptake of **Fe_3O_4-NH-RITC/CO-EPCAM** is highly

promoted by the interaction between the EPCAM antibody and their specific receptors present on the cancer cell surface.

3.4 Conclusions

The aim of the work presented in this chapter was to evaluate the imaging and targeting potential of the bifunctionalised **Fe_3O_4-NH_2/COOH** nanoparticles prepared and characterised in Chapter 2.

For this the **Fe_3O_4-NH_2/COOH** nanoparticles were successfully labelled with the RITC fluorescent dye and the specific antibody (EPCAM) taking advantage of the amine and carboxylic acid groups present on their surface.

The *in vitro* targeting specificity of **Fe_3O_4-NH-RITC/CO-EPCAM** nanoparticles was illustrated by fluorescence and confocal microscopy. **Fe_3O_4-NH-RITC/CO-EPCAM** demonstrated excellent ability to localise and bind the epithelial specific EPCAM receptors on the Panc-1 pancreatic cancer cells in one hour and initiated a fast internalisation of nanoparticles. However the **Fe_3O_4-NH-RITC/COOH** and **Fe_3O_4-NH-RITC/CO-ISO** nanoparticles also showed some non-specific interaction at longer exposure times. The targeting experiments showed the proof-of-concept that the antibody conjugated magnetic nanoparticles were able to selectively localise specific receptors on cancer cells with specific exemplification for pancreatic cancer.

In addition, the fluorescence imaging and targeting capability of these bifunctional nanoparticles was shown to be further complimented by the MR imaging capabilities. As expected the **Fe_3O_4-NH_2/COOH** nanoparticles influenced the signal intensity on T_2 weighted MRI images as a function of iron molar concentration. Their relaxivity values

were found to be superior to that of the commercial agent Feridex I.V. This nanoparticle system is adaptable for conjugation of any other amino containing protein or peptide which can be further used for targeting specific receptors on cancer cells.

3.5 References

1. F. M. Kievit, M. Q. Zhang, Surface Engineering of Iron Oxide Nanoparticies for Targeted Cancer Therapy, *Accounts Chem Res*, **2011**, 44, 853-862.
2. M. K. Yu, J. Park, S. Jon, Targeting Strategies for Multifunctional Nanoparticles in Cancer Imaging and Therapy, *Theranostics*, **2012**, 2, 3-44.
3. J. D. Byrne, T. Betancourt, L. Brannon-Peppas, Active targeting schemes for nanoparticle systems in cancer therapeutics, *Adv Drug Deliver Rev*, **2008**, 60, 1615-1626.
4. A. M. Wu, P. D. Senter, Arming antibodies: prospects and challenges for immunoconjugates, *Nat Biotechnol*, **2005**, 23, 1137-1146.
5. M. Arruebo, M. Valladares, A. Gonzalez-Fernandez, Antibody-Conjugated Nanoparticles for Biomedical Applications, *J Nanomater*, **2009**.
6. A. Toma, E. Otsuji, Y. Kuriu, K. Okamoto, D. Ichikawa, A. Hagiwara, H. Ito, T. Nishimura, H. Yamagishi, Monoclonal antibody A7-superparamagnetic iron oxide as contrast agent of MR imaging of rectal carcinoma, *Brit J Cancer*, **2005**, 93, 131-136.
7. J. S. Ross, J. A. Fletcher, K. J. Bloom, G. P. Linette, J. Stec, W. F. Symmans, L. Pusztai, G. N. Hortobagyi, Targeted therapy in breast cancer - The HER-2/neu gene and protein, *Mol Cell Proteomics*, **2004**, 3, 379-398.
8. H. M. Yang, C. W. Park, M. A. Woo, M. I. Kim, Y. M. Jo, H. G. Park, J. D. Kim, HER2/neu Antibody Conjugated Poly(amino acid)-Coated Iron Oxide Nanoparticles for Breast Cancer MR Imaging, *Biomacromolecules*, **2010**, 11, 2866-2872.

9. K. L. Vigor, P. G. Kyrtatos, S. Minogue, K. T. Al-Jamal, H. Kogelberg, B. Tolner, K. Kostarelos, R. H. Begent, Q. A. Pankhurst, M. F. Lythgoe, K. A. Chester, Nanoparticles functionalised with recombinant single chain Fv antibody fragments (scFv) for the magnetic resonance imaging of cancer cells, *Biomaterials*, **2010**, 31, 1307-1315.

10. L. L. Yang, H. Mao, Y. A. Wang, Z. H. Cao, X. H. Peng, X. X. Wang, H. W. Duan, C. C. Ni, Q. G. Yuan, G. Adams, M. Q. Smith, W. C. Wood, X. H. Gao, S. M. Nie, Single Chain Epidermal Growth Factor Receptor Antibody Conjugated Nanoparticles for in vivo Tumor Targeting and Imaging, *Small*, **2009**, 5, 235-243.

11. G. Baio, M. Fabbi, S. Salvi, D. de Totero, M. Truini, S. Ferrini, C. E. Neumaier, Two-step in vivo tumor targeting by biotin-conjugated antibodies and superparamagnetic nanoparticles assessed by magnetic resonance imaging at 1.5 T, *Mol Imaging Biol*, **2010**, 12, 305-315.

12. Y. M. Huh, Y. W. Jun, H. T. Song, S. Kim, J. S. Choi, J. H. Lee, S. Yoon, K. S. Kim, J. S. Shin, J. S. Suh, J. Cheon, In vivo magnetic resonance detection of cancer by using multifunctional magnetic nanocrystals, *J Am Chem Soc*, **2005**, 127, 12387-12391.

13. E. A. Schellenberger, R. Weissleder, L. Josephson, Optimal modification of annexin V with fluorescent dyes, *Chembiochem*, **2004**, 5, 271-274.

14. G. T. Hermanson. *Bioconjugate techniques*, **1996**, Academic Press, San Diego.

15. J. M. Davis. *Basic cell culture : a practical approach*, **2002**, Oxford University Press, New York.

16. C. F. Jones, D. W. Grainger, In vitro assessments of nanomaterial toxicity, *Adv Drug Deliver Rev*, **2009**, 61, 438-456.

17. M. R. Pickard, D. M. Chari, Robust Uptake of Magnetic Nanoparticles (MNPs) by Central Nervous System (CNS) Microglia: Implications for Particle Uptake in Mixed Neural Cell Populations, *Int J Mol Sci*, **2010**, 11, 967-981.

18. N. Lewinski, V. Colvin, R. Drezek, Cytotoxicity of nanoparticles, *Small*, **2008**, 4, 26-49.

19. B. Ankamwar, T. C. Lai, J. H. Huang, R. S. Liu, M. Hsiao, C. H. Chen, Y. K. Hwu, Biocompatibility of Fe3O4 nanoparticles evaluated by in vitro cytotoxicity assays using normal, glia and breast cancer cells, *Nanotechnology*, **2010**, 21.

20. T. K. Jain, M. K. Reddy, M. A. Morales, D. L. Leslie-Pelecky, V. Labhasetwar, Biodistribution, clearance, and biocompatibility of iron oxide magnetic nanoparticles in rats, *Mol Pharm*, **2008**, 5, 316-327.

21. S. J. H. Soenen, M. De Cuyper, Assessing iron oxide nanoparticle toxicity in vitro: current status and future prospects, *Nanomedicine-Uk*, **2010**, 5, 1261-1275.

22. H. Peng, X. Zhang, Y. Wei, W. Liu, S. Li, G. Yu, X. Fu, T. Cao, X. Deng, Cytotoxicity of Silver Nanoparticles in Human Embryonic Stem Cell-Derived Fibroblasts and an L-929 Cell Line, *J Nanomater*, **2012**, 2012, 1-9.

23. T. Cao, K. Lu, X. Fu, B. C. Heng, Differentiated fibroblastic progenies of human embryonic stem cells for toxicology screening, *Cloning Stem Cells*, **2008**, 10, 1-10.

24. D. Fong, M. Steurer, P. Obrist, V. Barbieri, R. Margreiter, A. Amberger, K. Laimer, G. Gastl, A. Tzankov, G. Spizzo, Ep-CAM expression in pancreatic and

ampullary carcinomas: frequency and prognostic relevance, *J Clin Pathol*, **2008**, 61, 31-35.

25. P. T. Went, A. Lugli, S. Meier, M. Bundi, M. Mirlacher, G. Sauter, S. Dirnhofer, Frequent EpCam protein expression in human carcinomas, *Hum Pathol*, **2004**, 35, 122-128.

26. L. J. Harris, E. Skaletsky, A. McPherson, Crystallographic structure of an intact IgG1 monoclonal antibody, *J Mol Biol*, **1998**, 275, 861-872.

27. P. Gillis, S. H. Koenig, Transverse Relaxation of Solvent Protons Induced by Magnetized Spheres - Application to Ferritin, Erythrocytes, and Magnetite, *Magnet Reson Med*, **1987**, 5, 323-345.

28. M. A. Funovics, B. Kapeller, C. Hoeller, H. S. Su, R. Kunstfeld, S. Puig, K. Macfelda, MR imaging of the her2/neu and 9.2.27 tumor antigens using immunospecific contrast agents, *Magn Reson Imaging*, **2004**, 22, 843-850.

29. S. Chen, L. J. Wang, S. L. Duce, S. Brown, S. Lee, A. Melzer, S. A. Cuschieri, P. Andre, Engineered Biocompatible Nanoparticles for in Vivo Imaging Applications, *J Am Chem Soc*, **2010**, 132, 15022-15029.

30. L. E. W. LaConte, N. Nitin, O. Zurkiya, D. Caruntu, C. J. O'Connor, X. P. Hu, G. Bao, Coating thickness of magnetic iron oxide nanoparticles affects R-2 relaxivity, *J Magn Reson Imaging*, **2007**, 26, 1634-1641.

31. Y. X. J. Wang, S. M. Hussain, G. P. Krestin, Superparamagnetic iron oxide contrast agents: physicochemical characteristics and applications in MR imaging, *Eur Radiol*, **2001**, 11, 2319-2331.

32. M. Balzar, M. J. Winter, C. J. de Boer, S. V. Litvinov, The biology of the 17-1A antigen (Ep-CAM), *J Mol Med-Jmm*, **1999**, 77, 699-712.

33. A. V. Salnikov, A. Groth, A. Apel, G. Kallifatidis, B. M. Beckermann, A. Khamidjanov, E. Ryschich, M. W. Buchler, I. Herr, G. Moldenhauer, Targeting of cancer stem cell marker EpCAM by bispecific antibody EpCAMxCD3 inhibits pancreatic carcinoma, *J Cell Mol Med*, **2009**, 13, 4023-4033.

34. R. E. Serda, N. L. Adolphi, M. Bisoffi, L. O. Sillerud, Targeting and cellular trafficking of magnetic nanoparticles for prostate cancer Imaging, *Mol Imaging*, **2007**, 6, 277-288.

35. S. Bhattacharyya, R. Bhattacharya, S. Curley, M. A. McNiven, P. Mukherjee, Nanoconjugation modulates the trafficking and mechanism of antibody induced receptor endocytosis, *P Natl Acad Sci USA*, **2010**, 107, 14541-14546.

36. V. Mailander, M. R. Lorenz, V. Holzapfel, A. Musyanovych, K. Fuchs, M. Wiesneth, P. Walther, K. Landfester, H. Schrezenmeier, Carboxylated superparamagnetic iron oxide particles label cells intracellularly without transfection agents, *Molecular Imaging and Biology*, **2008**, 10, 138-146.

37. X. Y. Shi, T. P. Thomas, L. A. Myc, A. Kotlyar, J. R. Baker, Synthesis, characterization, and intracellular uptake of carboxyl-terminated poly(amidoamine) dendrimer-stabilized iron oxide nanoparticles, *Phys Chem Chem Phys*, **2007**, 9, 5712-5720.

Chapter 4

Self-assembled structures of SPIONs and bioinspired amphiphilic polyoxazolines

4.1 Introduction

A major challenge in cancer diagnosis today is the detection limit of the current medical imaging technologies which does not allow for identification of cancers at the early stage, more importantly at the molecular or cellular level. Magnetic resonance imaging (MRI) is a non-invasive medical imaging technique which offers the most powerful contrast for soft tissues. For tumour detection MRI has to be used in combination with contrast agents. Biocompatible superparamagnetic iron oxide nanoparticles (SPIONs) have emerged as feasible contrast agents for MRI and some formulations are already clinically used for detection of liver tumours or abnormal lymph nodes.[1] However, the current MRI agents need to be optimised in order to achieve early stage diagnosis of other tumour types. The optimisation should include: synthesis of monodisperse and crystalline SPIONs, biocompatible and stealth coatings for improved colloidal stability and circulation times, incorporation of targeting ligands for selective and sensitive localisation of tumours.[2-5] Research in the area of iron oxide nanoparticles synthesis has been ongoing for many years and SPIONs with improved quality (monodisperse, crystalline and with high magnetisation) were achieved using the high temperature decomposition of iron-organic ligand precursors.[6-9] The monodisperse SPIONs synthesised using these methods are hydrophobic and can only be dispersed in organic solvents such as toluene or hexane. Therefore the SPIONs can not be directly introduced

in biological systems; before this can take place the surface of the SPIONs has to be coated with a protective hydrophilic layer.[10] From this point of view, polymeric micelles are anticipated as suitable structures with a unique core-shell architecture that can offer efficient surface coating to hydrophobic SPIONs. The hydrophobic core of the polymeric micelles can encapsulate and protect the hydrophobic SPIONs, while the hydrophilic shell can carry bioactive molecules, drugs or fluorescent tags for multifunctional applications (combined optical imaging with MRI and targeted drug delivery). Encapsulation of SPIONs within the hydrophobic micellar core has the advantage of avoiding direct exposure and interaction of the SPIONs surface with blood proteins, providing longer circulation blood time. Poly(ethylene glycol) (PEG) based phospholipids (**Figure 4.1a**) are commonly employed for transferring hydrophobic SPIONs to hydrophilic aqueous media.[11-14] However, these structures are usually expensive and PEG has been shown to have the tendency to auto-oxidize and to loose its protein resistant ability over time.[15]

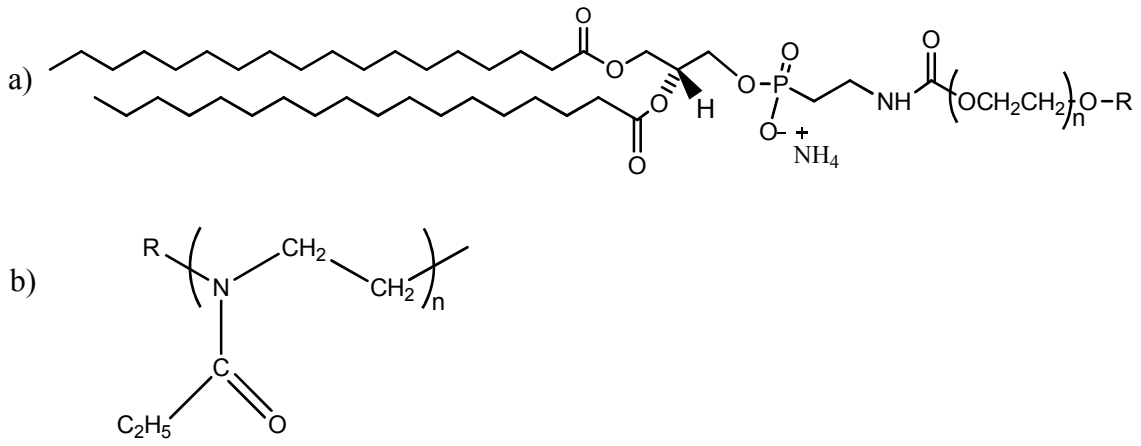

Figure 4.1 Polymeric structure of a) poly(ethylene glycol) based phospholipids and b) poly(2-ethyl-2-oxazoline).

Poly(2-oxazoline) based polymers have emerged as alternatives to PEG for applications in the biomedical field because they combine interesting properties such as hydrophilicity, biocompatibility and versatile end-group chemistry.[16-17] Hydrophilic poly(2-ethyl-2-oxazoline) (PEtOX, **Figure 4.1b**) is approved by the Food and Drug Administration (FDA) as a food additive and was shown to exhibit stealth and protein repellent properties comparable to PEG.[18-20] Polyoxazolines can be regarded as analogues of polypeptides and because of this structural similarity they are considered as bioinspired polymers.[16,21-22] Due to their stealth capabilities various combinations of amphiphilic block-copolymers containing poly(2-oxazolines) have been developed for drug delivery purposes (**Figure 4.2**).

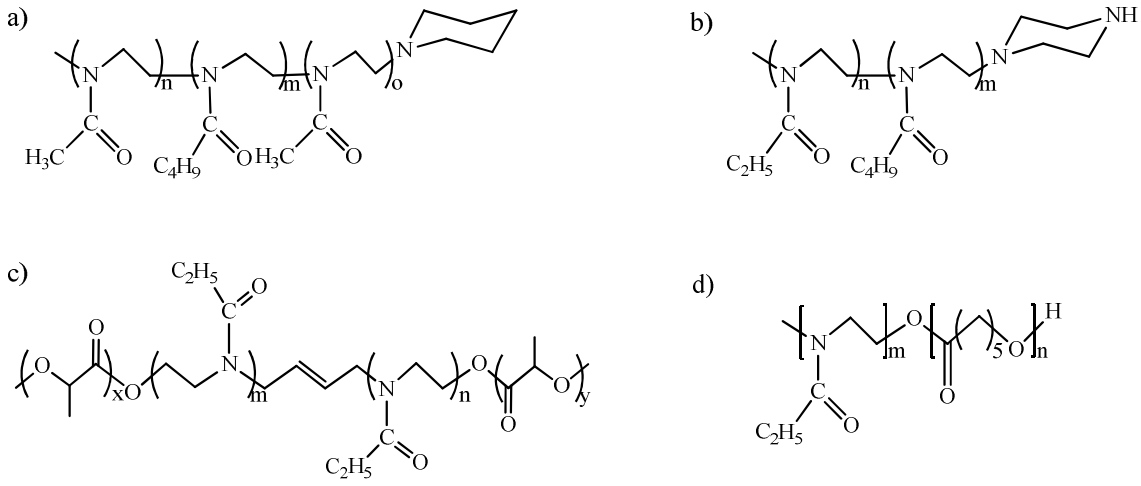

Figure 4.2 Polyoxazoline based polymers a) Methyl-poly(2-methyl-2oxazoline)-*b*-poly(2-buthyl-2-oxazoline)-b-poly(2-methyl-2-oxazoline)-piperidine triblock copolymer; b) Methyl-poly(2-ethyl-2oxazoline)-*b*-poly(2-buthyl-2-oxazoline)-piperazine diblock copolymer; c) poly(L-lactide)-*b*-poly(2-ethyl-2-oxazoline)-*b*-poly(L-lactide); d) poly(2-ethyl-2-oxazoline)-*b*-poly(ε-caprolactone) diblock copolymers.

Luxenhofer *et al.* developed well-defined amphiphilic di- and triblock copolymers based on polyoxazolines (**Figure 4.2a and 4.2b**) for encapsulation of the hydrophobic paclitaxel anti-cancer drug. The authors showed that the prepared micellar structures are stable, non-toxic, non-immunogenic and have high drug loading capabilities.[23] Other examples include systems based on triblock poly(L-lactide)-*b*-poly(2-ethyl-2-oxazoline)-*b*-poly(L-lactide) micelles (**Figure 4.2c**) as carriers of doxorubicin or poly(ε-caprolactone)-poly(2-oxazoline) micelles (**Figure 4.2d**) carrying paclitaxel.[24-25]

PEtOX has been studied as a potential solubilisation agent for fullerene C_{60}. Tong *et al.* prepared C_{60}-PEtOX complexes and studied their physicochemical properties along with their superoxide scavenging activities (**Figure 4.3**).[26]

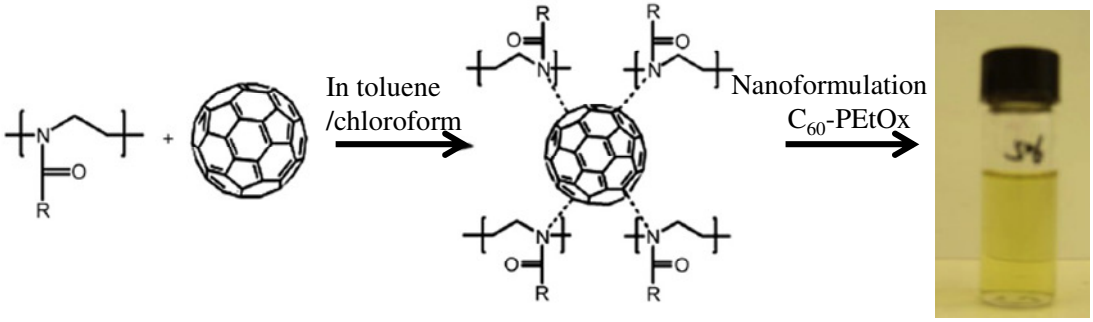

Figure 4.3 Formulation of C_{60}-Polyoxazoline and proposed charge-transfer complex formation between fullerene and polymer. Figure adapted from ref. 26

The authors showed that C_{60}-polyoxazoline complexes are non-toxic, neuronal cell permeable, superoxide scavenging antioxidants that could be promising candidates for the treatment of brain-related diseases associated with increased levels of superoxide.

The potential use of polyoxazoline based polymers as stabilising and functional coatings for inorganic materials has only recently started to be investigated. Volet *et al.* developed a method to anchor tailored amphiphilic poly(2-oxazoline)s on the surface of

silica nanoparticles using host–guest associations.[27] The group used adsorbed polymer bearing cyclodextrin units as a host layer on silica surface before complexation with hydrophobically end-capped poly(2-methyl-2-oxazoline) (**Figure 4.4**).

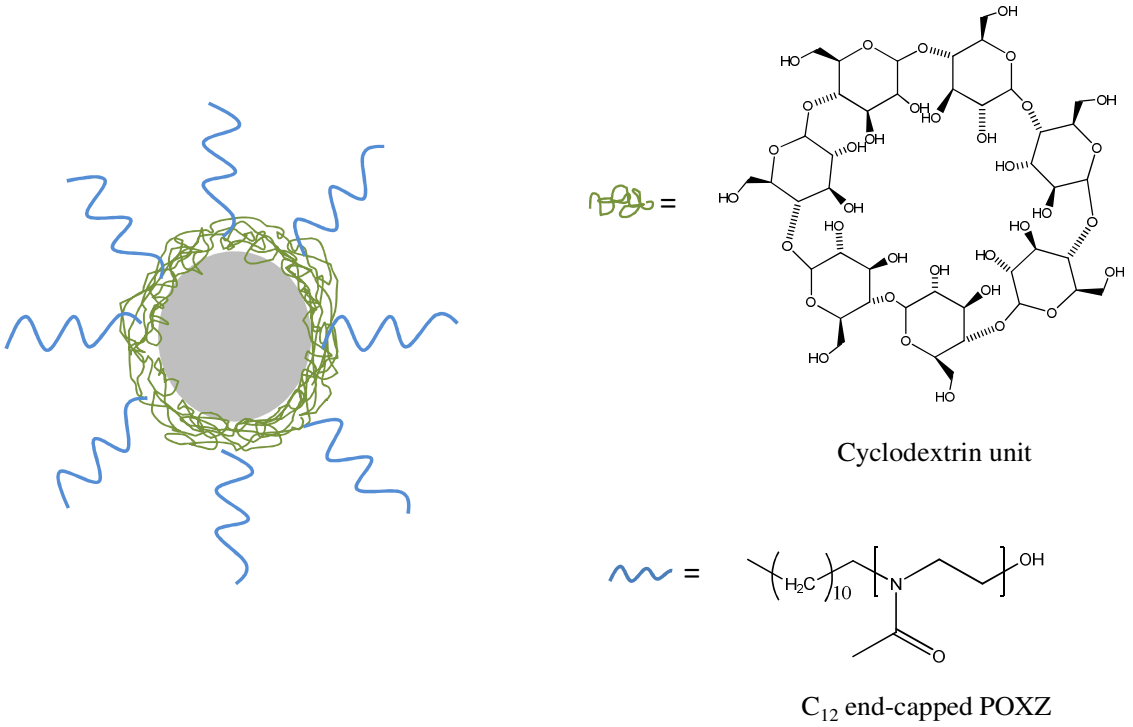

Figure 4.4 Silica nanoparticles (in grey) coated by poly(cyclodextrin) layer (in green) and POXZ–C_{12} layer (in blue). The figure was adapted from ref. 27

To the best of our knowledge there are no reported SPIONs surface coated with poly(2-oxazoline)s.

The work in this chapter describes the synthesis of monodisperse SPIONs (Fe_3O_4) and their surface modification chemistry using amphiphilic poly(2-ethyl-2-oxazoline)s.

A high-temperature decomposition method was used to prepare monodisperse SPIONs of 8 nm diameter in the presence of surfactant molecules such as oleic acid. A C_{16} alkyl end-capped poly(2-ethyl-2-oxazoline) amphiphilic polymer with hydroxyl functional group was synthesised and further modified with carboxylic acid functionalities. The

cytotoxicity of the synthesised amphiphilic polyoxazolines was evaluated before their application as coating materials for hydrophobic SPIONs. The carboxyl-functional polymer was used to transfer, solubilise and stabilise the hydrophobic SPIONs in aqueous solutions. Different ratios of SPIONs and polymer were studied to evaluate the influence on the size and the stability of the formed multifunctional magneto-micellar structures (**MMMs**). The colloidal stability of the **MMMs** was evaluated in media similar to physiological conditions with salt concentrations up to a few hundred mM and pH range between 5 and 9. Both of these are typical conditions used in biological applications. To provide fluorescence imaging capabilities to the **MMMs** their surface was modified with fluorescent dye molecules. The carboxylic acid functional groups present on the surface of fluorescently labelled magneto-micelles allowed for covalent conjugation with bioactive molecules (proteins and antibodies). Quantification of the proteins and antibodies conjugated to the surface of the **MMMs** was estimated using a standard Bradford protein assay method. The cytotoxicity of fluorescent and non-fluorescent **MMMs** was assessed with different cells lines using the standard cell proliferation assay MTS. The selective uptake and the targeting capabilities of the fluorescent **MMMs** conjugated with specific antibodies was evaluated using live cell confocal laser scanning microscopy with pancreatic cancer cells. Their MRI contrasting properties were assessed by relaxation time measurements with specific focus on the T_2 relaxation time.

4.2 Experimental Section

4.2.1 Materials

Iron(III) acetylacetonate ($Fe(acac)_3$, ≥ 99.9% trace metals basis), 1,2-hexadecanediol (90%), oleic acid (≥ 99%), oleylamine (70%), benzyl ether (98%), 2-ethyl-2-oxazoline (≥ 99%), hexadecyl methanesulfonate salt, chloroform anhydrous ($CHCl_3$, (≥ 99%), *N,N*-Dimethylformamide anhydrous (DMF, 99.8%), succinic anhydride (≥ 99%), triethylamine (≥ 99%), phosphotungstic acid solution (PTA solution, 10%, w/v), albumin from bovine serum (BSA, ≥ 98%), cytochrome C from equine heart (CytC, ≥ 95%), anti-rabbit IgG (whole molecule) antibody produced in goat (IgG), phosphate buffered saline tablets (PBS, 10 mM phosphate buffer, 2.7 mM potassium chloride and 137 mM sodium chloride, pH 7.4), Bradford reagent (for 1-1400 µg/ml protein), Corning Spin-X UF 20 MWCO 5kDa, Corning Spin-X UF 20 MWCO 30kDa, Corning Spin-X UF 20 MWCO 100 kDa, Vivaspin 20 centrifugal concentrator MWCO 300 kDa were purchased from Sigma Aldrich. Octadecyl rhodamine B chloride (Rh) was purchased from Life Technologies. Dialysis membranes with MWCO of 1000 Da, 50 KDa and 300 KDa were purchased from Medicell International. 3-(4,5-Dimethylthiazol-2-yl)-5-(3-carboxymethoxyphenyl)-2-(4-sulfophenyl)-2H-tetrazolium (MTS assay) was purchased from Biomedica, Vienna, Austria. All aqueous solutions were prepared using ultrapure water Milli-Q (Millipore, resistivity 18.2 MΩ.cm at 25°C). All chemicals were used as received without any further purification.

4.2.2 Synthetic methods

4.2.2.1 Synthesis of monodisperse Superparamagnetic Iron Oxide Nanoparticles (SPIONs)

Hydrophobic SPIONs were synthesized by thermo-decomposition of iron triacetyl acetonate ($Fe(acac)_3$) in the presence of oleic acid and oleylamine using a modified procedure published by Sun *et al.*[6] A mixture of $Fe(acac)_3$ (3.52 g, 10 mmol), 1,2-hexadecanediol (12.92 g, 50 mmol), oleic acid (8.47 g, 9.5 mL, 30 mmol), oleylamine (8.02 g, 9.85 mL, 30 mmol) and benzyl ether (50 mL) was charged in a 3 neck round bottom flask. The flask was degassed three times using "evacuation-filling with nitrogen" cycles ending with filling with nitrogen. The mixture was heated at 2°/minute to 200 °C and maintained at this temperature for 2 hours. Then the temperature was increased to reflux (298 °C) and kept for another hour. During the whole reaction, the mixture was kept under nitrogen. The black coloured mixture was cooled down to room temperature. Under ambient conditions, ethanol (200 mL) was added to the mixture and the black material was precipitated and separated using centrifugation. The black product was dissolved in THF (100 mL) and centrifuged at 8000 rpm for 10 min to remove any undispersed residue. The nanoparticles were again precipitated with ethanol (200 mL), centrifuged (8000 rpm, 10 min) and finally redispersed in THF to a concentration of 5 mg/mL. The nanoparticles were stored at 4 °C until further use.

4.2.2.2 Synthesis of hydroxyl functional amphiphilic polyoxazoline polymers

Cationic ring-opening polymerisation was employed to synthesise amphiphilic poly(2-ethyl-2-oxazoline) (PEtOX) polymeric structures with end-functional hydroxyl groups. The amphiphilic polymer structure comprised a C_{16} alkyl chain which is the

hydrophobic segment and the PEtOX polymer backbone as the hydrophilic segment containing an end-functional hydroxyl group.

Hexadecyl methanesulfonate initiator (1.6 g, 0.005 mol) and 2-ethyl-2-oxazoline (10g, 0.1 mol) were dispersed and mixed in 8 mL anhydrous chloroform in a Schlenk flask under nitrogen and then sealed with rubber septum. The reaction mixture was heated to 75 °C and left under stirring overnight. The polymerisation was quenched by hydroxyl end-capping method using 20 mL of methanolic KOH (5%) for 3 hours, under stirring, at room temperature. Then the reaction mixture was concentrated to dryness using rotary evaporation. The product was extracted with chloroform from the formed solid followed by filtration. Subsequently, the polymer was purified three times by precipitation from chloroform into cooled diethyl ether. The sample was denoted **Polymer 1**.

This experiment was performed by Dr. Erol Hasan at the University of Liverpool, Centre for Materials Discovery.

4.2.2.3 Synthesis of carboxylic acid functional amphiphilic polyoxazoline polymers

Amphiphilic polyoxazoline polymer containing carboxylic acid end-group was synthesised using an esterification reaction with succinic anhydride.[28] **Polymer 1** (800 mg, 0.17 mmol hydroxyl groups) was dissolved in anhydrous DMF (5 mL) under nitrogen atmosphere. Succinic anhydride (178 mg, 1.7 mmol) and triethylamine (0.2 mL, 1.7 mmol) dissolved in anhydrous DMF (5 mL) were added to the polymer solution. The reaction mixture was stirred for 24 hours at 45 °C under nitrogen. The modified polymer was purified three times by precipitation from DMF into cooled diethyl ether followed by 24 hours dialysis into methanol. The sample was denoted as **Polymer 1S**.

4.2.2.4 Self-assembly of SPIONs and bioinspired amphiphilic polyoxazoline polymers into multifunctional-magneto-micelles (MMMs)

The formation of multifunctional-magneto-micellar structures (**MMMs**) between hydrophobic SPIONs and amphiphilic PEtOX polymers was performed using a solvent exchange method. The size and stability of the micellar structures could be controlled by varying the weight ratio of polymer to SPIONs and are summarised in **Table 4.1** in the Results section.

In a typical experiment, for weight ratio of polymer to SPIONs 10:1, hydrophobic SPIONs dispersed in THF (1 mg/mL, 1 mL) were added dropwise to a solution of the **Polymer 1S** dispersed in water (1 mg/mL, 10 mL) while sonicating at room temperature. Any residues of THF were removed by dialysis against deionised water or phosphate buffered saline (PBS) at room temperature for 48 hours (molecular weight cut off MWCO 50 kDa). After dialysis the **MMMs** solutions was stored at 4 °C until further use.

Seven samples were prepared using different weight ratio of polymer to SPIONs and were denoted **MMM-1**, **MMM-2**, **MMM-3**, **MMM-4**, **MMM-5**, **MMM-6** and **MMM-7**.

4.2.2.5 Synthesis of fluorescently labelled magneto-micelles

The preparation of fluorescently labelled **MMMs** followed the same assembly procedure as before except that a mixture of SPIONs (1 mg) and a fluorescent dye (Octadecyl Rhodamine B, Rh, 0.01 mg) in 1 mL THF/DMSO was added to the **Polymer 1S** solution in deionised water (1 mg/mL, 10 mL). The mixed-assembled structures were

purified by dialysis to remove the organic solvents. The sample was denoted as **Rh-MMM**.

4.2.2.6 Bioconjugation of Rh-MMM with proteins and antibody molecules

Bioactive molecules such as proteins and antibodies were covalently conjugated to the **Rh-MMM** using the carbodiimide coupling chemistry between the carboxylic acid groups present on the coating polymer and the amino groups in the lysine residues of protein structures.

A 2.5 mL aliquot of **Rh-MMMs** in PBS (0.75 mg/mL, 1.7×10^{12} micelles/mL, 2.8×10^{-12} mol micelles/mL) was activated for 5 minutes with EDC (3 times molar excess with respect to the added protein) and for 10 minutes with sulfo-NHS (3 times molar excess with respect to the added protein) at room temperature. Then a 100 µL aliquot of serum albumin (BSA) or Cytochrome C (CytC) in PBS (2 mg/mL) or non-specific immnunoglobulin G (IgG) in PBS (3 mg/mL) was added to the activated micelles. The mixture was allowed to react at room temperature for 4 hours. To remove the unreacted free BSA, CytC or IgG the reaction mixture was purified by dialysis against PBS and stored at 4 °C until further use. **Rh-MMMs** conjugated with BSA or CytC or IgG were denoted as **Rh-MMM-BSA**, **Rh-MMM-CytC** and **Rh-MMM-IgG**.

Conjugation of **Rh-MMMs** with a specific antibody, namely CA19.9, was carried out using a maximum of 8 µg antibody per conjugation reaction due to a availability of this antibody. The sample was denoted as **Rh-MMM-CA19.9**.

4.2.2.7 Quantification of protein molecules conjugated to the Rh-MMMs

The concentration of protein/antibody molecules conjugated to the **Rh-MMMs** was estimated using the Bradford assay. After the conjugation reaction (see **section 4.2.2.6**)

any unreacted BSA, CytC and IgG were separated using centrifugal concentrators with MWCO which allowed the molecule filtration: 30 kDa, 100 kDa and 300 kDa. The filtrates from 3 washing steps containing the unreacted molecules were collected, concentrated and mixed with Bradford reagent to give a blue solution with a maximum absorbance at 595 nm. A calibration curve of known protein concentrations was plotted and the concentration of unreacted BSA, CytC, IgG was determined. The concentration of BSA, CytC, IgG conjugated on the nanoparticles was determined by difference from the initial concentration. The conjugation yield was calculated as:

$$Conjugation\ (\%) = \frac{Conjugated\ protein\ concentration}{Initial\ protein\ concentraion} \times 100$$

Each reaction was performed in triplicate and the average value with standard deviation is reported.

4.2.3 Characterisation methods

4.2.3.1 Thermogravimetric Analysis (TGA)

TGA was carried out using a TA instrument Q600 thermal balance. Typically 2-5 mg of SPIONs or freeze-dried **MMMs** from deionised water were heated to 600 °C at 10 °C/min in air and kept at 600 °C for 30 min. TGA was used for determination of the nanoparticle composition and surface coverage with small organic ligands or polymeric chains.

4.2.3.2 Powder X-ray Diffraction (PXRD)

Powder X-ray diffraction patterns of the synthesised SPIONs sealed in a 0.5 mm glass capillary were collected on a Bruker D8 diffractometer using Mo Kα radiation (λ = 0.7107 Å). The PXRD data was used to identify the iron oxide phase composition and to confirm the size distribution of the nanoparticles (X'Pert Highscore Plus version 2.0). The particle size was calculated using the Scherrer equation:

$$\tau = \frac{K\lambda}{\beta cos\theta}$$

Where τ is the particle size, β the line broadening at half the maximum intensity (FWHM), k the shape factor (k=0.9), λ the x-ray wavelength (Mo, λ = 0.7107 Å) and θ the Bragg diffraction angle.

4.2.3.3 Transmission Electron Microscopy (TEM)

TEM images were recorded using a FEI Tecnai G2 Spirit BioTWIN instrument with a W filament and a SIS Megaview III digital camera, operating at 100 kV. The hydrophobic SPIONs dispersed in THF (50 µL sample) were deposited onto a carbon coated 300 mesh copper grid. The grids were then allowed to dry in air prior to imaging.

In case of magneto-micelles, the polyoxazoline shell was stained for TEM imaging using a 2% phosphotungstic acid solution (PTA) during sample preparation. The polyoxazoline coated sample dispersed in water was deposited on the TEM grid. The excess water was wicked with filter paper and an aliquot of 50 µL of 2% PTA was deposited on the grid. The grid was allowed to dry overnight in air prior to imaging. The polyoxazoline shell interacted with the PTA stain and gave a dark grey contrast on the TEM image as previously shown for polyamide type polymers. For a full description of the TEM staining technique see ref. 29 and 30.

The size distribution of the nanoparticles was derived from TEM images using ImageJ software from 200 measurements.

4.2.3.4 Fourier Transform Infrared spectroscopy (FTIR)

FTIR spectra were recorded using a Bruker Tensor 27 Spectrometer. SPIONs samples were analysed as powder (precipitated and dried from THF dispersions). Polymer samples were first dissolved in chloroform at 10 mg/mL and then deposited onto a KBr plate to form a uniform layer after solvent evaporation. For each sample, 100 scans in the region from 400 to 4000 cm^{-1} with a resolution of 4 cm^{-1} were accumulated. Spectra were recorded and evaluated with OPUS/MAP version 4.0 software.

4.2.3.5 Nuclear Magnetic Resonance (NMR)

All ^{1}H-NMR spectra of polymer solutions were recorded using a Bruker Avance NMR spectrometer (resonance frequency 400MHz ^{1}H). DMSO-d_6 and $CDCl_3$ were used as solvents. The polymer composition and number average molecular weight (M_n) were calculated using the intensity ratio of the initiator signal to the signal of the monomer

units of the polymer. The NMR measurements were performed by Dr. Erol Hasan at the University of Liverpool, Centre for Materials Discovery.

4.2.3.6 Gel Permeation Chromatography (GPC)

The polymer samples were dissolved (2 mg/mL) in a mixture of THF/triethylamine (97.5/2.5, v/v) and filtered using 0.22 μm PTFE filters prior to GPC analysis. Molecular weights and molecular weight distributions were measured using a Viscotek TDA-302 triple-detection GPC equipped with two ViscoGel HHR-N columns and a guard column with a mobile phase mixture of THF/triethylamine (97.5/2.5, v/v) at 35 °C and a flow rate of 1 mL/min. The GPC measurements were performed by Dr. Erol Hasan at the University of Liverpool, Centre for Materials Discovery.

4.2.3.7 Measurements of magnetic properties

Magnetic measurements were performed in a Quantum Design MPMS XL Superconducting Quantum Interference Device (SQUID) magnetometer using the system DC measurement capabilities. Milligram quantities of the sample were placed in a gelatine capsule. Magnetisation measurements were made at room temperature by varying fields over a +1T to -1T range. The magnetic measurements were performed by Dr. Pavel Borisov at the University of Liverpool, Department of Chemistry.

4.2.3.8 Dynamic Light Scattering (DLS)

The hydrodynamic diameters of SPIONs and **MMMs** samples were measured using a Malvern Zetasizer Nano ZS equipped with a helium laser at a wavelength of 633 nm. 1 mL sample was used for each measurement. Scattered light was collected at a fixed angle of 173° and measurements were performed at 25 °C. The intensity-average

hydrodynamic diameters reported are obtained from 3 independent measurements; for each measurement at least 20 repeat runs were used.

4.2.3.9 Zeta potential

The zeta potential of the **MMMs** samples dispersed in deionised water or buffers were measured using a Malvern Zetasizer Nano ZS equipped with a helium laser 633 nm wavelength. An aliquot of 1 mL sample was used for each the measurement. The measurements were performed at 25 °C. The zeta potential values reported are obtained from 3 independent measurements; for each measurement at least 50 repeat runs were used.

4.2.3.10 Fluorescence spectroscopy

Fluorescence spectra were recorded on a Perkin Elmer LS 55 fluorescence spectrometer. All measurements were carried out at 25 °C using 4 mL aliquots of sample. The spectra of the **Rh-MMM** micellar structures were recorded from 590 to 700 nm using an excitation wavelength of 565 nm. Slit widths were set at 10 and 20 nm for the excitation and emission monochromators respectively.

4.2.3.11 Ultraviolet–visible spectroscopy (UV/Vis)

Absorbance spectra were recorded on a Perkin Elmer 650 S Spectrophotometer. All measurements were carried out at 25 °C using 4 mL aliquots of sample. The absorbance spectra of the fluorescently labelled **Rh-MMM** structures were recorded from 500 to 650 nm. The absorbance values for the Bradford assay-protein complexes were recorded at 595 nm.

4.2.3.12 *In vitro* cytotoxicity evaluation of synthesised polymers and Rh-MMM using pancreatic cancer cells

Viability of cells in the presence of the synthesised polymers was examined using the MTS assay. This cell viability test is based on the cleavage of the tetrazolium salt MTS 3-(4,5-dimethylthiazol-2-yl)-5-(3-carboxymethoxyphenyl)-2-(4-sulfophenyl)-2H-tetrazolium by mitochondrial dehydrogenases in metabolically active cells.

SUIT-2 and MiaPaca cells, derived from human pancreatic carcinoma, were seeded into 96-well plates at 1500 and 3000 cells/well in a final volume of media of 100 μL/well. After 24 h incubation at 37˚C, polymer or **Rh-MMM** samples in media were added to the cells at different concentrations. At 48 hours, the media was removed and MTS assay in media at 1:10 dilution was added to each well. After 2 hours incubation at 37 °C the absorbance was read at 450 nm. Values were corrected using media blank readings. Experiments were performed in triplicate using 8 wells for each condition. The cytotoxicity experiments were performed by Mr. Paul Sykes at the Liverpool Cancer Research UK Centre, Department of Molecular and Clinical Cancer Studies.

4.2.3.13 Cell labelling using of fluorescent Rh-MMM

Cell labelling experiments were carried out to evaluate the fluorescence imaging capabilities of the Rh-MMM magneto-micelles. BxPC-3 cells, derived from human pancreatic cancer, were seeded into 4 chamber glass bottom plates at 4500 cells/chamber in a final volume of media of 1.5 mL/chamber. After 24 h incubation at 37˚C, the **Rh-MMM** sample was added to the cells at different concentrations (0.5 and 0.125 mM Fe, corresponding to a theoretical Rh dye concentration of 340 and 85 nM). After 12 hours of incubation with the nanoparticles, the live cells were imaged using a

Carl Zeiss 710 confocal scanning laser microscope. The cell labelling experiments were performed by Mr. Paul Sykes at the Liverpool Cancer Research UK Centre, Department of Molecular and Clinical Cancer Studies.

4.2.3.14 Antibody cell targeting experiments using pancreatic cancer cells

BxPC-3 cells expressing the CA19.9 antigen were used to evaluate the targeting capabilities of the antibody magneto-micelles conjugates. BxPC-3 cells were cultured into 4 chamber glass bottom plates at 4500 cells/chamber in a final volume of media of 1.5 mL/chamber. After 24 h incubation at 37˚C, the **Rh-MMM-CA19.9**, **Rh-MMM-ISO** and **Rh-MMM** samples were added to the cells at 0.1 mM Fe concentration (corresponding to a theoretical Rh dye concentration of 68 nM). The cells were incubated with the nanoparticles for an 18 hours period during which confocal microscopy slices were taken every 2 minutes, using a Carl Zeiss 710 confocal scanning laser microscope. The antibody targeting experiments were performed by Mr. Paul Sykes at the Liverpool Cancer Research UK Centre, Department of Molecular and Clinical Cancer Studies.

4.2.3.15 Magnetic Resonance Imaging (MRI) capability of Rh-MMM

To evaluate the MRI contrasting property of the magneto-micelles, serial dilutions of the Rh-MMM sample were prepared in deionised water at concentrations of 0.05, 0.075, 0.01 and 0.15 mM Fe. The samples were aliquoted in eppendorf tubes (300 μL) and placed in a polystyrene MRI holder. The samples were then scanned and images were acquired using a Bruker Avance III console and gradient system interfaced to a Magnex Scientific 7 T horizontal bore magnet at a ^{1}H resonant frequency of 300 MHz. T_2 relaxation time was calculated from a set of RARE[60] images acquired with TR=5000 ms

and TE values of 11, 33, 55 and 77 ms. The MRI measurements were carried out by Ms. Karen Davies at the Department of Imaging Science and Biomedical Engineering, University of Manchester.

4.2.3.16 Statistical analysis

Each cytotoxicity experiment was performed in triplicate. Data are presented as means ± standard deviation. Differences between values of groups were tested for statistical significance using Student t-test. A *P* value of less than 0.05 was considered to indicate a significant difference.

4.3 Results and discussion

4.3.1 Synthesis and characterisation of SPIONs

Monodisperse SPIONs in the form of Fe_3O_4, which are commonly used as contrast agents for MRI, were synthesised by one pot thermal decomposition of iron triacetylacetonate precursor in the presence of oleic acid, oleylamine and 1,2 hexadecanediol (**Figure 4.5**). The method was adapted from Sun and co-workers.[6,31]

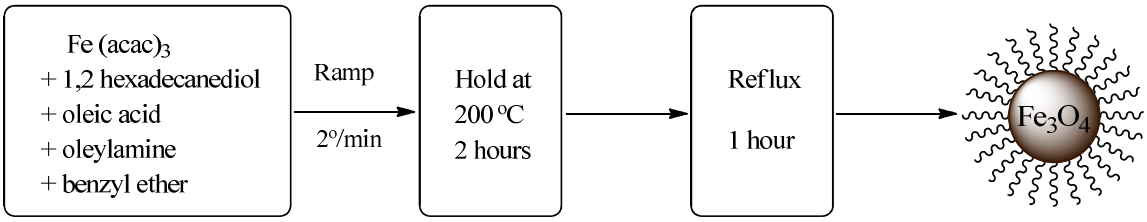

Figure 4.5 General schematic for the synthesis of monodisperse SPIONs using thermal decomposition.

The key condition for making monodisperse nanoparticles using this method is the 200 °C heating step before increasing the temperature to reflux (298 °C when using benzyl ether as solvent).[6,32] At the 200 °C temperature step the precursor starts to decompose and form nuclei, while the later increase in temperature is responsible for nanoparticles growth. The formation mechanism of the nanoparticles is not completely understood. Experimental observations suggested that the acetylacetonate ligands in $Fe(acac)_3$ were replaced by 3 equivalents of oleic acid and that the nanoparticles were formed from condensation of the respective atomic species. The atomic species were formed during the reductive decomposition iron oleate complex in the presence of 1,2 hexadecanediol. It is reported that 1,2 hexadecanediol acts as an organic reducing agent and facilitates

the Fe_3O_4 formation. The atomic species cluster to form numerous nuclei which then aggregate into Fe_3O_4 nanoparticles. The resulting Fe_3O_4 nanoparticles are coated with a thin layer of oleic acid and therefore are hydrophobic. The hydrophobic SPIONs were characterised by different techniques including PXRD, TGA, FTIR, DLS and TEM to obtain the full structural and chemical composition of the nanoparticles. Structural information on the hydrophobic SPIONs was obtained from PXRD (**Figure 4.6**). The position and intensity of the diffraction peaks in the PXRD pattern were found to match well with standard magnetite diffraction data (JCPSD file No 19-0629) with no other iron oxide impurity phases.[6,33]

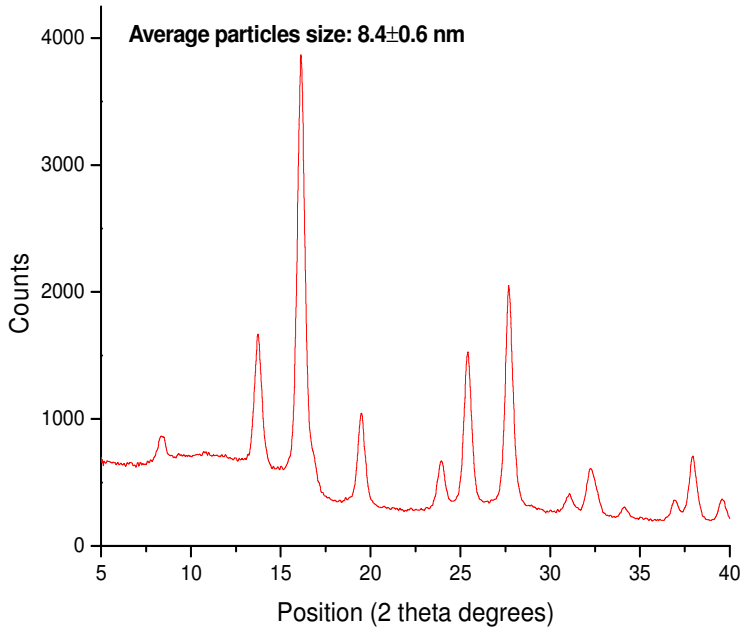

Figure 4.6 PXRD pattern of the hydrophobic SPIONs. All diffraction peaks in the XRD pattern match with the reported standard magnetite according to JCPDS No. 19-0629.

Although this synthetic method should provide Fe_3O_4 it can not be concluded that the composition is 100% Fe_3O_4 because the nanoparticles could contain a small amount of γ-Fe_2O_3 especially on their surface.[6] The PXRD pattern showed also peak broadening effects which are consistent with a reduced particle size. The average nanoparticles size is 8.4 ± 0.6 nm calculated using Scherrer's equation,[34] which is in good agreement with the average diameter of the iron oxide cores measured from TEM images (**Figure 4.7**).

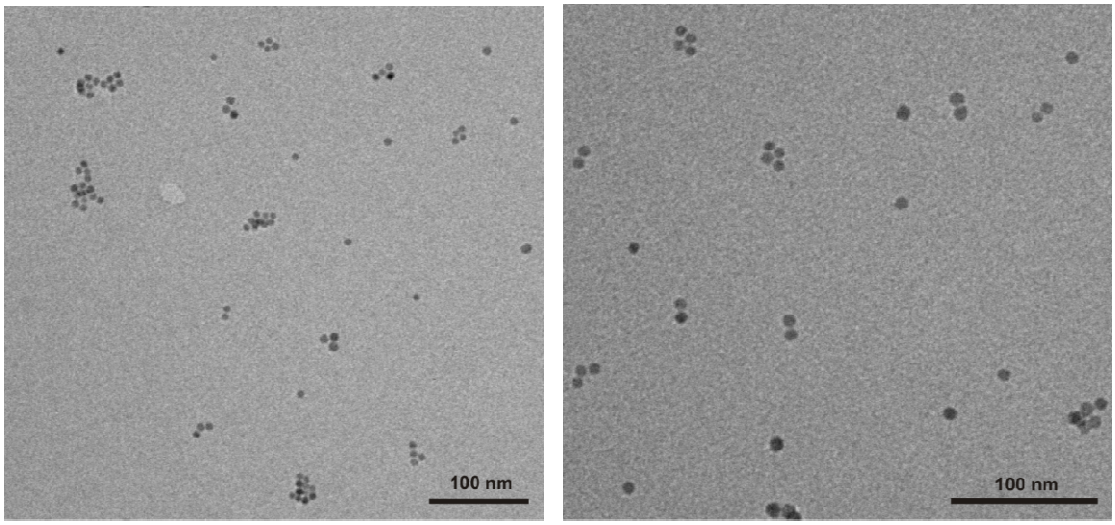

Figure 4.7 TEM images of 8.2 ± 0.9 nm hydrophobic SPIONs.

As evidenced from TEM images, the nanoparticles have spherical morphology and were monodisperse with very narrow size distribution 8.2 ± 0.9 nm in diameter.

The DLS plot shown in **Figure 4.8** evidenced a single narrow peak which suggests uniform size distribution of the nanoparticles in the organic solvent with no large aggregates. The measurements were carried out on non-filtered and filtered samples and the results were the same. The SPIONs have an average hydrodynamic diameter of 13.5 ± 1.1 nm in THF that is close to a simple addition of the particle inorganic core size

(8.2 nm in diameter) and the organic shell coating (~2 nm, corresponding to the extended oleic acid chains).[35]

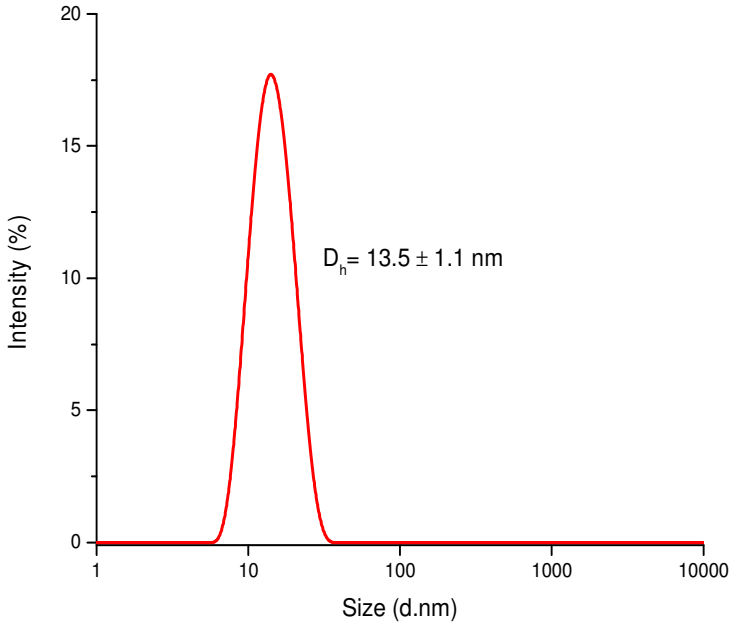

Figure 4.8 The hydrodynamic diameter of the hydrophobic SPIONs dispersed in THF measured by DLS.

Thermogravimetric analysis (TGA) in air of the hydrophobic SPIONs showed a weight loss of 12.4 % between 120 °C and 600 °C (**Figure 4.9**). The weight loss was attributed to the decomposition of the organic ligands present on the nanoparticle surface, corresponding to a monolayer of oleic acid. This correlates that each nanoparticle is covered by 380 oleic acid ligands on the surface (see Chapter 2, equation 2.13 for coverage calculations). The coverage values are in good agreement with previous literature reports.[36,37]

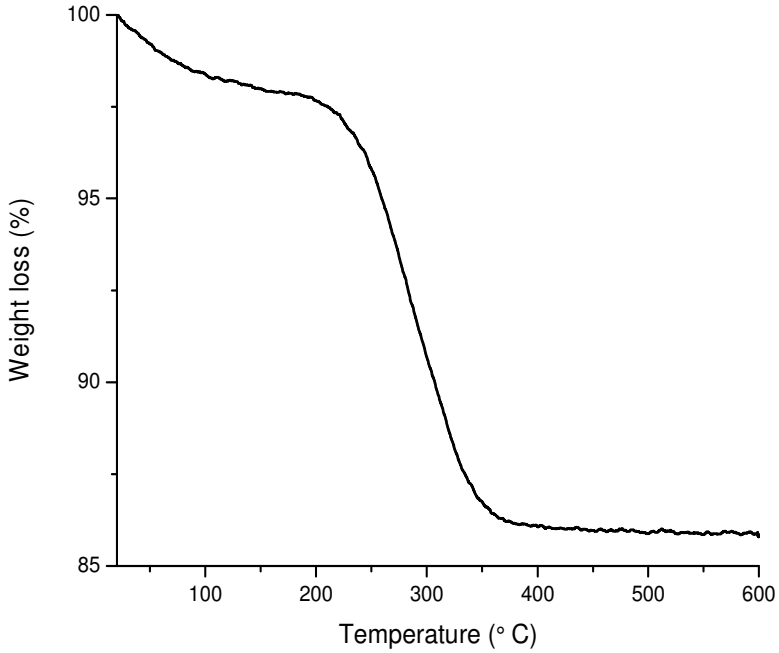

Figure 4.9 TGA of hydrophobic SPIONs showed a weight loss of 12.4 % corresponding to the decomposition of organic ligands found on the nanoparticle surface.

Magnetic measurements were carried out on the SPIONs powder precipitated from THF dispersions. **Figure 4.10** shows the field dependence of magnetisation measured at room temperature (300 K) from -1T to +1T. The hydrophobic SPIONs have a saturation magnetisation of 61.8 emu/g. As expected, the saturation magnetisation value obtained was lower than that of bulk magnetite (92 emu/g) which was attributed to particle size and to surface effects such as the presence of a magnetically inactive layer.[38] The measured magnetisation value is in line with the magnetisation reported by Sun for similar size nanoparticles.[32]

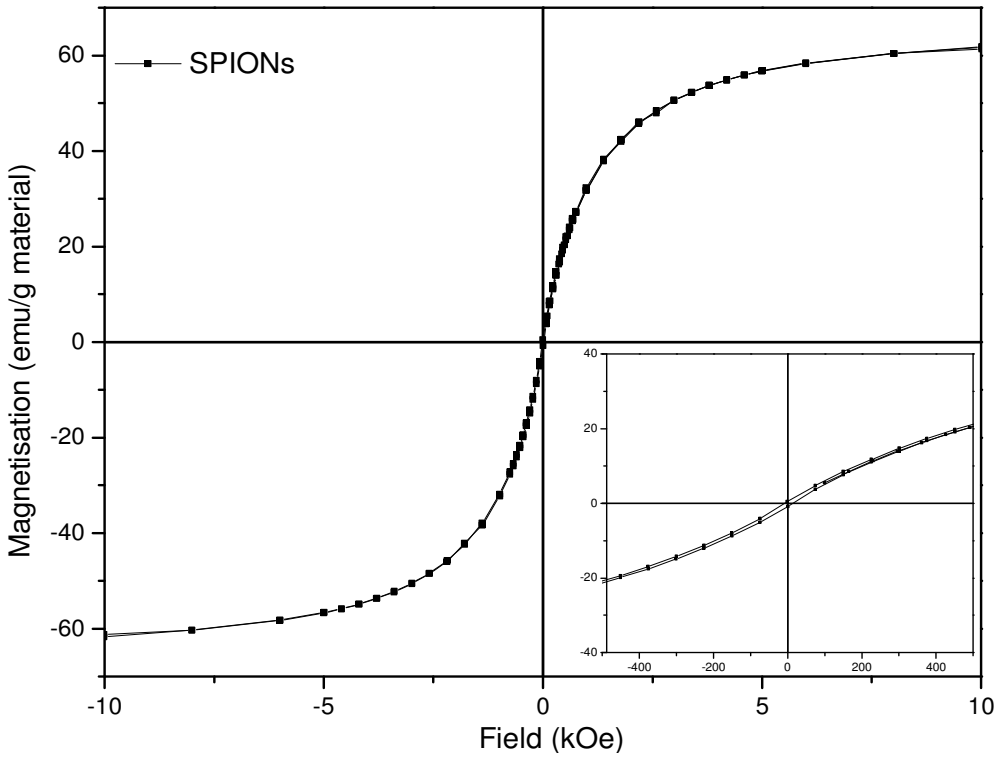

Figure 4.10 Magnetic field dependence of magnetisation at room temperature for hydrophobic SPIONs. Inset shows a zoom-in plot between -500 Oe and 500 Oe magnetic field.

The hydrophobic SPIONs exhibited the expected superparamagnetic behaviour. The hydrophobic SPIONs did not exhibit any remanence or coercivity at zero fields, meaning there is no hysteresis in the magnetisation curve. The superparamagnetism of SPIONs is attributed to their small size so that each nanoparticle is a single magnetic domain and the energy barrier for the spin reversal can be overcome by thermal vibrations.

4.3.2 Synthesis and characterisation of bioinspired amphiphilic polyoxazoline polymers

Bioinspired amphiphilic poly(2-ethyl-2-oxazoline) polymers were prepared using cationic ring opening polymerisation. It is documented that the polymerization of 2-oxazolines started with functional initiators and terminated with a variety of nucleophiles leads to well-defined polymeric structures functionalised at both terminal ends.[39] A general schematic for the polymerisation process is shown in **Figure 4.11**.

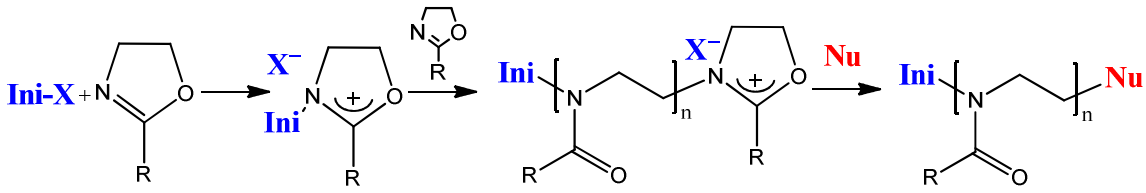

Figure 4.11 Schematic representation of the cationic ring opening polymerisation of 2-oxazolines. **Ini-X** represents an electrophilic initiator where X is the leaving group which forms the counter ion. **Nu** represents the nucleophilic terminating agent which can be used to end-cap the polymerisation.

PEtOX polymers with amphiphilic character, bearing a hydroxyl (-OH) end-functionality and an alkyl chain (C_{16}) as hydrophobic segment, were prepared using hexadecyl methanesulfonate initiators (see **Figure 4.12** for schematic representation of the polymerisation steps). The prepared polymer sample was denoted as **Polymer 1**.

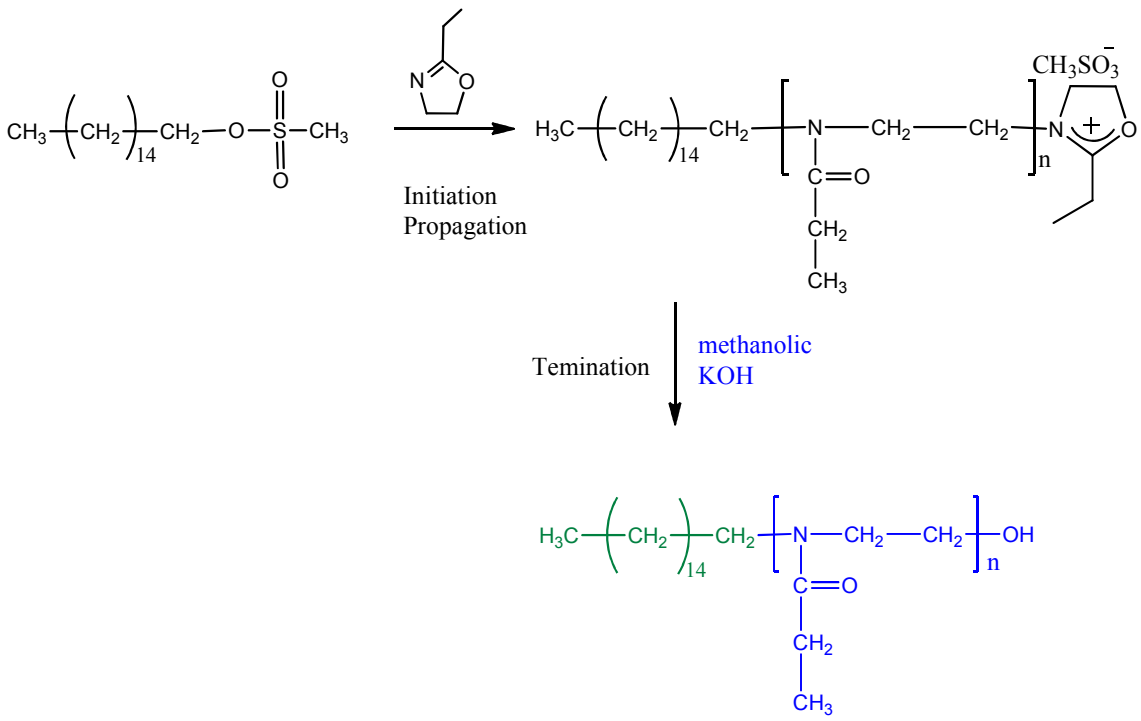

Figure 4.12 Synthesis steps for amphiphilic α-hexadecyl, ω-hydroxyl poly(2-ethyl-2-oxazoline) polymer, **Polymer 1**.

The resulting polymer after termination step with methanolic KOH had a molecular weight of 4500 as calculated from ^{1}H-NMR. In the ^{1}H-NMR spectrum of the **Polymer 1** with M_n=4500 shown in **Figure 4.13** all peaks could be assigned indicating the successful polymerisation and propagation reaction without side reactions based on the ^{1}H-NMR analysis. The characteristic proton peaks for the polymer backbone (-N-C**H**$_2$-C**H**$_2$-) were found at 3.4 ppm, while the pendant methyl protons were present at 1 ppm. The α- terminus methyl protons in the C_{16} hydrophobic segment were found at 0.8 ppm and the methylene group protons in the alkyl chain at 1.2 ppm, **Figure 4.13**.

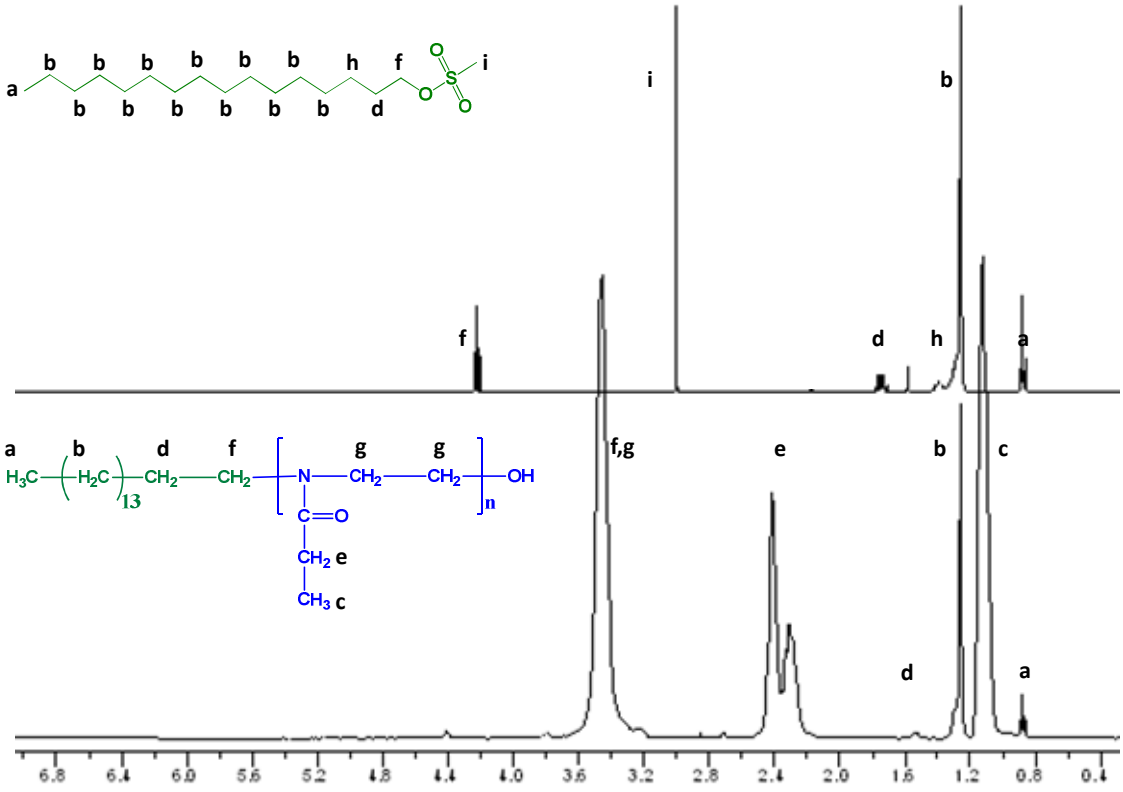

Figure 4.13 ^{1}H NMR representative spectra (in $CDCl_3$, 400 MHz) of the hexadecyl methanesulfonate initiator and hydroxyl functional amphiphilic polyoxazoline (**Polymer 1**) and assignment of the proton signals.

The molecular weight of the polymers calculated from ^{1}H-NMR was confirmed by GPC measurements. The GPC results showed M_n= 4500 and M_w= 5600 and the polydispersity index (PDI) was calculated as 1.21. The GPC elution trace is symmetrical, monomodal, with no shoulder indicative of a well-defined polymer (**Figure 4.14**).

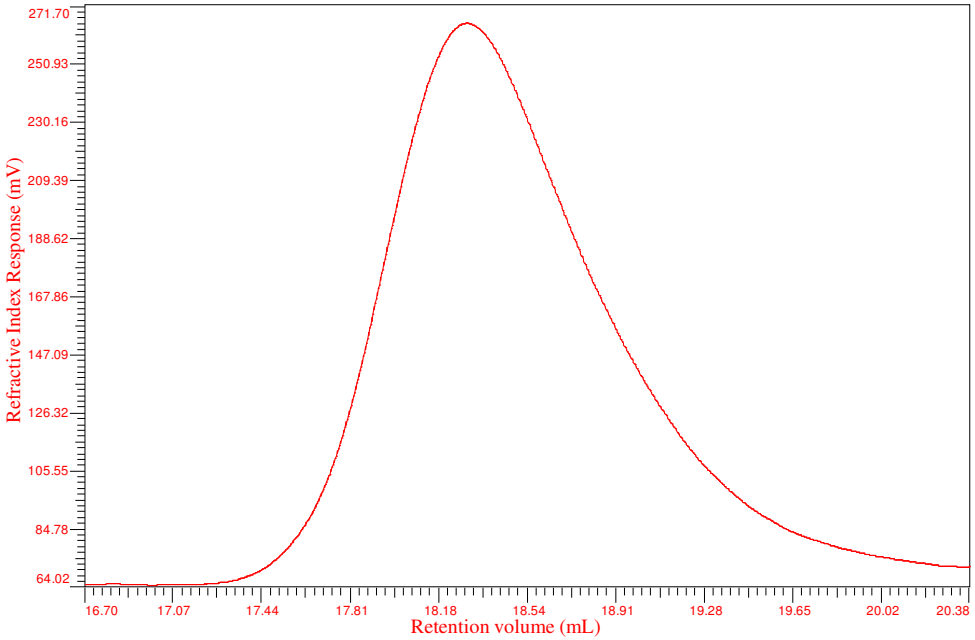

Figure 4.14 GPC elution profile for **Polymer 1** (THF/triethylamine, polystyrene standards).

Polymer 1 was modified with carboxylic acid end-functional groups using an esterification reaction with succinic anhydride catalysed by triethylamine. The modified polymer sample was denoted as **Polymer 1S** (**Figure 4.15**). The reaction of an alcohol with an acid anhydride is well-established in organic chemistry and has been successfully used for modification of other polymers.[28] **Polymer 1** was reacted with 10 fold molar excess of succinic anhydride per OH residue in anhydrous DMF as shown in **Figure 4.15**.

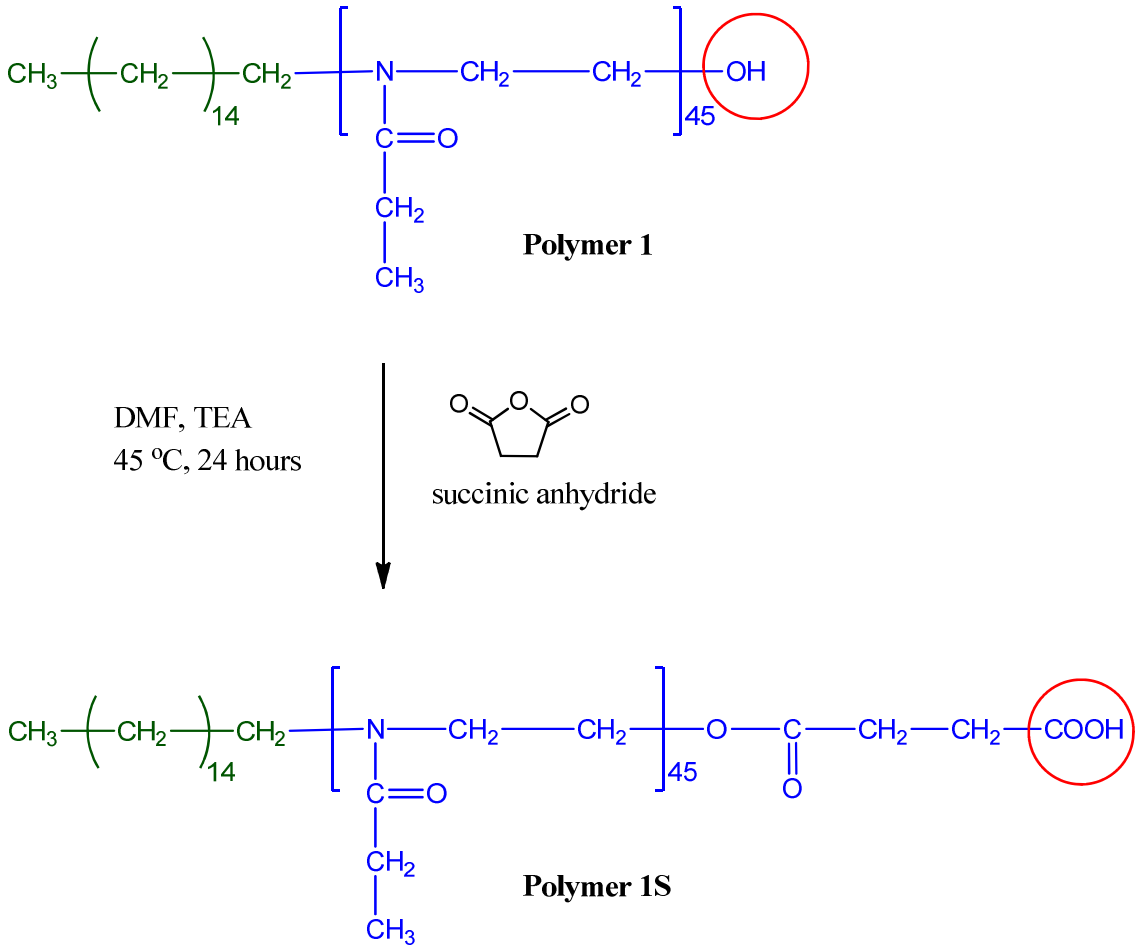

Figure 4.15 Schematic representation of the chemical modification of hydroxyl group in **Polymer 1** with succinic anhydride.

The attachment of the succinic acid functionality to **Polymer 1** was confirmed by ^{1}H NMR, FTIR and zeta potential measurements. The ^{1}H NMR spectra for non-modified **Polymer 1** and succinylated **Polymer 1S** are shown in **Figure 4.16.**

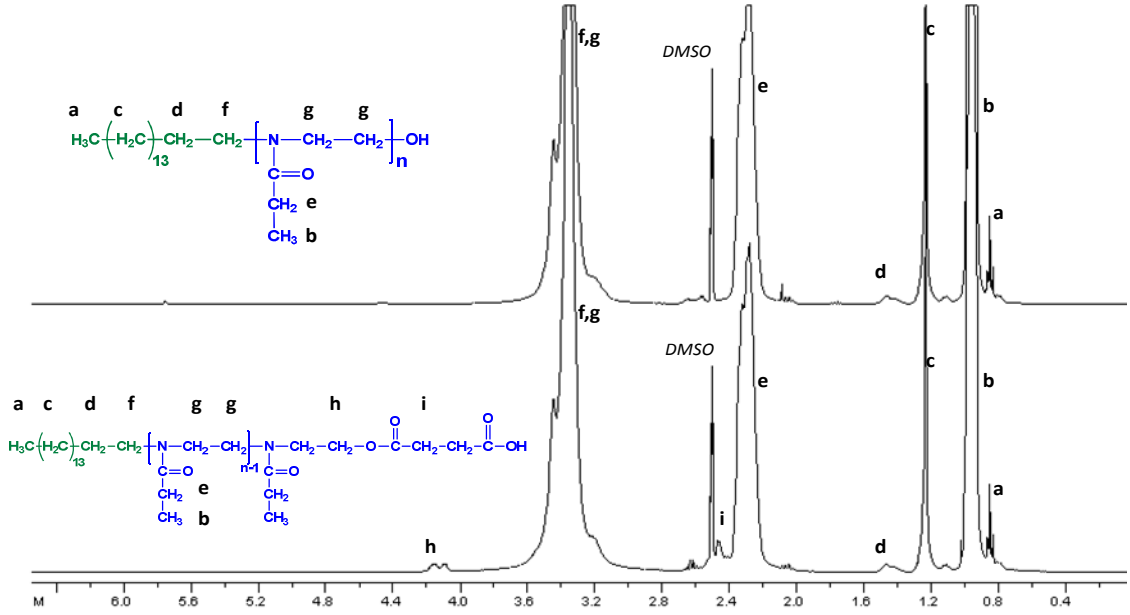

Figure 4.16 Representative ^{1}H NMR spectra (in DMSO, 400 MHz) of (a) of **Polymer 1** and (b) **Polymer 1S** and assignment of the proton signals to the schematic representation of the polymeric structure.

The ^{1}H NMR spectrum of modified **Polymer 1S** showed the presence of an extra peak at 4.2 ppm belonging to the protons in the polymer backbone which are the closest to the ester peak in the succinate linkage.[40] The protons belonging to the succinic anhydride ring would show as a single characteristic peak at 3 ppm. As part of succinic anhydride they are not distinct from one another. However, the protons closest to the ester linkage between the succinic acid and the PEtOX polymer were identified at 2.4 ppm. The protons closest to the carboxylate end group are overlapping with the methylene protons in the polymer backbone at 2.2 ppm. The complete functionalisation with carboxylic acid groups was established based on the integral values of the peaks *a* and *h* which were 3 and 2.

The successful modification of the polymer with carboxylic acid functional groups was additionally confirmed using FTIR spectroscopy (**Figure 4.17**). The characteristic band of the carbonyl (C=O) deriving from free carboxylic acid groups was evidenced at 1720 cm^{-1} in the succinylated **Polymer 1S** spectrum. This peak was not present in the **Polymer 1** spectrum. The rest of the peaks fully overlap with the spectrum for **Polymer 1**, indicating no alteration to the structure of the polymer backbone. The characteristic bands for the C-H stretching vibrations in $–CH_2$ and $–CH_3$ were present in the region between 2975 and 2871 cm^{-1}. Additionally the C=O stretching from the PEtOX was evidenced at 1640 cm^{-1}. Overall the FTIR analysis showed that the **Polymer 1** was modified with carboxylic acid groups.

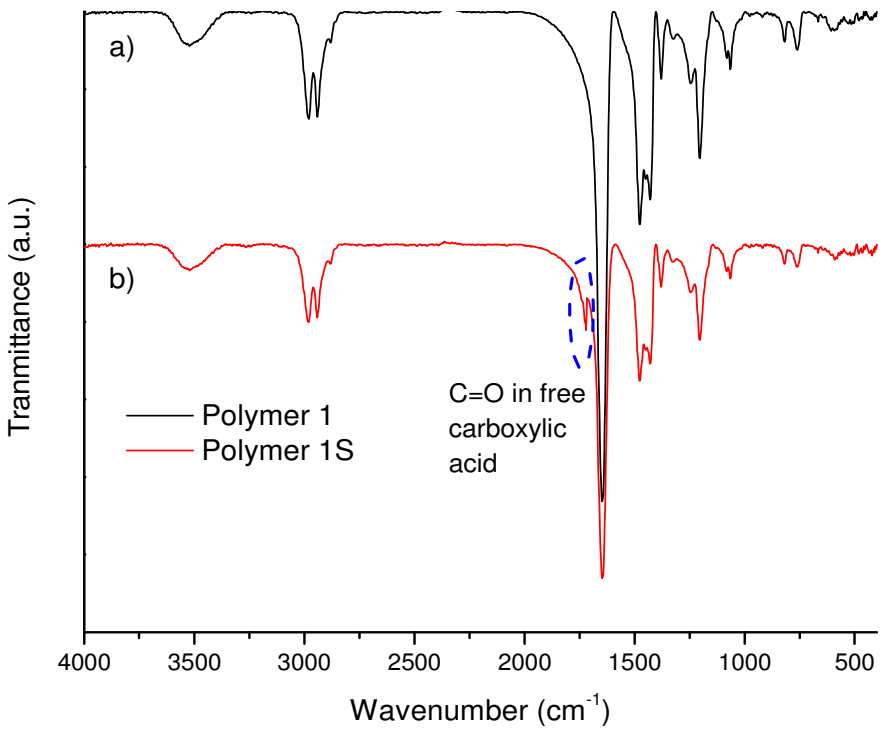

Figure 4.17 FTIR spectra of **Polymer 1** (a) and **Polymer 1S** (b) amphiphilic polyoxazolines.

The presence of end-functional carboxylic groups on the polymer was further confirmed by zeta potential measurements of aqueous solutions of **Polymer 1S** at different pH values (**Figure 4.18**).

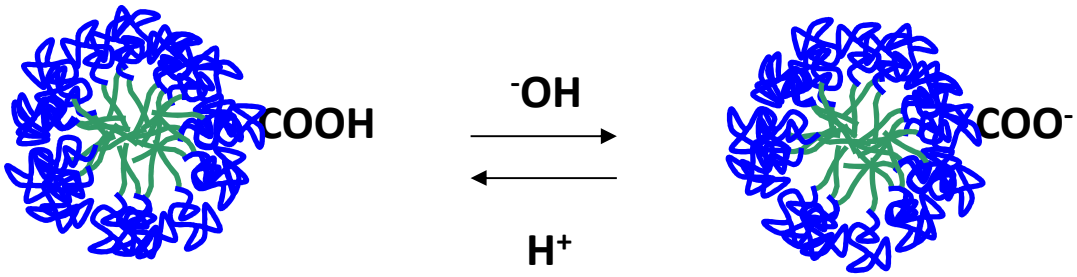

pH	2	4	6	8
ZP (mV)	1.8 ± 0.5	-1.3± 0.8	-5.7 ±0.2	-14.2 ± 0.3

Figure 4.18 Schematic representation of the protonation/deprotonation of the carboxylic end-functional groups and zeta potential values of polymeric solutions at different pHs.

It was found that the polymer solutions have a zeta potential of -14.2 ± 0.3 mV at pH 8 attributed to the deprotonated carboxylic groups. At low pH values the zeta potential increases so that at pH 2 a positive value of 1.8 ± 0.5 mV was recorded due to full protonation of the carboxylic end-functional groups. These measurements showed that the isoelectric point of the polymer is around pH 3. Literature reports that the pKa value for succinic acid is 4.16.[41] Therefore a pKa value below 4 was found reasonable in this case.

Taken together these results showed that **Polymer 1** was successfully modified to have a –COOH end-functionality which will provide opportunities to couple specific bioactive molecules and to confer targeting capabilities to the polymeric structures.

4.3.3 Cytotoxicity pre-screening of synthesised amphiphilic poly(2-ethyl-2-oxazoline) polymers

The effect of the amphiphilic polymers (**Polymer 1** and **Polymer 1S)** on viability of cells was assessed using the MTS cell proliferation assay. The assay measures the metabolic activity of living cells and their ability to reduce the MTS tetrazolium dye into a coloured formazan compound which absorbs at 450 nm. Nonviable cells lose their metabolic capacity and do not generate a colored signal.

Human pancreatic cancer cells (SUIT-2) were incubated with the polymers for 48 hours and the viability was compared with non-treated cells as control. As the cell viability is usually concentration dependent, the cells were exposed to polymer concentrations ranging from 0–1 mM.

Although the PEtOX polymer without hydrophobic segment is not toxic and used as a food additive it was important to confirm that the modifications of the structure did not modify the behaviour of the polymer.

Under these conditions the MTS results showed that introducing a hydrophobic segment on the polymer structure did not cause any visible toxicity over 48 hours on the cell type investigated. At the same time modification of the end-functionality from hydroxyl to carboxylic acid did not change the toxicity profile. As seen in **Figure 4.19** the average

viability of SUIT-2 cells treated with **Polymer 1** and **Polymer 1S** for 48 hours was 90-95 % for all concentrations investigated.

The cytotoxicity data was analysed using Student's t test and no significant difference was observed for all groups ($p>0.05$).

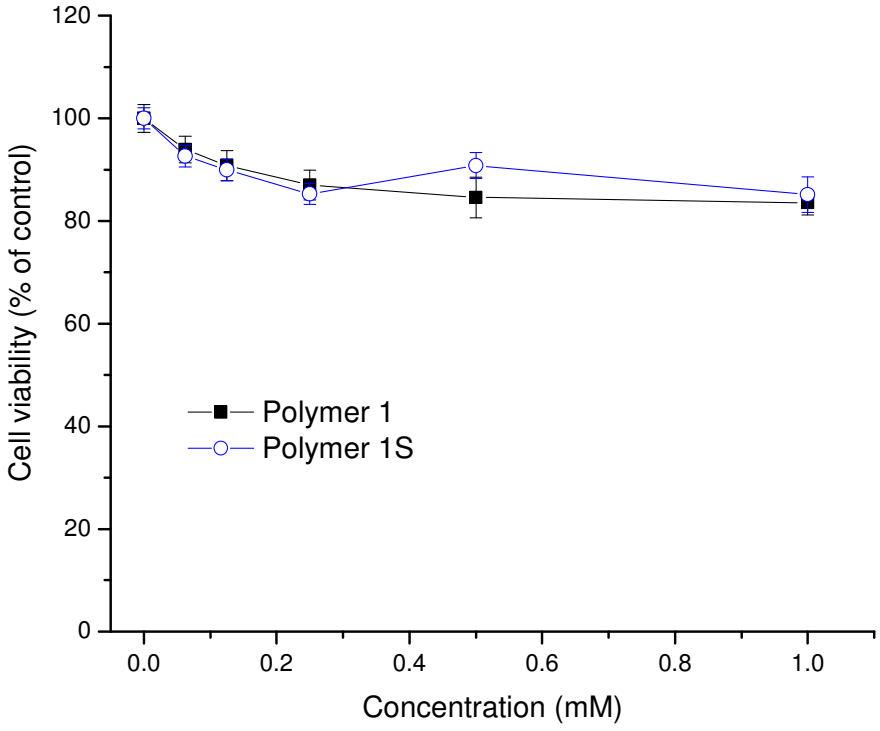

Figure 4.19 Cell viability of human pancreatic cancer derived cells (SUIT-2) after incubation for 48 hours with different polymers at various concentrations. The viability was measured by a MTS assay. The results are the average ± standard deviation.

Considering the physicochemical properties and pre-screening toxicity results, the synthesised polymer structures would be suitable candidates for coating the surface of hydrophobic SPIONs.

4.3.4 Self-assembly of SPIONs and bioinspired amphiphilic polyoxazoline polymers into multifunctional-magneto-micelles (MMMs)

Monodisperse SPIONs prepared using the high temperature decomposition method are hydrophobic and can only be dispersed in organic solvents such as hexane, THF or chloroform. In order to make the nanoparticles water soluble and biocompatible, a surface modification step is necessary. Bioinspired amphiphilic polyoxazoline polymers are suitable candidates to make the hydrophobic SPIONs dispersible in aqueous medium. Amphiphilic block copolymers can assemble into core-shell micelles with hydrophobic core and hydrophilic shell. The core can be loaded with hydrophobic compounds or nanoparticles through a co-micellisation approach. In this case the hydrophobic segment of the polymer will interact with the hydrophobic SPIONs, while the hydrophilic PEtOX polymer will provide solubility and stability in aqueous environments. At the same time the hydroxyl or carboxylic acid end-functionalities available on the polymer allow for further functionalisations with bioactive molecules. The polyoxazoline polymers are reported to have excellent colloidal stability in physiological buffers, low interaction with serum proteins resulting in longer blood circulation time and bioavailability.[19,21]

For preparation of **MMMs** a solvent exchange method was adopted with dialysis as the final purification step. Briefly, a dispersion of hydrophobic SPIONs in THF was added to an aqueous solution of **Polymer 1S** and mixed using sonication to achieve a brown transparent solution. Then the organic solvent was removed using dialysis. The

schematic representation of the self-assembly between hydrophobic SPIONs and amphiphilic polyoxazoline is shown in **Figure 4.20**.

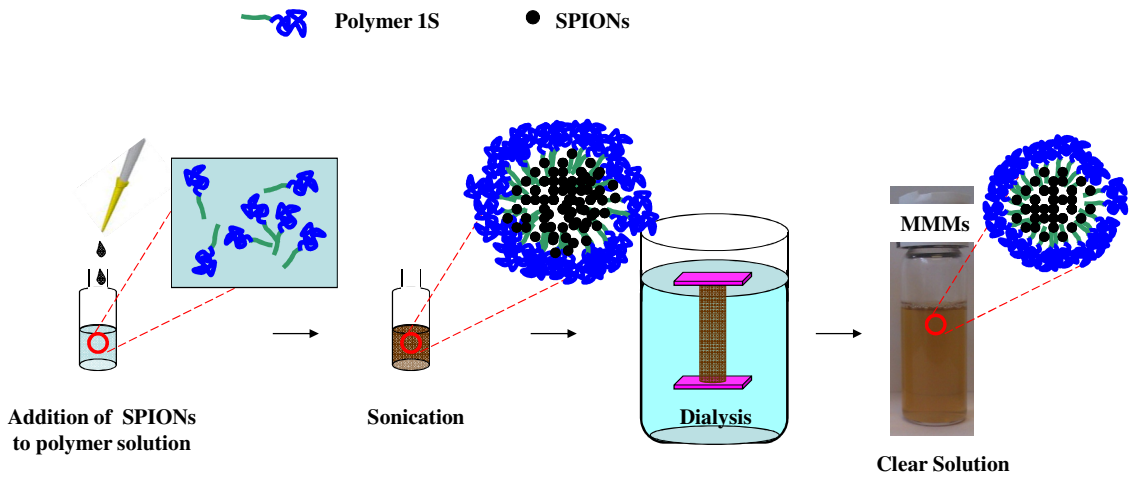

Figure 4.20 Schematic representation of the synthetic procedure used to prepare **MMMs** that encapsulate SPIONs within the polyoxazoline micelles.

The general parameters which were varied during the assembly procedure were the polymer and SPIONs concentrations as shown in **Table 4.1.**

Table 4.1 Self-assembly parameters varied during the procedure, average hydrodynamic diameters measured by DLS and stability of **MMMs** obtained.

Micelles	Polymer 1S (mg)	SPIONs (mg)	Solvent (mL)	Z-average[a] (d/nm)	Observations
MMM-1	10	1	10	91.8 ± 1.5	Stable
MMM-2	5	1	10	112.0 ±1.1	Precipitation after 1 month
MMM-3	1	1	10	134.4 ± 3.2	Precipitation after 1 month

MMM-4	20	1	10	93.9 ± 2.0	Stable
MMM-5	40	1	10	94.0 ± 2.6	Stable
MMM-6	10	2	10	121.7 ± 1.2	Precipitation after 1 month
MMM-7	10	4	10	140.9 ± 1.8	Precipitation after 1 month

[a] Average intensity–weighted size and standard deviation values obtained from 3 measurements using a Zetasizer DLS.

For preparation of **MMMs**, 1 mg SPIONs were assembled with various amounts of **Polymer 1S** (1-40 mg, M_n = 4500). **Figure 4.21** shows the size evolution of the **MMMs** when the polymer was varied from 1 to 40 mg during the assembly process. Increasing the amount of polymer from 1 to 10 mg led to a decrease in the size of the assembled hybrid magneto-micellar structures. The size decrease is because more polymer chains are available per hydrophobic SPION and less SPIONs are included in one micellar core; therefore the final size of the assembled magneto-micelle decreases up to a point when equilibrium is reached. The average diameter measured using DLS for **MMM-1** was 91.8 ± 1.5 nm, while for **MMM-2** and **MMM-3,** prepared with lower amounts of polymer, the z-average diameter was 112.0 ± 1.1 and 134.4 ± 3.2 nm respectively.

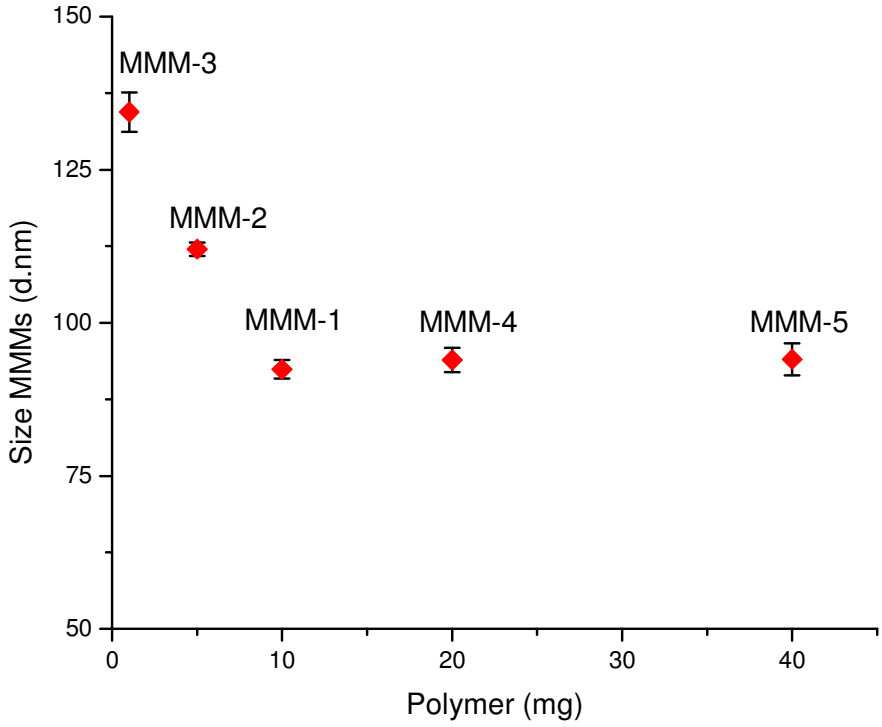

Figure 4.21 Size evolutions of **MMMs** measured by DLS at various mass proportions of amphiphilic polymer with 1 mg SPIONs.

From **Figure 4.21** it can be noticed that when the used polymer mass was more than 10 mg, the size of **MMM-4** and **MMM-5** was not significantly different from **MMM-1**. The size evolution of **MMMs** was also assessed when the SPIONs loading was increased (e.g. 2 mg and 4 mg) while keeping the amount of polymer constant at 10 mg. The samples were denoted as **MMM-6** and **MMM-7** (**Figure 4.22**). The rationale for using higher SPIONs loadings is related to the possibility of having increased magnetic properties and therefore enhanced abilities to shorten the T_2 relaxation times of protons in case of application as MRI contrast agents. The average hydrodynamic size of the obtained **MMMs** increased with the increase in SPIONs loading. From DLS

measurements the average diameters for **MMM-6** and **MMM-7** were found to be 121.7 ± 1.2 and 140.9 ± 1.8 nm respectively (shown in **Figure 4.22**).

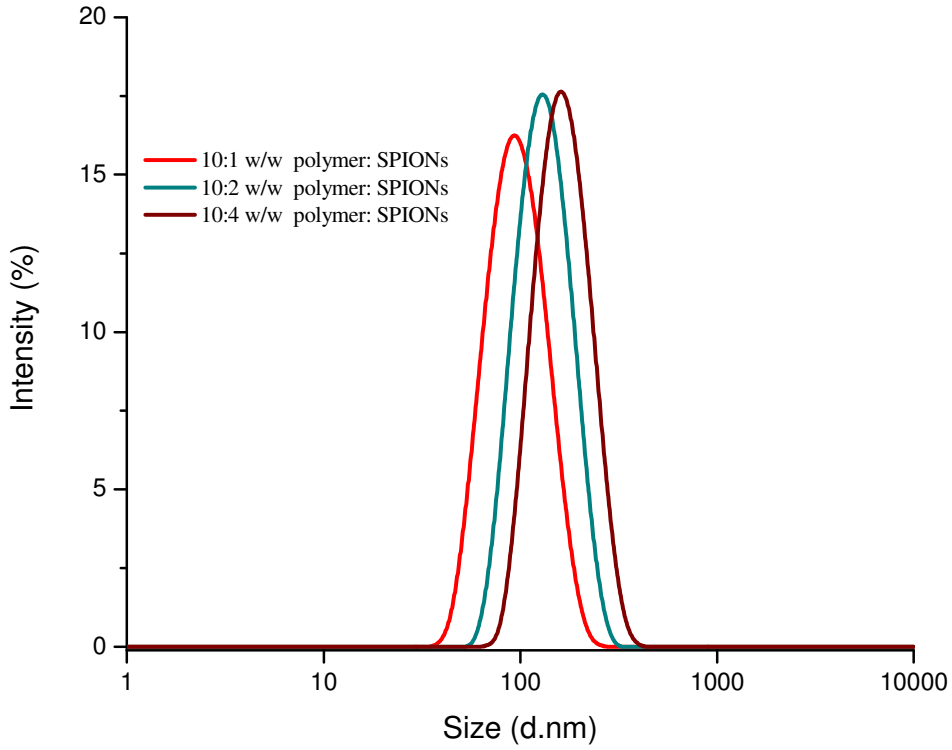

Figure 4.22 Hydrodynamic diameters distribution measured by DLS for **MMM-6** and **MMM-7** prepared with higher loadings of SPIONs while keeping the mass of polymer constant at 10 mg.

Figure 4.23 shows the optical images of **MMMs** formulated with 1 mg SPIONs in the core. At 10:1 and 20:1 w/w ratios between the polymer and the SPIONs, the solutions maintained a brown transparent colour without apparent precipitation for a month due to the self-assembled micellar state. Whereas for the lower polymer/SPIONs ratios investigated, precipitation was observed after 1 month. This suggested that the minimum polymer mass required to obtain stable **MMMs** is 10 mg.

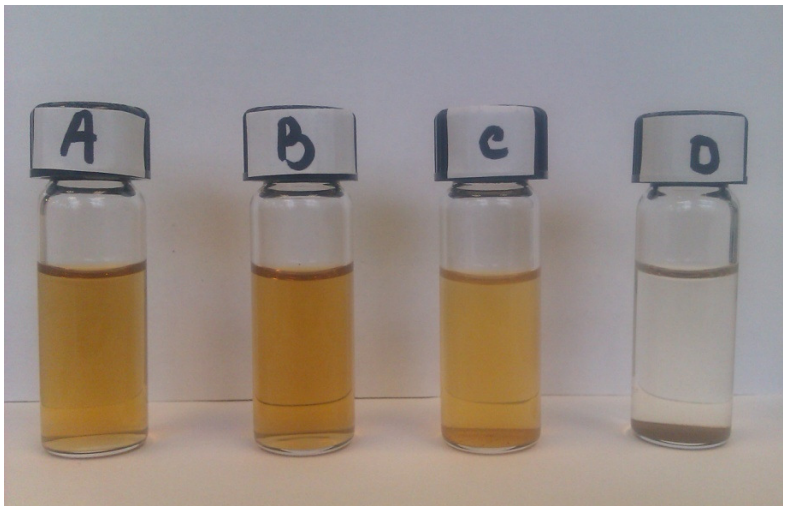

Figure 4.23 Digital photographs of different hybrid micellar structures: **MMM-1** (A), **MMM-4** (B), **MMM-2** (C) and **MMM-3** (D) dispersed in deionised water after 1 month.

The micellisation experiments showed that particle size and stability were highly dependent on the polymer/SPION wt ratio used in the self-assembly process, i.e. larger **MMMs** size with higher SPIONs loadings. Highly monodisperse **MMMs** with average sizes of 92 nm were obtained consistently when polymer/SPIONs ratio was at least 10:1. Therefore, all samples from hereafter were prepared with the fixed w/w ratio of 10:1 between polymer and SPIONs.

The **MMM-1** hybrid structures were characterised by various physico-chemical techniques such as TGA, FTIR, SQUID magnetometry, DLS, zeta potential and TEM to examine the distribution of SPIONs in the polymeric micelles.

TGA measurements for SPIONs, **Polymer 1S** and **MMM-1** were performed to determine the composition of the structures (**Figure 4.24**). The weight losses were 12.4% and 88% for SPIONs and **MMM-1** respectively. The weight loss in the SPIONs was attributed to the thermal decomposition of organic ligands on their surface. The

weight loss in **MMM-1** had two steps: one step between 120-400 °C attributed to the decomposition of the hydrophobic part and the second one between 400-600 °C was attributed to the decomposition of the hydrophilic polymer backbone. Based on the TGA results the iron oxide nanoparticles loading in **MMM-1** was calculated to be 12 wt%.

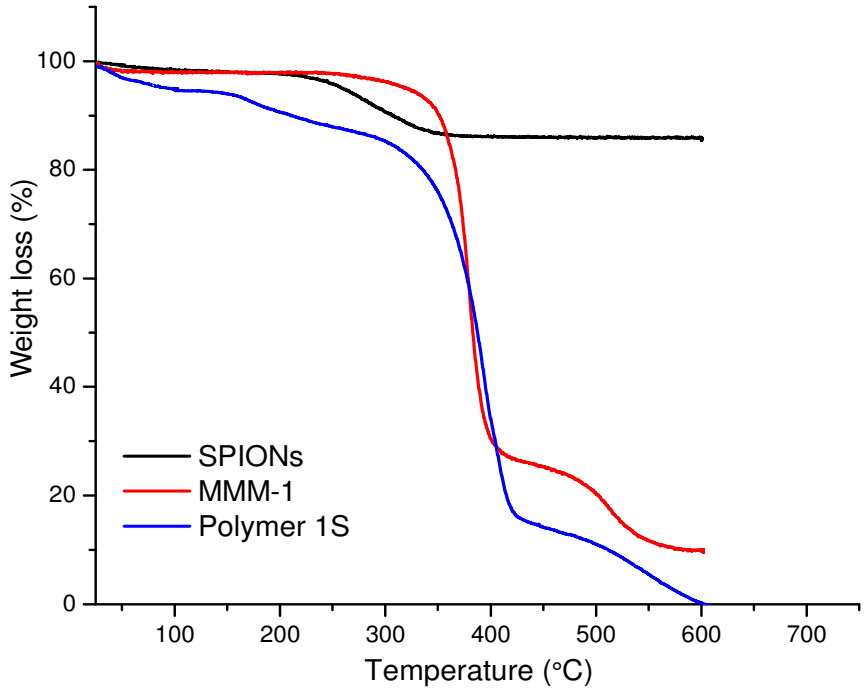

Figure 4.24 TGA of hydrophobic SPIONs, **Polymer 1S** and **MMM-1** hybrid structures.

Further evidence for the assembly of the SPIONs into **MMM-1** hybrids was obtained from FTIR spectroscopy. **Figure 4.25** shows the FTIR spectra of **Polymer 1S** containing the carboxylic acid end-functionality (a), the hydrophobic SPIONs (b) and the assembled magneto-micellar structures **MMM-1** (c). The FTIR spectrum of **MMM-1** in **Figure 4.25c** showed the characteristic bands arising from the presence of both components: iron oxide nanoparticles and the polyoxazoline polymer. This proved that the micelles were a composite mixture of these two different materials.

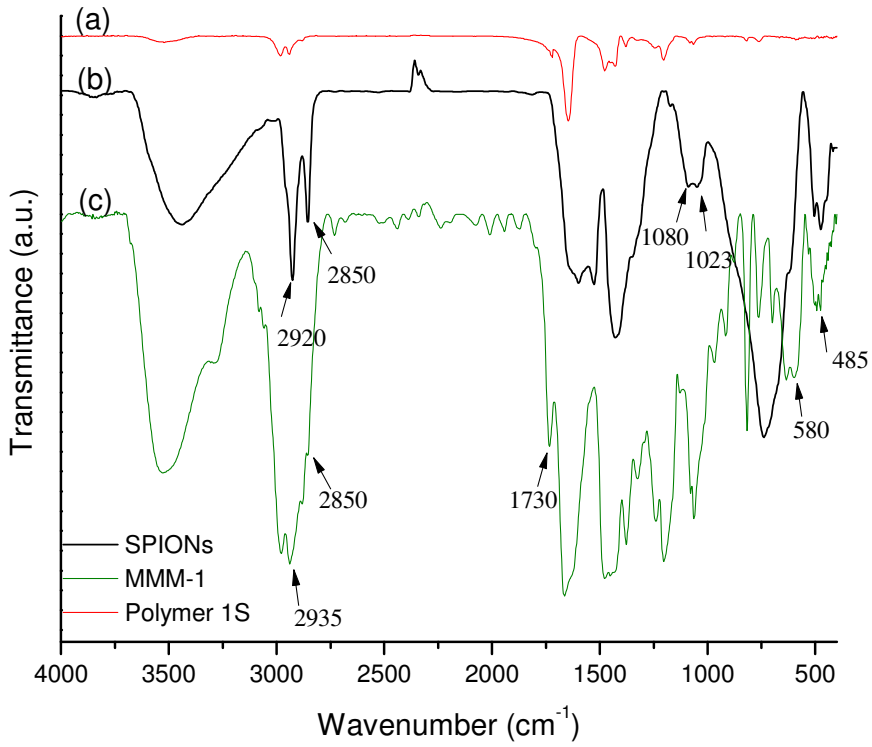

Figure 4.25 FTIR spectra of (a) **Polymer 1S**, (b) hydrophobic SPIONs and (c) assembled **MMM-1** hybrid structures.

The bands at 485 and 580 cm^{-1} in the spectrum of **MMM-1**, characteristic for Fe-O stretching indicated the presence of iron oxide nanoparticles. The band at 1730 cm^{-1} corresponding to C=O stretch of the free carboxylic acid groups of the polymer is also present in the assembled **MMM-1** structures. The CH_2 asymmetric and symmetric stretching bands are evidenced at 2935 and 2850 cm^{-1} and can be found in both the polymer and the oleic acid ligands. It is important to notice the absence of the 1730 cm^{-1} band for the C=O stretching in free carboxylic acid groups from the oleic acid coating in hydrophobic SPIONs (**Figure 4.25b**). Moreover, the bands at 1080 and 1023 cm^{-1} corresponding to the C-O stretching showed that the oxygen atoms in the carboxylate are coordinated onto the surface of the SPIONs as previously reported.[38]

The morphology of **MMM-1** structures was analysed by transmission electron microscopy (TEM) and is shown in **Figure 4.26**.

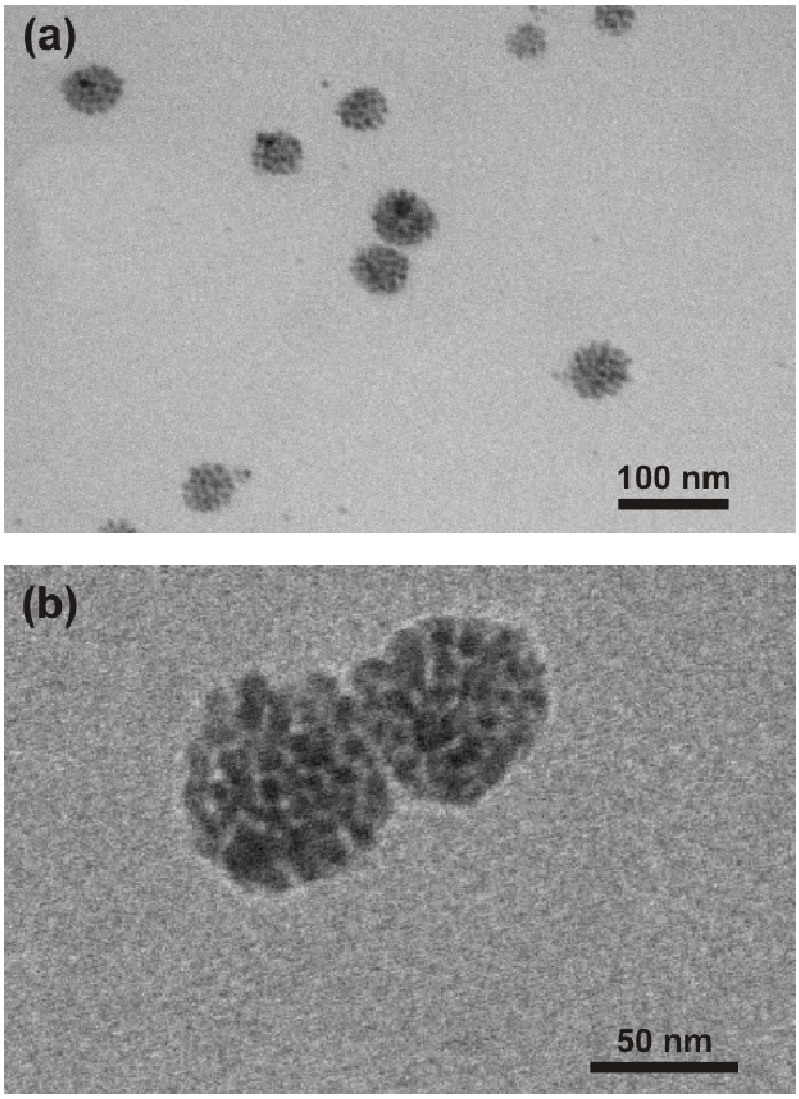

Figure 4.26 TEM images of **MMM-1** assembled structures at (a) lower and (b) higher magnification.

The polymeric part is not clearly visible owing to its low electron density, while SPIONs give a high contrast and it is possible to observe that they are confined in a circular area that confirmed that they are loaded in the hydrophobic core of **MMM-1**

due to their interaction with the hydrophobic part of **Polymer 1S**. The SPIONs are densely packed and homogeneously distributed within the micellar core, forming multi-SPIONs loaded polymeric micelles (magneto-micelles). The average diameter of the magnetic core of **MMM-1** structures was determined to be 61 ± 4 nm. From DLS the measured intensity-average hydrodynamic diameter of **MMM-1** was 92 nm. During DLS measurements the magneto-micelles are dispersed in aqueous solutions and therefore the polymer chains are expanded in solution.

The micellar morphology was improved after staining the polymer with 2% PTA, which enhanced the hydrophilic polymeric corona (**Figure 4.27**). Due to the nature of the polymer the micellar structures look positively stained rather than negatively stained, because the metal atoms in the stain solution are chemically interacting with reactive sites in the polymer structure.

The hydrophilic polymeric corona was evidenced as a thin diffuse layer around the uniformly distributed SPIONs inside the hydrophobic core. The SPIONs were seen as clear dark spots embedded in the low contrast micellar core. This type of magneto-micellar conformation is most probably due to the fact that THF is a good solvent for both hydrophobic SPIONs and for the hydrophobic segment of the amphiphilic polymer. The structures are similar to the ones obtained by the groups of Taton *et al.*[42] and Park *et al.* [43] when using amphiphilic block copolymers composed of poly(acrylic acid) and poly-styrene (PAA-*b*-PS) for coating the hydrophobic magnetic nanoparticles.

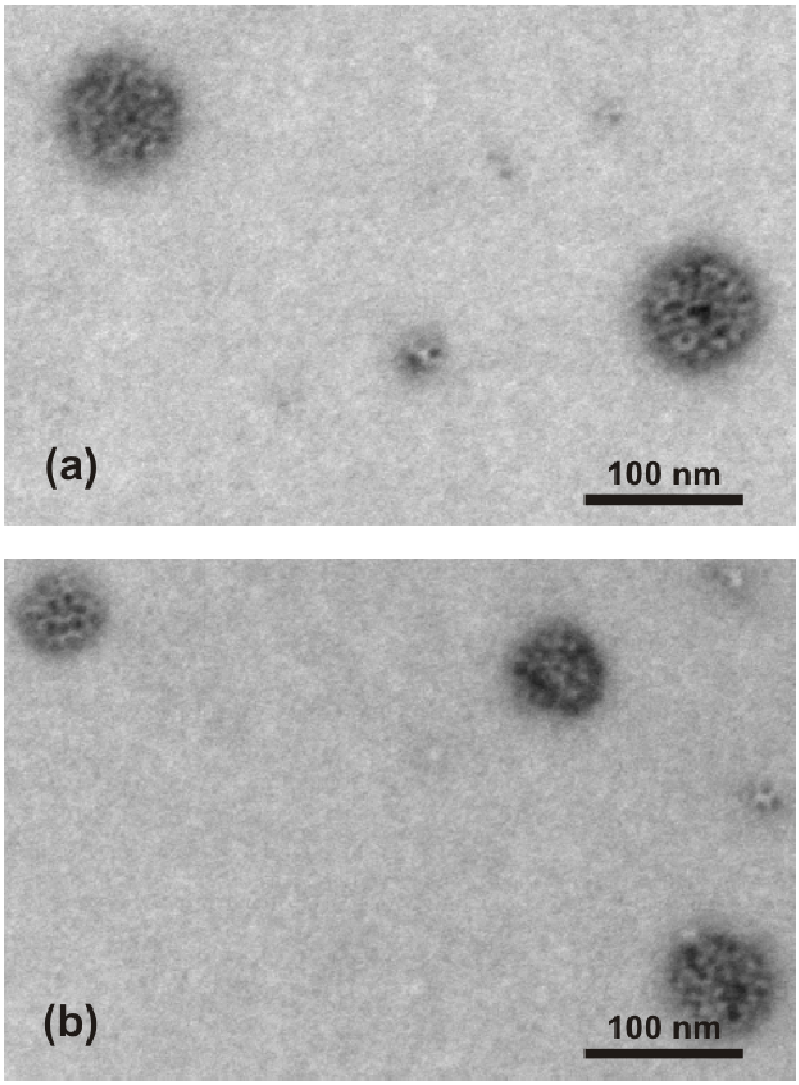

Figure 4.27 TEM images of **MMM-1** hybrids stained with 2% PTA to enhance the polymeric corona.

After the TEM staining procedure the average size of the magneto-micelles was determined as 76 ± 7 nm. The **MMM-1** sizes observed under the electron microscope were smaller than from DLS measurements. This was because the polymeric corona is hydrated and expanded when dispersed in aqueous solutions during DLS measurements.

To determine the magnetic properties of **MMM-1**, the lyophilized powder was analyzed using a superconducting quantum interference device (SQUID) at room temperature (300 K). The magnetisation curve shows that **MMM-1** exhibited the expected superparamagnetic property due to the absence of a remanent magnetisation when the applied magnetic field is removed (**Figure 4.28**).

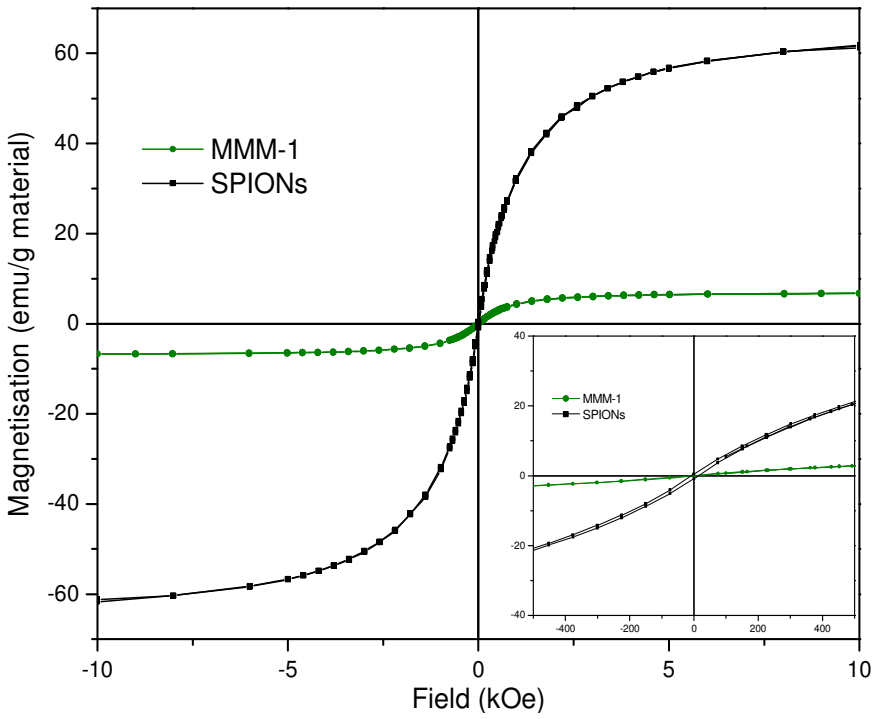

Figure 4.28 Magnetic field dependence of magnetisation at room temperature for hydrophobic SPIONs (black) and assembled **MMM-1** (blue) magnetic structures. Inset shows a zoom-in plot between -500 Oe and 500 Oe magnetic field.

The measured magnetisation at saturation for **MMM-1** structures was 7.6 emu/g. Compared with the value measured for SPIONs, 61.8 emu/g material, the magneto-micelles have a lower magnetisation which is attributed to the presence of the non-magnetic polymeric shell. The contribution for the magnetisation value in **MMM-1** is based only on the ratio of SPIONs present. According to the thermogravimetric analysis

the percentage weight of magnetic cores accounts only for 12% of the total mass of the **MMM-1** structures, therefore a value of 0.12 × 61.8 would be expected. Similar reduction in magnetisation values was observed for other polymer coated systems and was attributed to the presence of organic shell.[44-46]

4.3.5 Evaluation of MMMs stability

The stability of the **MMM-1** was assessed in PBS, over time and under pH values between 4 and 10. The stability in PBS (buffer which mimics the ionic strength of the body fluids) was evaluated by an absorption assay as reported by R. de Palma *et al.*[37] The procedure involved monitoring the time-evolution of the absorbance of the **MMM-1** solution (in water and PBS) at a fixed wavelength of 850 nm, where the absorbance correlates with the concentration and stability of magneto-micellar structures present in solution. If the magneto-micelles are not stable during the aging time, they are likely to agglomerate resulting in large particles which would precipitate, therefore showing a decrease in absorbance.

The time dependent absorbance results showed that **MMM-1** has good stability in PBS comparable to the stability in water. **MMM-1** solution remained transparent and did not show significant decrease in absorbance during the continuous 24 hour monitoring at ambient temperature, which confirmed that the magneto-micellar structures are stable in PBS buffer (**Figure 4.29**).

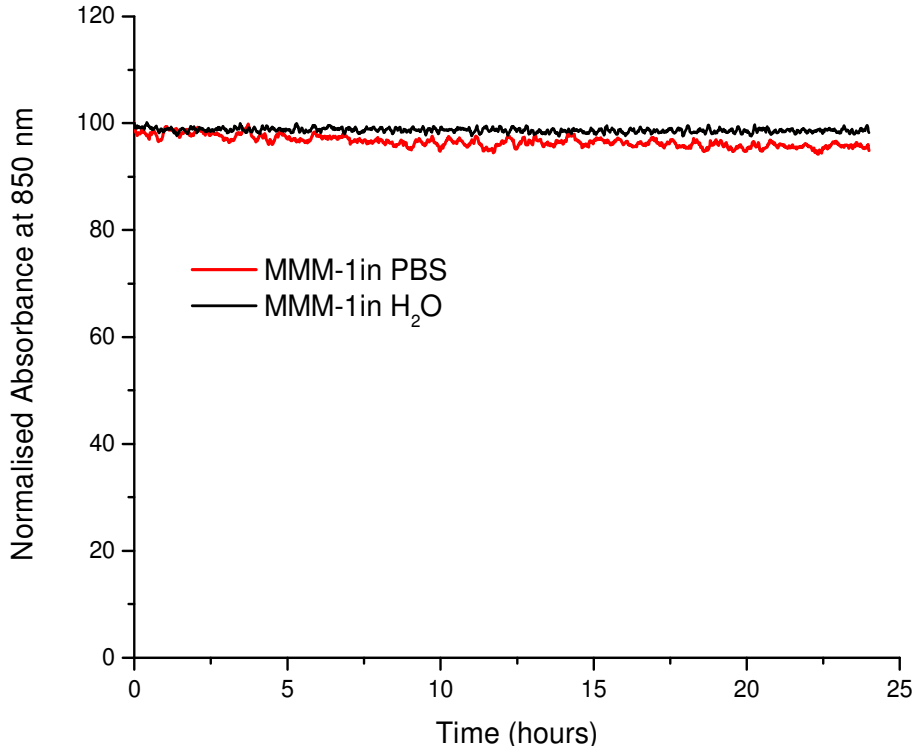

Figure 4.29 Evolution of **MMM-1** absorbance dispersed in water (black) and PBS (red) during 24 hours.

DLS measurements also confirmed that **MMM-1** had excellent colloidal stability in both water and PBS (**Figure 4.30**) after 21 days, since there was no apparent change in size or any sign of agglomeration. During this period the solution was kept in the fridge at 4 °C and the size of **MMM-1** was measured by DLS at the shown time points on non-filtered samples. DLS would show an increase in size if the structures would not be stable. The **MMM-1** solutions in PBS were monitored for another 2 months while kept in the fridge. During this time the solutions remained transparent and the measured average hydrodynamic diameter at 2 months was 93.4 ± 1.2 nm.

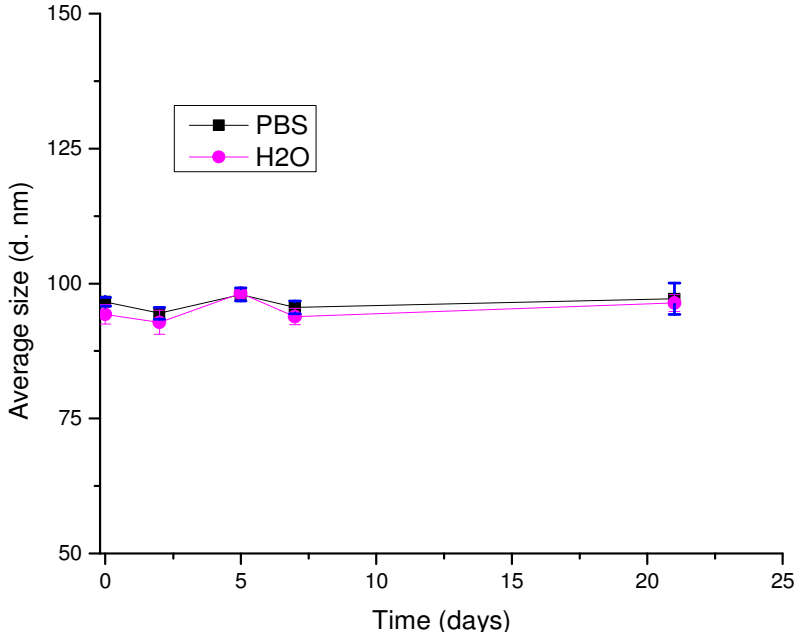

Figure 4.30 Size stability evaluations of **MMM-1** magnetic structures using DLS measurements at different time points.

The size stability and zeta potential values of **MMM-1** were also evaluated at different pH values and the results are shown in **Figure 4.31**. The average size of **MMM-1** did not show a significant change upon pH variation. The measured hydrodynamic diameter values were from 89.2 ± 0.9 nm to 96.3 ± 2.5 nm. The negative charge on the surface of **MMM-1** due to the deprotonation of the COOH groups was confirmed using zeta potential measurements. As can be seen in **Figure 4.31**, the zeta potential values at pH 8 and pH 10 were -15.8 ± 0.2 mV and -19 ± 1.2 mV respectively. The surface negative charges are also responsible for enhanced the stability of the **MMM-1** in solution together with the steric stabilisation by the polymeric chains. The isoelectric point for **MMM-1** was around pH 6. Comparing with the pKa of 4.16 for succinic acid the increase it was found reasonable considering that pKa values can vary depending on the molecular weight and the polymeric conformational changes.

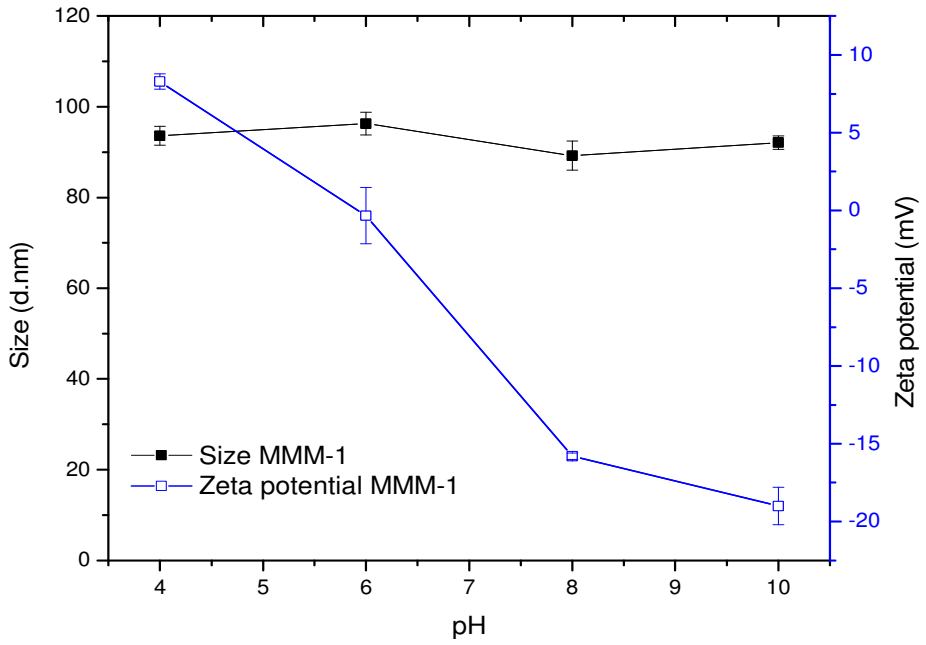

Figure 4.31 Evaluation of size stability and zeta potential of **MMM-1** in aqueous solution at different pH values.

Taken together the results from the absorbance assay, DLS and zeta potential measurements in different dispersion media show that the **MMM-1** structures have good colloidal stability properties. **MMM-1** solutions were found stable in PBS (buffer which mimics the ionic strength of the body fluids 135 mM NaCl, 27 mM KCl) and at pH values found in the biological environments (between 5 and 8). These are typical conditions used in biological applications.

The hydrodynamic diameter of **MMM-1** is well within the acceptable size range (20-200 nm) for *in vivo* applications and preferential accumulation at tumour sites through an enhanced permeability and retention effect (EPR).[47-48] Therefore the **MMM-1** structures could be suitable as MRI contrast agents and tumour diagnosis markers based on the EPR effect.

4.3.6 Fluorescence labelling of MMMs structures

To be able to trace the **MMMs** during cellular uptake studies, a red fluorescent dye, octadecyl Rhodamine B (Rh), was selected to be encapsulated into the **MMMs** during the initial self-assembly process. The Rh fluorescent molecule is widely used to label cell membrane because the C_{18} long alkyl tail inserts within the lipid bilayer while the fluorophore stays at the aqueous interface. This behaviour was previously reported in the case of poly(styrene)-b-poly(methacrylic acid) (PS-PMA) polymeric micelles when Rh strongly binds at the core-shell interface of the micelle with the alkyl tail inserted in the PS core.[49] In the case of the magneto-micellar system **MMM-1** the C_{18} aliphatic tail of the fluorescent dye will interact with the hydrophobic segment of the amphiphilic polymer, the oleic acid and together will stabilise the surface of SPIONs (**Figure 4.32**).

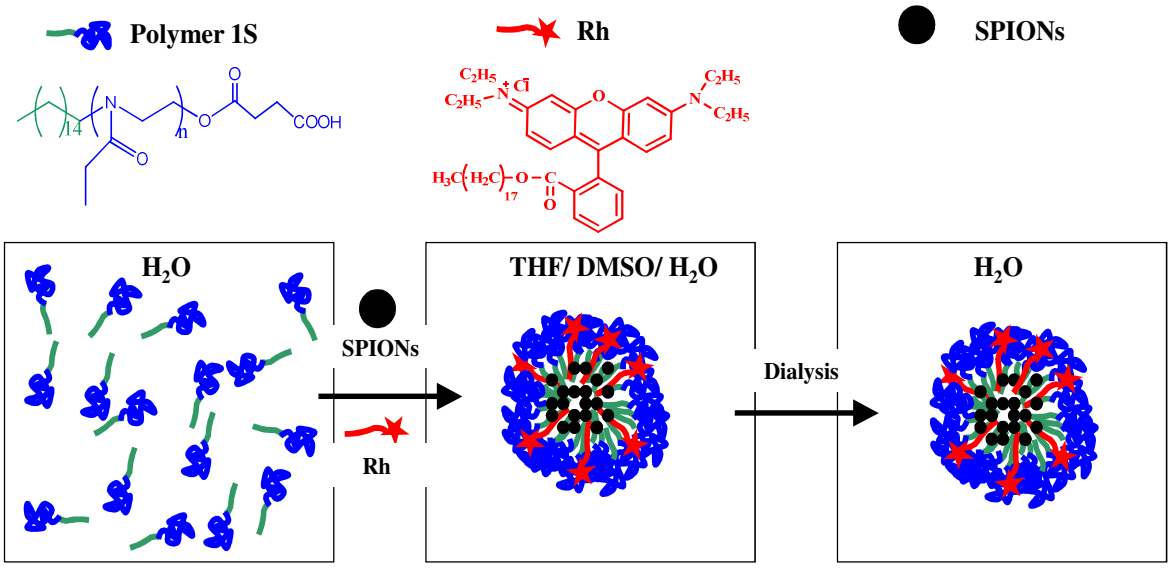

Figure 4.32 Schematic representation of the synthesis of fluorescent magneto-micelles (**Rh-MMMs**).

Fluorescent magneto-micelles were prepared by assembly of **Polymer 1S**: SPIONs: Rh at 10:1:0.01 wt ratio. The fluorescent sample was denoted as **Rh-MMM.**

To confirm the incorporation of the fluorescent dye within the magneto-micellar structures, the **Rh-MMMs** were analysed using UV/Vis absorbance and fluorescence spectroscopy. The absorption spectrum of the **Rh-MMM** showed the characteristic maximum absorption for the Rh fluorescent molecule at 565 nm as seen in **Figure 4.33a.**

Figure 4.33b shows the fluorescence emission spectrum of **Rh-MMM** at the excitation wavelength of 565 nm showing the maximum emission wavelength at 605 nm for **Rh-MMM**. A red shift was observed for the **Rh-MMM** structures compared with the reported emission of the dye (λ_{emi} =580 nm measured in methanol, from the manufacturer). The red emission shift confirmed the assembly of the Rh dye tail with the hydrophobic segments of the polymer. Similar shifts in emission have been previously reported in other systems when there is an interaction between the dye and the surrounding hydrophobic environment, in this case, the hydrophobic segment of the polymer and hydrophobic ligands on SPIONs.[50-51]

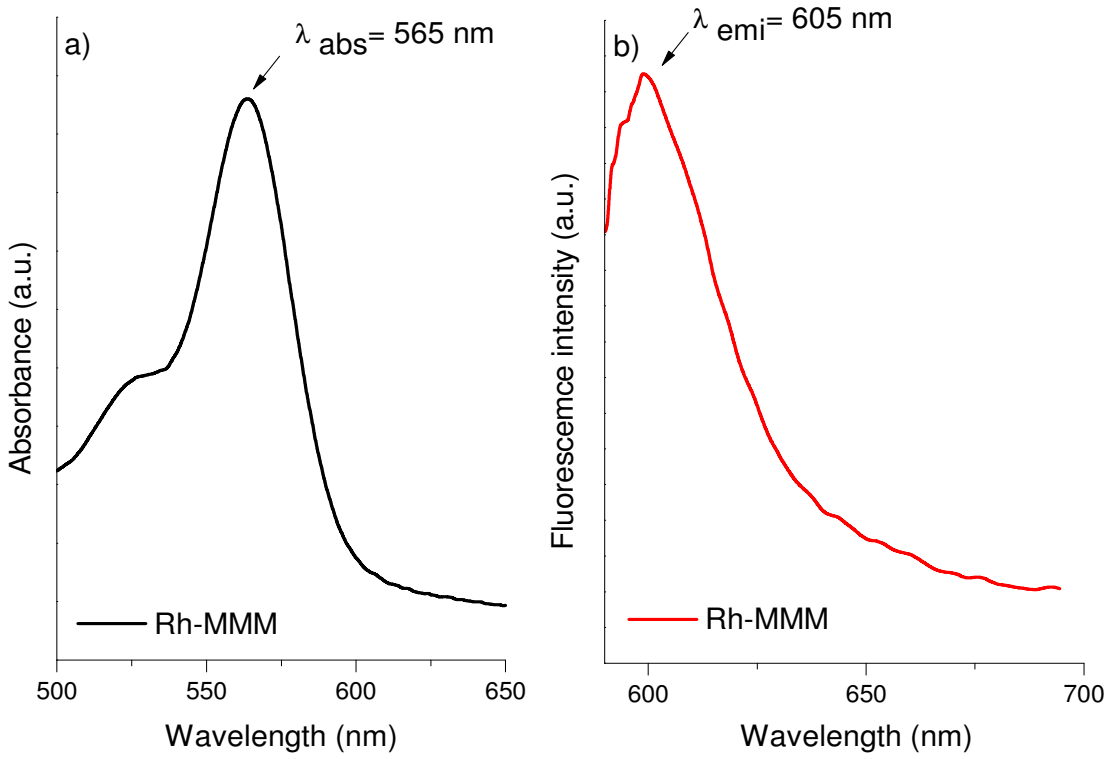

Figure 4.33 Spectrophotometric characterisation of fluorescently labelled **Rh-MMM** micellar structures. a) UV/Vis spectrum showing the maximum absorbance at 565 nm indicating the presence of the Rh dye, b) fluorescence emission spectrum at λ_{ex}=565 nm showing intensity maximum at 605 nm confirming the effective fluorescence labelling of magneto-micelles.

DLS studies of the **Rh-MMM** confirmed the presence of monodisperse nanoparticles with an average diameter of 91.2 ± 1.8 nm. Compared with the non-fluorescent **MMM-1** structures, the labelling with the fluorescent molecule Rh did not affect the size and stability of the micelles. **Figure 4.34** shows the DLS size measurements of the fluorescent (**Rh-MMM**) and the corresponding non-fluorescent (**MMM-1**) samples. Both distributions are overlapping with each other, confirming that the addition of Rh dye did not change the particle/micelle assembly.

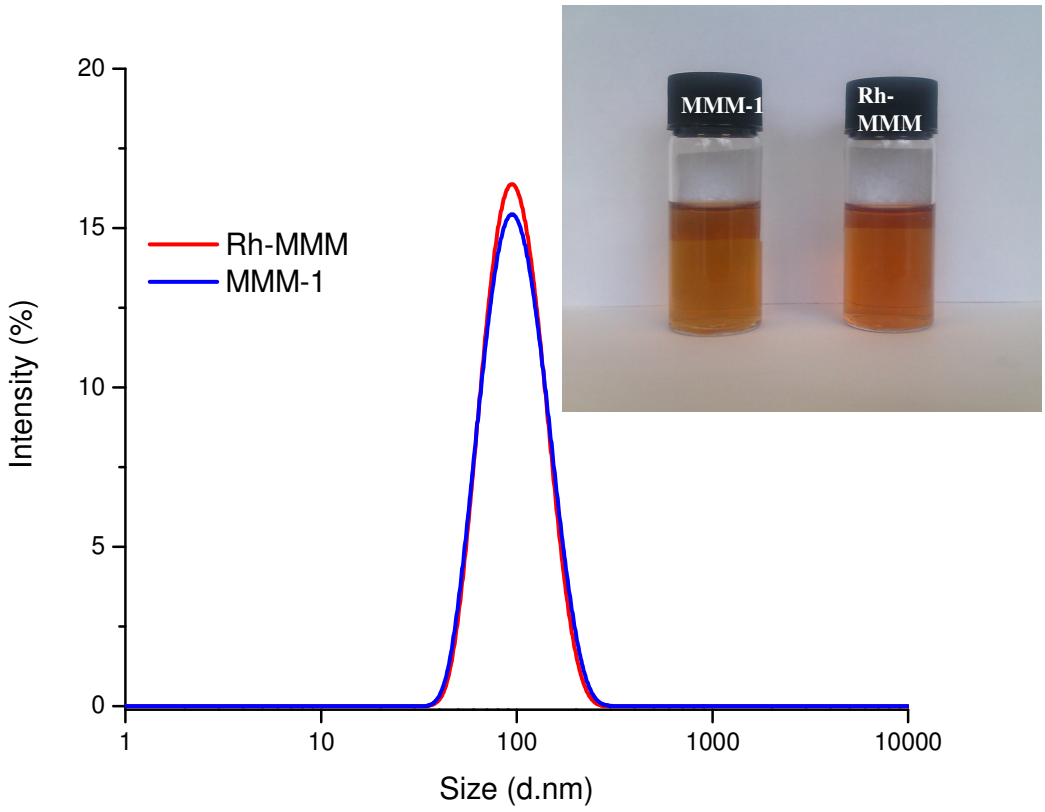

Figure 4.34 Size distribution of the fluorescent **Rh-MMM** (red) and non-fluorescent **MMM-1** (blue) structures.

The fluorescence signal of the **Rh-MMM** structures could not be quantified due to the emission shift. However, the fluorescently labelled **Rh-MMM** displayed strong fluorescence intensities and the signal was found to be sufficient to detect the presence of the magneto-micelles during cell labelling experiments (**Figure 4.35**).

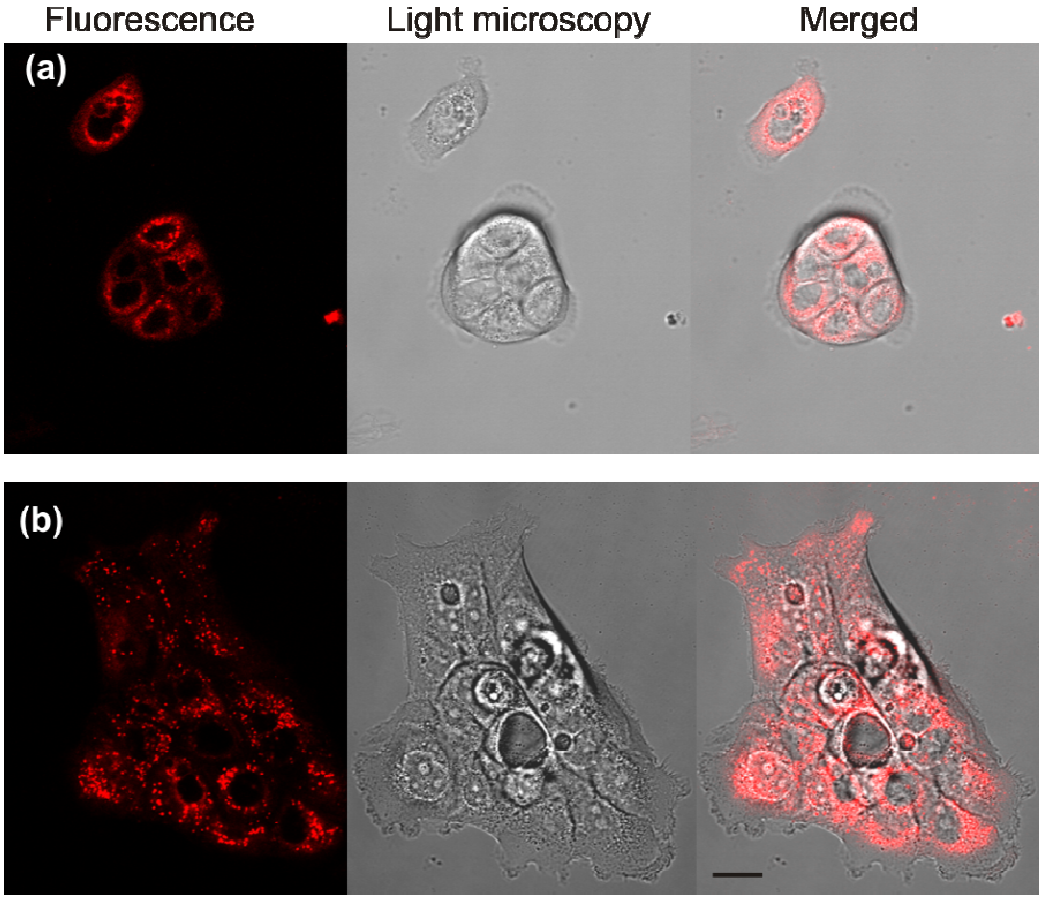

Figure 4.35 Fluorescence microscopy and optical images of BxPC-3 human pancreatic cancer cells incubated with **Rh-MMM** for 12 hours at (a) 0.5 mM Fe and (b) 0.125 mM Fe. Scale bar represents 10 μm.

Cell labeling studies were conducted at different concentrations of **Rh-MMM** for a fixed 12 hours incubation time using human pancreatic cancer cells BxPC-3. Live cell confocal scanning lased microscopy images showed that fluorescence intensities increased with increasing concentrations of **Rh-MMM** hence rhodamine. After the 12 hour the BxPC-3 cells presented the characteristic fluorescent signal associated with the accumulation of nanoparticles within the cells in the perinuclear region, most probably in endosomal vesicles. The fluorescent signal was sufficient to detect the nanoparticles

even at concentrations as low as 0.125 mM Fe, corresponding to a theoretical concentration of Rh dye of 85 nM.

4.3.7 Protein and antibody bioconjugations to fluorescently labelled magneto-micelles (Rh-MMMs)

The **Rh-MMMs** have multiple reactive carboxylic acid surface groups originating from the polyoxazoline coating. The carboxylic acid groups can be chemically conjugated under mild conditions with primary amino groups *via* carbodiimide coupling with EDC/sulfo-NHS, providing a convenient route for coupling of amine containing bioactive molecules such as proteins and antibodies. EDC can react with the carboxylic acid groups to form a reactive O-acylisourea intermediate. The addition of sulfo-NHS stabilizes the intermediate by converting it to an amine-reactive sulfo-NHS ester, thus increasing the efficiency of EDC-mediated coupling reactions. This succinimidyl activated species can then react with a nucleophile such as a primary amine to form an amide bond.[52]

Rh-MMMs were covalently conjugated with two model proteins (BSA and CytC) and a model antibody molecule (IgG) to demonstrate the protein immobilisation capability and the chemical reactivity of the carboxylic acid groups. The bioconjugation reactions were carried out at pH 7.4 in order to maintain the stability of **Rh-MMMs** during the EDC and sulfo-NHS mediated coupling. The EDC/sulfo-NHS coupling reactions had been reported to occur with high efficiency at pH values between 4.5 and 7.5.[52] When performed at neutral pH the sulfo-NHS-ester reactions were usually performed in phosphate-buffered saline (PBS) at pH 7.2-7.5.[53] Using a 7.4 pH buffer allowed to

minimise the positive charges of the amine groups on protein molecules and therefore increase their reactivity towards the succinimidyl activated species. Using this method stable protein or antibody conjugates were prepared. After the conjugation reactions the formed micelle-conjugates showed a hydrodynamic size increase 117.3 ± 2.1 nm for **Rh-MMM-BSA**, 96.2 ± 1.8 nm for **Rh-MMM-CytC** and 126.4 ± 1.8 nm for **Rh-MMM-IgG** (**Table 4.2**). The size increase was attributed to the conjugation of the protein and antibody molecules to the nanoparticle surface. Zeta potential measurements were utilised to characterise the protein and antibody conjugates. It was found that the **Rh-MMM-BSA** conjugates were more negatively charged than **Rh-MMMs** due to the overall negative charge of BSA at pH 7.4 (isoelectric point 4.8). On the other hand in case of the **Rh-MMM-CytC** conjugates an increase in zeta potential was observed due to the positively charged CytC proteins (isoelectric point 10.2). The zeta potential of the **Rh-MMM-IgG** conjugates was not influenced by the presence of coupled antibody molecules as the IgG isoelectric point is between 6.5 and 7.5.[54]

A standard Bradford protein assay method was used to quantify the concentration and the conjugation rate of protein or antibody to the **Rh-MMMs**. The unreacted biomolecules were separated from the micelle-conjugates using centrifugal filtration and mixed with the assay to give a blue coloured complex. The protein concentration was measured by matching to standard calibration curves of known protein concentrations in each case. The conjugation rate was calculated using the formula:

$$Conjugation\ (\%) = \frac{Conjugated\ protein\ concentration}{Initial\ protein\ concentration} \times 100$$

The resulting conjugation rates from the coupling reaction with each type of protein and antibody are shown in **Table 4.2**. The EDC/sulfo-NHS coupling reactions are reported to have high efficiencies up to 95%.[55] The average conjugation rate with BSA, CytC and IgG in this case was 88%. The EDC/sulfo-NHS conjugation rates were found to be comparable for the three types of bioactive molecules involved. At the same time the conjugation rates were comparable with the values reported by others.[55-56]

Table 4.2 Z-average hydrodynamic sizes, zeta-potential and bioconjugation rates of **MMM-1**, **Rh-MMM**, **Rh-MMM-BSA**, **Rh-MMM-CytC** and **Rh-MMM-IgG**

Sample	Z-average diameter[a] (d/nm)	Zeta potential (mV)	Bioconjugation rate[b] (%)
MMM-1	91.8 ± 1.5	-22.5 ± 0.2	-
Rh-MMM	91.2 ± 1.8	-19.2 ± 0.8	-
Rh-MMM-BSA	117.3 ± 2.1	-33.7 ± 0.3	88.6 ± 0.7
Rh-MMM-CytC	96.2 ± 1.8	-12.8 ± 0.2	87.3 ± 0.6
Rh-MMM-IgG	126.4 ± 1.8	-20.8 ± 0.9	88 ± 1.2

[a]Average intensity–weighted diameter and standard deviation values obtained from 3 measurements using a Zetasizer DLS. [b]Average and standard deviation values of bioconjugation obtained from three independent reactions.

The results from particle size and zeta-potential measurements as well as from Bradford protein quantification assay showed that the **Rh-MMMs** were successfully labelled with bioactive molecules using carboxylic acid groups available on the micelle surface.

4.3.8 Evaluation of the cytotoxicity of Rh-MMMs

When evaluating toxicity it is necessary to consider how the assembled SPION-polymer system will interact with the body. To evaluate the potential for biomedical applications of the **Rh-MMMs** both *in vitro* and *in vivo*, their potential toxicity was tested using the standard proliferation MTS assay on two different cell lines (**Figure 4.36**).

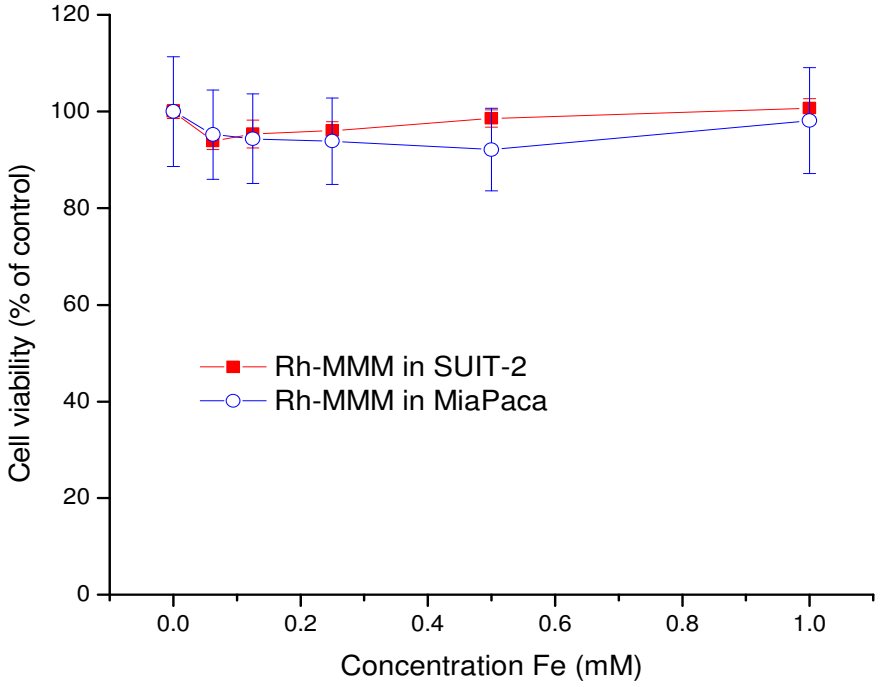

Figure 4.36 Cell viability SUIT-2 and MiaPaca cells after 48 hour incubation with **Rh-MMM** at various concentrations. The results are presented as average ± standard deviation.

Human pancreatic cancer cells (SUIT-2 and MiaPaca) were used to examine the cytotoxicity *in vitro* following exposure to **Rh-MMM** at different Fe concentrations. As shown in **Figure 4.36**, there was little effect of the **Rh-MMM** on the cell viability in the nanoparticle range evaluated, 0 - 1 mM Fe. The average viability of both types of cells treated with **Rh-MMMs** was above 90% for all concentrations. The cytotoxicity data was analysed using Student's t test and no significant difference was observed between all groups ($p>0.05$).

It should be noted that at concentrations between 0.1-0.125 mM Fe that are typically used in cell labelling and targeting experiments the cytotoxicity values were above 95% for both cell lines.

4.3.9 Cancer cell targeting experiments using antibody-magneto micelles conjugates

To evaluate the potential for specific targeting, Rh-MMMs were conjugated with a specific antibody, namely CA19.9, resulting in **Rh-MMM-CA19.9** conjugates. This antibody is known to bind to the CA19.9 antigen which is highly expressed on the surface of BxPC-3 cells, making it an accessible target for binding and imaging.[57] Therefore BxPC-3 cells were incubated with **Rh-MMM-CA19.9** nanoparticles and two controls: non-conjugated **Rh-MMM** and nonspecific **Rh-MMM-ISO** nanoparticles, where ISO stands for isotype control antibody-that does not have no binding specificity for CA19.9 antigen.

These experiments were performed by Mr. Paul Sykes at the Liverpool Cancer Research UK Centre, Department of Molecular and Clinical Cancer Studies.

The specific cellular binding and uptake was monitored during an 18 hours live cell experiment using a confocal laser scanning microscope which was programmed to take image slices every 2 minutes. Representative confocal images of the nanoparticles cell binding at 2 and 6 hours are show in **Figure 4.37**. The images showed that the **Rh-MMM-CA19.9** magneto-micelles are able to specifically localise and bind to the BxPC-3 cells. These nanoparticles were distributed into the cell cytoplasm in the perinuclear region, forming localised clusters which are usually attributed to endosomal uptake.

Cells incubated with the controls showed only minimal uptake of the non-conjugated and nonspecific nanoparticles. The cellular uptake of nonspecific nanoparticles was also observed in the previous experiments presented in Chapter 3 and by other groups during targeting experiments.[58-59] However, the **Rh-MMM-CA19.9** conjugates showed at all times more binding avidity due to the antibody-antigen interactions which positively influenced their internalisation into the cells. Therefore, specific targeting to CA19.9 expressing cells was successfully achieved by conjugation of the **Rh-MMMs** with the CA19.9 antibody.

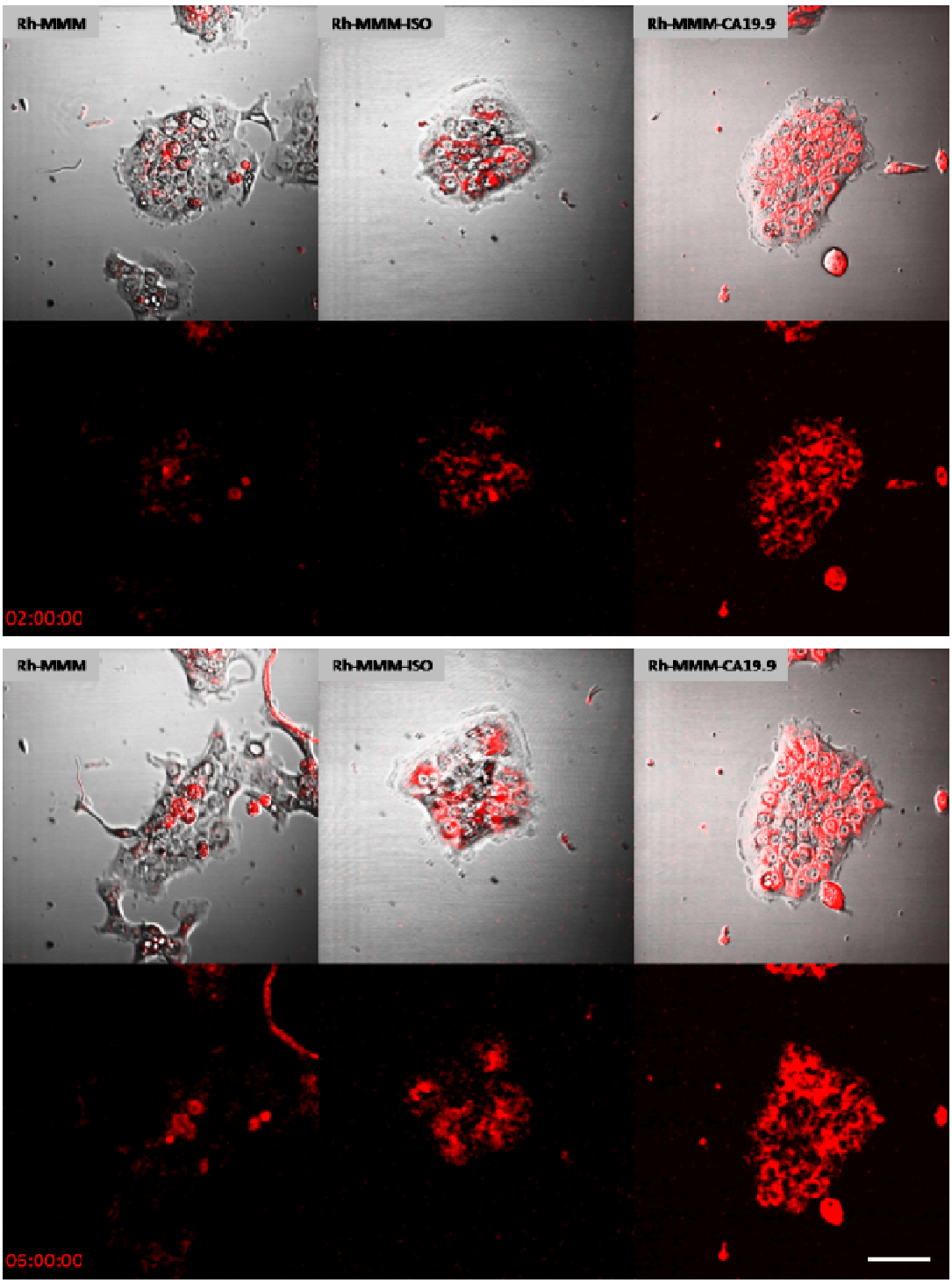

Figure 4.37 Confocal microscopy images acquired at 2 and 6 hours of BxPC-3 cells expressing the CA19.9 receptor which were incubated with **Rh-MMM**, **Rh-MMM-ISO** and **Rh-MMM-CA19.9** magneto-micelles at 0.1 mM Fe. Scale bar represents 50 μm.

The results presented here demonstrate that the conjugation of the magneto-micelles with a targeting ligand such as CA19.9 antibody is essential for specific binding and uptake into pancreatic cancer cells. High levels of uptake could be achieved for **Rh-MMM-CA19.9**, **Figure 4.37**, thus setting these nanoparticles as potential candidates for use as targeted imaging agents.

4.3.10 MRI capability of Rh-MMM

The MRI capability of **Rh-MMM** was evaluated by T_2 relaxation time measurements. These measurements were carried out using a 7 T horizontal bore Magnex Scientific imaging system, operating at 300 MHz resonant frequency. The T_2 relaxation times were measured for increasing concentrations of nanoparticles ranging from 0.05 to 0.15 mM Fe. The **Rh-MMM** magneto-micelles were measured in deionised water and blanks consisting of deionised water were taken as a control. MRI analysis was performed at TR 5000 ms and multiple TE values of 11, 33, 55 and 77 ms for various concentrations of nanoparticles. These measurements were performed by Ms. Karen Davies at the Department of Imaging Science and Biomedical Engineering, University of Manchester. Their efficiency as T_2 MRI enhancement agents was determined by calculation of the r_2 relaxivities as the slopes of the linear fit of the inverse relaxation times as a function of iron concentration (**Figure 4.38**).

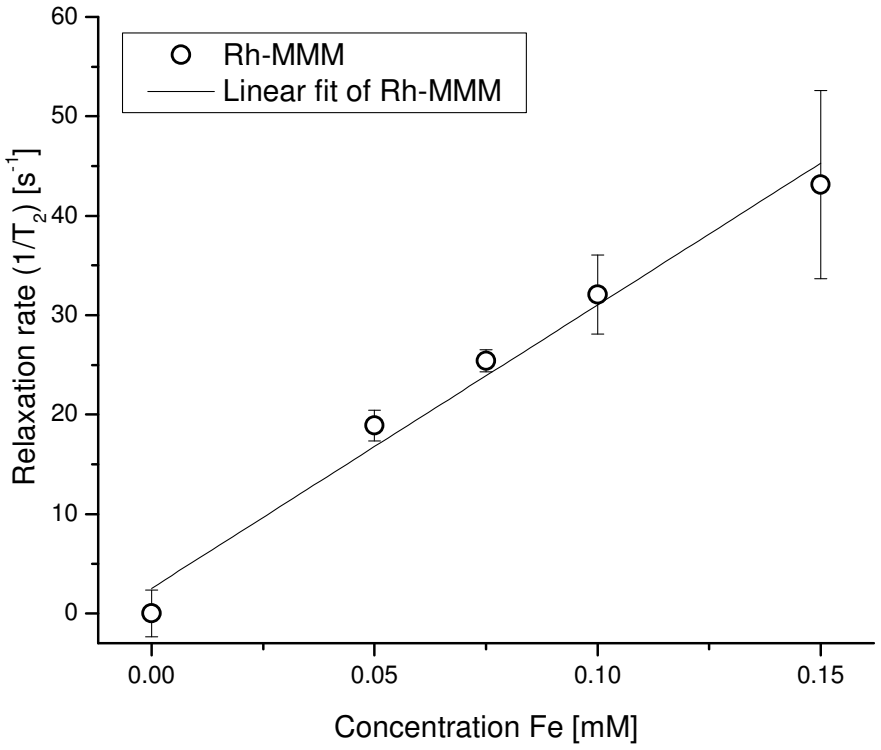

Figure 4.38 Inverse transverse relaxation times $1/T_2$ for **Rh-MMM** magneto-micelles nanoparticles as a function of the iron molar concentration.

The inverse relaxation times varied linearly with the iron concentration[60] and the r_2 relaxivity value for **Rh-MMM** was found to be 285 ± 9 $s^{-1}mM^{-1}$. The relaxivity value is two times higher than that of the clinical contrast agent Feridex I.V. (reported value of 148 ± 2, measured at 7 T).[61] The increased value of r_2 is attributed to the effect of clustering of SPIONs within polymeric micelles.[62-63] Therefore is interesting to compare the results obtained in this work to those reported for other SPION clusters encapsulated in polymeric micellar. For example, Ai *et al.*[63] have shown that increasing the SPIONs loading and the SPION size within polymeric micelles, the r_2 values can vary from 25 to 471 $s^{-1}mM^{-1}$. The investigators obtained a similar r_2 value with the one obtained in this work for 8 nm SPIONs encapsulated into the hydrophobic cores of polymeric micelles.[63]

In another study it was reported that a PEG based magneto-micellar system having a diameter of approximately 97 nm and a SPIONs loading of 15%, similar size and loading to the ones obtained in this work, produces an r_2 relaxivity of 254 $s^{-1}mM^{-1}$.[64] The results quoted in these studies support those reported in the present work. They indicate that clusters of SPIONs have enhanced the transverse relaxivity.

Figure 4.39 shows the T_2-weighted MRI image (TE/TR 11/5000 ms) of the analysed nanoparticles at various iron molar concentrations.

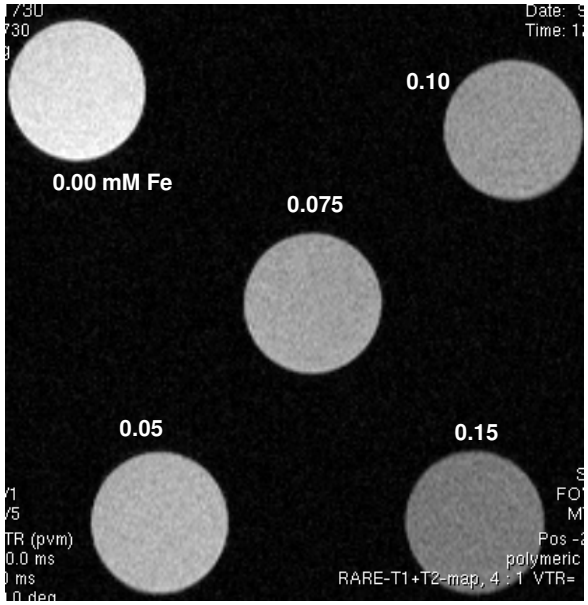

Figure 4.39 T_2 weighted magnetic resonance images of **Rh-MMM** in deionised water at various molar iron concentrations (0.05, 0.075, 0.1 and 0.15 mM) and at 25 °C, 7 T MRI, TR=5000 ms, TE=11 ms. Blanks consisting of deionised water were taken as a control.

The T_2 weighted image showed that the **Rh-MMM** nanoparticles produce an observable change in T_2 signal. The image appears darker, hypointensity, as the iron molar concentration increases. The nanoparticles produce a darker contrast effect at concentrations as low as 0.05 mM Fe which could lower the administration dose.

These results confirmed the effective MRI contrasting capabilities of the magneto-micelles. Therefore, the **Rh-MMMs** potentially present suitable properties for use as MRI contrast enhancement agents.

4.4 Conclusions

The micellisation strategy presented in this chapter is an effective method to develop stable and multifunctional magneto-micelles (**MMMs**). Monodisperse hydrophobic SPIONs coated with a monolayer of oleic acid were successfully synthesised and transferred into aqueous solutions using synthetic amphiphilic polymers based on poly(2-ethyl-2-oxazoline). The polymers comprised of a short C_{16} hydrophobic segment and a 4.5k hydrophilic polymer segment with a carboxylic acid end functional group. Using this polymer structure various formulations of **MMMs** were prepared with average hydrodynamic diameters between 91 and 140 nm. The prepared **MMMs** have sizes below the accepted limit of 200 nm which is reported as effective for extravasations and accumulation at the tumour sites by the EPR effect.[46]

The stability of the prepared **MMMs** was intensively studied in media similar to physiological conditions. The **MMMs** were found stable in water, phosphate buffered saline (ionic strength which mimics the body fluids) as well as at different pH values. The **MMMs** did not exhibit any sign of aggregation or size change for more than 2 months.

Fluorescent tags were introduced in the structure of the magneto-micelles during the assembly process to provide fluorescence imaging capabilities to the nanoparticles. The fluorescent signal was used to monitor the nanoparticles localisation during targeting or cell labelling experiments. The carboxylic acid groups on surface of **MMMs** offered an

advantageous possibility for coupling of various bioactive molecules through bioconjugation reactions. The CA19.9 antibody-labelled **MMMs** were able to efficiently target and internalise into pancreatic cancer cells expressing the CA19.9 antigen. Their performance in the relaxivity measurements suggested that the clustering effect of the SPIONs within the polymeric micelle core is particularly favourable for enhancing the T_2 contrast on MRI images. The development of multifunctional nanoparticles with complementary properties such as targeting, optical and MRI imaging is a challenging task. This is because it requires meeting the different needs without compromising the efficiency of either one. Overall the results have shown that SPIONs, bioinspired polymers, fluorescent molecules and targeting ligands can be incorporated into stable magneto-micelles which have the expected targeting and dual imaging capabilities.

4.5 References

1. Y. X. J. Wang, S. M. Hussain, G. P. Krestin, Superparamagnetic iron oxide contrast agents: physicochemical characteristics and applications in MR imaging, *Eur Radiol*, **2001**, 11, 2319-2331.
2. N. Tran, T. J. Webster, Magnetic nanoparticles: biomedical applications and challenges, *J Mater Chem*, **2010**, 20, 8760-8767.
3. J. Xie, G. Liu, H. S. Eden, H. Ai, X. Y. Chen, Surface-Engineered Magnetic Nanoparticle Platforms for Cancer Imaging and Therapy, *Accounts Chem Res*, **2011**, 44, 883-892.
4. H. B. Na, I. C. Song, T. Hyeon, Inorganic Nanoparticles for MRI Contrast Agents, *Adv Mater*, **2009**, 21, 2133-2148.
5. A. J. Cole, V. C. Yang, A. E. David, Cancer theranostics: the rise of targeted magnetic nanoparticles, *Trends Biotechnol*, **2011**, 29, 323-332.
6. S. H. Sun, H. Zeng, D. B. Robinson, S. Raoux, P. M. Rice, S. X. Wang, G. X. Li, Monodisperse MFe_2O_4 (M = Fe, Co, Mn) nanoparticles, *J Am Chem Soc*, **2004**, 126, 273-279.
7. J. Park, K. J. An, Y. S. Hwang, J. G. Park, H. J. Noh, J. Y. Kim, J. H. Park, N. M. Hwang, T. Hyeon, Ultra-large-scale syntheses of monodisperse nanocrystals, *Nat Mater*, **2004**, 3, 891-895.
8. T. Hyeon, S. S. Lee, J. Park, Y. Chung, H. Bin Na, Synthesis of highly crystalline and monodisperse maghemite nanocrystallites without a size-selection process, *J Am Chem Soc*, **2001**, 123, 12798-12801.

9. T. Hyeon, Chemical synthesis of magnetic nanoparticles, *Chem Commun*, **2003**, 927-934.

10. D. K. Kim, Y. Zhang, W. Voit, K. V. Rao, M. Muhammed, Synthesis and characterization of surfactant-coated superparamagnetic monodispersed iron oxide nanoparticles, *J Magn Magn Mater*, **2001**, 225, 30-36.

11. J. Park, M. K. Yu, Y. Y. Jeong, J. W. Kim, K. Lee, V. N. Phan, S. Jon, Antibiofouling amphiphilic polymer-coated superparamagnetic iron oxide nanoparticles: synthesis, characterization, and use in cancer imaging in vivo, *J Mater Chem*, **2009**, 19, 6412-6417.

12. J. H. Park, G. von Maltzahn, E. Ruoslahti, S. N. Bhatia, M. J. Sailor, Micellar hybrid nanoparticles for simultaneous magnetofluorescent imaging and drug delivery, *Angew Chem Int Ed Engl*, **2008**, 47, 7284-7288.

13. X. Y. Chen, R. Wong, I. Khalidov, A. Y. Wang, J. Leelawattanachai, Y. Wang, M. M. Jin, Inflamed leukocyte-mimetic nanoparticles for molecular imaging of inflammation, *Biomaterials*, **2011**, 32, 7651-7661.

14. K. L. Hultman, A. J. Raffo, A. L. Grzenda, P. E. Harris, T. R. Brown, S. O'Brien, Magnetic resonance imaging of major histocompatibility class II expression in the renal medulla using immunotargeted superparamagnetic iron oxide nanoparticles, *Acs Nano*, **2008**, 2, 477-484.

15. A. Hucknall, S. Rangarajan, A. Chilkoti, In Pursuit of Zero: Polymer Brushes that Resist the Adsorption of Proteins, *Adv Mater*, **2009**, 21, 2441-2446.

16. R. Hoogenboom, Poly(2-oxazoline)s: A Polymer Class with Numerous Potential Applications, *Angew Chem Int Edit*, **2009**, 48, 7978-7994.

17. K. Knop, R. Hoogenboom, D. Fischer, U. S. Schubert, Poly(ethylene glycol) in Drug Delivery: Pros and Cons as Well as Potential Alternatives, *Angew Chem Int Edit*, **2010**, 49, 6288-6308.

18. S. Zalipsky, C. B. Hansen, J. M. Oaks, T. M. Allen, Evaluation of blood clearance rates and biodistribution of poly(2-oxazoline)-grafted liposomes, *J Pharm Sci-Us*, **1996**, 85, 133-137.

19. R. Konradi, B. Pidhatika, A. Muhlebach, M. Textort, Poly-2-methyl-2-oxazoline: A peptide-like polymer for protein-repellent surfaces, *Langmuir*, **2008**, 24, 613-616.

20. B. Pidhatika, M. Rodenstein, Y. Chen, E. Rakhmatullina, A. Muhlebach, C. Acikgoz, M. Textor, R. Konradi, Comparative Stability Studies of Poly(2-methyl-2-oxazoline) and Poly(ethylene glycol) Brush Coatings, *Biointerphases*, **2012**, 7, 1.

21. R. Hoogenboom, H. Schlaad, Bioinspired Poly(2-oxazoline)s, *Polymers*, **2011**, 3, 467-488.

22. H. Schlaad, C. Diehl, A. Gress, M. Meyer, A. L. Demirel, Y. Nur, A. Bertin, Poly(2-oxazoline)s as Smart Bioinspired Polymers, *Macromol Rapid Comm*, **2010**, 31, 511-525.

23. R. Luxenhofer, A. Schulz, C. Roques, S. Li, T. K. Bronich, E. V. Batrakova, R. Jordan, A. V. Kabanov, Doubly amphiphilic poly(2-oxazoline)s as high-capacity delivery systems for hydrophobic drugs, *Biomaterials*, **2010**, 31, 4972-4979.

24. C. H. Wang, C. H. Wang, G. H. Hsiue, Polymeric micelles with a pH-responsive structure as intracellular drug carriers, *J Control Release*, **2005**, 108, 140-149.

25. S. C. Lee, C. Kim, I. C. Kwon, H. Chung, S. Y. Jeong, Polymeric micelles of poly(2-ethyl-2-oxazoline)-block-poly(epsilon-caprolactone) copolymer as a carrier for paclitaxel, *J Control Release*, **2003**, 89, 437-446.

26. J. Tong, M. C. Zimmerman, S. M. Li, X. Yi, R. Luxenhofer, R. Jordan, A. V. Kabanov, Neuronal uptake and intracellular superoxide scavenging of a fullerene (C-60)-poly(2-oxazoline)s nanoformulation, *Biomaterials*, **2011**, 32, 3654-3665.

27. G. Volet, C. Amiel, Polyoxazoline adsorption on silica nanoparticles mediated by host-guest interactions, *Colloid Surface B*, **2012**, 91, 269-273.

28. X. Bories-Azeau, T. Merian, J. V. M. Weaver, S. P. Armes, H. J. W. van den Haak, Synthesis of near-monodisperse acidic homopolymers and block copolymers from hydroxylated methacrylic copolymers using succinic anhydride under mild conditions, *Macromolecules*, **2004**, 37, 8903-8910.

29. M. A. Hayat. *Basic techniques for transmission electron microscopy*, **1986**, Academic Press, Orlando.

30. R. W. Smith, V. Bryg, Staining polymers for microscopical examination, *Rubber Chem Technol*, **2006**, 79, 520-540.

31. S. H. Sun, H. Zeng, Size-controlled synthesis of magnetite nanoparticles, *J Am Chem Soc*, **2002**, 124, 8204-8205.

32. J. Xie, S. Peng, N. Brower, N. Pourmand, S. X. Wang, S. H. Sun, One-pot synthesis of monodisperse iron oxide nanoparticles for potential biomedical applications, *Pure Appl Chem*, **2006**, 78, 1003-1014.

33. R. M. Cornell, U. Schwertmann. *The iron oxides : structure, properties, reactions, occurrence, and uses*, **1996**, VCH, Weinheim ; New York.

34. A. R. West. *Solid state chemistry and its applications*, **1984**, Wiley, Chichester West Sussex ; New York.

35. M. Delample, F. Jerome, J. Barrault, J. P. Douliez, Self-assembly and emulsions of oleic acid-oleate mixtures in glycerol, *Green Chem*, **2011**, 13, 64-68.

36. G. Gnanaprakash, J. Philip, T. Jayakumar, B. Raj, Effect of digestion time and alkali addition rate on physical properties of magnetite nanoparticles, *J Phys Chem B*, **2007**, 111, 7978-7986.

37. R. De Palma, S. Peeters, M. J. Van Bael, H. Van den Rul, K. Bonroy, W. Laureyn, J. Mullens, G. Borghs, G. Maes, Silane ligand exchange to make hydrophobic superparamagnetic nanoparticles water-dispersible, *Chem Mater*, **2007**, 19, 1821-1831.

38. S. Verma, D. Pravarthana, One-Pot Synthesis of Highly Monodispersed Ferrite Nanocrystals: Surface Characterization and Magnetic Properties, *Langmuir*, **2011**, 27, 13189-13197.

39. M. Einzmann, W. H. Binder, Novel functional initiators for oxazoline polymerization, *J Polym Sci Pol Chem*, **2001**, 39, 2821-2831.

40. C. Weber, C. R. Becer, W. Guenther, R. Hoogenboom, U. S. Schubert, Dual Responsive Methacrylic Acid and Oligo(2-ethyl-2-oxazoline) Containing Graft Copolymers, *Macromolecules*, **2010**, 43, 160-167.

41. J. Koetz, S. Kosmella. *Polyelectrolytes, Polyelectrolytes and Nanoparticles*. **2007**, Springer Berlin Heidelberg, pp. 5-46.

42. B. S. Kim, J. M. Qiu, J. P. Wang, T. A. Taton, Magnetomicelles: Composite nanostructures from magnetic nanoparticles and cross-linked amphiphilic block copolymers, *Nano Lett*, **2005**, 5, 1987-1991.

43. R. J. Hickey, A. S. Haynes, J. M. Kikkawa, S. J. Park, Controlling the Self-Assembly Structure of Magnetic Nanoparticles and Amphiphilic Block-Copolymers: From Micelles to Vesicles, *J Am Chem Soc*, **2011**, 133, 1517-1525.

44. G. Gao, H. Heo, J. Lee, D. Lee, An acidic pH-triggered polymeric micelle for dual-modality MR and optical imaging, *J Mater Chem*, **2010**, 20, 5454-5461.

45. P. Chandrasekharan, D. Maity, C. X. Yong, K. H. Chuang, J. Ding, S. S. Feng, Vitamin E (D-alpha-tocopheryl-co-poly(ethylene glycol) 1000 succinate) micelles-superparamagnetic iron oxide nanoparticles for enhanced thermotherapy and MRI, *Biomaterials*, **2011**, 32, 5663-5672.

46. P. Couvreur, C. Vauthier, Nanotechnology: Intelligent design to treat complex disease, *Pharm Res-Dord*, **2006**, 23, 1417-1450.

47. H. Maeda, J. Wu, T. Sawa, Y. Matsumura, K. Hori, Tumor vascular permeability and the EPR effect in macromolecular therapeutics: a review, *J Control Release*, **2000**, 65, 271-284.

48. S. E. McNneil, Nanotechnology for the biologist, *J Leukocyte Biol*, **2005**, 78, 585-594.

49. J. Humpolickova, K. Prochazka, M. Hof, Z. Tuzar, M. Spirkova, Fluorescence correlation spectroscopy using octadecylrhodamine B as a specific micelle-binding fluorescent tag; Light scattering and tapping mode atomic force

microscopy studies of amphiphilic water-soluble block copolymer micelles, *Langmuir*, **2003**, 19, 4111-4119.

50. S. Santra, C. Kaittanis, J. Grimm, J. M. Perez, Drug/Dye-Loaded, Multifunctional Iron Oxide Nanoparticles for Combined Targeted Cancer Therapy and Dual Optical/Magnetic Resonance Imaging, *Small*, **2009**, 5, 1862-1868.

51. K. Nakashima, Y. Fujimoto, T. Anzai, Photoluminescent Properties of Octadecylrhodamine-B in Micelles of Low-Molecular-Weight Detergents and Water-Soluble Triblock Copolymers, *Photochem Photobiol*, **1995**, 61, 592-599.

52. G. T. Hermanson. *Bioconjugate techniques*, **1996**, Academic Press, San Diego.

53. Z. Grabarek, J. Gergely, Zero-Length Crosslinking Procedure with the Use of Active Esters, *Anal Biochem*, **1990**, 185, 131-135.

54. P. Kocbek, N. Obermajer, M. Cegnar, J. Kos, J. Kristl, Targeting cancer cells using PLGA nanoparticles surface modified with monoclonal antibody, *J Control Release*, **2007**, 120, 18-26.

55. S. M. Lee, N. Murthy, Targeted delivery of catalase and superoxide dismutase to macrophages using folate, *Biochem Bioph Res Co*, **2007**, 360, 275-279.

56. K. Wang, J. Ruan, Q. R. Qian, H. Song, C. C. Bao, X. Q. Zhang, Y. F. Kong, C. L. Zhang, G. H. Hu, J. Ni, D. X. Cui, BRCAA1 monoclonal antibody conjugated fluorescent magnetic nanoparticles for in vivo targeted magnetofluorescent imaging of gastric cancer, *J Nanobiotechnol*, **2011**, 9.

57. M. D. Girgis, T. Olafsen, V. Kenanova, K. E. McCabe, A. M. Wu, J. S. Tomlinson, CA19-9 as a Potential Target for Radiolabeled Antibody-Based

Positron Emission Tomography of Pancreas Cancer, *Int J Mol Imaging*, **2011**, 2011, 834515.

58. L. Yang, H. Mao, Y. A. Wang, Z. Cao, X. Peng, X. Wang, H. Duan, C. Ni, Q. Yuan, G. Adams, M. Q. Smith, W. C. Wood, X. Gao, S. Nie, Single chain epidermal growth factor receptor antibody conjugated nanoparticles for in vivo tumor targeting and imaging, *Small*, **2009**, 5, 235-243.

59. A. Villanueva, M. Canete, A. G. Roca, M. Calero, S. Veintemillas-Verdaguer, C. J. Serna, M. D. Morales, R. Miranda, The influence of surface functionalization on the enhanced internalization of magnetic nanoparticles in cancer cells, *Nanotechnology*, **2009**, 20.

60. M. A. Funovics, B. Kapeller, C. Hoeller, H. S. Su, R. Kunstfeld, S. Puig, K. Macfelda, MR imaging of the her2/neu and 9.2.27 tumor antigens using immunospecific contrast agents, *Magn Reson Imaging*, **2004**, 22, 843-850.

61. S. Chen, L. J. Wang, S. L. Duce, S. Brown, S. Lee, A. Melzer, S. A. Cuschieri, P. Andre, Engineered Biocompatible Nanoparticles for in Vivo Imaging Applications, *J Am Chem Soc*, **2010**, 132, 15022-15029.

62. E. S. G. Choo, X. S. Tang, Y. Sheng, B. Shuter, J. M. Xue, Controlled loading of superparamagnetic nanoparticles in fluorescent nanogels as effective T-2-weighted MRI contrast agents, *J Mater Chem*, **2011**, 21, 2310-2319.

63. H. Ai, C. Flask, B. Weinberg, X. Shuai, M. D. Pagel, D. Farrell, J. Duerk, J. M. Gao, Magnetite-loaded polymeric micelles as ultrasensitive magnetic-resonance probes, *Adv Mater*, **2005**, 17, 1949-1952.

64. S.-M. Lai, J.-K. Hsiao, H.-P. Yu, C.-W. Lu, C.-C. Huang, M.-J. Shieh, P.-S. Lai, Polyethylene glycol-based biocompatible and highly stable superparamagnetic iron oxide nanoclusters for magnetic resonance imaging, *J Mater Chem*, **2012**, 22, 15160-15167.

Chapter 5

Conclusions and outlook

In this work, multifunctional magnetic nanoparticles were developed for advanced biomedical applications, specifically for targeted detection of cancer cells using simultaneous optical and enhanced MRI contrast imaging.

Silanisation was demonstrated to be an efficient approach to introduce functional groups on the surface of SPIONs *via* covalent interactions. For example, amine and carboxylic acid-functionalised SPIONs were successfully synthesised and studied in terms of level of surface coverage, size, dispersability in aqueous solutions and magnetic properties. After coupling with fluorescent dyes and specific antibodies, these multifunctional nanoparticles were tested *in vitro* for their potential to target cancer cells. The conjugated antibody SPIONs demonstrated superior ability to localise and bind specific receptors on pancreatic cancer cells compared to the non-conjugated counterparts. These nanoparticles showed good relaxivity properties and contrast enhancement in T_2 weighted magnetic resonance imaging. This multifunctional system is adaptable for conjugation of any amino containing protein or peptide and therefore can be further used for targeting specific receptors on other types of cancer cells.

Besides covalent interactions, hydrophobic interactions were also employed to successfully synthesise multifunctional magneto-micelles incorporating four essential components (1) clustered hydrophobic SPIONs inside the core of the polymeric micelle for ultrasensitive MRI detection; (2) stealth polyoxazoline shell for long circulation blood time and bioavailability; (3) encapsulated fluorophores for fluorescent imaging

capabilities and (4) antibodies for target-specific detection of cancer cells. This colloidally stable and multifunctional system showed excellent ability to localise and accumulate in pancreatic cancer cells *via* receptor-mediated endocytosis. The clustering of SPIONs inside the magneto-micelles core provided enhanced relaxivity and magnetic resonance imaging capabilities compared with commercial MRI agents. These interesting properties make the multifunctional magneto-micelles promising candidates for future *in vivo* evaluations.

To take the work presented in this thesis forward, extensive biological evaluations of the prepared multifunctional magneto-micelles (MMMs) are needed, especially if these materials are to be translated into clinic. Characterisations could include:

(1) Screening of the colloidal stability of the MMMs in buffers containing proteins (similar protein concentrations found in the human blood) or in human serum;

(2) Evaluation of the iron oxide core degradation and iron leaching from the magneto-micelles – this could be achieved using model experiments and parameters which mimic the endosomal/lysosomal environment;

(3) Quantitative analysis of the nanoparticle uptake at the cellular level which could be achieved using special staining for iron and comparing with standard curves;

(4) Evaluation of the antibody binding efficiency during in vitro competitive inhibition experiments – this could be achieved by saturating the cell receptors with specific antibodies and then apply the antibody-nanoparticle conjugates.

Furthermore site specific antibody conjugation strategies could be developed. This would provide a greater level of control over the number and the orientation of the antibodies conjugated to the magneto-micelles. One approach could involve the fragmentation of the antibody molecule using proteolytic enzymes such as pepsin followed by a mild reduction of the disulfide bonds with mercaptoethylamine to obtain two separate F(ab') fragments. Each F(ab') fragment would have a reduced size ~55 kDa and exposed thiol functional groups which would enable an oriented attachment of the antibody onto the surface of the MMMs. The conjugations reactions could be followed by comparative in vitro studies of whole antibody-conjugated and fragmented antibody-conjugated SPIONs as targeting agents for over expressed tumour receptors.

To further extend the capabilities of the magneto-micellar system, hydrophobic anti-cancer drugs could be encapsulated in the hydrophobic core together with the SPIONs and fluorescent molecules. For example, paclitaxel or methotrexate could be used as model drugs to test their encapsulation efficiency. The successful encapsulation of the drugs could be followed by in vitro cytotoxicity evaluations as a measure of their therapeutic effectiveness and as targeted drug delivery agents in vivo. In such a scenario, the magneto-micellar system could have combined therapeutic and diagnostic applications (theranostic nanoparticles).

Other future work would include in vivo animal targeting studies, where antibody-conjugated and non-conjugated MMMs are directly injected into the blood stream followed by analysis of the tumour selective localisation capabilities. From histological analysis of tumour tissues the advantage of using specific antibody-conjugated MMMs could be identified. In vivo studies would allow for determination of the feasibility of

such MMMs to be used as targeted contrast agents for MRI. Additionally in vivo studies of the nanoparticle blood circulation times, their interaction with blood proteins and their clearance by the cells of the immune system would be the key mission for the future.

Overall the results presented in this work are a contribution to the development of multifunctional nanocomposites for biomedical applications and may open exciting opportunities for early stage diagnosis of cancer.

Appendix

Publications

Cristina I. Olariu, Humphrey H. P. Yiu, Laurent Bouffier, Taoufik Nedjadi, Eithne Costello, Steve R. Williams, Christopher M. Halloran, Matthew J. Rosseinsky, M*ultifunctional Fe_3O_4 nanoparticles for targeted bi-modal imaging of pancreatic cancer,* Journal of Materials Chemistry, 2011, 21, 12650–12659

Humphrey H. P. Yiu, Mark R. Pickard, **Cristina I. Olariu**, Stephen R. Williams, Divya M. Chari, Matthew J. Rosseinsky, *Fe_3O_4-PEI-RITC magnetic nanoparticles with imaging and gene transfer capability: development of a tool for neural cell transplantation therapies,* Pharmaceutical Research, 2012, 29, 1328–1343

Robert T. Woodward, **Cristina I. Olariu**, Erol A. Hasan, Humphrey H. P. Yiu, Matthew J. Rosseinsky, Jonathan V. M. Weaver, *Multi-responsive polymer-stabilized magnetic engineered emulsions as liquid-based switchable magneto-responsive actuators*, Soft Mater, 2011, 7, 4335–4340.

Humphrey H. P. Yiu, Stuart C. McBain, Zoe A. D. Lethbridge, Martin R. Lees, Iryna Palona, **Cristina I. Olariu**, Jon Dobson, *Novel magnetite-silica nanocomposite (Fe_3O_4-SBA-15) particles for DNA binding and gene delivery aided by a magnet array*, Journal of Nanoscience and Nanotechnology, 2011, 11, 3586-3591.

Participating conferences

Nanomedicine: Visions, Risks, Potential Conference 2012, April 19th-20th, Berlin-Brandenburg Academy of Sciences and Humanities, Germany- Poster presentation

ISMRM Workshop on MRI-Based Cell Tracking 2012, January 29th-Ferbruary 1st, Florida, USA- Poster presentation

Royal Society of Chemistry (RSC) Dalton Division Conference 2011, June 29th, Sheffield, United Kingdom - Oral presentation

Royal Society of Chemistry (RSC) Christmas Meeting 2010, December 20th-21st, UCL London, United Kingdom - Poster presentation

Third International NanoBio Conference 2010, August 24th- 27th, ETH Zurich, Switzerland - Poster presentation

Acknowledgements

Firstly, I would like to acknowledge my primary supervisor Professor Matt Rosseinsky for an exciting research topic, constructive feedback on my research progress and for giving me the opportunity to work in a challenging interdisciplinary research environment. The suggestions from Matt and my secondary supervisor Dr. John Claridge helped me understand the research goals and bridge modern materials chemistry and nanotechnology with biomedical sciences.

I wish to thank Dr. Humphrey Yiu and Dr. Laurent Bouffier for their ideas, guidance and support during the initial stage my PhD. I thank Dr. Erol Hasan and Dr. Donocadh Lydon for their input and help with polymer and organic chemistry.

I would like to thank collaborators Dr. Chris Halloran, Dr. Eithne Costello and Mr. Paul Sykes at the Liverpool Cancer Research UK Centre for their help and support with biological studies. I also want to thank Professor Steve Williams and Ms. Karen Davies at the Department of Imaging Science and Biomedical Engineering, University of Manchester for their support with MRI measurements.

I am especially thankful to Dr. Alexey Ganin, Dr. Solène Cauët and Miss Anita Peacock for their interest in my work, proof-reading of the thesis, helpful suggestions and vivid discussion.

I would also like to thank Ema, Dorel, Maria, Kyriakos and Chris for their constant support, enthusiasm and for making my life in Liverpool an enjoyable experience.

Finally, I want to express my gratitude to my mum, dad, sister and brother for all their help and support during tough times. “Mama şi tata, vă mulţumesc din suflet pentru încurajările voastre şi pentu că aţi fost alături de mine în toţi aceşti ani”.